

Humidity controlled water uptake and conductivities in polymeric mixed conductor thin films

Von der Fakultät Chemie der Universität Stuttgart zur Erlangung der Würde eines Doktors der Naturwissenschaften (Dr. rer. nat.) genehmigte Abhandlung

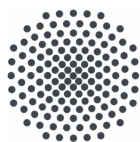
vorgelegt von

Matthias Eugen Andreas Wieland

aus Stuttgart

Hauptberichterin:	Prof. Dr. Sabine Ludwigs
Mitberichter:	Prof. Dr. Joris van Slageren
Prüfungsvorsitzender:	Prof. Dr. Guido Schmitz

Tag der mündlichen Prüfung: 17.03.2021



Universität Stuttgart



Institut für Polymerchemie
Lehrstuhl für Struktur und Eigenschaften polymerer Materialien

Erklärung über die Eigenständigkeit der Dissertation

Ich versichere, dass ich die vorliegende Arbeit mit dem Titel

*Humidity controlled water uptake and conductivities
in polymeric mixed conductor thin films*

selbständig verfasst und keine anderen als die angegebenen Quellen und Hilfsmittel benutzt habe; aus fremden Quellen entnommene Passagen und Gedanken sind als solche kenntlich gemacht.

Declaration of Authorship

I hereby certify that the dissertation entitled

*Humidity controlled water uptake and conductivities
in polymeric mixed conductor thin films*

is entirely my own work except where otherwise indicated. Passages and ideas from other sources have been clearly indicated.

Datum, Ort

Matthias Wieland

Danksagung

Die vorliegende Dissertation entstand im Zeitraum von Juni 2017 bis Dezember 2020 am *Institut für Polymerchemie am Lehrstuhl für Struktur und Eigenschaften polymerer Materialien* an der Universität Stuttgart. Im Folgenden möchte ich mich bei allen bedanken, die als Teil des Weges bis zum Gelingen dieser Arbeit beigetragen haben.

Zuallermeist möchte ich mich bei *Prof. Dr. Sabine Ludwigs* bedanken, die meine wissenschaftliche Ausbildung seit meiner Bachelorarbeit 2014 und meiner Masterarbeit 2017 geprägt hat. Für den Zeitraum der Promotion ab Juni 2017 möchte ich mich ganz herzlich für die Aufnahme in den Arbeitskreis, für die Möglichkeit an einem sehr spannenden Thema in einem Labor mit erstklassiger Ausrüstung zu forschen und für viele hilfreiche Diskussionen bedanken. Außerdem möchte ich mich für die Möglichkeit an den internationalen Konferenzen MRS 2018 und der ECChems 2019 teilzunehmen bedanken, die sehr wichtige fachliche und persönliche Erfahrungen für mich waren.

Bei *Prof. Dr. Guido Schmitz* und *Prof. Dr. Joris van Slageren* bedanke ich mich ganz herzlich für die Übernahme des Prüfungsvorsitzes und des Mitberichts meiner Promotionsprüfung.

Bei *Dr. Rotraut Merkle* vom *Max-Planck-Institut für Festkörperforschung* möchte ich mich herzlichst für viele praktische und theoretische Tipps zur Impedanzspektroskopie bedanken, die für das Gelingen dieser Arbeit sehr wichtig waren. Bei *Prof. Dr. Joachim Maier* vom *Max-Planck-Institut für Festkörperforschung* möchte ich mich für viel fachliche Hilfe bei der Erstellung der gemeinsamen Veröffentlichung bedanken.

Für die Synthese der in dieser Arbeit untersuchten konjugierten Polyelektrolyte bedanke ich mich bei *Roman Tkachov*.

Prof. Myung-Han Yoon und *Ji-Hwan Kim* vom *Gwangju Institute of Technology* (Republik Korea) danke ich für die langjährige Zusammenarbeit zu PEDOT:PSS-PVA Kompositmaterialien, leider musste mein Besuch am *Gwangju Institute of Technology* im Februar 2020 zur Vertiefung unserer Zusammenarbeit aufgrund der Corona-Pandemie abgesagt werden.

Boris Tschertsche, *Benjamin Hugues* und *Thomas Weigend* von den Werkstätten des In-

stituts für Physikalische Chemie möchte ich für viel Hilfe bei technischen Fragen und für Hilfe beim Aufbau des Messsystems danken.

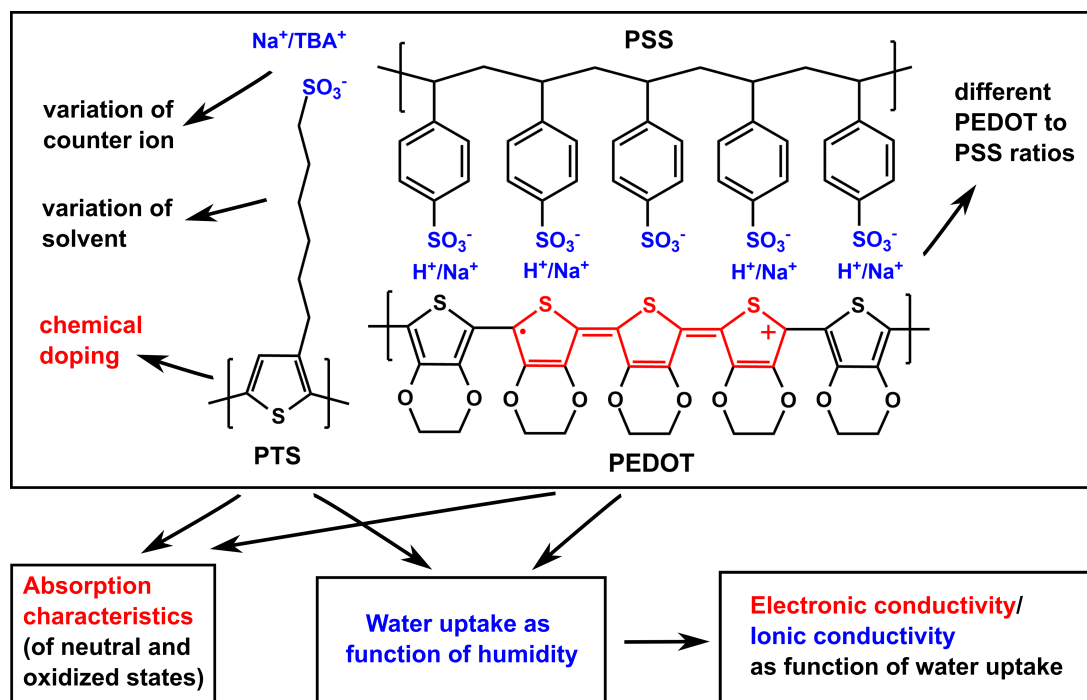
Bei *Jonas Groos* und *Prof. Dr. Michael Buchmeiser* vom *Lehrstuhl für Makromolekulare Materialien und Faserchemie* am *Institut für Polymerchemie* möchte ich mich für Atomemissionsspektroskopie Messungen bedanken.

Allen aktiven und ehemaligen Mitglieder des Arbeitskreis von Prof. Ludwigs danke ich für die schöne Zeit, auch wegen euch wird mir die Zeit meiner Promotion immer in guter Erinnerung bleiben. *Klaus Dirnberger* danke ich für viel fachliche Hilfe und ein offenes Ohr bei jeglichen Fragen und bei *Beatrice Omiecinski* möchte ich mich für ganz viel Einsatz und Hilfe bei der Bewältigung aller organisatorischer und formeller Aufgaben danken. Bei meinen Mitdoktoranden *Dr. Peter Reinold*, *Dr. Kirsten Bruchlos*, *Dr. Yannic Gross*, *Dr. Daniel Trefz*, *Jochen Kuhlmann*, *Carsten Dingler*, *Claudia Malacrida*, *David Gep Perth*, *Lukas Stein*, *Sherri Liu* und *David Neusser* bedanke ich mich für die schöne Zeit innerhalb und außerhalb des Labors. Im Speziellen möchte ich mich bei *Carsten Dingler* und *Claudia Malacrida* für viele aufschlussreiche und interessante Diskussionen und für die Zusammenarbeit bei den jeweiligen Veröffentlichungen bedanken. Meinen Masteranden *Qiulin Yu* und *Klaudia Opri* und Forschungspraktikanten *Philipp Jegl*, *Michael Herbst* und *Ayla Sirin* möchte ich mich für das Interesse an meinen Themen und viele spannende Ergebnisse aus ihren Arbeiten danken. *Simon Tannert* danke ich für das Erstellen von Origin Skripten und Hilfe beim Umgang mit den LabView Anwendungen. *Philipp Sliskovic* danke ich für Hilfe bei technischen und organisatorischen Fragen. Auch bei allen anderen aktiven und ehemaligen Mitgliedern des Arbeitskreises möchte ich mich für die schöne Zeit bedanken, dies sind *Dr. Miriam Goll*, *Dr. Christian Rothe*, *Daniel Bauer*, *Marc Schnierle*, *Qiwei Hu*, *Luca Scapinello*, *Sergio Gámez-Valenzuela*, *Yushi Lu*, *Tianao Guo*, *Zheyu Wu*, *Rong Wu*, *Claire Schlewitz*, *Andreas Stihl*, *Lydia Virginia*, *Xiuming Sun*, *Lea Veynand*, *Henry Müller*, *Jan Unseld* und *Lea-Sophie Hornberger*.

Meinen Kommilitonen *Jannik Sprengel*, *Peter Becker*, *Angelica Valadez* und *Felix Goerigk* danke ich für die vielen schönen Studienjahre und schöne Zeit innerhalb und außerhalb der Universität.

Meiner Familie danke ich für den Rückhalt und die Unterstützung auf meinem Lebensweg.

Summary



In the present work, two polymeric mixed conductor systems were examined, namely the conjugated polyelectrolyte poly(6-(thiophene-3-yl)hexane-1-sulfonate) (PTS) and the conjugated polymer/polyelectrolyte mixture poly(3,4-ethylenedioxythiophene):poly(styrene sulfonate) (PEDOT:PSS). Both systems contain electronically conducting conjugated polymer moieties and hydrophilic, ionically conducting polyelectrolyte moieties. In case of PTS, the ionically conducting polyelectrolyte and the electronically conducting conjugated polymer properties are combined in the repeating unit of PTS. On the other hand, in PEDOT:PSS both properties are combined by the polyelectrolyte PSS and the conjugated polymer PEDOT, in which PEDOT:PSS batches with various PEDOT to PSS weight ratios are examined. Both polymeric mixed conductor systems in this thesis were examined in the form of thin films.

In the first part of this thesis, the absorption characteristics of the neutral and the oxidized (doped) state of both systems were examined by means of UV/Vis absorption spectroscopy. In case of the PTS systems, variation of the counterion and variation of the solvent system from which PTS is processed resulted in varying aggregation of the polythiophene backbones, in agreement with literature [1, 2]. Variation of the redox state was conducted either with chemical doping with the help of a strong electron acceptor or electrochemical doping with the help of spectroelectrochemistry measurements (cyclic

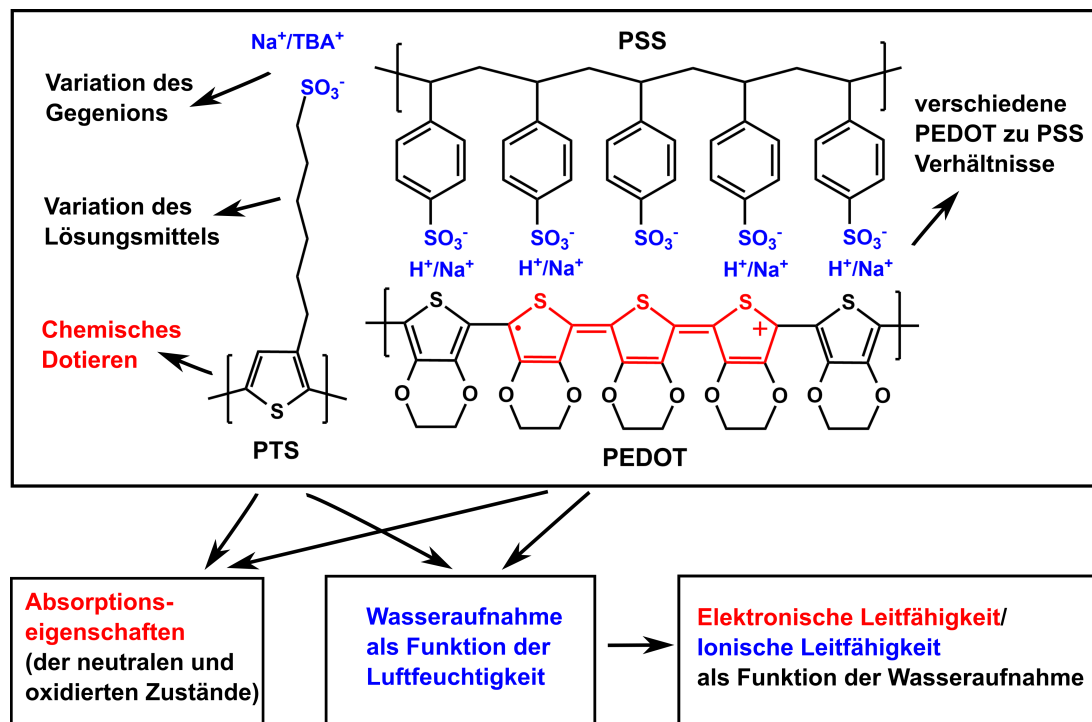
voltammetry coupled with in-situ UV/Vis absorption spectroscopy), in which partial evolution of low-energy absorption bands could be related to oxidized states in PTS. In case of the PEDOT:PSS systems, spectroelectrochemistry and in-situ conductance (cyclic voltammetry coupled with in-situ conductance) studies revealed differences depending on the PEDOT to PSS weight ratio: for the low PEDOT content PEDOT:PSS batch restricted accessibility of the redox state as observed with spectroelectrochemistry measurements and a bell-shaped in-situ conductance profile as function of applied potential was obtained but on the other hand full conversion between the redox states and an in-situ conductance plateau was obtained for the high PEDOT content PEDOT:PSS batch. These observations can be explained by a high connectivity of the PEDOT moieties in the high PEDOT content PEDOT:PSS batch.

The main aim of this thesis was to examine the electronic and ionic conductivity properties of both polymeric mixed conductor systems as function of water uptake. A custom made setup was built up which allows to examine the water uptake and the conductivity properties in controlled atmospheric conditions, so in variable temperature and relative humidity (r.h.) conditions. In order to determine the water uptake of thin films of the polymeric mixed conductor systems as function of relative humidity, a quartz crystal microbalance (QCM) technique was newly installed and tested for its validity and reliability. A typical water uptake trend could be identified for both polymeric mixed conductor systems: After a strong increase of the water content up to 5 – 10 wt% at ≈ 3 mbar H_2O (≈ 10 % r.h.), the water content increases moderately up to ≈ 30 wt% upon further increase of the water partial pressure up to ≈ 16 mbar H_2O (≈ 50 % r.h.). Upon increase to the highest water partial pressure of 29 mbar H_2O (≈ 92 % r.h.), the water content increases significantly up to 70 – 90 wt%. The obtained trend is typical for polyelectrolyte materials and can be explained by a dissociation of the bound cations and formation of solvation shells at low water contents, formation of multiple solvation shells at medium water contents and formation of bulk-like water regions at high water contents [3–5]. In case of the PTS systems, the water uptake per repeating unit (in λ) is similar for PTS with sodium (PTS-Na) or tetrabutylammonium (PTS-TBA) counterions and so independent from the counterion, which can be explained by a dominating effect of the anionic sulphonate group which is the same in both materials. Similar water uptakes were obtained for the PEDOT:PSS systems with various PEDOT to PSS ratios, which might be explained by different morphologies of the high and low PEDOT content PEDOT:PSS systems. For PEDOT:PSS films, which are two orders of magnitude thicker than the typical PEDOT:PSS films, similar water

uptakes were obtained as for the thin films. This might indicate that the water uptake occurs in the volume of the polymer film instead of only at the surface of the polymer films.

The conductivity properties of the polymeric mixed conductors as function of water uptake were examined with a combination of AC impedance spectroscopy and DC measurements. Pristine PTS-Na films revealed ionic conductivity in the entire examined water content range, in which the ionic conductivity increases significantly from 10^{-10} S/cm to $\approx 10^{-4}$ S/cm upon increase of the water content up to 20 wt% and then up to a plateau value of $\approx 10^{-2}$ S/cm at ≈ 70 wt% water content. This dependency of the ionic conductivity was observed previously in literature and can be explained by a significant dissociation of the mobile cation from the immobile sulphonate group at low water contents and uptake of water into bulk-like water regions at higher water contents, which increases the dissociation only slightly more [6, 7]. Upon chemical doping of PTS and in case of the low PEDOT content PEDOT:PSS system, mixed conductivity behavior could be obtained, so concurrently detectable electronic and ionic conductivities [8]. As for the pure ionic conductor, the ionic conductivity was observed to increase with water uptake. On the other hand, the electronic conductivity which is in the range of 10^{-4} S/cm in the dry state was observed to decrease upon increase of the water content, which is explained by a decrease of the connectivity between electronically conducting moieties [4]. For a high PEDOT content PEDOT:PSS batch, electronic conductivity could be determined over the entire examined water partial pressure range, which can presumably be explained by the fact that the electronic conductivity in the range of 1 S/cm is significantly higher than the ionic conductivity. The high electronic conductivity can be explained by the good connectivity between PEDOT moieties due to the high PEDOT content.

Zusammenfassung



In der vorliegenden Arbeit wurden zwei polymere gemischte Leiter untersucht, der konjugierte Polyelektrolyt Poly(6-(thiophen-3-yl)hexane-1-sulfonat) (PTS) und die konjugiertes Polymer/Polyelektrolyt Mischung Poly(3,4-ethylenedioxythiophen):Poly(styrolsulfonat) (PEDOT:PSS). Beide Systeme beinhalten elektronisch leitfähige konjugierte Polymereinheiten und hydrophile, ionisch leitfähige Polyelektrolyteinheiten. Im Fall von PTS sind die ionisch leitfähigen Polyelektrolyteigenschaften und elektronisch leitfähigen konjugierten Polymereigenschaften in der Wiederholungseinheit von PTS kombiniert. Andererseits sind in PEDOT:PSS beide Eigenschaften durch den Polyelektrolyten PSS und das konjugierte Polymer PEDOT kombiniert, wobei PEDOT:PSS Materialien mit verschiedenen PEDOT und PSS Verhältnissen (Gewichtsanteilen) untersucht wurden. Die polymeren gemischten Leitersysteme in dieser Thesis wurden in der Form von dünnen Filmen untersucht.

Im ersten Teil dieser Thesis wurden die Absorptionseigenschaften der neutralen und der oxidierten (dotierten) Zustände beider Systeme mithilfe von UV/Vis Absorptionsspektroskopie untersucht. Im Fall der PTS Systeme resultierte eine Variation des Gegenions und eine Variation des Lösungsmittels aus dem die Filme prozessiert werden in einer unterschiedlichen Aggregation der Polythiophene-Hauptketten, wie zuvor in der Literatur beobachtet [1, 2]. Variation des Redoxzustands wurde entweder mit chemischem

Dotieren mithilfe eines starken Elektronenakzeptors oder elektrochemischem Dotieren mithilfe von Spektroelektrochemie Messungen (Zyklovoltammetrie gekoppelt mit in-situ UV/Vis Absorptionsspektroskopie) durchgeführt, wobei eine teilweise Intensitätszunahme von Niedrigenergie-Absorptionswellen auf die Entstehung von oxidierten Zuständen hindeutete. Im Fall der PEDOT:PSS Systeme zeigten Spektroelektrochemie und in-situ Leitwert Messungen (Zyklovoltammetrie gekoppelt mit in-situ Leitwert) an PEDOT:PSS Proben Unterschiede in Abhängigkeit der PEDOT und PSS Gewichtsanteile: während PEDOT:PSS mit niedrigem PEDOT Gehalt eingeschränkte Zugänglichkeit der Redoxzustände in Spektroelektrochemie Messungen und ein glockenförmiges in-situ Leitwert Profil als Funktion des angelegten Potentials zeigte, wurde andererseits eine vollständige Konversion zwischen den Redoxzuständen und ein plateauförmiges in-situ Leitwert Profil für PEDOT:PSS mit hohem PEDOT Gehalten beobachtet. Diese Befunde können mit einer guten Konnektivität der PEDOT Einheiten in PEDOT:PSS Systemen mit hohem PEDOT Gehalt erklärt werden.

Das Hauptziel dieser Arbeit war die Untersuchung der elektronischen und ionischen Leitfähigkeitseigenschaften beider polymerer gemischter Leiter als Funktion der Wasseraufnahme. Ein selbstgebautes Setup wurde eingerichtet, das die Untersuchung der Wasseraufnahme und der Leitfähigkeitseigenschaften in kontrollierbaren atmosphärischen Bedingungen, also in variablen Luftfeuchtigkeits- und Temperaturbedingungen, erlaubt. Um die Wasseraufnahme von dünnen Filmen der polymeren gemischten Leiter als Funktion der Luftfeuchtigkeit zu untersuchen, wurde ein Quartz Kristallmikrowaage (QCM) System neu installiert und auf seine Gültigkeit und Verlässlichkeit getestet. Ein typischer Wasseraufnahmetrend konnte für beide polymeren gemischten Leiter identifiziert werden: nach einer starken Zunahme des Wassergehalts bis auf 5 – 10 Gew.-% im Wasserpartialdruckbereich bis 3 mbar H_2O (≈ 10 % r.F.) nimmt der Wassergehalt moderat bis auf ≈ 30 Gew.-% zu im Wasserpartialdruckbereich bis ungefähr 16 – 23 mbar H_2O ($\approx 50 - 70$ % r.F.). Bei weiterer Erhöhung des Wasserpartialdrucks bis auf 29 mbar H_2O (≈ 92 % r.F.) nimmt der Wassergehalt signifikant bis auf 70–90Gew.-% zu. Der erhaltene Trend ist typisch für Polyelektrolytmaterialien und kann mit einer Dissoziation der Kationen und Bildung von Hydrathüllen bei geringen Wassergehalten, weiterem Wachstum der Hydrathüllen bei mittleren Wassergehalten und Entstehung von wasserreichen Phasen bei hohen Wassergehalten erklärt werden [3–5]. Im Fall der PTS Systeme ist die Wasseraufnahme pro Wiederholungseinheit (in λ) ähnlich für PTS mit Natrium (PTS-Na) oder Tetrabutylammonium (PTS-TBA) Gegenionen und daher unabhängig vom Gegenion, was mit einem dominierenden Effekt der Sulfonatgruppe erklärt werden kann. Vergleichbare

Wasseraufnahmen wurden für die PEDOT:PSS Systeme mit verschiedenen PEDOT und PSS Gewichtsanteilen erhalten, was mit verschiedenen Strukturen der PEDOT:PSS Systeme mit hohem und niedrigem PEDOT Gehalt erklärt werden könnte. Für PEDOT:PSS Filme, die zwei Größenordnungen dicker sind als die typischen PEDOT:PSS Filme, wurden ähnliche Wasseraufnahmen wie für die dünnen Filme erhalten. Dies könnte darauf hindeuten, dass die Wasseraufnahme hauptsächlich im Volumen der Filme anstatt nur an der Oberfläche der Filme stattfindet.

Die Leitfähigkeitseigenschaften beider polymerer gemischten Leitersysteme wurden als Funktion der Wasseraufnahme mithilfe einer Kombination von AC Impedanzspektroskopie und DC Messungen untersucht. Unbehandelte PTS-Na Filme zeigten ionische Leitfähigkeit im gesamten untersuchten Wassergehaltbereich, wobei die ionische Leitfähigkeit stark von 10^{-10} S/cm auf $\approx 10^{-4}$ S/cm steigt beim Erhöhen des Wassergehalts auf ≈ 20 Gew.-% und in einem Plateau-Wert bei $\approx 10^{-2}$ S/cm beim Erhöhen des Wassergehalts auf ≈ 70 Gew.-% resultiert. Diese Abhängigkeit der ionischen Leitfähigkeit vom Wassergehalt wurde zuvor beobachtet und kann mit einer Dissoziation der mobilen Kationen von den stationären Sulfonatgruppen bei niedrigen Wassergehalten und einer Wasseraufnahme in wasserreiche Phasen bei hohen Wassergehalten, die die Dissoziation der Kationen nicht stark erhöht, erklärt werden [6, 7]. Beim chemischen Dotieren von PTS Filmen und im Fall von PEDOT:PSS (1:6) mit niedrigem PEDOT Gehalt konnte eine gemischte Leitfähigkeit erhalten werden, also eine gleichzeitig messbare elektronische und ionische Leitfähigkeit [8]. Wie für die reinen ionischen Leiter konnte eine Erhöhung der ionischen Leitfähigkeit bei steigendem Wassergehalt beobachtet werden. Andererseits kann beobachtet werden, dass die elektronischen Leitfähigkeiten, die im trockenen Zustand im Bereich von 10^{-4} S/cm waren, mit steigendem Wassergehalt abnahmen, was mit einer Abnahme der Konnektivität der elektronisch leitfähigen Phasen erklärt werden kann [4]. PEDOT:PSS mit hohem PEDOT Anteil zeigte elektronische Leitfähigkeit im gesamten untersuchten Wassergehaltbereich, was vermutlich damit erklärt werden kann, dass die elektronische Leitfähigkeit in der Größenordnung von 1 S/cm signifikant höher als die ionische Leitfähigkeit ist. Die hohe elektronische Leitfähigkeit kann mit einer guten Konnektivität der elektronisch leitfähigen Phasen aufgrund des hohen PEDOT Anteils erklärt werden.

Contents

1	Introduction	1
1.1	Organic electrochemical transistors	2
1.2	Basic components of polymeric mixed conductor systems	5
1.2.1	Conjugated polymers	5
1.2.1.1	Basics	5
1.2.1.2	Charged states and conductivity	6
1.2.2	Polyelectrolytes	12
1.2.2.1	Basics	12
1.2.2.2	Water uptake properties	12
1.2.2.3	Ionic conductivity properties	14
1.3	Polymeric mixed conductor materials	16
1.3.1	Conjugated polyelectrolyte: PTS	16
1.3.1.1	Synthesis	16
1.3.1.2	Properties	18
1.3.2	Conjugated polymer/polyelectrolyte mixture: PEDOT:PSS	23
1.3.2.1	History	23
1.3.2.2	Synthesis	24
1.3.2.3	Properties	25
1.3.2.4	Applications	35
2	Objectives	36
3	Experimental	38
3.1	Materials	38
3.1.1	PTS	38
3.1.2	PEDOT:PSS	41
3.1.3	Chemicals	41
3.2	Sample preparation	42
3.2.1	Substrates	42

3.2.2	Film preparation	43
3.3	Methods	44
3.3.1	In-Situ adjustable atmospheric conditions measurements	44
3.3.2	Setup	45
3.3.3	AC impedance and DC measurements	45
3.3.4	Thermogravimetric analysis	50
3.3.5	Quartz Crystal Microbalance	52
3.3.6	UV/Vis in reflection mode	53
3.3.7	Cyclic voltammetry (with in-situ techniques)	54
3.3.7.1	Cyclic voltammetry	54
3.3.7.2	In-situ Spectroelectrochemistry	55
3.3.7.3	Cyclic voltammetry with in-situ conductance (and UV/Vis NIR absorption) measurements	56
3.3.8	Further techniques	58
3.3.8.1	Profilometry	58
3.3.8.2	UV/Vis Lambda	58
3.3.8.3	Atomic Force Microscopy	58
4	Results	59
4.1	Absorption characteristics in neutral and doped states	61
4.1.1	PTS materials	61
4.1.1.1	Neutral state	61
4.1.1.2	Doped states	76
4.1.2	PEDOT:PSS	80
4.1.2.1	Spectroelectrochemistry	80
4.1.2.2	In-Situ conductance	84
4.1.3	Discussion and summary of absorption characteristics	85
4.2	Water uptake studies in controlled atmospheric conditions	88
4.2.1	Preliminary Thermogravimetric Analysis	88
4.2.1.1	PTS materials	88
4.2.1.2	PEDOT:PSS materials	91
4.2.2	Quartz Crystal Microbalance	94
4.2.2.1	General discussions	94
4.2.2.2	PTS materials	98
4.2.2.3	PEDOT:PSS materials	103
4.2.3	Discussion and summary of water uptake studies	108

4.3	Conductivity studies as function of water uptake	112
4.3.1	PTS materials	113
4.3.1.1	Pristine PTS-Na: ionic conductivity behavior	113
4.3.1.2	Chemically doped PTS-Na: mixed conductivity behavior .	118
4.3.1.3	Chemically doped PTS-TBA: electronic conductivity behavior	128
4.3.1.4	Pristine PTS-Na at elevated temperatures: Mixed conductivity behavior	131
4.3.2	PEDOT:PSS materials	134
4.3.2.1	PEDOT:PSS (1:6)	134
4.3.2.2	PEDOT:PSS-Na (1:6)	139
4.3.2.3	PEDOT:PSS (1:2.2)	144
4.3.3	PEDOT:PSS-PVA composite materials	146
4.3.3.1	PEDOT:PSS/PVA	147
4.3.3.2	PVA/PEDOT:PSS	150
4.3.4	Comparison of different interdigitated electrode geometries	151
4.3.5	Discussion and summary of conductivity studies	154
5	Conclusion and outlook	164
6	Bibliography	177
7	Appendix	191

List of Abbreviations

AC	Alternating current
AFM	Atomic Force Microscopy
CE	Counter electrode
CP	Conjugated/Conducting polymer
CPE	Conjugated polyelectrolyte
CV	Cyclic voltammetry/cyclic voltammogram
DC	Direct current
DMSO	Dimethyl sulfoxide
EDOT	3,4-ethylenedioxythiophene
EG	Ethylene glycol
EIS	Electrochemical impedance spectroscopy
F₄TCNQ	2,3,5,6-tetrafluoro-7,7,8,8-tetracyanoquinodimethane
GOPS	3-glycidoxypropyltrimethoxysilane
HOMO	Highest molecular orbital
IR	Infrared Spectroscopy
ITO	Indium doped tin oxide
LUMO	Lowest molecular orbital
MALDI-TOF	Matrix-assisted laser ionization time-of-flight
NMR	Nuclear Magnetic Resonance

OECT	Organic Electrochemical Transistor
OLED	Organic light emitting diode
P3HT	Poly(3-hexylthiophene)
PDI	Polydispersity index
PEDOT	Poly(3,4-ethylenedioxythiophene)
PFSA	Perfluorinated sulfonic-acid
PSS-H	Poly(4-styrene sulfonate acid)
PSS-Na	Poly(sodium 4-styrenesulfonate)
PT-ImBr	Poly(3-(6-(1-methylimidazolium-3-yl)hexyl)thiophene-2,5-diyl)-bromide
PTS-Na	Poly(6-(thiophene-3-yl)hexane-1-sulfonate)-sodium
PTS-TBA	Poly(6-(thiophene-3-yl)hexane-1-sulfonate)-tetrabutylammonium
PVA	Polyvinyl alcohol
QCM(-D)	Quartz Crystal Microbalance (with dissipation monitoring)
R.H.	Relative humidity
RE	Reference electrode
TFSI	Bis(trifluoromethylsulfonyl)imide
TGA	Thermogravimetric analysis
THF	Tetrahydrofuran
UV/Vis (NIR)	Ultraviolet/Visible (Near Infrared)
WE	Working electrode
XPS	X-ray photoelectron spectroscopy

Scientific contributions

Scientific Papers

Matthias Wieland, Carsten Dingler, Rotraut Merkle, Joachim Maier, Sabine Ludwigs, *Humidity-controlled water uptake and conductivities in ion and electron mixed conducting polythiophene films*, ACS Applied Materials & Interfaces, **2020**, *12*, 6742-6751

Matthias Wieland*, Claudia Malacrida*, Qiulin Yu, Claire Schlewitz, Luca Scapinello, Andrea Penoni, Sabine Ludwigs, *Conductance and Spectroscopic Mapping of EDOT polymer films upon electrochemical doping*, Flexible and Printed Electronics, **2020**, *5*, 014016
*both authors contributed equally

Juliane Ratzsch, Julian Karst, Jinglin Fu, Monika Ubl, Tobias Pohl, Florian Sterl, Claudia Malacrida, Matthias Wieland, Bernhard Reineke, Thomas Zentgraf, Sabine Ludwigs, Mario Hentschel and Harald Giessen, *Electrically Switchable Metasurface for Beam Steering Using PEDOT*, Journal of Optics, **2020**, *22*, 124001

Carsten Dingler, Henry Müller, Matthias Wieland, Dominik Fauser, Holger Steeb, Sabine Ludwigs, *From Understanding Mechanical Behavior to Curvature Prediction of Humidity-Triggered Bilayer Actuators*, Advanced Materials, **2021**, *33*, 2007982

Oral presentations

Matthias Wieland, Rotraut Merkle, Joachim Maier, Sabine Ludwigs, *Mixed Conductivity in Polymer/Polyelectrolyte Films*, **2019**, 13th ECHEMS Meeting, Bordeaux, France

Carsten Dingler, Matthias Wieland, Sabine Ludwigs, *Stimuli-Responsive Behavior of the Conducting Polymer PEDOT:PSS*, **2019**, Polydays 2019, Berlin

Poster presentations

Matthias Wieland, Rotraut Merkle, Peter Reinold, Joachim Maier, Sabine Ludwigs, *Mixed conductivity of polythiophene-based ionic polymers under controlled conditions*, **2018**, Materials for Organic Electronics: Synthesis, Spectroscopy and Theory, Symposium, Heidelberg

Matthias Wieland, Rotraut Merkle, Joachim Maier, Sabine Ludwigs, *Mixed conductivity of polythiophene-based ionic polymers under controlled conditions*, **2018**, MRS Fall Meeting, Boston, USA

1 Introduction

The undoubtedly greatest task of humanity is to reduce its emissions of carbon dioxide in order to diminish man-made climate change. If humanity achieves to limit the global warming to 1.5 °C compared to the pre-industrial level, the impacts on the ecosystem can be substantially reduced [9]. In order to limit the global warming to 1.5 °C, the carbon dioxide emissions have to be reduced by 30 % between 2010 and 2030, profound changes in the areas of energy, infrastructure and industry have to be made and techniques to remove carbon dioxide from the atmosphere have to be utilized. Therefore, one possible approach could include the replacement of expensive, resource consuming materials by cheaper, less resource consuming materials. One example therefore is the semiconductor technology, which is nowadays dominated by inorganic silicon. An alternative to silicon would be organic semiconductors, so materials based on carbon compounds. In general they have as advantages lower material costs, they can be processed at temperatures far below 100°C and they are amorphous and can therefore be processed onto flexible substrates [10]. On the other hand, decomposition under ambient conditions or long-term instability hamper their potential in applications. In spite of the difficulties, organic semiconducting materials have found their way into applications for example in organic light emitting diodes (OLEDs), which are among others widely used in the displays of mobile smartphones. Other potential applications are in organic solar cells (OSCs) or in organic field-effect transistors (OFETs). In general, field effect transistors (FETs) use semiconductor materials as channel material for their current switching and amplifying properties, which is essential in every modern electronic device. Until 2018, an estimated amount of $13 \cdot 10^{21}$ metal-oxide semiconductor field effect transistors (MOSFETs) have been manufactured, making it the most often manufactured component in human history [11]. The function principle and the utilized materials in inorganic and organic field effect transistors are similar, whereas in organic field effect transistors an organic semiconductor material is utilized as channel material [12]. As further development, by replacing the solid state insulator as used in inorganic and organic field effect transistors by a liquid electrolyte, the organic electrochemical transistors (OECT) could be realized, which opens an entire new field of potential applications [13].

1.1 Organic electrochemical transistors

Structure of organic electrochemical transistors

In 1984, Wrighton et al. introduced a device consisting of gold microelectrodes deposited on a silicon oxide substrate. By adjusting the charge state of polypyrrole films, which are deposited by electropolymerization in the gap between adjacent microelectrodes, the current flow between these microelectrodes can be controlled [14, 15]. In general, all materials which show a change in electronic conductivity are suitable for active materials in OEETs [16]. After decades of further development, channel materials which can be spin coated (with the technique spin coating thin films can be prepared, see experimental part section 3.2.2) into the electrode channel became more popular. The structure of a state-of-art OEET can be seen in figure 1.1.

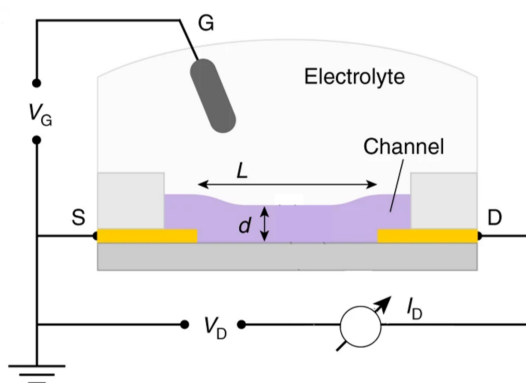


Figure 1.1: Structure of an organic electrochemical transistor. Adapted with permission from [17], © 2017, Springer Nature.

The source (S) and drain electrode (D) are connected by the channel material (violet), which has a certain thickness d . On top of the channel material is the electrolyte, in that the gate electrode (G) is placed. By varying the gate potential V_G , the drain current I_D (which flows between S and D) can be controlled.

Operation modes of organic electrochemical transistors

Depending on the charged state of the spin coated, pristine channel material, the accumulation and depletion mode have to be distinguished: in case of channel materials which are conducting in their pristine state after spin coating such as the well-known conjugated polymer/polyelectrolyte mixture poly(3,4-ethylenedioxythiophene:poly(styrene sulfonate)) (referred to as PEDOT:PSS in the following), OEETs are run in the depletion mode. Since PEDOT:PSS is in its oxidized, conducting state a certain I_D can be flowing, therefore the OEET is in its ON state after spin coating. Upon applying a positive V_G , cations of the electrolyte are injected into the channel and a reduction from the oxidized to the

neutral state of the channel material occurs. This corresponds in analogy to the terminology of inorganic silicon to a "dedoping" of the channel material, which causes a decrease of the conductance and therefore to a decrease of I_D . Therefore, applying of V_G leads to a switching from the ON to the OFF state of the OEET. In contrast to the depletion mode, for channel materials which are in their neutral state after spin coating such as the conjugated polyelectrolyte (CPE) poly(6-(thiophene-3-yl)hexane-1-sulfonate with tetrabutylammonium counterion (abbreviated as PTS-TBA in the following, without specification of the counterion the material is abbreviated as PTS in the following), the OEETs are run in the accumulation mode. This means that no current conduction occurs between S and D initially, therefore the OEET is in its OFF state. Upon applying a V_G , the channel material is doped to its oxidized, conducting state. This leads to a current flow between S and D, therefore the OEET switches to the ON state. In figure 1.2, the transfer curves (which are mainly used to characterize transistors) for a depletion-mode OEET and accumulation-mode OEET are shown.

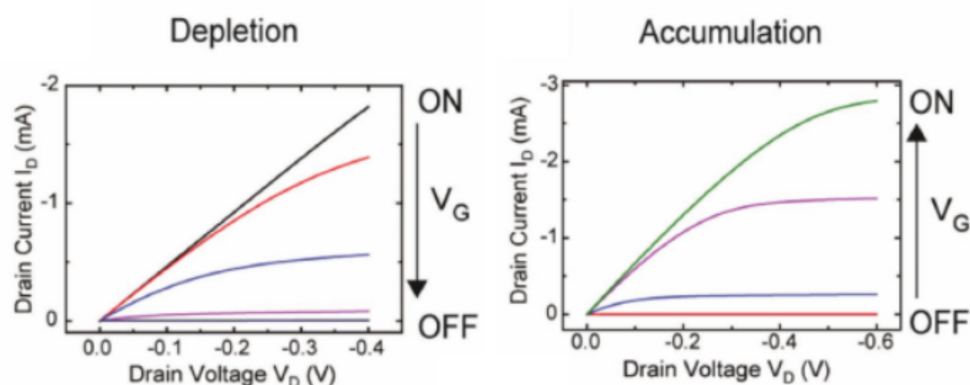


Figure 1.2: Transfer curve of a depletion-mode OEET (left) and accumulation-mode OEET (right). Adapted with permission from [18], ©, John Wiley and Sons.

A deciding characteristic of an OEET is that the entire channel volume participates in a change of the doping state. In contrast to that, in field effect transistors (FET), only a very thin layer at the interface between the semiconductor and the insulator participates in current conduction. Compared to FETs, the I_D in OEETs varies significantly more as function of V_G , since the entire channel volume participates in current conduction, even though OEETs are in general slower than FETs. A special case of FETs are the electrolyte gated organic field effect transistors (EGOFETs). The structure of an EGOFET is very similar to an OEET, in which in contrast to an OEET, the ions do not penetrate the channel upon applying V_G .

PTS and PEDOT:PSS materials are the two polymeric mixed conductor systems which are examined in this thesis. Both channel materials have in common that for an use as

the channel material in OECTs, the so called mixed conductivity in these materials is required, which means a concurrent electronic and ionic conductivity. Ionic conductivity is required since the ions need to move from the electrolyte into the channel material to neutralize variations of the charge on the polymer backbones caused by doping or dedoping of the channel material. Electronic conductivity of the channel material in OECTs is necessary to enable a current flow between S and D. Typically conjugated polymers (CPs, also often referred to as conducting polymers) are utilized in polymeric mixed conductors since they allow an efficient and reversible switching between the (typically) oxidized, highly conducting state and the neutral, low conducting state. Whereas the typically used channel material PEDOT:PSS and the less commonly used PTS inherently contain mobile ions, further polythiophene materials such as the widely studied poly(3-hexylthiophene) (abbreviated as P3HT, also see section 1.2.1.2) or P3HT with glycolated side chains (abbreviated as P(A2T-TT) and P(G2T-TT) by the authors), which do not contain ions, were successfully deployed in OECTs [19–21].

Comparison of PTS and PEDOT:PSS in organic electrochemical transistors

Both PTS and PEDOT:PSS and further polythiophene materials were previously compared on their performance as channel material in OECTs [17]. Ethylene glycol (EG) treated PTS exhibited a comparably high volumetric capacitance (capacitance per volume of polymer film), which might be explained by the high ion content due to the fact that every repeating unit contains ionic groups [22]. On the other hand, PTS revealed a comparably low electronic mobility, which resulted in an overall low performance as channel material in OECTs. By introducing 3-hexylthiophene units into PTS to form PTS-*co*-poly(3-hexylthiophene) (PTS-*co*-P3HT) copolymers, the volumetric capacitance could be improved significantly [23]. PEDOT:PSS after EG treating revealed a low volumetric capacitance but the highest reported electronic mobility, which might be explained by the good electron conducting properties, resulting in an average performance as channel material [24]. In a recent contribution, balancing of concurrent electronic and ionic conduction in the channel materials was revealed to be pivotal for application of mixed conductors in OECTs [25].

Applications of organic electrochemical transistors

In general, OECTs can be considered as devices which convert ion currents into electronic currents. Due to the very low required operation voltages, applications in aqueous media can be realized. Possible applications of OECTs are summarized in [26]. In bioelectronics, OECTs could be applied in neural sensing, where electrophysiological signals of human brains, human hearts or human muscles are recorded. Additionally, they could be utilized in impedance sensing, in which a monolayer of cells is grown between the gate electrode

and the channel [27]. Due to the arising barrier for ion motion, the working characteristics of the OECT are altered. Furthermore, OECTs could be utilized in analyte detection, where redox enzymes interact with metabolites. The resulting transfer of electrons to the gate of the OECT changes I_D , the change of I_D depends therefore on the concentration of the metabolite. OECTs could also be utilized in electrical (logic) circuits or in memory or neuromorphic devices [28].

Both the PTS and PEDOT:PSS polymeric mixed conductor systems possess conjugated polymer moieties and polyelectrolyte moieties. Before giving a detailed description of PTS and PEDOT:PSS in section 1.3, the two basic components of both materials, the conjugated polymers and polyelectrolytes are introduced in the following section.

1.2 Basic components of polymeric mixed conductor systems

1.2.1 Conjugated polymers

1.2.1.1 Basics

In 2000, the chemists Alan J. Heeger, Alan G. MacDiarmid and Hideki Shirakawa received the nobel prize in chemistry "for the discovery and development of electrically conductive polymers" [29]. Shirakawa et al. recognized that the electronic conductivity of polyacetylene can be increased by more than seven orders of magnitude from $3.2 \cdot 10^{-6}$ S/cm to 38 S/cm by treatment with bromine or chlorine vapor [30, 31]. Since these conductive polymers are in contrast to metals light-weight and can be processed from solution, expectations raised that they could replace metals in the future. Therefore, extensive research has been conducted in the field of conductive polymers in the past decades. Two classes of conductive polymers can be distinguished, on one hand the so called redox polymers which conduct current due to redox-active pendant side groups and on the other hand conjugated polymers which conduct current over their π -conjugated backbone [32, 33]. Since the examined PTS and PEDOT:PSS materials examined in this thesis are conjugated polymers, only this class of conductive polymers is discussed in the following. Some well-known examples of conjugated polymers are shown in figure 1.3.

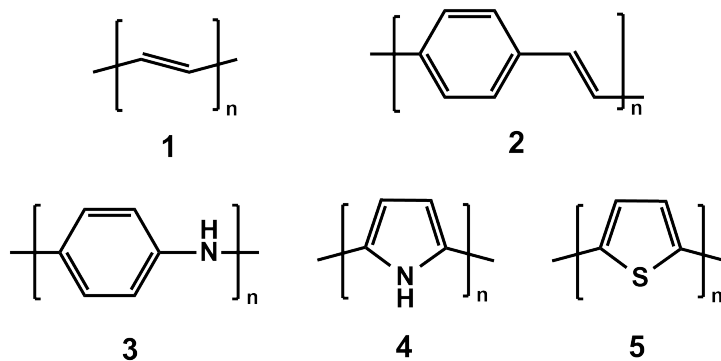


Figure 1.3: Molecular structures of common conjugated polymers: polyacetylene (1), poly(p-phenylenevinylene) (2), polyaniline (3), polypyrrole (4) and polythiophene (5).

Conventional polymers in everyday life, for example polyethylene or polystyrene, comprise sp^3 -hybridized carbon atoms in their polymer backbone, which results solely in σ -bonds in the polymer backbone. These conventional polymers are typically insulators and do not possess optical activity in the visible light. In contrast to the sp^3 hybridization of carbon atoms in conventional polymers, the carbon atoms in the polymer backbone in conjugated polymers are sp^2 -hybridized, which results in alternating ("conjugated") σ - and π -bonds, so alternating single and double bonds. This leads to electron delocalization and therefore to planarization of the conjugated polymer, which in turn leads to strong interchain interactions. Due to these strong interactions, the solubility of conjugated polymers is in general very low [34]. Due to the very low solubility of polyacetylene, focus was soon laid on more soluble conjugated polymers. According to a classification by Heeger, polyacetylene can be assigned to the first class of conjugated polymers [35]. The second class of conjugated polymers comprises among others poly(p-phenylenevinylene), polyaniline, polypyrrole or polythiophene (structures 2-5 in figure 1.3). The solubility issue of unsubstituted polythiophene was either tackled by introducing easily soluble side groups, either unpolar side groups such as hexyl (which results in poly(3-hexylthiophene), P3HT) or polar side groups such as hexane-1-sulfonate (which results in PTS, see section 1.3.1.2 for a detailed introduction of PTS) or by stabilizing the insoluble conjugated polymer PEDOT in a complex with a very soluble polymer (in case of PEDOT, PSS is commonly utilized as stabilizer to form PEDOT:PSS). PEDOT:PSS is introduced in detail in section 1.3.2.

1.2.1.2 Charged states and conductivity

Two requirements have to be fulfilled so that conjugated polymers are also conductive polymers: firstly charge carriers have to be created on the conjugated polymer backbone (since no charge carriers are in the conjugated polymer backbone in the neutral

state, conjugated polymers are insulating in their neutral state) and secondly a current path in the polymer material, where the charge carriers can move has to be established. Creation of charge carriers can be achieved by oxidation or reduction of the conjugated polymer, which results in additional holes or electrons in the polymer backbone. The process is therefore referred to as "doping" in analogy to inorganic semi-conductors. In case of the commonly used inorganic semi-conductor silicon as group 4 element of the periodic table of elements, adding of group 3 or group 5 atoms results in a local deficiency or excess of electrons. The already described doping of polyacetylene with halogen vapors corresponds for example to an oxidative doping respectively a p-doping process (adding of holes). Doping via a reduction, therefore referred to as n-doping, is known for example for the third generation conjugated polymer poly([N,N'-bis(2-octyldodecyl)-1,4,5,8-naphthalindicarboximid-2,6-diyl]-alt-5,5'-(2,2'-bithiophene)) (PNDI2OD-T2) [36]. Formation of charge carriers upon p- or n-doping result in local geometric distortions on the conjugated polymer backbone. These can be determined with ultraviolet/visible (UV/Vis) absorption spectroscopy and are in accordance to condensed-matter physicists referred to as solitons, polarons and bipolarons [37]. The charge carriers can be transported on the polymer chains (intrachain charge transport) and less efficiently between the polymer chains via hopping (interchain charge transport) [38, 39]. Since it could be shown that the interchain transport occurs mainly via π - π -stacked polymer chains, the largest improvements of the conductivity could be made when the π - π aggregation of the polymer chains could be improved (see also section 1.3.2.3). The mechanism of charge conduction in conjugated polymers and why the electronic conductivity increases significantly upon doping can be explained with the molecular orbitals in conjugated polymers [37, 40]. In figure 1.4, exemplary polythiophene chains in various charge states and the corresponding energy diagram is shown.

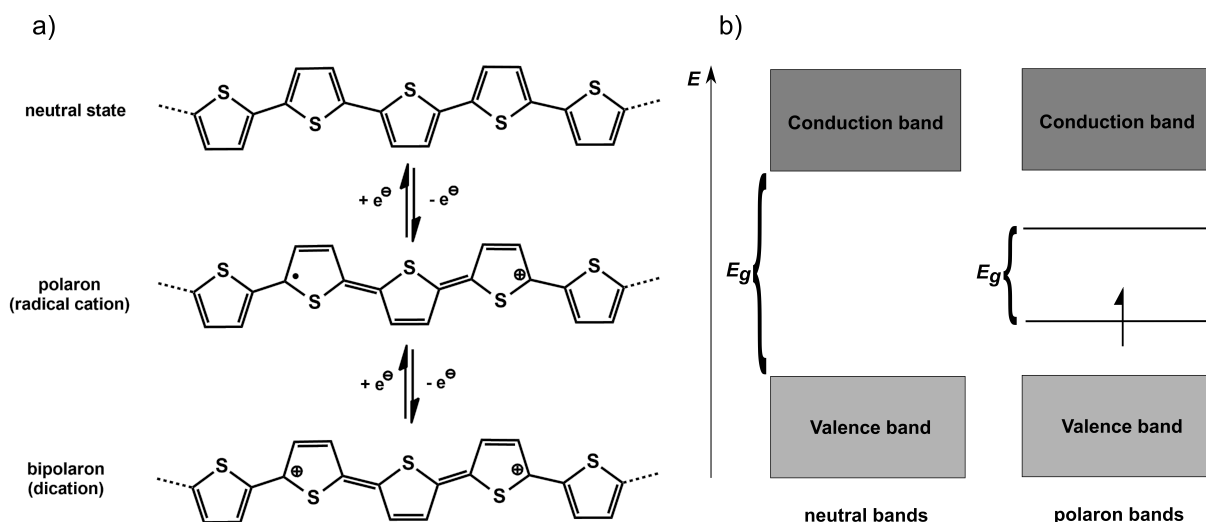


Figure 1.4: a) Molecular structure of polythiophene chains in different oxidation states and b) electronic molecular orbital scheme of the neutral and oxidized state with the band gap E_G , adapted from [40].

As shown in figure 1.4 a), upon oxidation of the neutral polythiophene chain a radical and a positive charge are generated on the polythiophene backbone. Whereas in the neutral state, the polythiophene backbone is in its aromatic benzoid state, upon oxidation the quinoid structure is partially formed due to delocalization of the generated charge over the conjugated backbone [41]. Increasing the doping level further, the radical is replaced by a further positive charge. The radical cation state is referred to as polaron state, the dication state is referred to as bipolaron (two polarons) state [37]. As can be seen in figure 1.4 b), two energy bands exist in conducting polymers: the valence band, which results from merging of the binding π -orbitals and the conduction band, which results from merging of the anti-binding π^* -orbitals. The energy between the highest occupied molecular orbital (HOMO) of the valence band and the lowest unoccupied molecular orbital (LUMO) is the band gap E_G . In the neutral state E_G is large (assuming room temperature), which leads to a very low electronic conductivity. Formation of the quinoid structures in the polaron states results in the formation of additional energy states between the valence band and the conduction band. As a result, the band gap energy E_G decreases, which results in a significantly higher electronic conductivity. Additionally, the decrease of E_G leads typically to a color change of the conjugated polymers, also referred to as electrochromism [42].

The doping, which is required to generate charges on the polymer backbone and which results in a higher electronic conductivity, can be achieved either with chemical or with electrochemical doping [43]. Poly(3-hexylthiophene) (abbreviated as P3HT in the following) is the polythiophene, which has been most studied in respect to its electronic and optical properties in the neutral state [44]. In figure 1.5, the molecular structure of P3HT,

the cyclic voltammogram with in-situ measured conductance and the UV/Vis absorption spectra recorded during spectroelectrochemistry measurements (cyclic voltammetry coupled with in-situ UV/Vis absorption spectroscopy) of P3HT films are shown [44, 45].

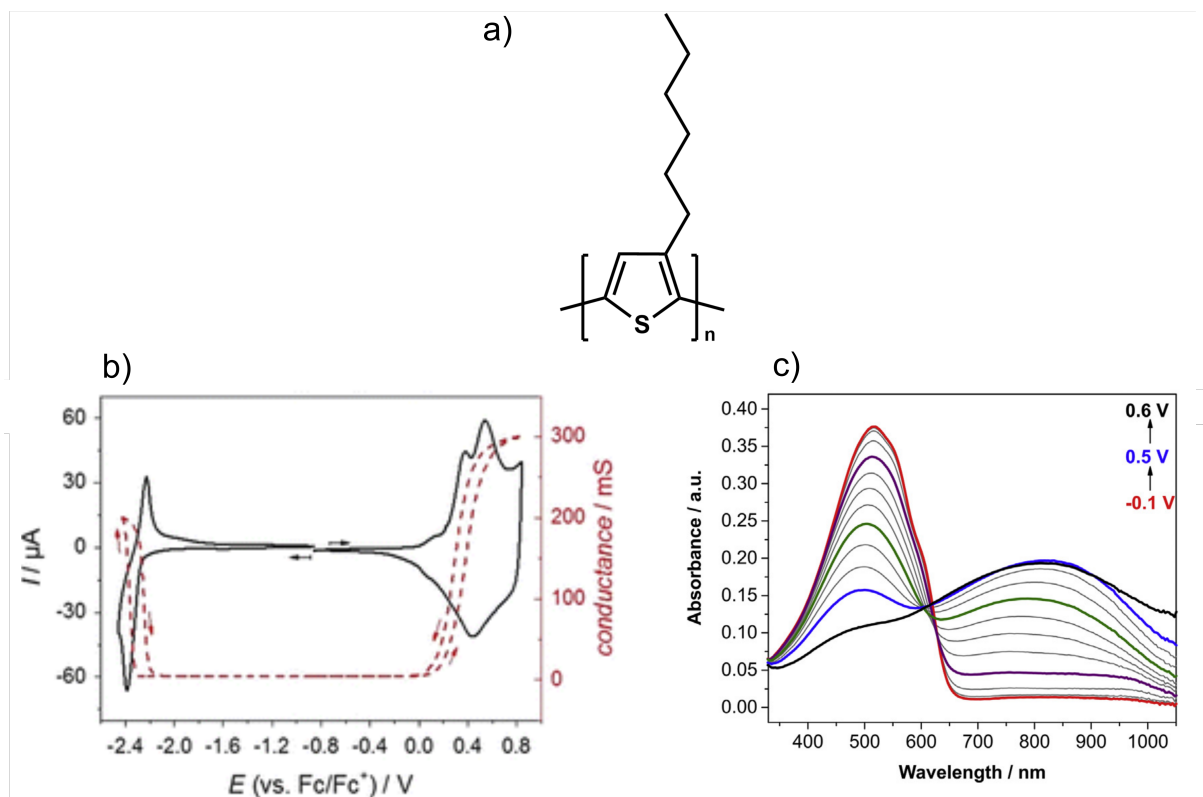


Figure 1.5: a) Molecular structure of P3HT and b) cyclic voltammogram (black curve) and in-situ conductance (red dashed curve) of the oxidation and the reduction of P3HT and c) UV/Vis NIR absorption spectra recorded in spectroelectrochemistry measurements of P3HT. Adapted with permission from [44], © 2014, Springer Nature and [45], © 2018, Elsevier.

In figure 1.5 b), the separately recorded cyclic voltammograms (black curve) of the reduction (at negative potentials) and the oxidation (at positive potentials) of P3HT indicate (at least partially) chemically reversible redox processes since after the reduction respectively oxidation in the forward scan, the oxidation respectively reduction back to the initial state can be observed. In contrast to molecular species which show distinct oxidation signals, the oxidation of P3HT shows several overlaying oxidation processes, which is due to different chain lengths or different morphologies [46]. The in-situ conductance (red dashed curve) in the neutral state of P3HT (in the potential range between -2.0 to 0 V indicates very low electronic conductance of P3HT. Upon oxidation in the positive potential range respectively reduction in the negative potential range, the in-situ conductance increases, which can be explained by the decrease of the band gap energy E_G (decrease of E_G results from an increase of the energy level of the highest occupied molecular orbital (HOMO) and subsequent decrease of the energy of the lowest unoccupied molecular

orbital (LUMO)) due to the formation of charge carriers on the polythiophene backbone. The reached in-situ conductance in the oxidized state is higher compared to the in-situ conductance in the reduced state and can be reached at low positive potentials, whereas in absolute numbers more negative potentials have to be applied to reduce P3HT. Therefore, it can be stated that the oxidized state of P3HT is more favorable than the reduced state. The accessibility of redox states is relevant for utilizing a conjugated polymer material as channel material in OECTs: the lower the gate potential V_G , which has to be applied to switch a material from its non-conducting to a conducting state and vice versa, the more energy-efficient the current amplifying property of the OECT is.

The red curve in figure 1.5 c) shows the UV/Vis absorption spectrum of the P3HT film at a potential of -0.1 V. The broad absorption band between 350 nm and 650 nm indicates the neutral polythiophene backbone, the vibronic fine structure (shoulder) at 610 nm indicates aggregation, which results from planarization of the polythiophene chains [47]. Upon increase of the potential, the absorption intensity of the neutral band decreases and a new, very broad band with a maximum at 820 nm evolves, which indicates the formation of a first oxidized state (often referred to as polaron). Presence of an isosbestic point at 640 nm indicates the conversion of the neutral species into the oxidized species. Upon further increase of the potential, the formation of a second absorption band at wavelengths higher than 1000 nm can be observed, which indicates a second oxidation state (often referred to as bipolaron). In the backward cycle of the cyclic voltammogram, the absorption bands of the oxidized states decrease and the absorption band of the neutral state is recovered, therefore it can be stated that the oxidation of P3HT is reversible.

The structure of polymer films in the nanometer scale is commonly referred to as thin film morphology ("morphology" originates from Greek: "study of forms"). The morphology of the surface of polymer thin films can be examined with Atomic Force Microscopy (AFM). In case of P3HT, different thin film morphologies can be obtained by controlling the crystallization conditions and the obtained morphology differences can be correlated to its electrochemical properties [45]. In general, features such as lamella or spherulite formation can be obtained in AFM images of P3HT thin films [47]. The influence of the film deposition conditions on the morphology, thin film absorption and electrochemical properties of P3HT films has been examined previously [33, 45].

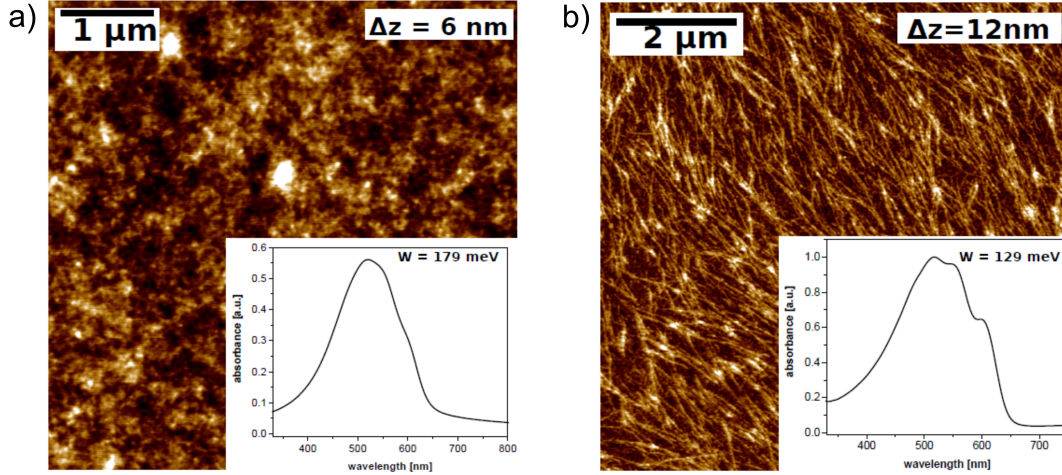


Figure 1.6: Morphology characterization of P3HT film after spin coating a) and subsequent solvent vapour annealing with AFM and UV/Vis absorption spectroscopy. Adapted with permission from [45], © 2018, Elsevier.

As can be seen in figure 1.6 a), spin coated P3HT films reveal predominantly amorphous structures with only limited $\pi - \pi$ -stacking as can be seen from the low-energy shoulders in the UV/Vis absorption spectrum. After heating the P3HT film in a saturated atmosphere of CS_2 (the procedure is commonly referred to as solvent vapor annealing) as can be seen in figure 1.6 b), the formation of P3HT nanowires which assemble in spherulitic structures can be observed from the AFM surface morphology. The UV/Vis spectrum after solvent vapor annealing reveals significantly more pronounced low-energy absorption shoulders.

Spano et al. developed a model to calculate the free exciton band width W from the absorption intensities of the transitions from the different vibrational states 0-0 and 0-1 (which correspond to the absorption intensities at the maximum absorption and at the shoulder) [48]:

$$\frac{A_{00}}{A_{01}} = \left(\frac{1 - 0.24 \cdot W/Ep}{1 + 0.073 \cdot W/Ep} \right)^2 \quad (1)$$

Here, A_{00} and A_{01} are the absorption intensities at the absorption maximum and at the low energy shoulder, W is the free exciton band width and Ep the energy of the main intermolecular vibration. Since the conjugation length is inversely proportional to the free exciton bandwidth, the variation of the conjugation length can be calculated from the variation of the absorption intensity ratio between the absorption maximum and the low energy shoulder. Since the absorption intensity of the low-energy absorption shoulder increases upon solvent vapor annealing (figure 1.6 b) the ratio A_{00}/A_{01} decreases, which corresponds to a decrease of W and accordingly to an increase of the conjugation length. Therefore, utilizing equation 1 and the absorption intensities, the increase of

the conjugation length and higher degree of crystallinity after solvent vapor annealing of P3HT films can be deduced.

1.2.2 Polyelectrolytes

1.2.2.1 Basics

According to a definition by the *International Union of Pure and Applied Chemistry (IUPAC)*, a polyelectrolyte is a "polymer composed of macromolecules in which a substantial portion of the constitutional units contains ionic or ionizable groups, or both" [49]. In figure 1.7, examples of common polyelectrolytes are shown.

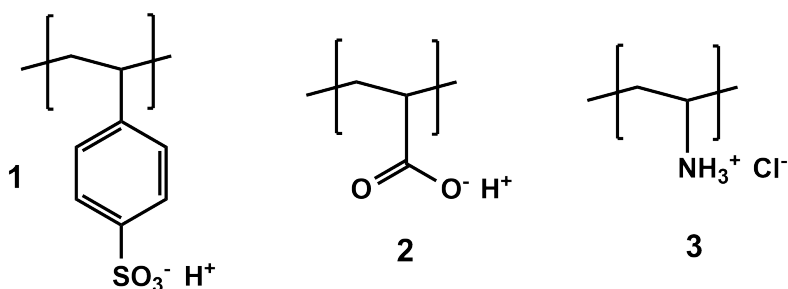


Figure 1.7: Examples of anionic and cationic polyelectrolytes: poly(4-styrenesulfonate acid) (PSS-H) (1), polyacrylic acid (2) and poly(allylamin hydrochloride) (3).

Depending on whether pendant anionic or cationic groups are present in the repeating unit, polyelectrolytes can be divided into polyanions, polycations or polyampholytes, if both anionic and cationic groups are present. Furthermore, polyelectrolytes could be classified according to if they react as acids or bases in aqueous solution by releasing or taking up protons, forming polyanions or polycations. Such polyacids and polybases can be classified according to their acidity respectively basicity [50]. Weak polyacids such as poly(acrylic acid) are only at pH values above 5 in their dissociated form and at pH values below 5 in their undissociated, protonated form. In contrast to that, strong polyacids such as PSS-H are at all pH values in their dissociated form [51]. Weak polybases such as poly(allylamin hydrochloride) are only at pH values below 8 in their associated ammonium form whereas at pH values above 8, the polybase is in its neutral amine form.

1.2.2.2 Water uptake properties

Due to the presence of ionic groups in polyelectrolytes, they are hydrophilic and therefore very soluble in water. Due to the hydrophilicity, they also take up water from humid atmospheres when they are present in the solid state, as studied for various polyelectrolyte materials [52–54]. At 90 % relative humidity, polyelectrolyte materials such as polyacrylic

acid sodium salt can take up 90 % water per weight (wt%) [52]. The water uptake mechanism of perfluorinated sulfonic-acid (PFSA) ionomer membranes has been studied in detail [3]. Membranes of poly(tetrafluoroethylene)-PFSA copolymers are often known according to their commercial name Nafion (brand name of *DuPont*) and are among others utilized as proton conducting membranes in proton exchange membrane fuel cells (PEMFC) [55]. In figure 1.8, the molecular structure of Nafion, the morphology of Nafion membranes and the water uptake as amount of water molecules per sulfonic acid group (in λ , see section 3.3.4 for details about the calculation of λ) of several PFSA materials as function of relative humidity is shown.

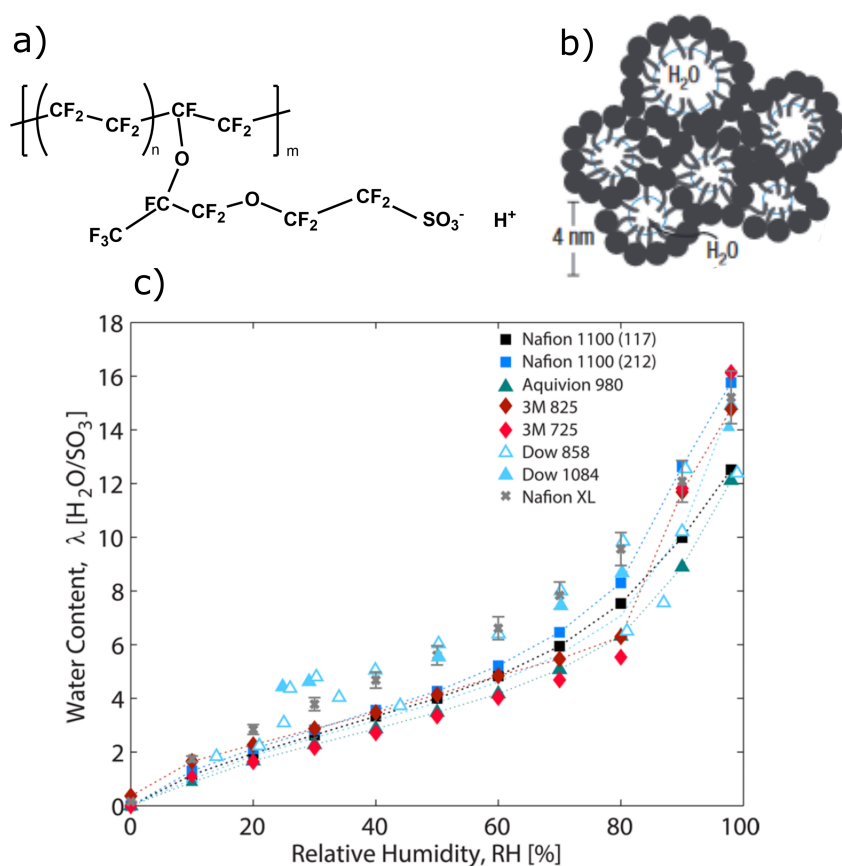


Figure 1.8: a) Molecular structure of Nafion and b) morphology of Nafion membranes and c) sorption isotherms (measured by gravimetric water uptake) at 25 °C as function of relative humidity for various PFSA membranes. Adapted with permission from [56], © 2008, Springer Nature and [3], © 2017, American Chemical Society.

The molecular structure of Nafion in figure 1.8 a) consists of copolymers of hydrophobic tetrafluoroethylene and hydrophilic perfluorinated ethylene units which contain sulfuric acid side groups [57]. The morphology of Nafion is still not entirely understood due to issues of inconsistent solubility and the presence of at least a three-phase nature [58]. One of the first morphology models of Nafion was the so-called cluster network which

includes ion clusters of inverted SO_3^- micelles of diameters of ≈ 40 nm that are connected by channels with diameters of ≈ 10 nm [59]. A more recent model (figure 1.8) proposes parallel water channels with diameters of 2 – 4 nm water rich (bright areas in figure 1.8 b) and physical crosslinks of Nafion crystallites (black structures in figure 1.8 b) which are responsible for the mechanical stability of Nafion films [56].

In the water uptake trend for all Nafion materials in figure 1.8 c), three different stages can be identified: up to 10 % relative humidity, the water content increases rather strongly. Between 10 and 80 % relative humidity, the water uptake increases slowly and above 80 % relative humidity, the water uptake increases very significantly. This trend is explained as follows: up to $\lambda = 1 - 2$, counter cations dissociate from the SO_3^- -groups, forming solvated cation complexes such as H_3O^+ . Going to higher water uptakes of $\lambda \approx 5 - 6$, multiple solvation shells form around the cation and the phase separation into hydrophilic, water rich moieties and hydrophobic, polymer backbone containing moieties is increased. At $\lambda > 6$, bulk-like water moieties are formed with hydration enthalpies between -40 and -45 kJ/mol, approaching the hydration enthalpy of pure water [60]. The presence of ionic clusters in PFSA membranes, which increase in size with increasing water content, is well-known [59].

1.2.2.3 Ionic conductivity properties

Since the water uptake of polyelectrolytes leads to a varying degree of dissociation of mobile ionic species from the oppositely charged, immobile ionic groups which are attached to the polyelectrolyte backbone, the ionic conductivity (σ_{ion}) of polyelectrolytes varies significantly as function of water content (and therefore as well as function of relative humidity) as previously studied in detail [3, 6, 7, 61, 62]. In figure 1.9, the ionic conductivity of a poly(sodium 4-styrenesulfonate) (PSS-Na) film as function of relative humidity is shown.

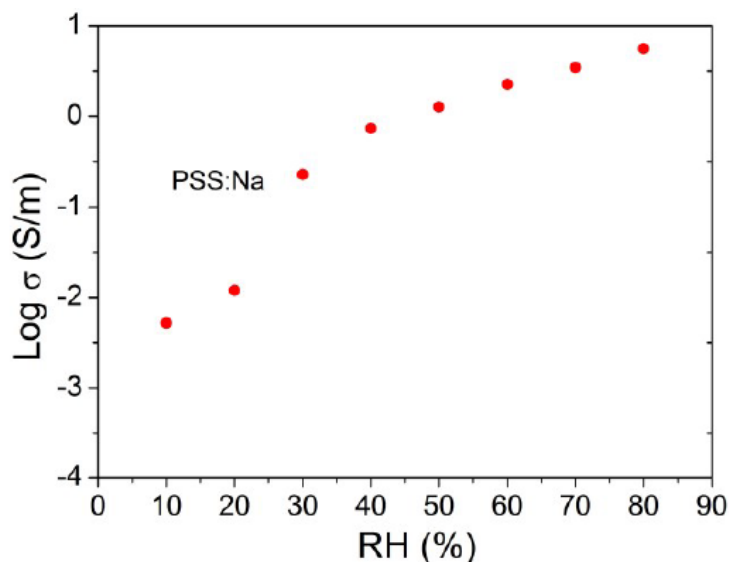


Figure 1.9: Ionic conductivity of a PSS-Na film as function of relative humidity. Adapted with permission from [63], © 2017, John Wiley and Sons.

At % 10 relative humidity, PSS-Na shows an ionic conductivity of 10^{-5} S/cm, which can be explained by the fact that the cations are immobile due to strong coulombic interactions with the opposite charged sulfonate groups which are attached to the side groups of the polymer backbone. Upon increase of the relative humidity, solvation shells form around the cations, which lead to a screening of the cations and therefore to a decreased activation energy for ion movement [64, 65]. Going to even higher humidities, continuous conduction channels are formed and the ionic conductivity reaches values of 10^{-1} S/cm, therefore approaching values of pure aqueous solutions [66]. The mechanical properties, the water uptake and conductivity properties of PFSA membranes were observed to be dependent on the type of cation, in which the water uptake and the ionic conductivity decreases with increasing cation size respectively cation radius [67].

Due to the discussed water uptake and conductivity properties as function of relative humidity, polyelectrolytes have the potential for application in the relative humidity sensing [68]. Since Nafion shows great proton conducting properties while electron conduction is entirely suppressed and since it also shows good thermal and mechanical stability, it is commonly used as proton conductor in proton exchange membrane fuel cells [7, 69]. Also Na^+ -exchanged Nafion membranes have been studied, in which the mobility of water molecules as well as Na^+ cations has been observed to increase with the water content [70–72]. It was observed that the conductivity occurs mainly in Gouy-Chapman type space-charge zones close to the interface between the water-rich hydrophilic moieties and the polymer backbone where the SO_3^- anions are attached [7].

After the given overview of the conjugated polymer and polyelectrolyte components, the

synthesis and the properties of the two polymeric mixed conductor materials PTS and PEDOT:PSS are introduced in the following. Due to the relevance of PEDOT:PSS in research and applications and its commercial availability, only for PEDOT:PSS the potential applications are briefly introduced.

1.3 Polymeric mixed conductor materials

1.3.1 Conjugated polyelectrolyte: PTS

PTS consists of a conjugated polythiophene backbone and pendant sulfonated hexyl side chains, therefore combining conducting polymer and polyelectrolyte moieties. Therefore, PTS belongs to the group of conjugated polyelectrolytes (CPEs). Depending on whether the side groups contain anionic or cationic end groups, anionic and cationic CPEs can be distinguished. In the following, the historic development of the synthesis and the properties of CPEs in general and in particular of PTS are given. For detailed explanations on CPEs, the reader is referred to in-depth literature [73–75].

1.3.1.1 Synthesis

In spite of their great promise for applicability due to their electronic and optical properties, conjugated polymers still had the problem of very poor solubility in organic solvents. Previously, this was tackled by introducing long alkyl chains to the conjugated backbone or by using strong oxidizing agents like a mixture of arsenic trifluoride and arsenic pentafluoride and subsequent dissolving of the conducting polymer/dopant mixture [76, 77]. Only several years after the discovery of conjugated polymers, in the group of Prof. Alan Heeger conjugated polymers which are water soluble were developed [78]. Heeger and his group solved the solubility issue for aqueous systems by introducing alkyl chains with methylester end groups as side chains into the thiophene monomer. After polymerization via electrochemical oxidation, the methylester end groups were converted to sulfonate end groups with sodium counterions. The resulting CPEs were soluble in H_2O .

In 1990, a way to prepare CPEs via chemical synthesis directly from the sulfonated thiophene monomer was reported [79]. The sodium 3-(3-thienyl)propane sulfonate monomer was chemically polymerized using $FeCl_3$ as oxidant in H_2O . After polymerization, the reaction mixture was treated with aqueous NaOH to yield poly(sodium 3-(3-thienyl)propane sulfonate). Cyclic voltammetry studies showed fast and reversible switching between the neutral and oxidized state. Later in 1995, Holdcroft et al. further optimized the synthesis procedure and analyzed the composition and structure of the obtained CPEs [80]. With the utilized synthesis method, the polymer reveals a head-to-tail to head-to-head ratio of 4:1, which corresponds to a regioregularity of $\leq 80\%$.

With the help of figure 1.10, the regioregularity in case of poly(3-alkylthiophenes) (therefore also being valid for P3HT as shown in figure 1.5 a) can be explained.

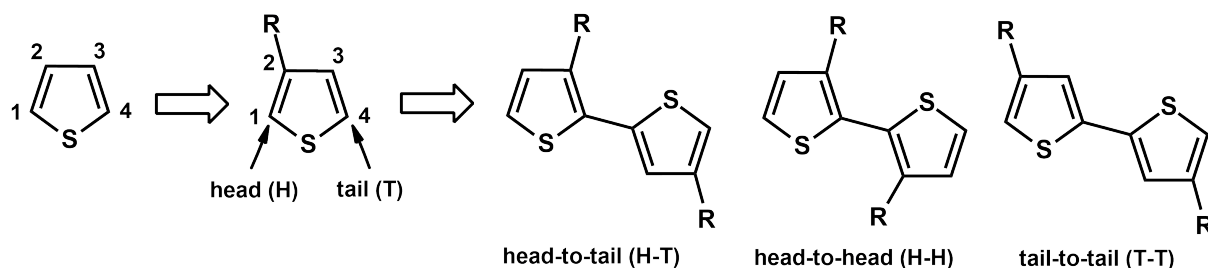


Figure 1.10: Three possible connection between thiophene monomers in poly(3-alkylthiophenes). Adapted from [81].

Depending on the position of the rest, the 2- and 5-carbon atoms of the thiophene unit can be assigned to the head and tail position. The thiophene monomers can accordingly couple in three different ways, in the head-to-tail, head-to-head and tail-to-tail connection. Since the head-to-tail connection is the most abundant connection, the regioregularity is given as share of head-to-tail connections among all connections. Only head-to-tail connections would therefore correspond to a regioregularity of 100%. From studies on P3HT it is known that higher degrees of regioregularity result for example in higher levels of crystallinity and larger charge carrier mobilities [82, 83], therefore high degrees of regioregularity are in general desirable.

In 2014, Thelakkat et al. introduced a synthetic route to prepare the CPE PTS-TBA as shown in figure 1.11 [22].

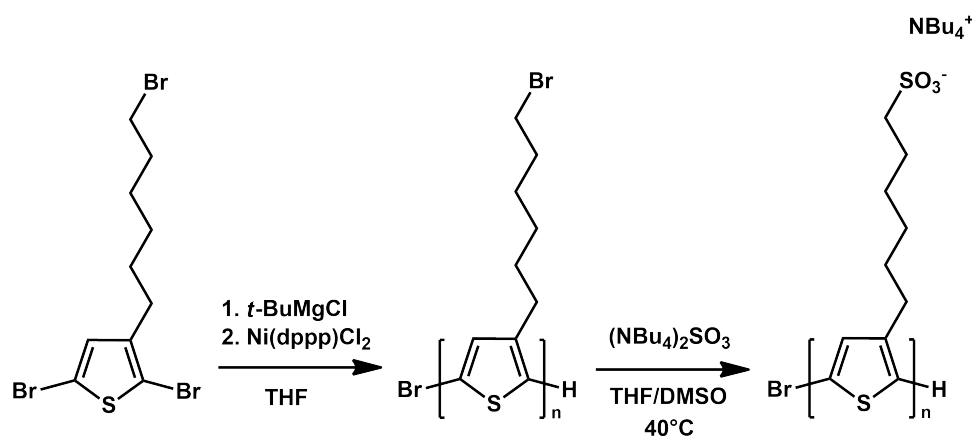


Figure 1.11: Synthesis route and molecular structure of PTS-TBA, adapted from [22].

2,5-Dibromo-3-(6-bromohexyl)thiophene monomers were polymerized with Kumada catalyst transfer polymerization to yield poly(3-(6-bromohexyl)thiophene) as precursor

polymer. Analysis of the precursor revealed a high regioregularity of $\geq 95\%$ and a polydispersity index (PDI) close to 1. Subsequent treatment with tetrabutyl ammonium sulfite yields PTS-TBA. The reported synthesis route was also utilized to prepare the PTS-TBA batch which was utilized in this thesis (see experimental part section 3.1.1 for more details).

1.3.1.2 Properties

Self- and auto-doping

In 1989, Heeger et al. studied the electrochemical cycling (alternating oxidation and reduction) of anionic CPE films with either H^+ or Na^+ counterions in detail [84]. By monitoring the ion concentrations in the electrolyte, the "cation-popping" effect was proclaimed: upon oxidation of the CPE, the concentration of the respective cation in the electrolyte increased. This was explained by an ejection of the H^+ respectively Na^+ cation into the electrolyte. Upon oxidation of the CPE, positive charges are formed on the polythiophene backbone. In conventional CPs, anions from the electrolyte are taken up in the polymer film in order to maintain charge neutrality. In case of CPEs however, ejection of the cationic counterions from the CPE film into the electrolyte is the predominant mechanism in order to establish charge neutrality [46]. Since the covalently bound anionic sulfonate ions serve as counterions for the positively charged conjugated polymer backbone and no external ions from the electrolyte are required, the oxidation of CPEs is referred to as "self-doping". This term however is also under discussion, since it would suggest that self-doped CPs are intrinsically conducting without any doping required. Since self-doped CPs require electrochemical doping, Heinze et al. rather suggest the term "self-ionized CPs" [46].

CPEs with protonic counterions revealed high four point probe conductivities of 0.1 S/cm, which is significantly higher than CPEs with sodium counterions [79]. Therefore, the term "self-acid-doping" was introduced: presence of H^+ as counterion leads to increased conductivity and the evolution of additional UV/Vis absorption bands since protons are added to the thiophene units [85]. High concentrations of free spins were obtained as in the chemical doping of poly(3-methylthiophene) with AsF_5 , which indicates that the addition of H^+ to the polythiophene backbone seems to involve a redox process. Later, the "acid-self-doping" effect was also referred to as "auto-doping" [75]. In a recent publication, the auto-doping effect was also observed in case of poly(1,4-bis(4-sulfonatobutoxy)benzene-alt-terthiophene) CPEs [86]. Interestingly, also for polyaniline CPEs an auto-doping effect could be observed: presence of Na^+ as counterion resulted in very low electronic conductivities, whereas a proton exchange resulted in significantly higher electronic conductivities [87]. The increased electronic conductivity was explained with the addition of protons

to the electron rich aniline nitrogen. Traces of oxygen, which might be present in the aqueous solutions of CPEs could eventually also participate in doping of the CPEs [43].

Further counterion dependency

In addition to the influence of either protons or other cations as counterions, which resulted in either self-doping or auto-doping effects, the influence of the type or size of counterions for example on the aggregation of CPEs was widely studied. Loewe et al. examined the UV/Vis absorption of solutions of poly(thiophene-3-propionic acid) CPEs after treatment with aqueous solutions of tetraalkylammonium hydroxide salts with various alkyl chain lengths, which resulted in a replacement of the counterion [2].

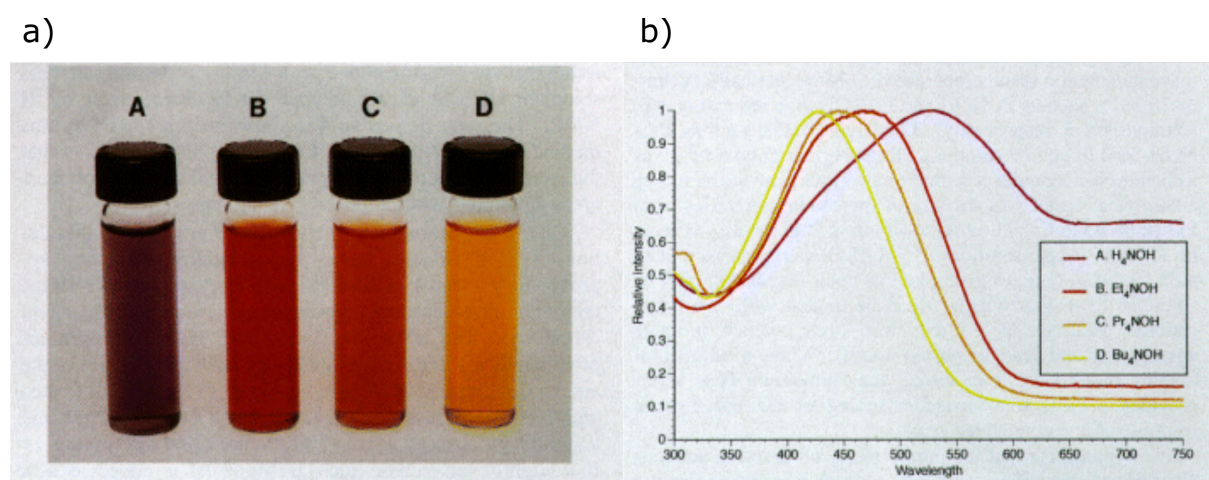


Figure 1.12: a) Vials of poly(thiophene-3-propionic acid) after adding various bases and b) UV/Vis absorption spectra of respective solutions. Adapted with permission from [2], © 1997, American Chemical Society.

As can be seen in figure 1.12 a), the colors of the CPEs vary significantly in dependency of the added tetraalkylammonium hydroxide solution. For the smallest counterion ammonium (A in figure 1.12) the UV/Vis spectrum (figure 1.12 b) showed an absorption maximum at ≈ 550 nm. Upon introducing alkyl side groups in the counterion and increasing these alkyl chain lengths (from B to D), the absorption maximum decreased, in which the absorption maximum was blue-shifted (hypsochromic shift, e.g. a shift to lower wavelengths) by 130 nm in case of tetrybutylammonium. This effect was explained by the fact that small cations favor the self-assembly of the CPEs whereas large cations can completely inhibit the aggregated state. Cerar et al. examined the properties of poly(thiophene-3-ylacetic acid) CPEs with different inorganic alkali and organic counterions with nuclear magnetic resonance (NMR) and diffusion coefficient measurements and found that the binding of tetraalkylammonium to the CPE can not be described thermodynamically, which is explained by the bulkiness of the tetraalkylammonium ions and their hydrophobic properties [88]. In another study poly(1,4-phenyleneethynylene

carboxylate) CPEs with various cationic counterions was examined and found that the electroluminescence maximum can be shifted from 430 nm in case of hard counterions to 515 nm in case of soft counterions [89]. Whereas amorphous film structures were found in case of nonamphiphilic counterions, smectic A and smectic B phases were found for amphiphilic counterions. The group of Guillermo Bazan has done research on CPEs for several years. In 2006, the group studied CPEs with various counterions and found varying degrees of self-doping effects after dialysis [90]. In a subsequent study, further counterions and varying side chain lengths were studied, which influenced the self-doping effects after dialysis [91]. It could be shown, that CPEs with small counterions and short side chain result in higher doping levels and more ordered films.

In a study from Thelakkat et al., PTS (which was also examined in this thesis) with either tetramethylammonium (TMA^+), tetraethylammonium (TEA^+) or TBA^+ counterions was analyzed with several optical and electrochemical methods [1]. In figure 1.13, the UV/Vis absorption in films and the UV/Vis absorption intensity trend at the wavelength of maximum absorption during spectroelectrochemical measurements (in order to prevent dissolution of the PTS films, (3-glycidyloxypropyl) trimethoxysilane (GOPS) crosslinker was added to the aqueous spin coating solution) for the three PTS materials is shown (note that PTS was named "PTHS" by the authors).

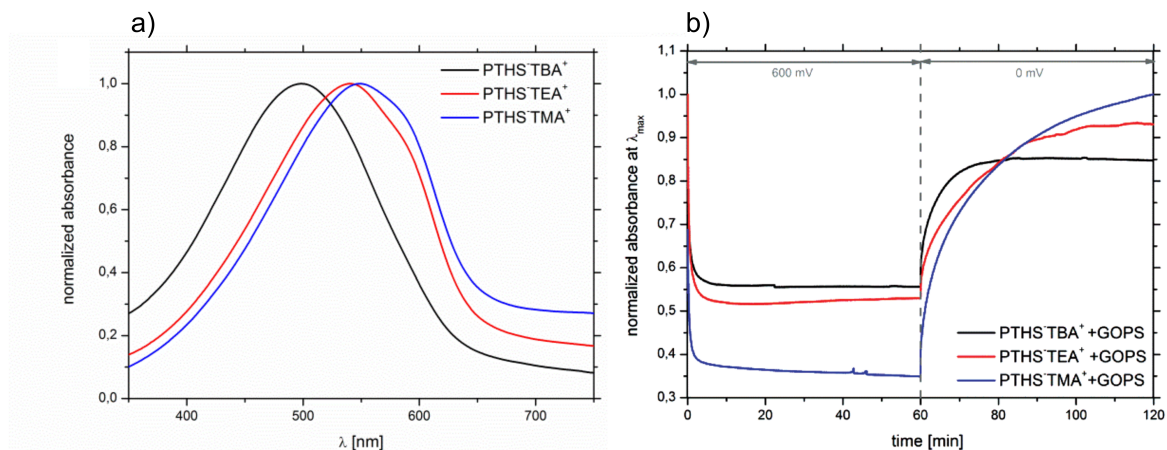


Figure 1.13: Studies on PTS with various counterions: a) UV/Vis absorption studies in film and b) trend of the UV/Vis absorption intensity in spectroelectrochemistry measurements at the wavelength of the absorption maximum upon applying a potential of 600 mV and subsequent switching to 0 mV. Adapted with permission from [1], © 2018, John Wiley and Sons.

As can be seen in figure 1.13 a), the UV/Vis absorption differs depending on the counterion. Whereas TBA^+ as counterion results in a nearly featureless spectrum with an absorption maximum at 499 nm, TEA^+ and TMA^+ counterions result in considerably

red-shifted absorption maxima at 540 respectively 549 nm and increasingly significant absorption shoulders at higher wavelengths. Therefore, it can be assumed that the smaller counterion TMA^+ promotes polythiophene backbone aggregation. In the trend of the absorption intensities upon applying a positive bias of +600 mV, it can be seen that for all materials, the absorption intensity decreases due to the oxidation of PTS. In case of PTS-TMA, the absorption intensity decreases most significantly which can be explained by the fact that more thiophene units are oxidized in PTS-TMA than in PTS-TEA and PTS-TBA. After switching back to 0 mV, PTS-TMA is the only material to show a completely reversible recovery to its neutral state. These effects can presumably be explained with more facile moving of TMA^+ cations out from and into the PTS film. In electrochemical impedance spectroscopy (EIS) measurements, a clear trend was obtained: the volumetric capacitance increased by more than one order of magnitude when decreasing the ion size in the row $\text{TBA}^+ - \text{TMA}^+$. In OEECT device performance measurements with the three different PTS materials as channel materials, the highest drain currents I_D and the fastest switching speeds were found for the OEECTs using PTS-TMA. In conclusion it can be stated that the solid state and electrochemical properties of PTS films depend considerably on the size of the counterion, in which it could be shown that the highest degree of aggregation in film and the best performance parameters in OEECTs were obtained for the smallest counterion. In a very recent publication, the Thelakkat group examined the OEECT performance with PTS-TMA-co-P3HT copolymers with varying P3HT contents [23]. For copolymers with 75 and 50 mol % PTS-TMA a lower threshold voltage and higher volumetric capacitance values compared to the PTS-TMA homopolymer were obtained, which gives indication that the P3HT content does not prevent the ion transport.

In contrast to the anionic CPEs discussed so far, also cationic CPEs were studied. Vohldal et al. synthesized poly(3-(6-(1-methylimidazolium-3-yl)hexyl)thiophene-2,5-diyl bromide) (PTImBr), which was also studied in a preliminary study of this thesis [92]. Solvent dependent UV/Vis absorption (solvatochromism) was found and evidence for the formation of micelle-like structures with the polythiophene core and 1-methylimidazolium shell was found. Maes et al. studied several cationic CPEs and found that with bis(trifluoromethylsulfonyl)imide (TFSI) as anionic counterion, the CPEs showed much lower glass transition temperatures and lower hydrophilicities compared to Br^- [93]. It could be shown that the CPEs as interlayers in OSC devices improved the efficiency, which was explained by the fact that the ion containing CPEs interlayers create a capacitive double layer. Bazan et al. studied cationic CPEs with various anionic counterions according to their performance in light emitting diodes and found significant different performance parameters, in which the reason for the differences remained unknown [94]. Nguyen et al. examined the influence of the anionic counterions of CPEs in light emitting diodes with voltage-driven current-density measurements and revealed that the opera-

tional mechanism is predominantly influenced by the electrochemical doping of the CPE [95]. The speed of the electrochemical doping decreases in the row Br^- to F^- to BIm_4^- (tetrakis(imidazolyl)borate), in which the ion size increases in the row F^- to Br^- to BIm_4^- . Therefore, the authors assume that not only the mobility but also the energy of dissociation determines the time till full electrochemical conversion is reached.

Morphology

For different CPEs systems, for example in case of cationic diblock-copolymers spherical particles were obtained [96]. For pristine PTS-TBA, AFM images of homogeneous and featureless films were revealed [22, 24]. Addition of EG results in an increase of the surface roughness and in fiber-like features with long range order [24]. The UV/Vis absorption maximum is shifted for around 30 nm to higher wavelengths, which can be explained by an increased stacking of conjugated segments. Interestingly, addition of EG to the PTS solution in prior to spin coating also improves the performance of PTS-TBA in OEECTs. In figure 1.14, the response time to a gate potential (V_G) pulse of an OEECT using either pristine or EG-treated PTS-TBA as channel material is shown.

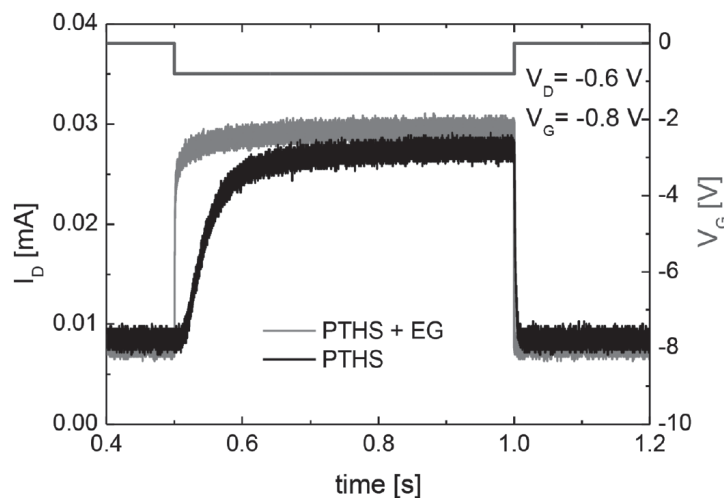


Figure 1.14: Response of an OEECT to a potential pulse. Adapted with permission from [24], © 2014, John Wiley and Sons.

As can be seen in the drain current (I_D) curve, the response time is significantly increased in case of the EG treated PTS channel material compared to the pristine PTS channel material. Also I_D increases significantly by a factor of approximately 7. From studies of PEDOT:PSS it is known that addition of EG increases the size of the PEDOT rich moieties and therefore leads to an increase of the electronic conductivity [97]. Therefore the authors assume that similar effects of the addition of EG on the structure of PTS could be expected, which might therefore result in a faster switching between the redox states of PTS.

1.3.2 Conjugated polymer/polyelectrolyte mixture: PEDOT:PSS

In addition to PTS, PEDOT:PSS is the second material examined in this thesis. Owing to the huge amount of publications dealing with the synthesis, properties and the (potential) applications of PEDOT:PSS, only a condensed overview of PEDOT:PSS is given in the following. The reader is referred to the very comprehensive book from Elschner et al. about all aspects of PEDOT and PEDOT:PSS, further literature about specific properties of PEDOT:PSS is given in the following [98].

1.3.2.1 History

With the discovery of conducting polymers, the central research department of *Bayer* attempted to utilize polyacetylenes in technical applications in the 1980s [98]. Due to the difficulties to stabilize polyacetylene in its doped state and to achieve processability, research on polyacetylenes was stopped. After further unsuccessful attempts on conductive tetracyano-quinodimethan complexes and polypyrroles, focus was laid on monoalkoxy- and 3,4-dialkoxy-substituted thiophenes since it was known that oxygen-bearing substituents can stabilize radicals and positive charges. The structures of all chemical compounds described in this section are shown in figure 1.15.

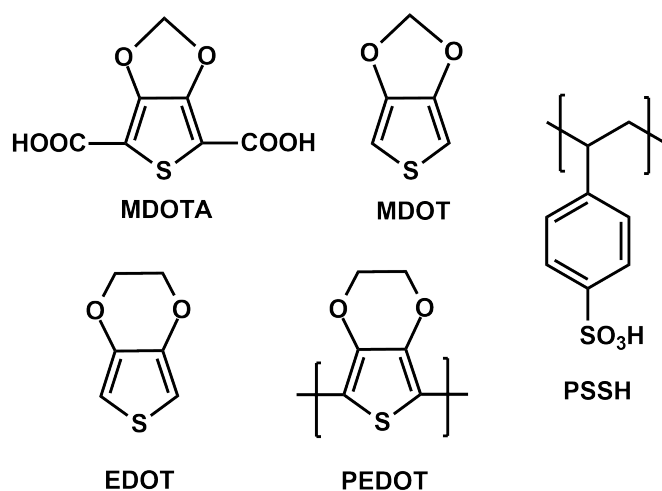


Figure 1.15: Molecular structures of compounds related to the chemical synthesis of PEDOT:PSS. Adapted from [98].

According to a previously reported synthesis of 3,4-methylenedioxythiophene-2,5-dicarboxylic acid (MDOTA), researchers Friedrich Jonas and Gerhard Heywang from *Bayer AG* tried to synthesize 3,4-methylenedioxythiophene (MDOT) [99]. After solving issues to decarboxylate MDOTA, MDOT was shown to be not polymerizable by chemical oxidation. Therefore, the researchers decided to extend the structure to the six-membered dioxane ring in 3,4-ethylenedioxythiophene (EDOT). The synthesis of EDOT

worked out nicely and the chemical polymerization of EDOT with FeCl_3 yielded poly(3,4-ethylenedioxythiophene) (PEDOT), the respective patents were filed in 1988. After polymerization, PEDOT was obtained in its oxidized state and revealed high conductivities and stability of its doped state even under air under high humidities. The group of Jürgen Heinze in Freiburg investigated the electropolymerization of EDOT and the electrochemical properties of the resulting PEDOT [100]. Despite its great properties, PEDOT still had the problem of bad processability. In 1989, a research collaboration between *Bayer* researcher Friedrich Jonas and Werner Krafft from *Agfa-Gevaert AG* started. *Agfa-Gevaert AG* was looking for new antistatic agents since the at that time used vanadium pentoxide had drawbacks such as toxicity and relative humidity dependent ionic conductivity of poly(styrenesulfonic acid) (PSS-H). It was found out, that PSS in its (partially) anionic form can serve as counterion for oxidized PEDOT to form a dispersion which is stable in aqueous media. The resulting composite material is therefore abbreviated as PEDOT:PSS.

1.3.2.2 Synthesis

In the following, an overview of the most frequently utilized method to prepare PEDOT:PSS is introduced. The method is according to the *Baytron P* process, which was patented in 1991 and which is also reproduced in literature [101–103]. The reaction scheme is shown in figure 1.16.

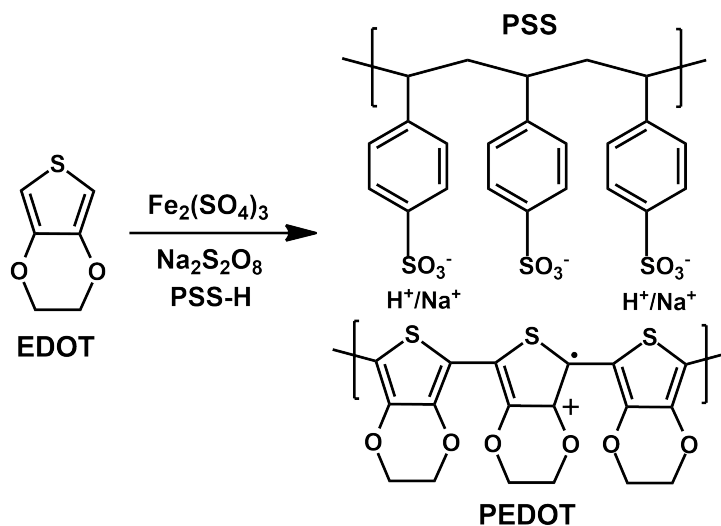


Figure 1.16: Synthesis and molecular structure of PEDOT:PSS. Adapted from [103].

EDOT is industrially prepared via the Gogte synthesis, which utilizes oxalic acid diester and thiodiacetic diester as reagents and which yields EDOT-2,5-dicarboxylic acid as intermediate step [104]. In order to prepare PEDOT:PSS, EDOT is mixed with PSS-H in varying ratios (depending on the desired PEDOT to PSS-H ratio in PEDOT:PSS, see section 1.3.2.3) and sodium persulfate ($\text{Na}_2\text{S}_2\text{O}_8$) in demineralized water. PSS-H is added, so

that the positively charged in-situ formed PEDOT can be stabilized by anionic charges of PSS, therefore an aqueous dispersion of PEDOT:PSS is formed [105]. Additionally PSS-H increases the solubility of EDOT and decreases the pH value, which prevents side reactions. Sodium persulfate ($\text{Na}_2\text{S}_2\text{O}_8$) was shown to be most beneficial as oxidizing agent, since it is water-soluble and prevents the precipitation of the PEDOT:PSS complex, as occurs upon utilizing compounds with multivalent cations such as Fe^{3+} . After short stirring of the aqueous solution of EDOT, $\text{Na}_2\text{S}_2\text{O}_8$ and PSS-H, iron sulfate ($\text{Fe}_2(\text{SO}_4)_3$) is added as initiator. The reaction mixture is stirred for typically 24 hours. Afterwards, the PEDOT:PSS particles are ion exchanged in an acidic resin and depending on the desired particle size filtered with varying mesh sizes.

1.3.2.3 Properties

Morphology

When discussing the properties of PEDOT:PSS, the first obvious question is how the structure respectively the morphology of the in-situ formed PEDOT:PSS is, in particular with respect to the question how the conducting polymer PEDOT is forming the composite material PEDOT:PSS together with the polyelectrolyte PSS. The different proposed structures are summarized in a recent publication [106]. Two repeatedly reported major features can be identified: crystallization respectively π - π -stacking of PEDOT units [107–113] and phase separation into PEDOT-rich and PSS-rich moieties [97, 105, 107, 113–117]. In figure 1.17, two representative models of PEDOT:PSS in thin films are shown.

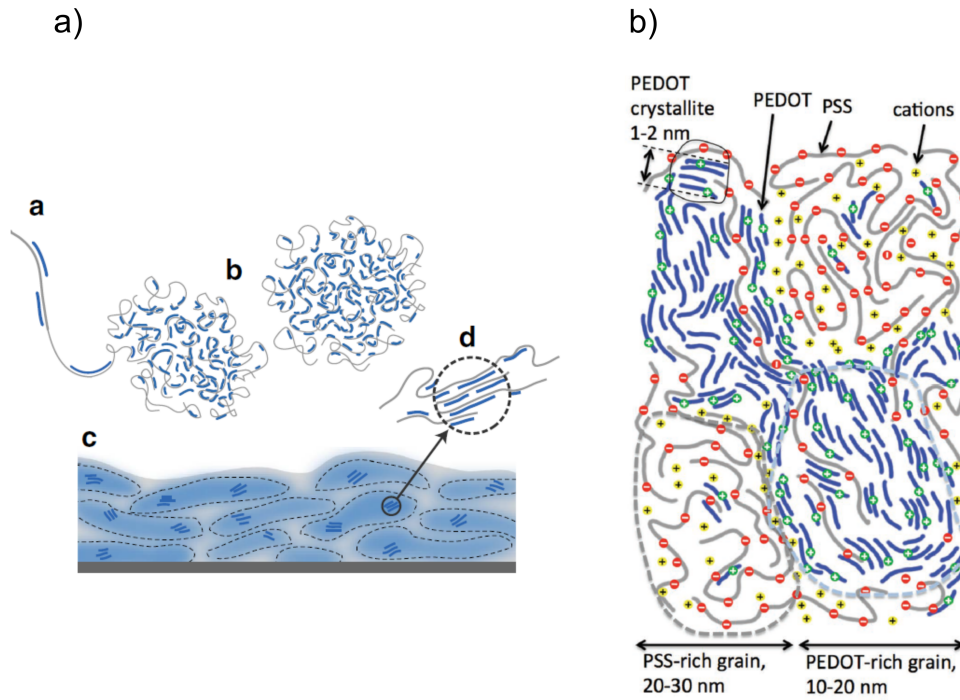


Figure 1.17: Two proposed morphology models of PEDOT:PSS. Adapted with permission from [97], © 2016, Springer Nature and [113], © 2017, John Wiley and Sons.

Figure 1.17 a) describes the structure formation during the chemical polymerization of PEDOT: during the polymerization of EDOT, oxidized PEDOT oligomers (see section 1.3.2.3 for a detailed discussion about the chain length of PEDOT) are polymerized onto the anionic PSS matrix (a) [97]. The PSS matrix with the attached PEDOT oligomers forms colloidal gel particles, resulting in a dispersion in the aqueous reaction medium (b). Upon deposition, disk-shaped "pancake-like" moieties with PEDOT and PSS rich moieties are formed, in which π - π stacking could be shown (c) and (d). Figure 1.17 b) corresponds to the morphology model of PEDOT:PSS model as determined by a combination of theoretical modeling and supporting experiments [113]. According to this model, PEDOT:PSS is a two-phase material with an amorphous, PSS-rich phase and a PEDOT-rich phase with characteristic sizes of 10 – 30 nm [106]. In the PEDOT-rich phase, PEDOT crystallites with dimensions of 1 – 2 nm were found. A percolative network of PEDOT moieties was proven to be pivotal for electronic conductivity whereas the amorphous PSS-rich phase provides ionic conductivity (see sections 1.3.2.3 and 1.3.2.3 for a discussion about electronic and ionic conductivity in PEDOT:PSS).

PEDOT to PSS ratio

One important parameter of PEDOT:PSS materials is the weight ratio of PEDOT to PSS (referred to as PEDOT:PSS ratio after herein), so the content of the PEDOT component and the PSS component in the composite material PEDOT:PSS. The commercial

PEDOT:PSS batches are predominantly high PEDOT content batches, so PEDOT:PSS batches with a PEDOT:PSS ratio of 1:2.5 or similar ratios. In contrast to that, also low PEDOT content PEDOT:PSS batches with a PEDOT:PSS ratio of 1:6 or with even lower PEDOT contents can be purchased. In this thesis, both the high and low PEDOT content PEDOT:PSS batches were examined (see also experimental section 3.1.2). Köhler et al. synthesized PEDOT:PSS batches by applying varying EDOT:PSS ratios ranging from 1:1 to 1:30 and examined films from the resulting PEDOT:PSS batches (full conversion of EDOT to PEDOT was assumed) by means of AC impedance spectroscopy and thermoelectric measurements [103]. In the AC impedance measurements, which were recorded in the frequency range from 0.5 Hz to 20 Mhz and which were conducted in dry N₂ conditions, for the PEDOT:PSS batches with PEDOT:PSS ratios of 1:6 to 1:30 a high-frequency semi-circle and a sloping low-frequency response was obtained, as can be seen in the Nyquist plots (also see in the experimental part section 3.3.3) in figure 1.18. According to [103], for PEDOT:PSS batches with higher PEDOT contents "dots" were obtained in the Nyquist plots (presumably due to high electronic conductivities), the Nyquist plots were therefore not shown.

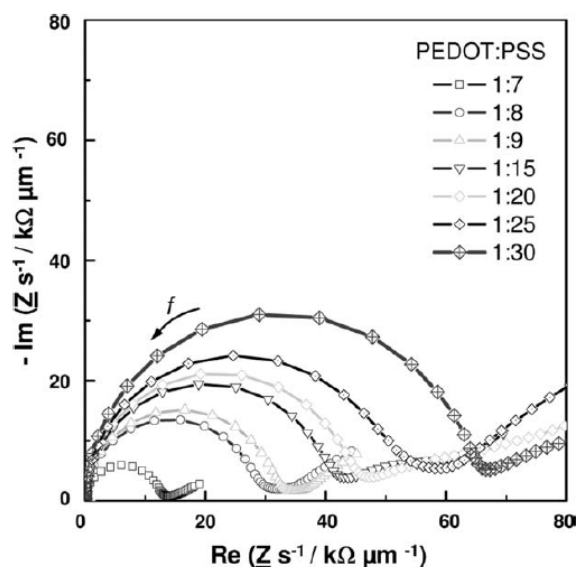


Figure 1.18: AC impedance spectroscopy of PEDOT:PSS films with various PEDOT:PSS ratios. Adapted with permission from [103], © 2012, John Wiley and Sons.

Whereas the diameter (resistance) of the high-frequency semi-circle can be assigned to the total resistance of the PEDOT:PSS film, the presence of the low-frequency signal indicates that the ionic conductivity is in a comparable range or higher than the electronic conductivity [8]. Since the resistance of the high-frequency semi-circle increases with decreasing PEDOT content, it can be stated that the total film resistance increases with decreasing PEDOT content. With the help of the high-frequency resistance, the electrical conductivity (the electrical conductivity comprises contributions both from the electronic

and ionic conductivity) as function of the PEDOT:PSS ratio is calculated, which can be seen in figure 1.19.

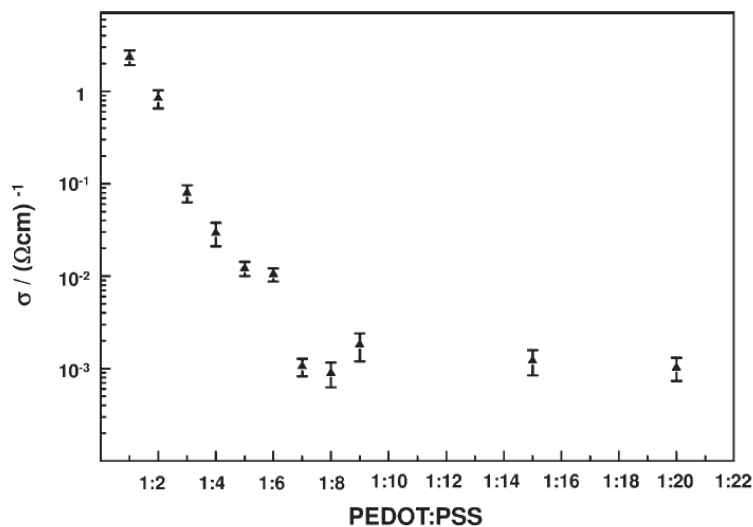


Figure 1.19: Electrical conductivity as function of PEDOT:PSS ratio. Adapted with permission from [103], © 2012, John Wiley and Sons.

According to Crispin et al., the high-frequency resistance comprises not only the electronic conductivity but also the ionic conductivity [8]. However, since the ionic conductivity does presumably not vary significantly due to the similar PSS contents in the different PEDOT:PSS batches, the large variations in the electrical conductivity can presumably be assigned to a variation of the electronic conductivity. Whereas the electrical conductivity is in the range of 1 S/cm in case of the PEDOT:PSS 1:1 batch, upon decreasing the PEDOT content the electrical conductivity levels off in the range of 10^{-3} S/cm at a PEDOT:PSS ratio equal or lower than 1:7 [103]. Since the charge carrier density was shown to be approximately constant for all PEDOT:PSS ratios, the variation of the electrical conductivity was explained with a loss of the percolation between the electronically conducting PEDOT moieties upon decreasing the PEDOT content. The large variation of the electrical conductivity with a concurrent small variation of the Seebeck coefficient as function of the PEDOT:PSS ratio for different PEDOT:PSS batches was also observed in a previous publication [118].

Lapkowski et al. examined various commercial PEDOT:PSS batches with varying PEDOT to PSS ratios with spectroscopic ellipsometry and UV/Vis spectroscopy and could separate the contributions from the PSS and PEDOT moieties [119]. Also the influence of the PEDOT:PSS ratio on the performance of PEDOT:PSS as hole injection layer in organic light emitting diodes (OLEDs) has been studied [120]. It could be obtained that different PEDOT:PSS ratios result in different work functions and hole barrier energies and therefore the optical and electrical device characteristics can be related to the

PEDOT:PSS ratio. The influence of the EDOT to PSS weight ratio, the EDOT to $\text{Na}_2\text{S}_2\text{O}_8$ molar ratio and the additive type and concentration in the synthesis on the resulting PEDOT:PSS material was also examined [121]. The EDOT:PSS ratio of 1:11 and the EDOT: $\text{Na}_2\text{S}_2\text{O}_8$ ratio of 1:2 was obtained to result in the highest conductivities of the pristine PEDOT:PSS films, a nonionic polyethylene oxide additive was revealed to improve the conductivity most significantly (see also section 1.3.2.3 for a discussion about strategies to improve the electronic conductivity of PEDOT:PSS).

Polymerization degree of PEDOT oligomers

Since PEDOT is prepared by chemical oxidation of the monomer EDOT, the resulting PEDOT oligomers are in their oxidized state after the chemical synthesis. In spite of the difficulty that PEDOT can only be examined in the complex with PSS, several efforts have been made to determine the polymerization degree of PEDOT, so the chain length of the PEDOT oligomers which are formed during the chemical polymerization. By extrapolation of the maximum absorption intensity of the EDOT dimer and the EDOT trimer in spectroelectrochemistry measurements, the chain length of PEDOT was estimated to 10 monomer units [122]. Matrix-assisted laser ionization time-of-flight (MALDI-TOF) measurements of PEDOT:PSS or substituted PEDOT derivatives indicated 6 – 18 monomer units in PEDOT oligomers [123]. Chain lengths between 10 and 20 monomer units have been estimated elsewhere [107].

Regarding PSS-H, it is important to mention that since the M_W of PSS-H exceeds typically 50.000 g/mol, its polymerization degree is therefore higher than 200 [124].

Electronic and optical properties of PEDOT:PSS

By comparing the peak intensities in the X-ray photoelectron spectroscopy (XPS) measurements as shown in figure 1.20, the doping level of pristine chemically polymerized PEDOT:PSS can be determined (note that PEDOT was named "PEDT" by the authors).

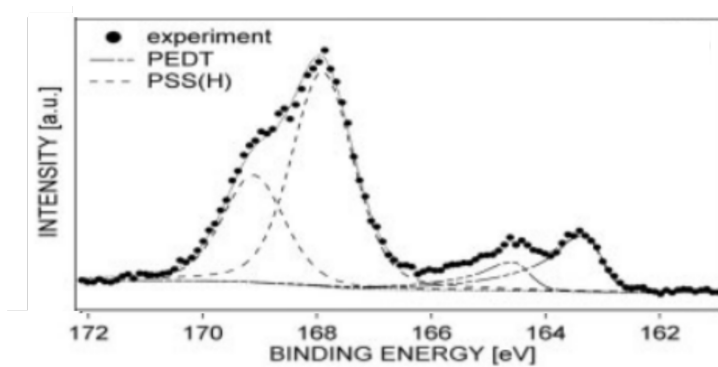


Figure 1.20: XPS measurement (S(2p) signals) of chemically synthesized PEDOT:PSS. Adapted with permission from [122], © 2003, American Chemical Society.

The peak intensity ratio of the deprotonated sulfonate SO_3^- -EDOT⁺ couple and the protonated sulfonate group SO_3H of the PSS counterion amounts roughly to 0.3 – 0.35 which corresponds also to the doping level of the pristine chemically polymerized PEDOT:PSS, therefore it can be concluded that 30 – 35 % of the EDOT monomers are in their oxidized form [122]. In a recent study by Zozoulenko et al. the unknown reason why the degree of oxidation in chemically polymerized PEDOT amounts to 33 % was approached with density functional theory [125]. The calculated Gibbs free energy was obtained to remain constant after reaching an oxidation level of 33 %, which is explained by the fact that at this degree of oxidation, all bonds in the backbone can switch from the aromatic to the energetically favored quinoid form.

Electronic conductivity in PEDOT:PSS

Because it was hoped that PEDOT:PSS and conducting polymers in general could be utilized for example in transparent electrode devices one day, many efforts have been made to improve the electronic conductivity of PEDOT:PSS [126]. Two principle strategies can be distinguished: firstly the additive method, where compounds are added to the PEDOT:PSS dispersion in prior to processing PEDOT:PSS into films or secondly the post-treatment method, where PEDOT:PSS films are treated after processing into films. In the additive method, typically high boiling point organic solvents such as dimethyl sulfoxide (DMSO), glycerol, sorbitol or EG are utilized [97, 127–130]. By adding 5% DMSO to the PEDOT:PSS dispersion, conductivities as high as 945 S/cm could be obtained [127]. In figure 1.21, the UV/Vis near infrared (NIR) absorption spectrum of PEDOT:PSS (1:2.5) films with and without EG treatment are shown [131].

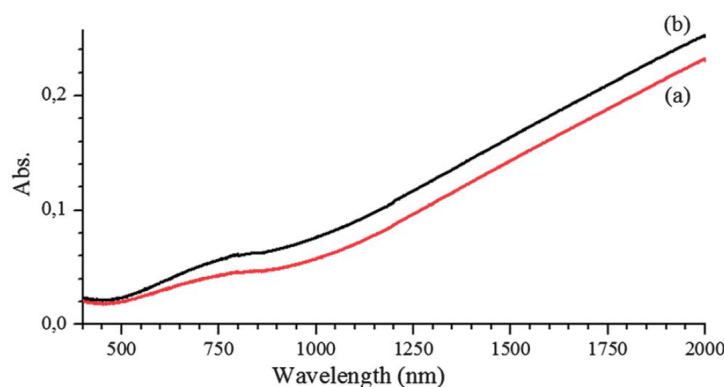


Figure 1.21: UV/Vis NIR absorption spectrum of a) a pristine PEDOT:PSS (1:2.5) film and b) a PEDOT:PSS (1:2.5) film which was dipped in EG. Adapted with permission from [131], © Royal Society of Chemistry 2014.

Four point probe measurements of the pristine and the EG dipped PEDOT:PSS films revealed conductivities of 9.6 and 714 S/cm, respectively [131]. Interestingly, the UV/Vis spectra do not show differences upon EG doping. This is due to the fact that secondary doping (such as the here reported EG doping) has no impact on the number of charge carriers in the film [132]. In the post-treatment method, the already deposited PEDOT:PSS films are treated for example with polar organic solvents or with acids [133–136]. Especially the treatment of PEDOT:PSS with H_2SO_4 yields conductivities as high as 4380 S/cm [137]. In figure 1.22, the effects of the acid treatment are shown.

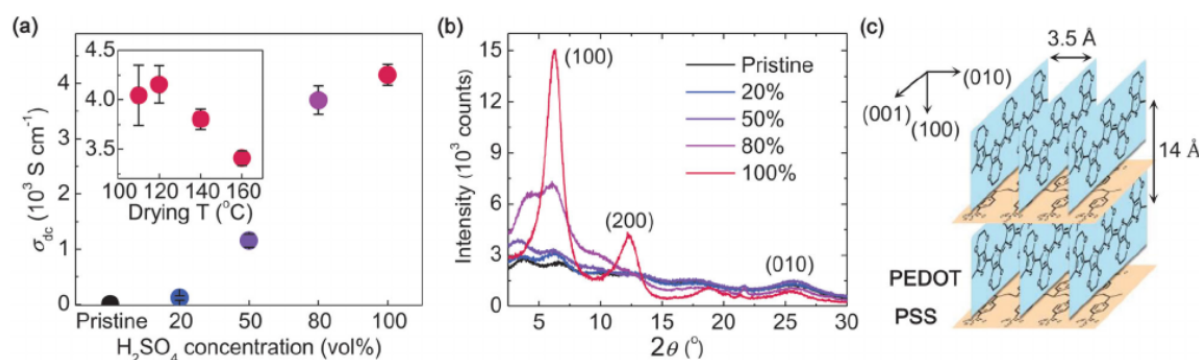


Figure 1.22: Post-treatment of PEDOT:PSS films with H_2SO_4 ; a) conductivity as function of H_2SO_4 concentration and at 100 vol% H_2SO_4 concentration as function of drying temperature and b) X-Ray diffractogram (XRD) pattern of PEDOT:PSS films as function of H_2SO_4 concentration and c) molecular packing structure of PEDOT:PSS. Adapted with permission from [137], © 2014, John Wiley and Sons.

In figure 1.22 a) it can be seen that the conductivity of the PEDOT:PSS films increases with increasing H_2SO_4 concentration and that subsequent drying at 120°C results in the highest conductivity. The effect of the acid treatment can be seen in the XRD patterns

in figure 1.22 b), which gives indication that PEDOT:PSS forms a lamellar stacking between two distinguishable, alternating orderings of PEDOT and PSS. As shown in case of H_2SO_4 , the conductivity increases since the $\pi - \pi$ -stacking of the PEDOT chains (figure 1.22 c) is improved and the interactions between the positive charged PEDOT chains and the negative charged PSS groups is weakened (this effect was also identified to be responsible for the conductivity increase for other pre- and post-deposition methods). Additionally, the acid treatment leads to a remove of the excess PSS, which increases the PEDOT content and therefore the conductivity [138].

In combination with the conventional additive and post-treatment methods, in which the PEDOT:PSS films are processed by spin coating, also sophisticated deposition methods were utilized to further increase the conductivity. For example, by adding EG to a PEDOT:PSS dispersion, subsequent concentrating of the PEDOT:PSS dispersion and preparing PEDOT:PSS fibers by means of bottom-up wet-spinning, conductivities of 3828 S/cm could be obtained [139]. By preparing PEDOT:PSS films with a solution-shearing method and subsequent post-treatment with methanol, conductivities as high as 4600 S/cm could be obtained [140]. According to a very recent publication, with the help of a PSS brush substrate and subsequent polymerization of PEDOT onto the brush, conductivities of 5000 – 6000 S/cm were reached [141].

Ionic conductivity in PEDOT:PSS

In addition to the examination and following improving of the electronic conductivity of PEDOT:PSS, attempts were made to determine the ionic conductivity in PEDOT:PSS. As Crispin et al. noticed, high electronic conductivity of PEDOT materials prevents to measure the ionic conductivity of these materials [8]. Berggren et al. examined the properties of PEDOT:PSS containing nano-fabricated cellulose, in which the ionic conductivity of PEDOT:PSS containing nano-fabricated cellulose could not directly be determined due to its high electronic conductivity [142]. Therefore, the ionic conductivity of PSS-H containing nano-fabricated cellulose was measured and the ionic conductivity of the PEDOT:PSS containing nano-fabricated cellulose was estimated to be the same.

Since the direct measurement of the ionic conductivity of the high PEDOT content PEDOT:PSS batches is not feasible, the ionic mobilities were studied instead. These can be extracted for example with Kelvin probe force microscopy [143]. As further possibility to extract ionic mobilities, the so called moving front method was developed [144, 145]. The scheme of the utilized device is shown in figure 1.23 a).

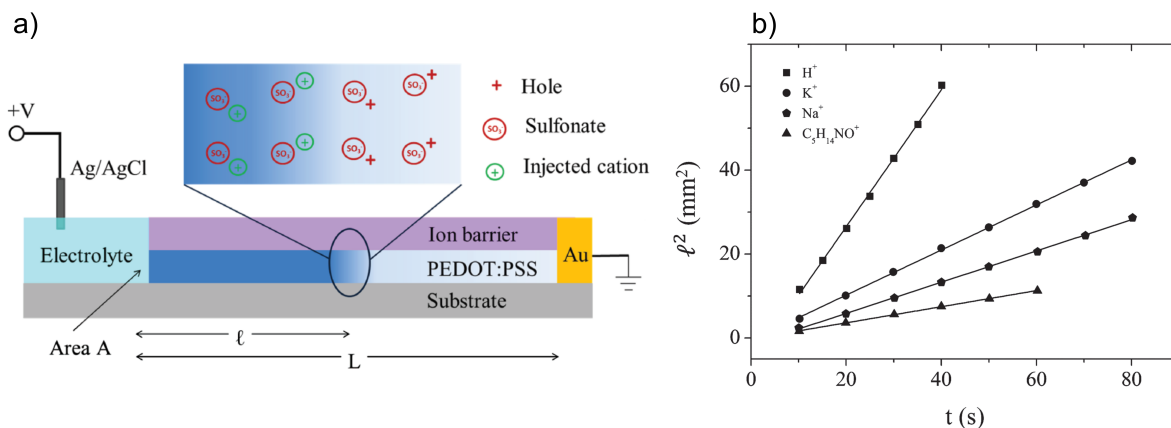


Figure 1.23: Determination of ionic mobilities in PEDOT:PSS. Scheme of moving front device a) and drift length of various cations b). Adapted with permission from [145], © 2013, John Wiley and Sons.

A PEDOT:PSS film is deposited on a glass substrate and encapsulated with an epoxy-based photoresist, which serves as an ionic barrier [145]. On one side of the PEDOT:PSS film a gold electrode was deposited and the planar open surface at the other side of the film was placed in an electrolyte. The electrolyte consists of an aqueous solution with varying conducting salts and in the electrolyte an Ag/AgCl reference electrode is placed. The optical transmission of the PEDOT:PSS film is measured spatially resolved through the glass substrate as function of the time after which a positive potential is applied at the Ag/AgCl electrode. According to the authors, the positive potential leads to a diffusion of the cations of the electrolyte into the PEDOT:PSS film and therefore to a concurrent dedoping (reduction from the oxidized to the neutral state) of the PEDOT:PSS film. The dedoping can be measured by a change of the optical transmission [146]. From the propagation of the dedoping front, the drift length and the ionic mobility of the respective cation can be calculated. In figure 1.23 b), the drift lengths of various cations are shown, in which the drift length is proportional to the ionic mobility. It can be seen that for all cations, a linear, yet significantly varying relationship between the drift length and the time can be obtained, which leads to the assumption that different cations move differently through the PEDOT:PSS material. For all cations except from H^+ (no assumption for the highest drift length in case of H^+ was given by the authors), fairly similar drift lengths are obtained, therefore it might be assumed that the water channels are spacious enough even for the large choline chloride cation. Interestingly, the here determined ionic mobilities of the four ions H^+ , K^+ , Na^+ and $\text{C}_5\text{H}_{14}\text{NO}^+$ in PEDOT:PSS films are larger than the respective electrophoretic mobility in bulk water, indicating a contribution of electroosmotic effects in PEDOT:PSS [147].

Rivnay et al. further improved the moving front method and also examined the variation

of the electrical conductivity and the ionic mobility upon adding various amounts of EG to the PEDOT:PSS dispersion before spin coating [97, 148]. The effect of the EG treatment on the electrical conductivity and the ionic mobility of PEDOT:PSS films and the suggested changes of the morphology are shown in figure 1.24.

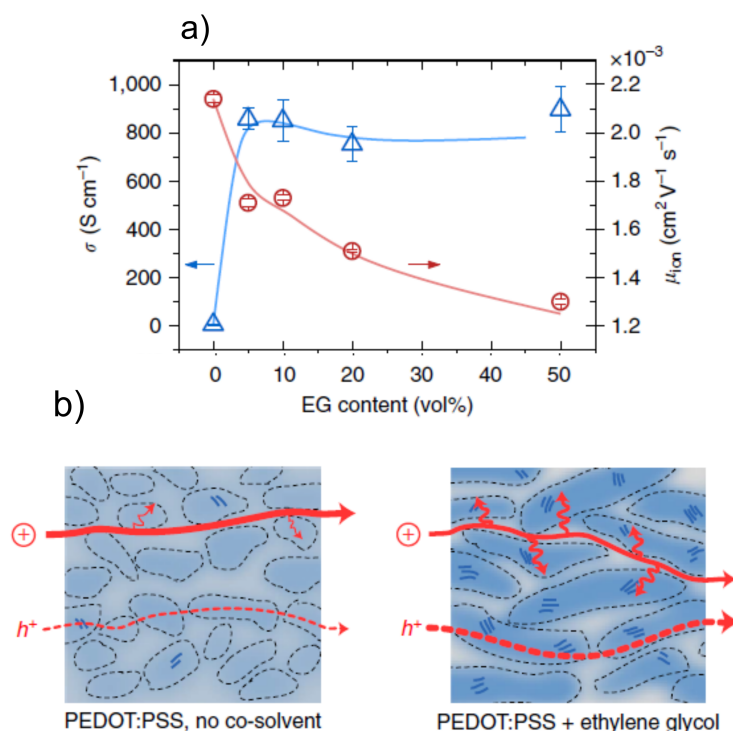


Figure 1.24: a) Variation of the electrical conductivity and the ionic mobility with EG content and b) proposed morphological changes upon addition of EG. Adapted with permission from [97], © 2013, Springer Nature.

In figure 1.24 a) it can be seen that addition of 10 vol% EG increases the electronic conductivity significantly, however adding of more EG does not lead to a further increase of the electronic conductivity. In contrast to the increase of the electronic conductivity, the ionic mobility decreases monotonically with increasing EG content. The proposed structure-related variation of the electronic conductivity and the ionic mobility is displayed in figure 1.24 b). In the PEDOT:PSS film with added EG, the PEDOT and PSS rich domains are further concentrated, so that in the PEDOT domains the maximum PEDOT to PSS ratio or minimum PSS content to preserve charge balancing is reached and that the PEDOT content in the PSS rich domains is decreased by 30 % [149]. As previously discussed, this is accompanied by an increase of the $\pi - \pi$ stacking of the PEDOT chains, which leads to an increase of the electronic conductivity. Whereas the bulk ion transport is presumed to take place in the PSS rich phase (which is only little affected by the EG addition), the diffusion of the ions into the PEDOT moieties is increasingly impeded due to the increased density of the PEDOT moieties as a result of the EG addition. Therefore,

the ionic mobility of the bulk PEDOT:PSS material decreases. It has to be noted, that with both Kelvin probe force microscopy as well as with moving front experiments, only the motion of external ions in the polymer films can be examined [97]. It is important to mention that the optimization of the electronic conductivity of the polymeric mixed conductor systems examined in this thesis was not the focus of this thesis, therefore no EG treatment was utilized.

1.3.2.4 Applications

Due to its superior properties and facile processability, attempts were taken to utilize PEDOT:PSS in a broad variety of applications, both in energy conversion and energy storage devices or in flexible and stretchable electronics [150, 151]. Xia et al. summarized all aspects of PEDOT:PSS leading to its potential for various applications: tunable conductivities up to 10^3 S/cm and tunable work functions, high stretchability and flexibility, long-term stability in air and high transparency [151]. In order to utilize PEDOT:PSS in stretchable electronics applications, composite materials of PEDOT:PSS and soft polymers such as poly(vinyl alcohol) (PVA), poly(acrylic acid) or poly(methacrylic acid) were examined which could combine the good conducting properties of PEDOT:PSS and the tensile properties of the soft polymers [152]. It could be seen that high conductivities such as in pure PEDOT:PSS could be maintained whereas the stretchability could be improved significantly, in which the stretchability was especially good in composite materials of PEDOT:PSS and PVA. The conductivity and tensile properties of fibers and films from PEDOT:PSS and PVA composites were examined previously [153, 154]. Due to their water uptake properties, polyelectrolyte materials are suitable for application in hydrogels [155]. Hydrogels consist of a network of crosslinked, hydrophilic polymers in which due to the crosslinks, the hydrogel does not dissolve even at high water uptakes. Hydrogels can be utilized in a broad range of applications, such as in hygienic products or in tissue engineering. PEDOT:PSS containing hydrogels were examined, therefore combining the mechanical properties of hydrogels with electrical properties of PEDOT:PSS [156]. The possible applications of PEDOT:PSS also depend from the PEDOT to PSS ratio: whereas the high PEDOT content PEDOT:PSS with PEDOT to PSS ratios of 1:2.5 is utilized as active layers in OECTs or as electrode replacement [17, 157], the low PEDOT content PEDOT:PSS is utilized as interlayers in OSCs or OLEDs [158, 159]. Few applications of PEDOT:PSS such as cathodes in solid electrolyte capacitors or antistatic layers in photographic and electronic films could be even industrially established, whereas applications in OLEDs, in OSCs or in smart windows are still in development [98].

2 Objectives

The aim of this thesis is to examine thin films of two polymeric mixed conductor systems, firstly the conjugated polyelectrolyte polythiophene-sulfonate (PTS) and secondly the well-known conjugated polymer/polyelectrolyte mixture poly(3,4-ethylenedioxythiophene): poly(styrene sulfonate) (PEDOT:PSS). Both material systems contain electronically conducting conjugated polymer moieties and ionically conducting hydrophilic polyelectrolyte moieties. At first, properties originating from the electronic properties of the polythiophene units in the mixed conductor systems, mainly the UV/Vis absorption properties shall be examined at various doping (oxidation) states. In the second part of this thesis, the water uptake properties originating from the polyelectrolyte moieties in both systems at variable atmospheric conditions should be examined. In part three the electronic and ionic conductivity properties originating from the polythiophene and polyelectrolyte moieties are examined as function of water uptake. The measurements of the water uptake, the conductivity and partially also the UV/Vis absorption properties are measured in self-built setups which allow to conduct the respective measurements in controlled atmospheric conditions as function of relative humidity.

Absorption characteristics in neutral and doped states

At first the UV/Vis absorption characteristics of PTS with either TBA⁺ or Na⁺ as counterions shall be examined. The cation type in anionic conjugated polyelectrolytes is known to have influence on the self-doping effects, the morphology in thin film and the electrochemical properties [1, 22, 84]. Additionally, the influence of the solvent system from which PTS is spin coated should be examined, so PTS-TBA and PTS-Na shall be spin coated from either pure H₂O or from a mixture of H₂O and THF. PTS was shown to exhibit different degrees of aggregation in thin films depending on the solvent system from which the film was spin coated [1, 22]. PTS shall be doped either chemically or electrochemically with the help of spectroelectrochemistry (cyclic voltammetry coupled with in-situ measurement of the UV/Vis absorption) and the UV/Vis absorption properties of the neutral and charged states in PTS shall be studied. The neutral and charged states of PEDOT:PSS should be examined with spectroelectrochemistry and additionally, in-situ conductance measurements (cyclic voltammetry coupled with in-situ conductance) shall be utilized to study the conductance in the neutral and the charged states of PEDOT:PSS. Specifically, the influence of the weight contents of PEDOT and PSS in PEDOT:PSS (PE-

DOT:PSS ratio) shall be investigated. PEDOT:PSS was shown to exhibit electronic and optical properties which depend on the PEDOT content in the PEDOT:PSS mixture [103, 119].

Water uptake studies in controlled atmospheric conditions

The water uptake properties of both polymeric mixed conductor systems as function of relative humidity shall be examined in detail. In literature, the water uptake of various hydrophilic polyelectrolyte materials as function of relative humidity is mainly determined using thermogravimetric analysis, weighing with a balance or by measuring the volumetric water vapor adsorption [5, 62, 160]. In all these methods the water uptake is determined with the polyelectrolyte materials being present in their bulk form, pressed into pellet form or as macroscopic, free standing film. In this thesis, the water uptake properties as function of relative humidity shall be determined with preliminary thermogravimetric analysis (TGA) measurements and a newly developed quartz crystal microbalance (QCM) technique in which the polymeric mixed conductor materials are deposited as thin films on the quartz crystals, which allows to precisely monitor the weight changes due to water uptake as function of humidity. Since in the conductivity measurements in this thesis the polymeric mixed conductor materials are also being present in thin films, a reasonable correlation between the water uptake and the conductivity properties upon variation of the atmospheric conditions can be achieved. The applicability, validity, reliability and reproducibility of the newly developed QCM technique shall be discussed in detail.

Conductivity studies as function of water uptake

The influence of the water uptake on the electronic and ionic conductivity properties of both polymeric mixed conductor systems shall be examined in detail. The ionic conductivity as function of relative humidity was studied previously in case of polyelectrolytes materials [6, 61, 63, 160]. On the other hand, the electronic conductivity of PEDOT:PSS materials as function of relative humidity was examined [4, 161]. The conductivity properties of the studied polymeric mixed conductor systems in this thesis are examined with in-depth AC impedance spectroscopy and DC measurements. The fitting procedure of the AC impedance spectra and the obtained fitting parameters, the extraction of the ionic and electronic conductivities from the AC impedance and DC measurements and the obtained dependencies of the conductivities from water content should be discussed. In case of the PTS systems, chemical doping shall be utilized to increase the electronic conductivity. The influence of the PEDOT:PSS ratio on the conductivity properties of the PEDOT:PSS systems should be examined. In addition to PTS and PEDOT:PSS materials, the conductivity properties of PEDOT:PSS-PVA composite materials shall be examined as function of water partial pressure.

3 Experimental

3.1 Materials

3.1.1 PTS

The synthesis of poly(6-(thiophene-3-yl)hexane-1-sulfonate)-tetrabutylammonium (PTS-TBA) was conducted by *Dr. Roman Tkachov* at the *Institute of Polymer Chemistry (IPOC) - Chair of Structure and Properties of Polymeric Materials* according to the procedure reported by Brendel et al. [22], the procedure and the respective NMR and gel permeation chromatography (GPC) structure analysis is also given in [162]. The precursor polymer poly(3-(6-bromohexyl)thiophene) (P3BrHT) had a molecular weight of $\overline{M}_n = 15$ kg/mol (as determined with size exclusion chromatography in THF with polystyrene standards), a polydispersity index of 1.1 and regioregularity $> 98\%$. P3BrHT was reacted with $((C_4H_9)_4N)_2SO_3$ (tetrabutylammonium sulfite) to yield PTS-TBA.

In order to study the influence of a second counterion, a cation exchange from TBA^+ to Na^+ was conducted, which yielded poly(6-(thiophene-3-yl)hexane-1-sulfonate)-sodium (PTS-Na). The reaction scheme can be seen in Figure 3.1.

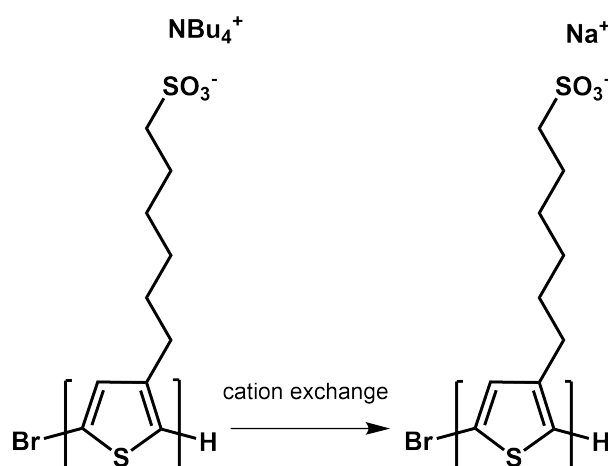
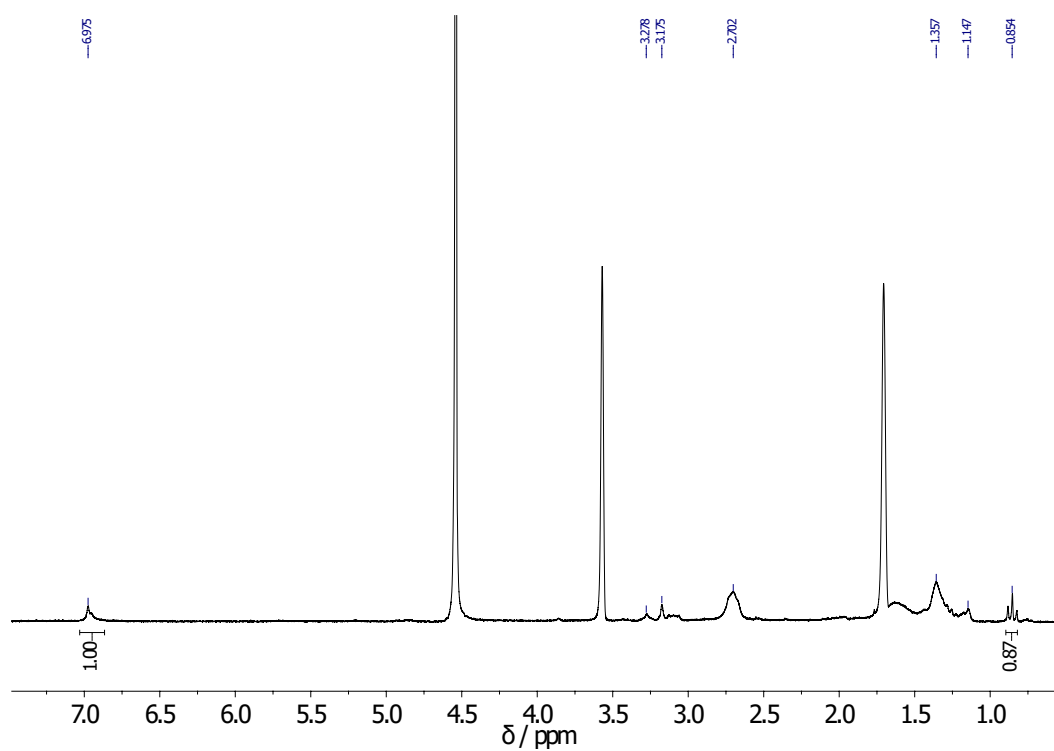
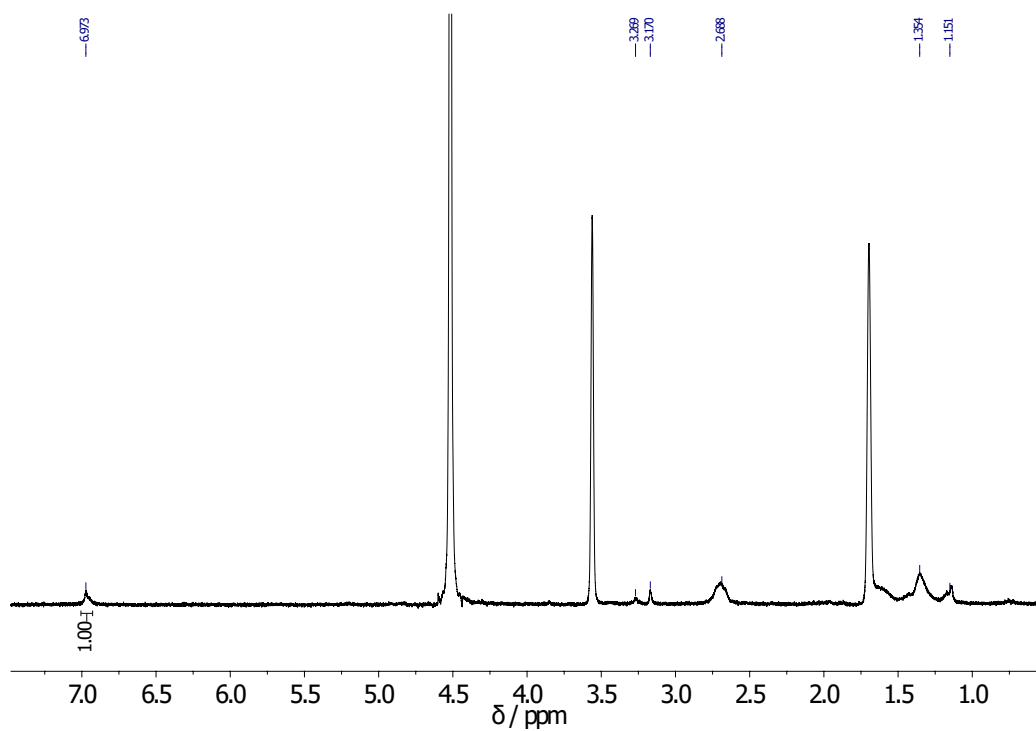


Figure 3.1: Molecular structures of PTS-TBA (left) and PTS-Na (right).

The cation exchange from TBA^+ to Na^+ was conducted using a Dowex Marathon C from Sigma Aldrich, which consists of NaPSS grains with particle sizes from 16-40 μm . A 0.5

mg/ml solution of PTS-TBA in H₂O (purified with a *Maxima* purification system from *USF ELGA*) was prepared for the cation exchange. Two cation exchanges were conducted, in which for the first cation exchange (referred to as cation exchange 1) 40 g NaPSS was used and for the second cation exchange (cation exchange 2) 100 g NaPSS was used and the solution was passed 10 times through the column. After conducting the cation exchange, the solvent was removed in vacuum and the polymer was freeze dried. In figures 3.2 and 3.3, the ¹H nuclear magnetic resonance spectra (NMRs) of the obtained product after the cation exchanges 1 and 2 are shown, each recorded in a 1:1 D₂O:THF-d₈ solution. The NMRs were measured by *Yannic Gross* in the *IPOC - Chair of Structure and Properties of Polymeric Materials* with a *Bruker Avance250* spectrometer from *Bruker* at 250 Mhz.

Since the signal at 6.9 ppm can solely be assigned to the aromatic thiophene proton (assuming the complete dissolution of the thiophene backbone) and the signals at 0.9 ppm to the aliphatic protons of the CH₃-group in TBA, the remaining share of TBA can be calculated. Since there is one thiophene proton in every repeating unit, the integral of the signal at 6.9 ppm can be set to 1. An integral of the CH₃-group of 12 would indicate one TBA cation for every thiophene repeating unit. Since the integral of the CH₃-group after cation exchange 1 (figure 3.2) amounts to 0.87, a conversion of TBA to Na of 93% can be calculated, thus the material after cation exchange is referred to as PTS-Na 93%. After cation exchange 2 (figure 3.3), no evaluable signals at 0.9 ppm are observed, thus a quantitative conversion to Na can be assumed. The resulting material is referred to as PTS-Na.

Figure 3.2: NMR spectrum of PTS-Na 93% (room temperature, 1:1 D₂O:THF-d₈).Figure 3.3: NMR spectrum of PTS-Na (room temperature, 1:1 D₂O:THF-d₈).

3.1.2 PEDOT:PSS

Several commercial poly(3,4-ethylenedioxythiophene):poly(styrene sulfonate) (PEDOT:PSS) batches were used in this thesis, the listed information are according to the data sheets by the respective suppliers. A low conductivity grade batch *Clevios PVP AI 4083* from *Hereaus* (1.3 wt% in aqueous solution, PEDOT to PSS weight ratio 1 to 6) was used. In order to compare the ionic conductivity of PTS-Na and PEDOT:PSS, the PEDOT:PSS (1:6) batch was titrated with NaOH to establish predominantly sodium cations to the counter balancing anionic sulfonate groups in PSS. The titration process was monitored with a pH-meter and the titration was stopped when a pH value of 7.4 was reached. The Na⁺ content of the PEDOT:PSS dispersion before and after titration was determined with atomic emission spectroscopy by *Jonas Groos* at the *IPOC - Chair of Macromolecular Materials and Fiber Chemistry*, in which a Na⁺ weight content of 1.8 wt% before titration and a Na⁺ content of 7.8 wt% after titration was obtained. The Na⁺ content after titration is lower than the theoretical content of 9.1 wt%, assuming the PEDOT to PSS ratio to be 1 to 6 and all styrene repeating units to be sulfonated. In the pristine PEDOT:PSS batches, presumably H⁺ is mainly present as counterion, traces of Na⁺ and Fe⁺³ are however also assumed to be present due to the chemical synthesis route. Additionally high conductivity grade PEDOT:PSS batches were used, firstly a batch from *Sigma Aldrich* (solid content 1.1 wt% in aqueous dispersion, the PEDOT to PSS weight ratio was determined with elementary analysis to 1 to 2.2) and secondly *Clevios PH 1000* from *Hereaus* (solid content 1.0 – 1.3 wt% in aqueous dispersion, PEDOT to PSS weight ratio 1 to 2.5). The PEDOT:PSS batches are referred according to the PEDOT to PSS weight ratio, for example PEDOT:PSS (1:6) denotes the PEDOT:PSS batch with a PEDOT to PSS weight ratio of 1 to 6.

3.1.3 Chemicals

For cleaning of the substrates, acetone (p.A., ≤ 99.5 %) and isopropanol (p.A., ≤ 99.5 %), both purchased from *Sigma-Aldrich* were used. For solutions of PTS, purified H₂O (demineralized H₂O was further purified with a *Millipore* purification system from *USF Elga*, if not otherwise mentioned H₂O is referred to purified H₂O) and THF (from *J.T.Baker*) were used. The evaporation bath of the adjustable atmospheric conditions setup (see section 3.3.2) was filled with demineralised H₂O from the internal house line. For cyclic voltammetric measurements, acetonitrile (p.A., ≤ 99.5 %, purchased from *Sigma-Aldrich*, MeCN in the following), tetrabutylammonium hexafluorophosphate (purchased from *Sigma-Aldrich*, NBu₄PF₆ in the following) were used.

3.2 Sample preparation

3.2.1 Substrates

Depending on the technique to use different types of substrate were required. For UV/Vis absorption measurements glass (for UV/Vis measurements in transmission) or gold (for UV/Vis measurements in reflection) substrates were used. The glass substrates were purchased as slides from *Glasbearbeitung Henneberg & Co.* Gold slides were prepared with an internal *UNIVEX 350* vapour deposition system from *Oerlikon Leybold Vacuum* by coating glass slides with a 5 nm thick chromium adhesion layer and 50 nm thick gold layer. Glass and gold coated glass slides were cut after cleaning (see below) into pieces of 1×1 cm. For Quartz Crystal Microbalance measurements, disk-shaped quartz crystals from *Inficon* (AT-cut, on the top side plated with gold, on the back side plated with a gold anchor structure, see section 3.3.5) with a resonance frequency of 6 Mhz were used. For AC impedance and DC measurements platinum (Pt) microarray interdigitated electrodes (in the following referred to as IDE, the IDEs were purchased from *Fraunhofer Institute of Physical Measurement Techniques IPM*) with different channel lengths l and channel widths w were used. The geometry parameters are listed in table 3.1. The IDEs consist of a Pt structure evaporated onto a quartz substrate. The Pt structure has a thickness of 220 nm, in which a 5 nm thick tantalum layer contact layer is between the quartz substrate and the Pt structure. The IDE types are abbreviated according to their channel length in the following, e.g. 5 μm IDE for an IDE with a channel length of 5 μm .

Table 3.1: Geometry parameters of interdigitated electrodes.

IDE type	Number of Digits	Channel Length l [μm]	Channel Width w [μm]
5 μm	720	5	191.70
10 μm	360	10	95.85
20 μm	180	20	47.95
50 μm	90	50	19.17
100 μm	45	100	9.59

Cyclic voltammetric measurements with in-situ measurement of UV/Vis absorption (spectroelectrochemistry) or in-situ conductance measurements were conducted using IDEs or indium doped tinn oxide (ITO) substrates. The ITO substrates were purchased from *PGO Präzisions Glas & Optik GmbH* and had surface resistances of $R \leq 20 \Omega/\text{sq}$. All substrates were cleaned each for five minutes in isopropanol and acetone with ultrasonification. In case of IDEs which were already coated with polymer films, the polymer films were removed from the IDE by cleaning the IDE with a cotton stick soaked with H_2O . The recycled IDEs were cleaned each for five minutes in H_2O , acetone and isopropanol. Depending on the used substrates, the substrates were subsequently treated with oxygen

plasma in order to increase the hydrophilicity of the substrate surface. All glass substrates were exposed to oxygen plasma for 10 minutes. The gold substrates and the IDEs were exposed to oxygen plasma for only 10 seconds since longer times would result in a further oxidation of the metallic substrate. The quartz crystals were not exposed to oxygen plasma since even slight changes of the gold coating on both sides of the quartz crystal would probably result in significant changes in the resonance frequency of the crystal.

3.2.2 Film preparation

Polymer films were prepared by spin coating with the help of a *WS-400BZ-6NPP/LITE* from *Laurell*. After applying the polymer solution/polymer dispersion on the substrate, which is fixed with vacuum in the center of the spin coater chuck, the spin coating was started. If not otherwise mentioned, all polymer films in this work were prepared with the identical spin coating parameters. The parameters are listed in table 3.2.

Table 3.2: Spin coating parameters for polymer films.

Step	acceleration [rpm/s]	rotation velocity [rpm]	rotation time [s]
1	10	3000	180
2	60	4000	60

All PTS films were prepared by spin coating PTS-TBA and PTS-Na from 5 mg/ml solution in pure H₂O or in 1:1 H₂O/THF mixture. In chapter 4.1, films from PTS-TBA respectively PTS-Na solutions are abbreviated according to the solution from which they were spin coated, therefore as PTS-TBA from H₂O, PTS-TBA from H₂O/THF, PTS-Na from H₂O or PTS-Na from H₂O/THF. In case the solvent system from which the PTS material is spin coated is not specifically indicated, PTS was spin coated from H₂O/THF. In order to utilize chemical doping on PTS films, 30 µl of a 0.5 M F₄TCNQ solution in THF were applied onto the PTS films and after a waiting time of 5 seconds, the excess solution was spun off at 3000 rpm for 180 seconds (the doping procedure is referred to as sequential doping) [163, 164]. The PEDOT:PSS films were prepared by spin coating from the respective aqueous dispersion (see section 3.1.2), in which in the following the PEDOT:PSS films are referred to as PEDOT:PSS (1:2.2) for the high conductivity batch from *Sigma Aldrich*, PEDOT:PSS (1:2.5) for the *Clevios PH 1000* batch from *Heraeus*, PEDOT:PSS (1:6) for the *Clevios PVP AI 4083* batch from *Heraeus* and PEDOT:PSS-Na (1:6) for the Na-exchanged *Clevios PVP AI 4083* batch from *Heraeus*. Depending on the solution respectively dispersion and depending on the substrate used, different volumes were used. For the glass and gold substrates 15 - 30 µl were used, for the quartz crystals 20 - 25 µl and for the IDEs 8 - 15 µl were used. In case of the quartz crystals, additional polymer films were prepared by drop casting 40 µl polymer dispersion onto the quartz crystal and drying for 10 minutes at 75°C. Before depositing polymer films on the IDEs, the resistance of the IDE was measured with

a multimeter. Only if no resistance could be measured (which corresponds to a higher resistance than 250 M Ω , this value is the highest measurable resistance of the multimeter), polymer films were deposited on the electrodes, otherwise the electrodes were further cleaned.

3.3 Methods

3.3.1 In-Situ adjustable atmospheric conditions measurements

The AC impedance and DC measurements (for determining the conductivity properties of the polymeric materials), QCM and preliminary TGA measurements (for determining the water uptake properties) and the UV/Vis absorption measurements in transmission and reflection mode (in order to determine the absorption properties of the polymeric materials) were conducted in controlled temperature and water partial pressure (denoted as $p\text{H}_2\text{O}$) conditions. For the QCM measurements a measurement cell was manufactured, which allowed to conduct the QCM measurements in controlled atmospheric conditions. Towards the end of 2017, the adjustable atmospheric conditions setup was newly built up in the *IPOC - Chair of Structure and Properties of Polymeric Materials*. Up till then, the AC impedance and DC measurements and the TGA measurements were conducted in an identical setup in the *Max-Planck Institute of Solid State Research (MPI)* by *Dr. Rotraut Merkle*. The temperatures in the AC impedance and DC measurements at the *MPI* were controlled with a self-made oven which is controlled with a *Eurotherm* controller. At the *IPOC*, the temperature in the QCM and AC impedance and DC measurement cells were controlled with a *R 50/500/12* tube furnace equipped with a *B180* controller by *Nabertherm*. If not otherwise mentioned, all measurement were conducted at a temperature of 25 ± 1 °C. All measurements were conducted in variable water partial pressure ranges $p\text{H}_2\text{O}$ from 0 – 29 mbar H_2O , which corresponds to relative humidity ranges from 0 – 92 % r.h. In prior to the $p\text{H}_2\text{O}$ ramp, in all QCM and AC impedance and DC measurements an initial drying step was conducted via drying the respective samples at 0 mbar H_2O and 40°C. According to equation 2, the relative humidity can be calculated from the water partial pressure $p\text{H}_2\text{O}$ and the saturated water partial pressure $p\text{H}_2\text{O}_{sat}$ [165]:

$$\text{relative humidity} = \frac{p\text{H}_2\text{O}}{p\text{H}_2\text{O}_{sat}} \cdot 100 \% [\% \text{ r.h.}] \quad (2)$$

Due to inaccuracies of the adjustable atmospheric conditions setup, the measured water partial pressure was observed to be up to 0.7 mbar H_2O below the set value, this error is however not expected to influence the general dependencies of the examined properties. In the present thesis, the discussion will be lead using water partial pressure instead of the relative humidity since water partial pressure is a temperature independent quantity.

3.3.2 Setup

A scheme of the controlled temperature and water partial pressure conditions setup can be seen in figure 3.4.

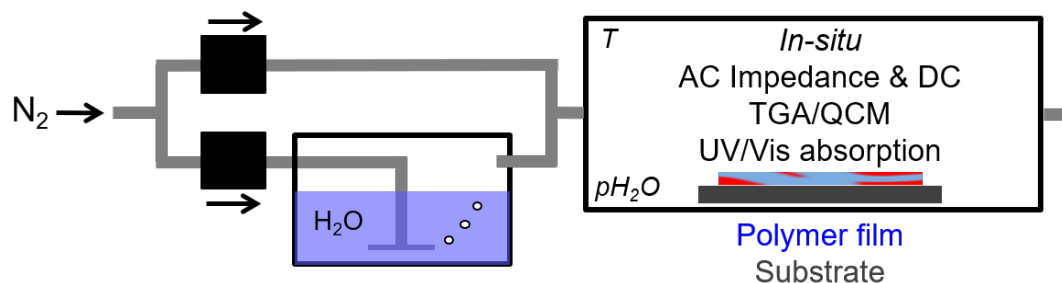


Figure 3.4: Scheme of the adjustable atmospheric conditions setup.

In order to set different water partial pressures, two nitrogen gas flows are mixed, in which one nitrogen gas is dry and one is lead through a water evaporation bath. After saturating one nitrogen flow in water, the gas flows are mixed again together. The gas flow rates of both nitrogen gas flows can be set, which results in a variable saturation of the mixed nitrogen flow which flows into the respective measurement cell. The total gas flow rate amounts to 40 sccm/min (equals roughly 40 ml/min). The temperature of the evaporation bath is set to 5°C, 18°C or 24°C, so at temperatures lower than the temperature in the fumehood (where the atmospheric conditions setup is located) in order to avoid water condensation in the gas tubes. For all measurements, the measurement takes place in sealed measurement cells, through which the mixed nitrogen flow with various water partial pressures is led through. The set water partial pressure was monitored with a *Hygro Clip 2* relative humidity sensor from *Rotronic* which was installed at the gas outlet of the measurement chamber. In case of AC impedance and DC measurements and TGA/QCM measurements, the temperature of the sample can be controlled by setting the temperature of the oven in which the measurement cell is placed inside, in case of the UV/Vis measurements the temperature of the sample can be varied by setting different temperatures of a peltier element heating the polymer film coated sample.

3.3.3 AC impedance and DC measurements

All electrical characterization measurements of the polymeric thin film materials in this thesis were conducted either in direct current (DC) mode or alternating current (AC) mode [166]. Impedance spectroscopy is a powerful technique which is also widely used in battery and fuel cell research [167, 168]. The technique to apply either alternating currents or alternating potentials [169] with variable frequencies to the system to be analyzed is called AC impedance spectroscopy. It is a powerful tool to study on one hand

electric properties or conduction mechanisms of solid state materials (as it is the case in the present study) or on the other hand to study electrochemical systems where redox reactions and mass transfer processes occur (in this case the technique is called electrochemical impedance spectroscopy, EIS) [170]. For example, informations of batteries like charge state or reaction mechanisms can be analyzed with electrochemical impedance spectroscopy [167]. In this thesis, AC impedance and DC measurements were conducted in order to extract the electronic and ionic conductivities of the polymeric mixed conductors. An electrical conductivity σ (both valid for electronic and ionic conductivity) is defined as the proportional constant between current density j and electrical field strength E [171]:

$$\sigma = \frac{j}{E} \quad (3)$$

The definition can be understood easily: in case of a constant j and a decreasing E , σ increases since a lower field strength E is required for a constant current density j . In the following, the calculation of the electronic conductivity σ_e and ionic conductivity σ_{ion} with the help of AC impedance and DC measurements is derived.

Starting with the most simple case of direct current (DC) measurements in case of an Ohmic resistor, the system to be analyzed is exposed to constant currents. According to the Ohmic Law, the resistance R , which opposes a direct current flow, can be calculated from the applied current I and the resulting potential U :

$$R = \frac{U}{I} \quad (4)$$

The impedance Z opposes current flows in alternating current (AC) circuits. In addition to Ohmic resistors, also capacitances or inductances can impede the current flow in alternating current circuits. The impedance Z , which can be calculated according to the equation

$$Z = \frac{U}{I} \quad (5)$$

can not be determined with DC measurements due to the time-dependency of the capacitance or the inductance. Therefore, in alternating current (AC) impedance measurements, the system is exposed to sine-shaped potentials of variable frequencies f with a certain potential amplitude U_0 in the following form:

$$U(t) = U_0 \cdot \sin(2\pi ft) \quad (6)$$

A sinusoidal current in the form

$$I(t) = I_0 \cdot \sin(2\pi ft + \phi) \quad (7)$$

is obtained as response of the excitation signal. In case of no phase shift of the current signal ($\phi = 0$), the sine-shaped current signal is referred to as "in-phase", whereas in case of a phase shift ($\phi \neq 0$), the sine-shaped current signal is referred to "out-of-phase". An exemplary excitation signal with a out-of-phase current response signal can be seen in figure 3.5.

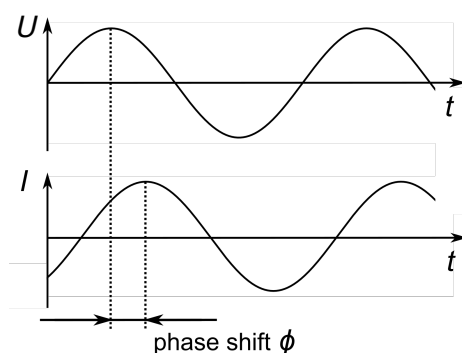


Figure 3.5: Excitation potential sinusoidal wave and current response sinus wave.

Information can be obtained from the amplitude of the sinusoidal current signal (I_0 , Ohmic contributions to the sample's total impedance) and phase shift of the sinusoidal current signal (in case $\phi \neq 0$, capacitive or inductive contributions to the sample's total impedance occur) at each analyzed frequency. Using the Euler equation to express the impedance as complex function, the total impedance can be expressed with the following equation:

$$Z = \frac{U' + jU''}{I' + jI''} = Z' + jZ'' \quad (8)$$

The Ohmic contributions are expressed as the real part impedance Z' and the capacitive and inductive contributions are expressed as the imaginary part impedances Z'' . Plotting the imaginary impedance Z'' as function of the real part impedance Z' , the so-called Nyquist plot can be obtained. The advantage of the Nyquist plot is that a relaxation process can be easily identified by the presence of a characteristic semi-circle, in which the amount of semi-circles allows to identify the amount of relaxation processes in close proximity. As alternative, in the so called Bode plot the phase shift and the modulus of the impedance Z are plotted as function of the frequency. This allows for example to better depict the frequency dependency of the system.

Analysis and fitting of AC impedance spectroscopy data requires establishing of an equivalent circuit, which should describe the physical processes occurring in the analyzed system

qualitatively as good as possible with as little elements as possible. An equivalent circuit can contain elements like resistors (circuit element R), capacitances (circuit element C), inductances (circuit element I) or more complex elements like Warburg elements W (for long range diffusion processes) or constant phase elements Q (for non-ideal capacitors). For the present study the circuit elements resistor R , constant phase elements Q and Warburg Open elements W_o were utilized [172]. In the following, these circuit elements including the dependency of the circuit elements from the angular frequency ω ($\omega = 2\pi f$) are described.

A resistor R contributes to the real part impedance Z' and shows no frequency dependence:

$$\begin{aligned} Z(\omega) &= R \\ Z'(\omega) &= R \\ Z''(\omega) &= 0 \end{aligned} \tag{9}$$

A constant phase element Q describes the capacitive behavior of non-homogeneous and therefore non-ideal systems with the following equation:

$$Z(\omega) = \frac{1}{Q-T \cdot (j \cdot \omega)^{Q-P}} \tag{10}$$

If $Q-P = 1$, then equation 10 describes an ideal capacitor. An ideal capacitor can be described as follows:

$$\begin{aligned} Z(\omega) &= \frac{1}{Q-T \cdot j \cdot \omega} \\ Z'(\omega) &= 0 \\ Z''(\omega) &= -\frac{1}{\omega \cdot C} \end{aligned} \tag{11}$$

Parameter $Q-T$ describes therefore the capacitive contributions, $Q-P$ describes the homogeneity of the system.

A Warburg element in general describes mass diffusion from or to an electrode. The frequency dependence of W_o is given in equation 12.

$$Z(\omega) = W-R \cdot \frac{\coth[(j \cdot W-T \cdot \omega)]^{W-P}}{(j \cdot W-T \cdot \omega)^{W-P}} \tag{12}$$

Here $W-T$ corresponds to the diffusion resistance, $W-T$ corresponds via $W-T = L^2/D$ (L corresponds to the effective diffusion thickness and D the effective diffusion coefficient) to a diffusion time of the system and $W-P$ corresponds to a coefficient which equals

$P = 0.5$ in case of an ideal Warburg element. Two Warburg elements can be utilized in equivalent circuits: whereas the Warburg Short element W_s describes finite-length diffusion to a transmissive boundary, the above described Warburg Open element W_o describes finite-length diffusion to a reflective boundary [173]. In the examined frequency ranges in this thesis in case of pure ionic conductors, AC impedance spectra were obtained which resemble the features of spectra which can be modeled with the Warburg Open element. However, if the spectra would have been measured to lower frequencies, a second semi-circle would be obtained due to the finite electronic resistance of the polymer films. These spectra could be fitted with either the equivalent circuit for mixed conductors as shown in figure 4.35 or with a Warburg Short element instead of the Warburg Open element, as shown in figure 4.29. The experimentally obtained spectra are fitted using the chosen equivalent circuit and the required parameters for the circuit elements, which are in the present study the values for the ionic resistance R_{ion} and/or the electronic resistance R_e can be obtained.

The equivalent circuits utilized to describe the PTS and PEDOT:PSS materials in the present study and the physical meaning of the obtained parameters for the circuit elements can be found in section 4.3.1. With the help of the ionic resistances R_{ion} or electronic resistances R_e and with the geometry factor g the electronic and ionic conductivities σ_{ion} and σ_e can be calculated with the following equation:

$$\sigma_{ion} = \frac{1}{R_{ion}} \cdot g = \frac{1}{R_{ion}} \cdot \frac{l}{w \cdot h} \left[\frac{\text{S}}{\text{cm}} \right] \quad (13)$$

$$\sigma_e = \frac{1}{R_e} \cdot g = \frac{1}{R_e} \cdot \frac{l}{w \cdot h} \left[\frac{\text{S}}{\text{cm}} \right] \quad (14)$$

The geometry parameter g consists of the channel length l , the channel width w and the average film height h (as determined with profilometry, see section 3.3.8.1). Measuring the film thickness of theoretically identical prepared films showed an error of $\approx \pm 30\%$, which results in errors of the calculated conductivities of $\approx 30\%$. Due to the combined effects of a lack of reproducibility due to the spin coating procedure, the error of the film thickness determination and device-specific inaccuracies of resistance measurements an error of a factor of 2 – 3 for the conductivity values is estimated.

In the present study, all AC impedance and DC measurements were conducted in a two-electrode configuration (by contacting both sides of the polymer film coated IDE) with an *IM 6 device* from *Zahner* respectively an *Alpha A Analyzer* from *Novocontrol* (the measurements with the Novocontrol device were conducted at the *Max-Planck-Institute of Solid State Research* by *Dr. Rotraut Merkle*, all other measurements were conducted at the *Institute of Polymer Chemistry*). AC impedance measurements were conducted in

a frequency range from $f = 8 \text{ MHz} - 10 \text{ mHz}$ with an excitation voltage amplitude of $U_0 = 50 \text{ mV}$. All spectra were fitted with the *ZView* software from *Scribner Associates*. DC measurements were conducted by applying constant currents I for times between 30 seconds and several hours. Afterwards, the relaxation of the potential was measured without any applied current for the same time as the time of applied current. The currents were applied in a way that the resulting potential does not exceed $U = 100 \text{ mV}$ in order to avoid decomposition of the polymer film. After spin coating, the polymer film coated IDE was installed in the measurement chamber. In order to initialize the film, the measurement chamber was set to 45°C and low water partial pressures for six to twelve hours. After initialization, the chamber was cooled down to 25°C and the impedance measurements were conducted at this temperature in different water partial pressures, in which the impedance was measured two hours after setting a new partial pressure. After increasing the water partial pressure up to the highest partial pressure, the water partial pressures were decreased to a low water partial pressure in order to prove the reversibility of the measurements.

3.3.4 Thermogravimetric analysis

All preliminary TGA studies were conducted at the *Max-Planck-Institute of Solid State Research* by *Dr. Rotraut Merkle* and the used device is a *STA 449* from *Netzsch*. PTS-TBA was examined with TGA in a previous collaboration [160]. The PTS materials were available in powder form after synthesis (PTS-TBA) respectively after cation exchange (PTS-Na). In order to obtain solid PEDOT:PSS, 4 – 5 g of PEDOT:PSS dispersion was poured in a Petri dish. After drying at 40°C on air, the resulting film was removed with a spatula from the Petri dish, upon which the film crumbled into small pieces with lengths of 1 – 2 mm. Typically 30 – 50 mg of the bulk material in powder form (PTS materials) respectively in crumbs (PEDOT:PSS materials) were placed in a crucible, which was then placed in the measurement chamber of the TGA. After initializing the sample at 30°C and dry N_2 flow in order to obtain the dry polymer mass $m_{\text{polymer,dry}}$, in the typical measurement procedure the samples were heated with 0.1 K/min up to the final temperature and afterwards back to 25°C at a constant water partial pressure of $16.7 \text{ mbar H}_2\text{O}$ in order to obtain the polymer mass with incorporated water $m_{\text{polymer,wet}}$. This procedure was utilized for PTS-TBA. Since significant hysteresis effects could be observed in the heating and cooling sweep in case of PTS-Na, the water contents were not determined in the heating and cooling sweep, but instead determined at several constant temperature steps ranging from 25 to 80°C . TGA measurements of PTS-Na were also conducted at a constant water partial pressure of $16.7 \text{ mbar H}_2\text{O}$.

The hydration enthalpy constant K_{hy} describes the reaction constant of the reaction of

the water uptake H_2O (gas) \rightleftharpoons H_2O (absorbed) [160]:

$$K_{hy} = \frac{[\text{H}_2\text{O}]_{abs}}{p\text{H}_2\text{O}/p_0} \quad (15)$$

Here $[\text{H}_2\text{O}]_{abs}$ is the number of H_2O molecules per repeating unit (therefore also per ionic group) and $p_0 = 1$ mbar is the ambient air pressure. The value for $[\text{H}_2\text{O}]_{abs}$ is calculated analogous to λ from the water content per mass in equation 17. Since K_{hy} is constant at every temperature, after calculating one value for $[\text{H}_2\text{O}]_{abs}$ at a certain $p\text{H}_2\text{O}$, $[\text{H}_2\text{O}]_{abs}$ at the same temperature and other $p\text{H}_2\text{O}$ can be calculated. The values for K_{hy} can be obtained by calculating from the respective $[\text{H}_2\text{O}]_{abs}$ and $p\text{H}_2\text{O}$ values at each temperature in the above described temperature ramp. For PEDOT:PSS, after the initialization $m_{\text{polymer,wet}}$ was determined at 25°C and various $p\text{H}_2\text{O}$. The water uptake as water content per mass and water content per thiophene unit λ (which corresponds to the amount of water molecules per repeating unit) can be calculated as follows:

$$\text{water content} = \frac{m_{\text{polymer,wet}} - m_{\text{polymer,dry}}}{m_{\text{polymer,dry}}} = \frac{m_{\text{H}_2\text{O}}}{m_{\text{polymer,dry}}} \cdot 100\% \text{ [wt\%]} \quad (16)$$

$$\lambda = \frac{n_{\text{H}_2\text{O}}}{n_{\text{thiophene}}} = \frac{\frac{\text{water content}}{M(\text{H}_2\text{O})}}{\frac{100\text{g}}{M(\text{repeating unit})}} \quad (17)$$

As an example, for a water content of 20 wt% in case of a PTS-Na film, λ can be calculated as follows:

$$\lambda = \frac{\frac{20\text{ g}}{18\text{ g/mol}}}{\frac{100\text{ g}}{245.35\text{ g/mol} + 22.99\text{ g/mol}}} = 2.98 \quad (18)$$

The value for λ can be calculated by assuming 100 g of polymeric material, which results in a mass of water taken up of 20 g. The molecular mass of H_2O is $M_{\text{H}_2\text{O}} = 18$ g/mol, the molecular mass of the repeating unit of PTS amounts to $M_{\text{PTS}} = 245.35$ g/mol and the molecular mass of the Na^+ cation amounts to $M_{\text{Na}} = 22.99$ g/mol. Whereas calculating of λ is simple in case of PTS where only the molecular masses of the repeating unit and the corresponding cation have to be summed up, calculating of λ in case of PEDOT:PSS is less trivial due to the presence of the two polymers PEDOT and PSS. The values for λ were calculated in respect to the sulfonate groups in PSS, since PEDOT is expected to be in a complex with PSS and therefore not expected to take up water. In order to calculate the quantity of moles n , the molecular masses of both PEDOT and PSS have to be weighted according to the weight ratio between PEDOT and PSS in the composite material PEDOT:PSS which is indicated by the supplier. For calculating the weight ratio between PEDOT and PSS, several assumptions have to be made. These include firstly that all polystyrene units are sulfonated. Secondly it is assumed, that only H^+ is present in the case of PEDOT:PSS (1:2.2) and PEDOT:PSS (1:6) and only Na^+ in

case of PEDOT:PSS-Na (1:6). Eventually, this leads to a small error since also Fe^{+3} of the used catalyst in the chemical synthesis of PEDOT:PSS (as described in section 1.3.2.2) might still be present in the PEDOT:PSS dispersion. Also Na^+ is still present in the PEDOT:PSS (1:2.2) and PEDOT:PSS (1:6) dispersion due to adding of the initiator (as shown with atomic emission spectroscopy measurements, see section 3.1.2). As third assumption, it has to be taken into account that a certain amount of sulfonate groups in PSS do not participate in water uptake, since some sulfonate groups are deprotonated and counterbalance positive charges on PEDOT. According to literature, it was assumed that every third EDOT unit in PEDOT is oxidized [8]. After taking all assumptions into account, the weight content of PSS which is not counterbalanced by positive charges on PEDOT and which is expected to participate in water uptake amounts to 55 wt% in PEDOT:PSS (1:2.2), to 80 wt% in PEDOT:PSS (1:6) and to 81 wt% in PEDOT:PSS-Na (1:6).

3.3.5 Quartz Crystal Microbalance

In Quartz Crystal Microbalance measurements, a quartz crystal is brought into oscillation, utilizing the piezoelectric properties of the quartz crystal. By applying oscillating potentials at both sides of the quartz crystal, shear oscillation perpendicular to the electrical contacts occurs. Quartz crystals for microbalance measurements are "AT-cut". This term refers to the specific angle of $35^\circ 15'$ to the Z-axis of the quartz crystal, in which the disc-shaped quartz crystal is cut out from the bulk quartz crystal. At this specific angle, the resonance frequency in the temperature range from $25 \pm 10^\circ\text{C}$ changes only by few ppm [174]. The measurement principle of all quartz crystal microbalance measurements can be described with the Sauerbrey equation [175]:

$$\Delta f = -\frac{2f_0^2}{A\sqrt{\rho_q\mu_q}} \cdot \Delta m = -C_f \cdot \Delta m \text{ [Hz]} \quad (19)$$

It postulates that a frequency change Δf of the quartz crystal can be correlated to a mass change Δm of the quartz crystal. Since the mass of the oscillating crystal itself does not change, the mass of the crystal changes for example due to deposition of material on top of the quartz crystal, assuming the deposited material to have the same rigidity as the quartz crystal. The further parameters in equation 19 are the resonant frequency of the quartz crystal f_0 , the active area of the quartz crystal A and the density ρ_q and the shear modulus μ_q of the quartz crystal. Since these parameters are constant for each crystal, they are usually summarized in the sensitivity coefficient C_f of the quartz crystal, which means that Δf and Δm are proportional to each other. For a discussion about the validity of the Sauerbrey equation in the application of the quartz crystal microbalance technique for the present study see 4.2.2.1.

In order to determine the water content of the polymer in the present study, first an empty crystal was inserted into the sensor head, the resonance frequency f_0 was measured and the indicated mass of the empty crystal was set to zero $m_0 = 0$ g. The utilized *STM-2* device from *Inficon* displays the thickness h of an imaginary deposited layer on the exposed area of the crystal in [Å], assuming a uniform layer with a density of $\rho = 1\text{g/cm}^3$. The h -value indicated after inserting a new empty crystal in the sensor depends on the set h value of the previously measured crystal. Due to this and due to the fact that every crystal displays a unique resonance frequency, the resonance frequency had to be measured and the indicated mass had to be set to $m_0 = 0$ g for every QCM measurement. The thickness value h can be converted to a mass via $m = (\pi \cdot A^2) \cdot h$. Here m is the mass of the polymer film and A is the exposed area of the crystal where deposition can occur. After removing the crystal from the sensor, the polymer film to be analyzed was spin coated or drop casted onto the exposed upper side of the crystal (the quartz crystal is plated with a gold layer on the top and a gold anchor structure on the bottom side for electrical contacting). After removing polymer residues at the edge of the crystal which might disturb the contacting of the crystal, the crystal was reinserted to the sensor. In order to equilibrate the film, the measurement chamber was set to 45°C for six to twelve hours in a dry N₂ flow. After switching back to 25°C, the dry polymer film mass $m_{\text{polymer,dry}}$ could be determined. In the following, the weight of the polymer film $m_{\text{polymer,wet}}$ at 25°C and various water partial pressures was measured. The reversibility of the water uptake was checked by switching back to dry N₂. The water contents per mass and per thiophene unit λ were calculated as for the TGA measurements according to equations 16 and 17. In case the water contents should be calculated via the frequencies, the following equation can be utilized:

$$\text{water content} = \frac{f_{\text{polymer,dry}} - f_{\text{polymer,wet}}}{f_0 - f_{\text{polymer,dry}}} \quad (20)$$

Equation 20 is equal to equation 16 with the only difference that the frequencies correspond to absolute values. Occasionally the *STM-2* software used for controlling the QCM experiment crashed, which deleted the set thickness h of the crystal that was assigned to the crystal mass of $m_0 = 0$ g. Therefore, the water content could still be calculated from the frequencies. As previously done in literature [4, 176], the water adsorption on the blank surface was taken into consideration by subtracting the water adsorption of the blank quartz crystal from the water uptake of the polymer film at each water partial pressure.

3.3.6 UV/Vis in reflection mode

The UV/Vis absorption of polymer films on gold can be measured in reflection mode with a *Zeiss* device, which is equipped with a *CLH 600 F* lamp and a *MCS621 VIS II* detector.

The temperature of the polymer films can be varied with a peltier element, on which the polymer film coated gold substrates are placed on.

3.3.7 Cyclic voltammetry (with in-situ techniques)

3.3.7.1 Cyclic voltammetry

Cyclic voltammetry is a powerful analysis method to study both kinetic and thermodynamic properties of electron transfer processes in redox-active substances in solution, or in case of polymer films, of redox-active substances in solid form [46, 177]. All measurements were conducted in a three-electrode configuration with working electrode (WE), counter electrode (CE) and reference electrode (RE). The electrodes are positioned in an electrochemical cell, which contains a solvent and an organic salt in order to ensure charge transport in the electrolyte. All electrodes are connected to a potentiostat, which controls the cyclic voltammetric measurement. The potential sweep during a cyclic voltammetric measurement can be seen in figure 3.6 a).

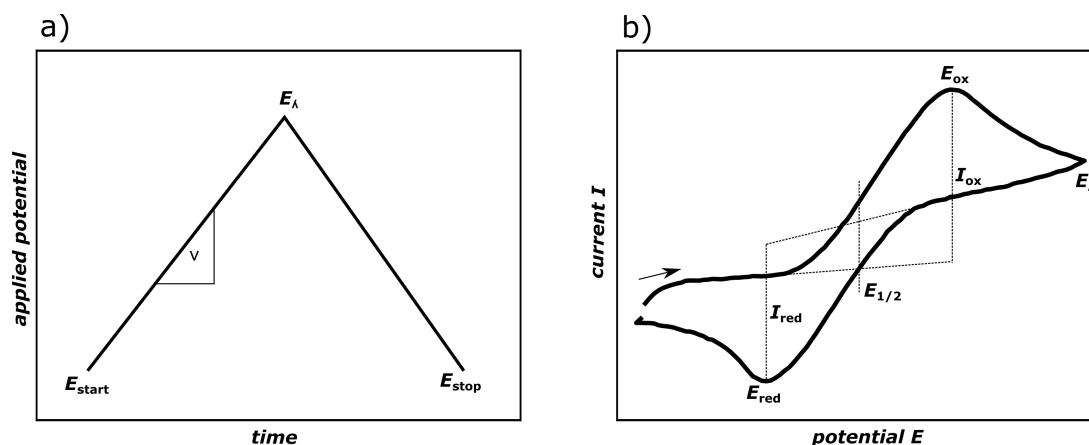


Figure 3.6: a) Potential sweep of cyclic voltammetric measurements and b) typical cyclic voltammogram of one-electron process.

After starting at a certain start potential E_{start} , the potential is increased/decreased linearly with a certain potential change rate per time, the scan rate v . After reaching the turning potential E_{λ} , the potential is decreased/increased linearly down to the potential E_{stop} , which corresponds in most cases to the initial potential. The potentiostat adjusts the potential between WE and RE in a way that the potential between WE and RE matches the desired cyclic potential sweep. When current flows between WE and CE, the potential niveau of the WE changes during the potential sweep, which requires the potentiostat to readjust the potential between WE and RE. Due to a high resistance, which is internally toggled between WE and RE, no current can flow between WE and RE. This prevents changing of the potential niveau of the RE, which allows to separably control the potential between WE and RE and monitor the resulting current flow between

WE and CE. The cyclic voltammogram of a typical one-electron transfer redox reaction can be seen in figure 3.6 b). From the oxidation potential E_{ox} in the oxidation sweep and the reduction potential E_{red} in the reduction sweep the half step potential $E_{1/2}$, which roughly equals the formal potential E_0 can be calculated via equation 21:

$$E_{1/2} = \frac{E_{ox} + E_{red}}{2} \approx E_0 \text{ [V]} \quad (21)$$

Whereas the formal potential E_0 allows to obtain thermodynamic information of the redox couple examined, kinetic information can be obtained from the peak currents I_{ox} and I_{red} [177, 178]. The half-step potential can only be determined for monodisperse systems like in the shown cyclic voltammogram of a one-electron redox species. For polydisperse systems like conducting polymers where many redox states overlap, no half-wave potential can be determined due to the overlapping of the current waves of the redox states. Therefore, only the so-called onset potential E_{onset} can be discussed, which is the potential where the oxidation or the reduction process initially starts. It is determined by the intersection of two tangents, one on the basic current and one on the initial slope of the oxidation or reduction peak.

In the present study, cyclic voltammetric measurements were conducted while measuring the in-situ UV/Vis absorption (referred to as spectroelectrochemistry, see section 3.3.7.2) or while measuring the in-situ conductance and the UV/Vis absorption (referred to as in-situ conductance measurements, see section 3.3.7.3). For all measurements, an *Autolab PGSTAT101* potentiostat from *Metrohm*, the measurement software *Nova* (version 1.10) and a 0.1 M solution of NBu_4PF_6 in MeCN were used. A platinum plate was used as CE and polymer films deposited on ITO electrodes (for in-situ UV/Vis absorption measurements) or IDEs (for in-situ conductance and UV/Vis absorption measurements) were used as WE. Typical scan rates are between $v = 10 - 50$ mV/s. Since standard Ag/AgCl REs are only defined for aqueous electrolytes, an Ag wire coated with AgCl was used as "pseudo" RE in the organic electrolytes in all cyclic voltammetric measurements. All experimentally obtained potentials were calibrated after each measurement against ferrocene/ferrocenium (Fc/Fc^+), all discussions are lead according to the potential values calibrated against Fc/Fc^+ [179]. In order to avoid disturbance of the measurements by oxygen or water, pre-dried chemicals were used and the measurements were conducted in an inert atmosphere, which was ensured by degassing the electrolyte with argon before every measurement.

3.3.7.2 In-situ Spectroelectrochemistry

Cyclic voltammetry with in-situ measurement of the UV/Vis absorption (referred to as spectroelectrochemistry) allows a more in-depth analysis of electron transfer processes

and the identification of redox species and intermediates [180]. The setup used for spectroelectrochemistry measurements can be seen in figure 3.7.

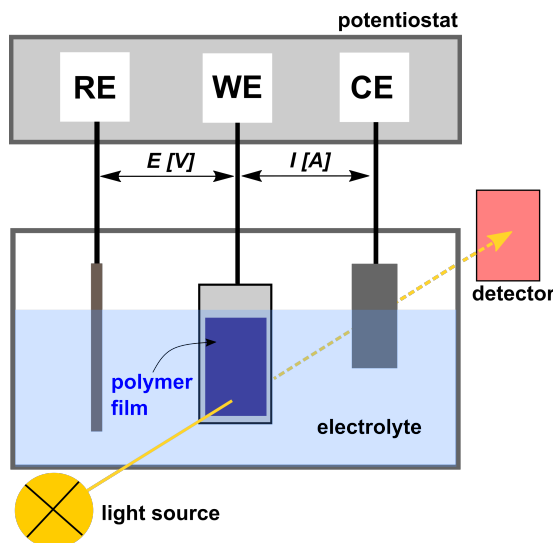


Figure 3.7: Schematic setup of spectroelectrochemistry measurements.

As difference to conventional cyclic voltammetric measurements, an ITO electrode is used as WE. While conducting the cyclic voltammetric measurement, utilizing the polymer film coated ITO electrode as WE, the UV/Vis absorption was measured through the transparent ITO electrode. Therefore, a *CLH 600 F* halogen lamp was connected to one side of the electrochemical cell in a way that the light passes through the ITO electrode in a 90° angle. A *MCS621 Vis III* detector was connected to the opposite side of the cell in order to detect the light passing through the electrode. The light paths from lamp and detector are directed through optic fibers from *Ocean Optics* to the cell. Both lamp and detector are located in a spectrometer housing from *Zeiss*.

3.3.7.3 Cyclic voltammetry with in-situ conductance (and UV/Vis NIR absorption) measurements

In the in-situ conductance measurements in this thesis, the conductance S of the polymer film deposited on the WE is measured while conducting the cyclic voltammetric measurement, as introduced in 1989 by Zotti et al. [181]. In general, information like the type of charge carrier, the conductivity model or other charge and mass transport phenomena can be obtained [16, 182]. The setup of the in-situ conductance measurements can be seen in figure 3.8.

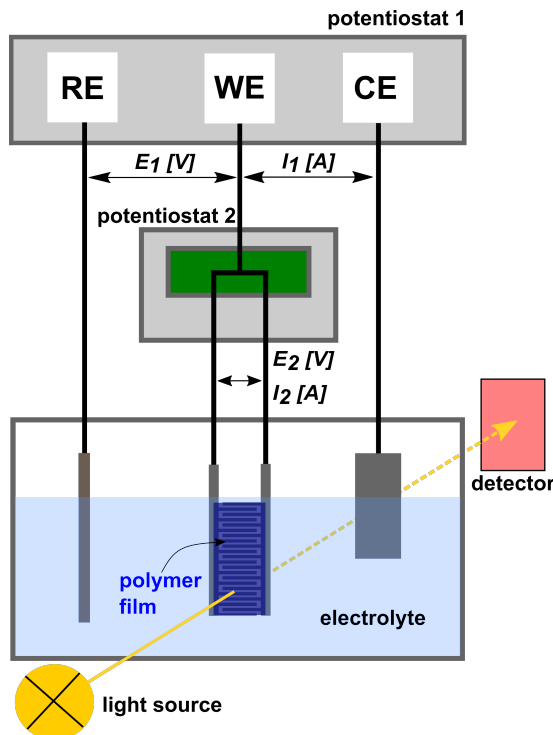


Figure 3.8: Schematic setup of the in-situ conductance (and in-situ UV/Vis absorption) measurements.

The setup used for measuring in-situ conductance comprises two potentiostats. Potentiostat 1 conducts the cyclic voltammetric measurement as in the previously described conventional cyclic voltammetry and spectroelectrochemistry measurements by recording the current I_1 as function of the applied potential E_1 , in which an polymer film coated IDE is used as WE. Potentiostat 2 applies a potential E_2 between both sides of the IDE and by measuring the resulting current I_2 , the conductance G can be determined according to the following equation:

$$G = \frac{I_2}{E_2} \text{ [S]} \quad (22)$$

Both potentiostats are connected to a *Conductance Interface CIP 2* from *HEKA Elektronik Dr. Schulze GmbH*. By toggling two resistors in the interface, potentiostat 1 can use both sides of the IDE as WE, whereas potentiostat 2 (a *μStat 400* potentiostat from *Dropsense*) can use one side of the IDE as WE and the other side as CE/RE. By measuring the UV/Vis absorption through the IDE as described in section 3.3.7.2, a second in-situ technique could be measured additionally.

3.3.8 Further techniques

3.3.8.1 Profilometry

The average thickness h of polymer films was determined with a *Dektak 150* surface profiler from *Veeco* by averaging over at least three single measurements for each film. The surface profiler is located in the *Mikrostrukturlabor* in the *4th Institute of Physics*.

3.3.8.2 UV/Vis Lambda

The UV/Vis absorption of polymer films on glass substrates in transmission under ambient conditions was measured with a *Lambda 35* device from *Perkin Elmer*.

3.3.8.3 Atomic Force Microscopy

Atomic force microscopy (AFM) measurements of thin polymer films on glass substrates were conducted on a *Dimension Icon* AFM (from *Bruker*) in tapping mode.

4 Results

In this thesis, the properties of the two polymeric mixed conductor systems poly(6-(thiophene-3-yl)hexane-1-sulfonate) (PTS) and poly(3,4-ethylenedioxythiophene):poly(styrene sulfonate) (PEDOT:PSS) have been examined. The structures of the analyzed materials are shown in figure 4.1.

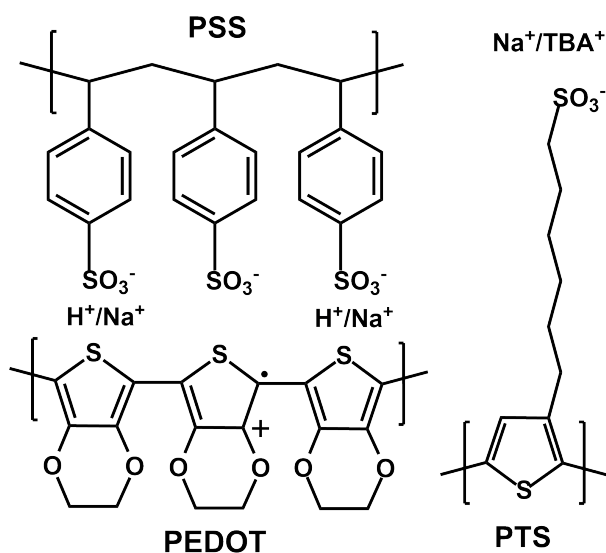


Figure 4.1: Structure of PEDOT:PSS (left) and PTS (right).

The results part is structured as follows: In section 4.1, first the UV/Vis absorption characteristics of both polymeric mixed conductors PTS and PEDOT:PSS materials thin films are examined in different charged states. In case of PTS, the influence of the counterion, the solvent system from which PTS is spin coated and the influence of humidity on the UV/Vis absorption of neutral films is examined. Parts of these studies have been contributed by Michael Herbst in his research project at the *IPOC*. Furthermore, the UV/Vis absorption of PTS after chemical or electrochemical doping is examined. PEDOT:PSS is examined with spectroelectrochemistry and in-situ conductance measurements, in which in particular the influence of the PEDOT to PSS ratio is examined. Parts of these studies have been contributed by Qiulin Yu in her master thesis at the *IPOC*.

In the main parts of this thesis, the water uptake and conductivity properties of thin films of both polymeric mixed conductors are studied. The water uptake measurements

are given in section 4.2. Starting with the water uptakes as determined with preliminary TGA measurements in section 4.2.1, the measurement technique QCM and its general measurement procedure and further aspects such as its validity are discussed in section 4.2.2.1 and 4.2.2.1. The results for the water uptake measurements of the PTS and PEDOT:PSS materials determined with QCM are given in section 4.2.2.

In section 4.3, the conductivity results for the PTS and PEDOT:PSS materials showing ionic conductivity behavior, mixed conductivity behavior and electronic conductivity behavior are discussed. Furthermore, the influence of the utilized interdigitated electrode and conductivity results for PEDOT:PSS - poly(vinyl alcohol) (PVA) composite materials are discussed in sections 4.3.4 and 4.3.3. The conductivity and water uptake behavior of the PTS and PEDOT:PSS materials are published:

Humidity-Controlled Water Uptake and Conductivities in Ion and Electron Mixed Conducting Polythiophene Films, M. Wieland, R. Merkle, C. Dingler, J. Maier, S. Ludwigs, *ACS Applied Materials & Interfaces* **2020**, 12, 5, 6742-6751

The spectroelectrochemistry and in-situ conductance measurements of PEDOT:PSS (1:2.5) and PEDOT:PSS (1:6) are published:

Conductance and spectroscopic mapping of EDOT polymer films upon electrochemical doping, M. Wieland*, C. Malacrida*, Q. Yu, C. Schlewitz, L. Scapinello, A. Penoni, S. Ludwigs, *Flexible and Printed Electronics* **2020**, 5, 014016 *both authors contributed equally

4.1 Absorption characteristics in neutral and doped states

This chapter of the studies on the UV/Vis absorption characteristics is started with the UV/Vis absorption behavior and AFM results of neutral PTS under ambient conditions and under variable atmospheric conditions in section 4.1.1.1. The UV/Vis absorption was studied with PTS films on glass substrates in transmission mode as well as with PTS films on gold substrates in reflection mode. This is followed by the UV/Vis absorption behavior of chemically and electrochemically doped (via spectroelectrochemistry) PTS in section 4.1.1.2. In section 4.1.2, the spectroelectrochemistry and in-situ conductance (cyclic voltammetry coupled with in-situ conductance measurements) results of two PEDOT:PSS batches are given, in which the influence of different PEDOT to PSS ratios are discussed. In section 4.1.3 the results of this chapter are summarized. As described in the experimental section 3.3.2, the results are discussed as function of water partial pressure (in mbar) and the measurements were conducted in water partial pressure ranges between 0 and 29 mbar $p_{\text{H}_2\text{O}}$, which corresponds to relative humidity ranges of 0 and 92 % r.h.

4.1.1 PTS materials

4.1.1.1 Neutral state

In the following section, the UV/Vis absorption properties of PTS thin films are discussed. As described in the experimental part in section 3.2.2, PTS materials with either TBA⁺ or Na⁺ as counterion were examined and the films were spin coated from either a mixture of H₂O and THF or from pure H₂O. Therefore two different PTS systems from two solvent systems are distinguished, so PTS-TBA from H₂O/THF, PTS-Na from H₂O/THF, PTS-TBA from H₂O or PTS-Na from H₂O.

Ambient conditions

In order to examine the influence of the counterion and the solvent from which the PTS films are spin coated from, the two PTS systems from two solvent systems are spin coated on glass substrates and the UV/Vis absorption spectra of the pristine films are recorded. For each PTS system, at least 5 films are spin coated. One exemplary spectrum for each system can be found in figure 4.2. All spectra were normalized since a quantitative comparison of the absorption intensity is not reliable due to the fact that for the same film mass, PTS-Na contains a higher amount of optically active polythiophene backbone (for the corresponding discussion see 4.2.1.1).

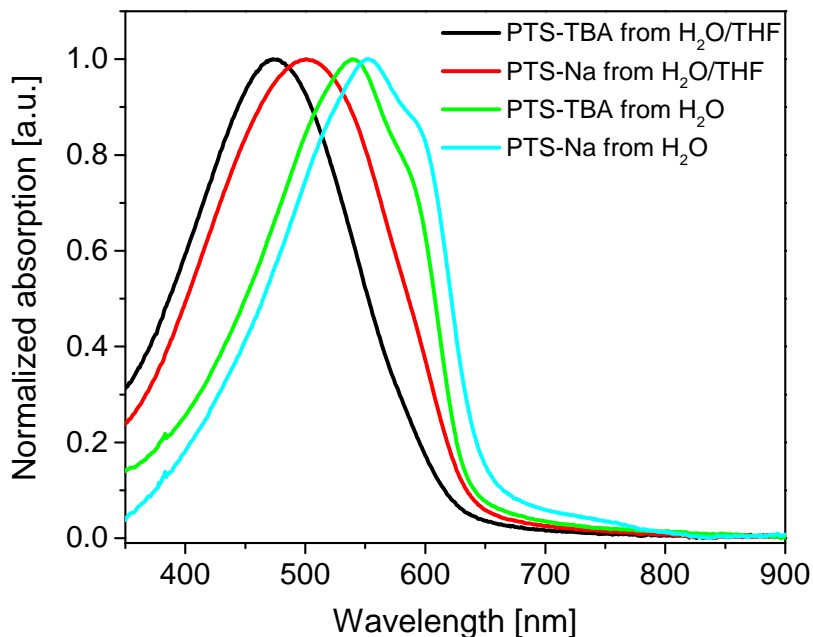


Figure 4.2: UV/Vis absorption spectra of PTS-TBA and PTS-Na spin coated from 5 mg/ml H_2O or $\text{H}_2\text{O}/\text{THF}$ on glass substrates.

Several qualitative differences can be observed in the four spectra: whereas the films spin coated from the $\text{H}_2\text{O}/\text{THF}$ mixture show a featureless absorption band with absorption maxima at $\approx 480 - 500$ nm, the films spin coated from H_2O show a vibronic fine structure with absorption maxima at $\approx 540 - 550$ nm and a shoulder at higher wavelengths. The absorption maxima of the films spin coated from the solvent mixture is at lower wavelengths compared to the absorption maxima of the films spin coated from pure H_2O . The featureless absorption in case of the PTS films spin coated from $\text{H}_2\text{O}/\text{THF}$ resembles the typical spectra of dissolved, coiled P3HT whereas the spectra of the PTS films spin coated from H_2O resemble the spectra of aggregated P3HT [47, 183]. Accordingly, it can be assumed that PTS spin coated from $\text{H}_2\text{O}/\text{THF}$ is in its unaggregated, coiled form whereas PTS spin coated from H_2O results in rather aggregated films.

Comparing the PTS films with TBA^+ as cation and the films with Na^+ as cation, it can be seen that for both solvent systems the films with TBA^+ as counterion exhibit an absorption maximum at shorter wavelengths. This might be explained by the fact that the smaller, less bulky Na^+ cation promotes the aggregation of the polythiophene backbone while the larger, more bulky TBA^+ cation prevents the backbone aggregation. The wavelength at the absorption maximum, a description of the shape of the spectra and the colors of the films can be found in table 4.1.

Table 4.1: Summary of UV/Vis absorption spectra from figure 4.2.

	Wavelength of abs. max. [nm]	Comment	Film colour
PTS-TBA from H ₂ O/THF	473	Featureless	Orange
PTS-Na from H ₂ O/THF	501	Featureless	Orange red
PTS-TBA from H ₂ O	539	Shoulder	Pink
PTS-Na from H ₂ O	553	Shoulder	Violet

Due to the inaccuracies in the measurement technique and typically observed deviations between identically prepared films, deviations of the UV/Vis absorption maximum wavelength of below 5 nm can not be discussed. The wavelengths of the absorption maxima are however separated to a significantly larger extent: the values for the films spin coated from the solvent mixture are at least 40 nm below the values for the films spin coated from pure H₂O. Also the absorption maxima in dependency of the cation show a notable separation of 23 nm for the films spin coated from the solvent mixture and 13 nm for the films spin coated from H₂O, respectively. The differences in the experimentally determined UV/Vis absorption spectra can also be visibly observed: whereas the PTS films from H₂O/THF exhibited a pale orange color, the PTS films from H₂O exhibited a stronger pink or violet color.

As already mentioned, the PTS films spin coated from H₂O exhibit a shoulder at high wavelengths. In case of P3HT which has the same polythiophene backbone as PTS, this feature is assigned to a planarization of the polymer backbone induced by aggregation of the polymer chains [45, 48, 184]. Therefore, in the present studies a strong aggregation in case of the PTS films spin coated from H₂O can be assumed. On the other hand, in the PTS films spin coated from H₂O/THF lower aggregation can be assumed. Since the absorption intensity of the shoulder in relation to the absorption intensity at the absorption maximum is higher for PTS-Na (turquoise) compared to PTS-TBA (green), it can be assumed that the polythiophene backbone in PTS-Na reveals more aggregation than PTS-TBA. This assumption is also supported by the fact that the aqueous solution is violet non-transparent, which gives indication for larger aggregate particles, whereas solving PTS in the H₂O/THF mixture results in an orange, transparent solution.

Regarding the UV/Vis absorption spectra of the PTS-TBA and PTS-Na films from H₂O (green and turquoise line), it can be seen that the absorption intensity of the low-energy shoulder is higher for PTS-Na than for PTS-TBA in relation to the maximum absorption intensity. According to eq. 1 in introduction section 1.2.1.2, this leads qualitatively to a decrease of W and therefore to an increase of the conjugation length. The crystallographic ion radii of Na⁺ and TBA⁺ amount to 102 and 413 pm, respectively [185]. Comparing the TBA⁺ and the Na⁺ cation in terms of the Lewis acidity, Na⁺ represents a hard cation and

therefore a strong Lewis acid. On the other hand TBA^+ is a soft, non-coordinating cation since the positive charge is shielded by the surrounding butyl groups, therefore TBA^+ is a weak Lewis acid [186, 187]. Without consideration of significant water uptake (which is reasonable under ambient conditions and which would lead to larger ion sizes), the higher conjugation length in PTS-Na can presumably be understood easily: the smaller ion size of Na^+ leads to less disturbance of the thiophene backbone aggregation compared to the larger ion TBA^+ . The solvent system and counterion dependency on the absorption behavior in conjugated polyelectrolytes was observed before: for a series of anionic conjugated polyelectrolytes with tetramethylammonium (TMA^+), tetraethylammonium (TEA^+) and tetrabutylammonium (TBA^+) counterions, strongest aggregation in solution and in thin films was observed in case of the smallest counterion TMA^+ [1]. For the parent system PTS-TBA which was also used in the present study, strong aggregation in solution was observed in H_2O , less aggregation in MeOH and no aggregation was detected in formamide and DMSO [22]. By gradually changing the solvent mixture composed from H_2O and DMSO, the extent of aggregation could be varied gradually.

Interestingly, it was observed that the conjugated polyelectrolytes PTS-TBA and PTS-Na in the present study showed differences in their solubility in MeOH: whereas PTS-TBA dissolved in MeOH, PTS-Na did not dissolve in MeOH. This might be explained by the fact that Na^+ is a hard cation whereas TBA^+ corresponds to a soft cation. The cationic, imidazolium bearing CPE PTIm-Br revealed solvent dependent UV/Vis absorption as well [92]. Bazan et al. examined conjugated polyelectrolytes consisting of alternating dithiophene and ionic groups containing benzothiadiazole repeating units and observed counterion dependent UV/Vis absorption, self-doping effects and diode device behavior [90, 91, 95]. The cation dependency was also observed in solution for several polythiophene based conjugated polyelectrolytes [2, 88].

At least three films of each of the PTS - solvent system combinations was spin coated. It could be obtained that the wavelength of the absorption maximum in case of the PTS films spin coated from H_2O were always within an error of 1 – 2 nm at the same wavelength, whereas the PTS films spin coated from $\text{H}_2\text{O}/\text{THF}$ showed strong deviations between identically prepared films. A possible reason for this might be that THF evaporates quickly at room temperature, therefore some THF might be already evaporated after applying the spin coating solution on the substrate before starting the spin coating procedure. This might lead to a slightly increased aggregated structure in case of the PTS films spin coated from $\text{H}_2\text{O}/\text{THF}$.

Atomic Force Microscopy und ambient conditions

In order to examine the surface morphology of the PTS films in dependence of the solvent system and the counterion, the two PTS systems from two solvent systems were spin coated on glass substrates and examined with AFM. The AFM images are shown in figures A.1 - A.4. In the AFM images, for the PTS films spin coated from the solvent mixture H₂O/THF, a homogeneous and aggregation-free structure can be observed, which is in accordance with literature [22]. For the PTS films spin coated from H₂O, different structures were expected due to the presence of aggregated PTS as detected with UV/Vis absorption spectroscopy. However, no aggregation structures were found in the AFM images of the PTS materials spin coated from H₂O/THF and eventually evidence for slight aggregation is found in case of PTS-Na spin coated from H₂O. The AFM image of PTS-Na spin coated from H₂O in figure A.4 is similar to the AFM image of an as cast P3HT film as shown in figure 1.6, therefore a partially aggregated structure of PTS-Na from H₂O could be assumed. The lateral resolution in AFM measurements can be as low as 20 pm [188]. Even though the resolution limit would be low enough to detect aggregates, no aggregation or eventually only a slight aggregation can be obtained from the AFM image in figure A.3. Whereas no adding of additives results in amorphous structures, adding ethylene glycol to PTS solutions is known to result in fiber-like features in film, in which the resulting fibrillar morphology is observed to promote faster ion transport in OECT devices [24].

Stability tests of PTS films: Influence of Time

Whereas the UV/Vis absorption for PTS-Na and for PTS-TBA from H₂O/THF was observed to remain constant over weeks, for PTS-TBA from H₂O, the absorption profile was observed to change. The UV/Vis absorption of a PTS-TBA from H₂O film at different times after spin coating is shown in figure 4.3.

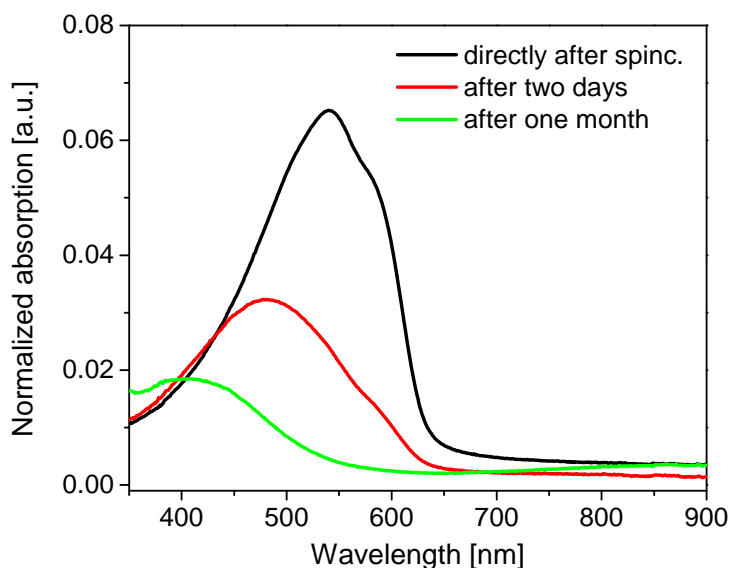


Figure 4.3: UV/Vis absorption spectra of PTS-TBA spin coated from 5 mg/ml H_2O on glass substrates at different times after spin coating.

Directly after spin coating of PTS-TBA from H_2O , the typical absorption profile with a pronounced aggregation shoulder could be detected. Even after two days where the film was stored in inert atmosphere, the absorption intensity decreased and the absorption maximum underwent a blue shift (hypsochromic shift), so a shift of the absorption maximum to lower wavelengths. After two months, the intensity decreased even further and the absorption maximum shifted even more to lower wavelengths. Since this observation was not or only to a very small extent observed for PTS-Na from H_2O films, the effect is explained by the presence of the TBA^+ cations. While the presence of TBA^+ as counterion results in a PTS film with lower conjugation length already in the as spin coated film, the aggregated backbone structure might be increasingly disturbed over time due to the bulkiness of the TBA^+ cation. The disturbance of the aggregation by the TBA^+ cation might be increased by a low amount of water remaining in the polymer film. The films were stored in a desiccator at roughly 30 mbar air pressure, therefore low amount of water can be assumed in the polymer film. If the films would have been stored at completely air free atmosphere, the stability might have been better.

Stability tests of PTS films: Influence of temperature

In addition to examination of the PTS films under ambient conditions, studies in controlled atmospheric conditions were conducted. The in-situ UV/Vis measurements on gold substrates in reflection were recorded at various times during a temperature ramp at constant $p\text{H}_2\text{O}$, since presence of atmospheric H_2O is known to enable PTS-TBA to recover to its original aggregated structure whereas dry N_2 atmospheres have been shown

to impede the recovering of the aggregated structures [160]. After initialization (see experimental section 3.3.2), a temperature ramp depicted in figure 4.4 was run while applying a constant $p\text{H}_2\text{O}$ in the measurement chamber.

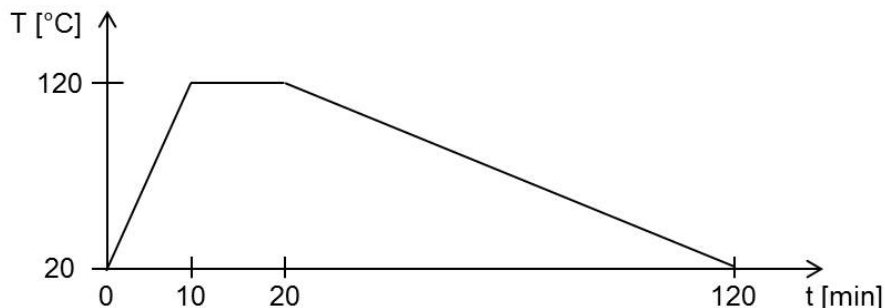


Figure 4.4: Temperature ramp applied in in-situ UV/Vis measurements.

In figure 4.5, the UV/Vis absorption spectra of the two PTS systems from two solvent systems PTS systems which were deposited on gold substrates are shown. The temperature ramp from 20°C to 120°C was conducted while applying 20 mbar H_2O and while recording the UV/Vis absorption spectra. The obtained UV/Vis absorption spectra at the beginning of the measurement (black curve), at 120°C (red curve) and after decreasing the temperature back to 20°C (blue) curve are shown in figure 4.5. For the measurement of the PTS-Na from H_2O film a time of 120 min was applied in the cooling sweep instead of a time of 100 min, the deviation does presumably not change the results.

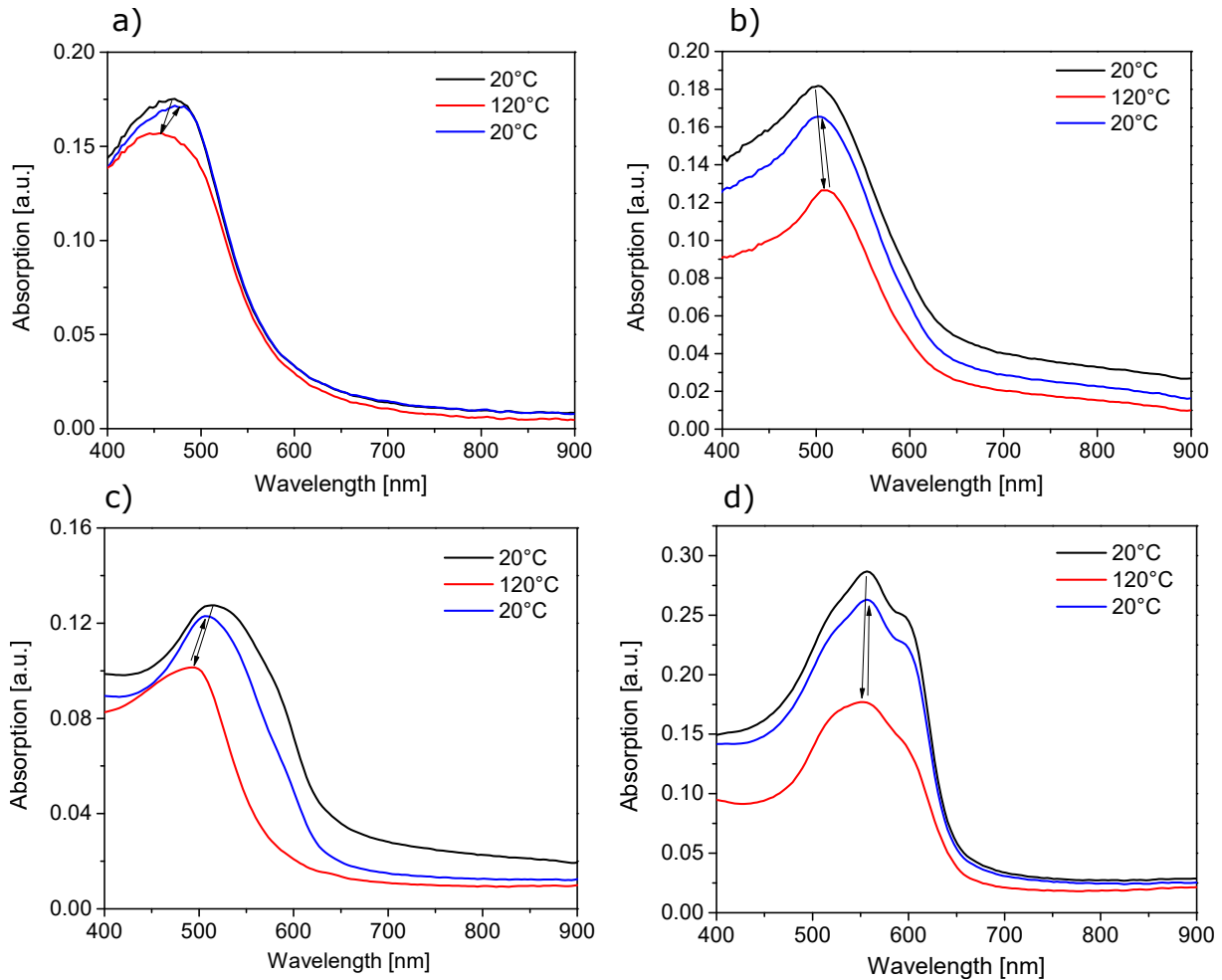


Figure 4.5: In-situ UV/Vis absorption spectra of PTS films on gold substrates at a water partial pressure of 20 mbar H_2O recorded at various temperatures during the temperature ramp. a) PTS-TBA spin coated from 5 mg/ml $\text{H}_2\text{O}/\text{THF}$, b) PTS-Na spin coated from 5 mg/ml $\text{H}_2\text{O}/\text{THF}$, c) PTS-TBA spin coated from 5 mg/ml H_2O and d) PTS-Na spin coated from 5 mg/ml H_2O .

Comparing the spectra, which are recorded in reflection with PTS films on gold substrates with the spectra in transmission on glass substrates (figure 4.5), it can be seen that the spectra give similar features, but the absorption in the low wavelength range at 400 nm in relation to the absorption intensity at the absorption maximum is significantly higher in case of the PTS films on gold substrates. This might be explained by a different morphology due to the different substrate, however since the trends of the two PTS systems from two solvent systems that were observed on glass substrates can be detected also on the gold substrates, it is assumed that only the absorption at low wavelengths at 400 nm is affected by the substrate. For the PTS films spin coated from H_2O in c) and d), the vibronic fine structure can be observed at the initial room temperature step. In case of the PTS-TBA film from H_2O the vibronic fine structure might already be slightly decomposed as discussed in figure 4.3. Upon increase of the temperature up to 120°C, a decrease of the absorption intensity can be detected for all PTS films, which

could be explained by a decrease of the inter- and intramolecular interactions as it is occurring in the dissolution process of polythiophenes [183, 189]. Both PTS-TBA films show a different behavior upon temperature increase than the PTS-Na films: whereas in the UV/Vis absorption spectra of the PTS-TBA films a notable blue shift (hypsochromic shift) occurs, no shift of the absorption maximum in the PTS-Na from H₂O film and even a slight red shift (bathochromic shift, shift to higher wavelengths) in the PTS-Na from H₂O/THF film can be observed. This might be explained by the presence of the TBA⁺ cation: the bulky structure of TBA⁺ might lead to a disturbance of the backbone structure at high temperature due to increased movement of the butyl-side chains. On the other hand, in case of the small Na⁺ cation even at high temperature no disturbance of the backbone structure occurs. After cooling down to 20°C, the spectra of all PTS films resemble the initial spectra, therefore it could be stated that the vanishing of the structure at high temperatures is reversible. In figure 4.6, the wavelength of the absorption maximum and the absorption intensity of the maximum of the UV/Vis spectra recorded during the temperature ramp is plotted as function of time.

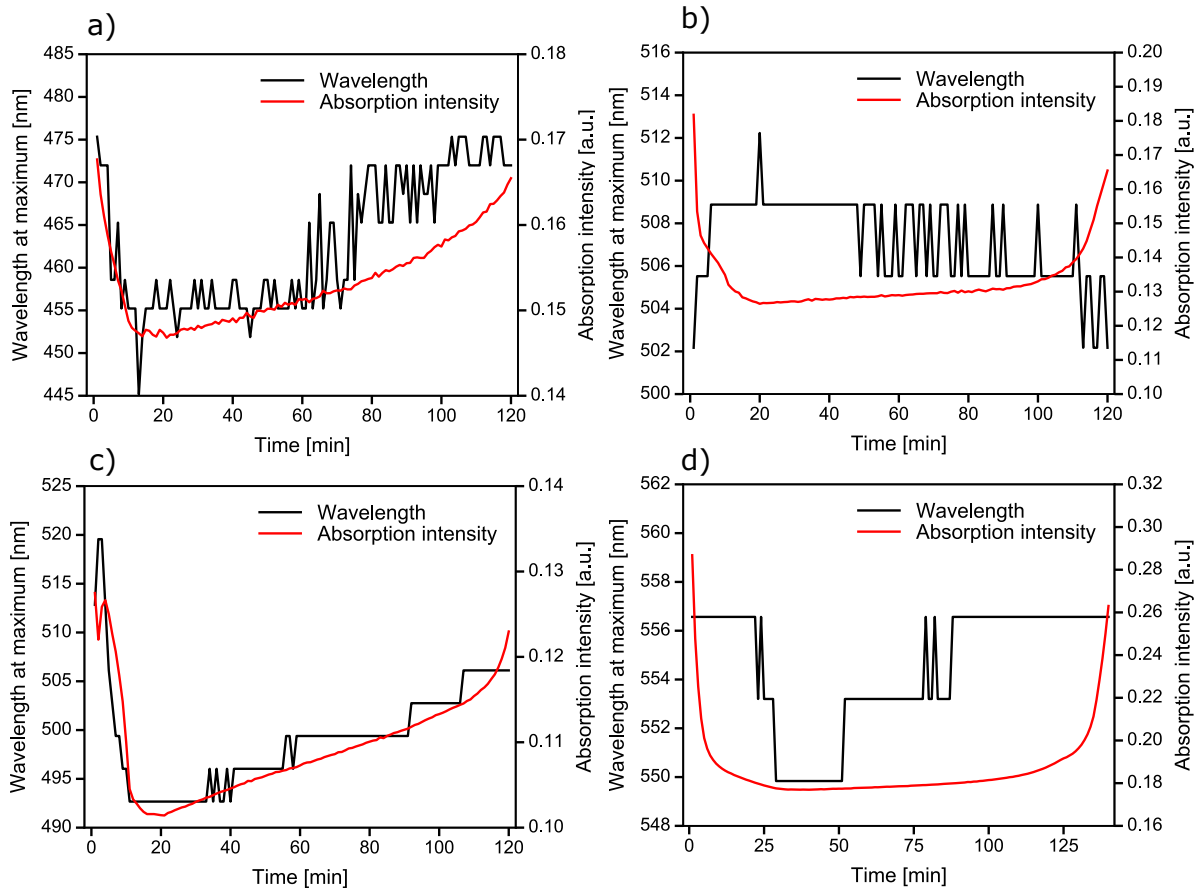


Figure 4.6: Wavelength of the UV/Vis absorption maximum (black curve) and maximum absorption intensity at this wavelength (red curve) at a water partial pressure of 20 mbar at various temperatures during the temperature ramp, extracted from the UV/Vis absorption spectra in 4.5. a) PTS-TBA spin coated from 5 mg/ml $\text{H}_2\text{O}/\text{THF}$, b) PTS-Na spin coated from 5 mg/ml $\text{H}_2\text{O}/\text{THF}$, c) PTS-TBA spin coated from 5 mg/ml H_2O and d) PTS-Na spin coated from 5 mg/ml H_2O .

The scattering of the wavelength at the absorption maximum (black curve) is due to the limited wavelength resolution of the measurement device. As described previously, the wavelength shifts and the absorption intensity changes (red curve) are reversible for the two PTS systems from both solvent systems. The absolute wavelength shift is significantly larger for the PTS-TBA materials (figure 4.6 a) and c)) than for the PTS-Na materials (PTS-Na from $\text{H}_2\text{O}/\text{THF}$ shows the opposite trend than both PTS-TBA films and PTS-Na from H_2O). Interestingly, in case of the PTS-TBA films both the wavelength change and the absorption intensity profile directly correlate with the temperature ramp profile (strong change up to minute 20 and then slow recovery to the original state up to minute 120). On the other hand in case of the PTS-Na films, the wavelength does not show strong dependency from the temperature, the absorption intensity on the other hand reaches a minimum at the highest temperature, remains constant up to minute 100 for the PTS-Na from $\text{H}_2\text{O}/\text{THF}$ film and minute 120 for the PTS-Na from H_2O film,

therefore the absorption intensity changes back to its original state at much lower temperatures than the PTS-TBA films. The difference between the PTS-TBA and PTS-Na films might be explained by the fact that the disturbance of the TBA⁺ cation increases with temperature, whereas in case of the PTS-Na films the disturbance of the backbone structure might not be explained by an increasing disturbance of the interactions between backbone moieties at high temperatures.

Very similar trends for the UV/Vis absorption and the variations upon conducting the temperature ramps were also observed for additional studies on the two PTS systems from two solvent systems (figures A.9 and A.10). Upon applying temperature sweeps, the better recovery of the initial state was observed for PTS-TBA from H₂O/THF, for the three further PTS systems presence of water in the atmosphere resulted in a much more significant change of the UV/Vis absorption spectrum in the temperature sweep compared to the temperature sweep in dry atmosphere, which might be explained by higher softness of the PTS films due to incorporated water.

Stability tests of PTS films: Influence of humidity

In addition to the temperature ramp at constant $p\text{H}_2\text{O}$, a $p\text{H}_2\text{O}$ ramp at a constant temperature of 25°C was applied. In figure 4.7, the UV/Vis absorption spectra of four new films of the two PTS systems from two solvent systems recorded during the $p\text{H}_2\text{O}$ sweep at 25°C are shown. For the PTS-Na from H₂O film no absorption spectra was recorded at 16 mbar H₂O.

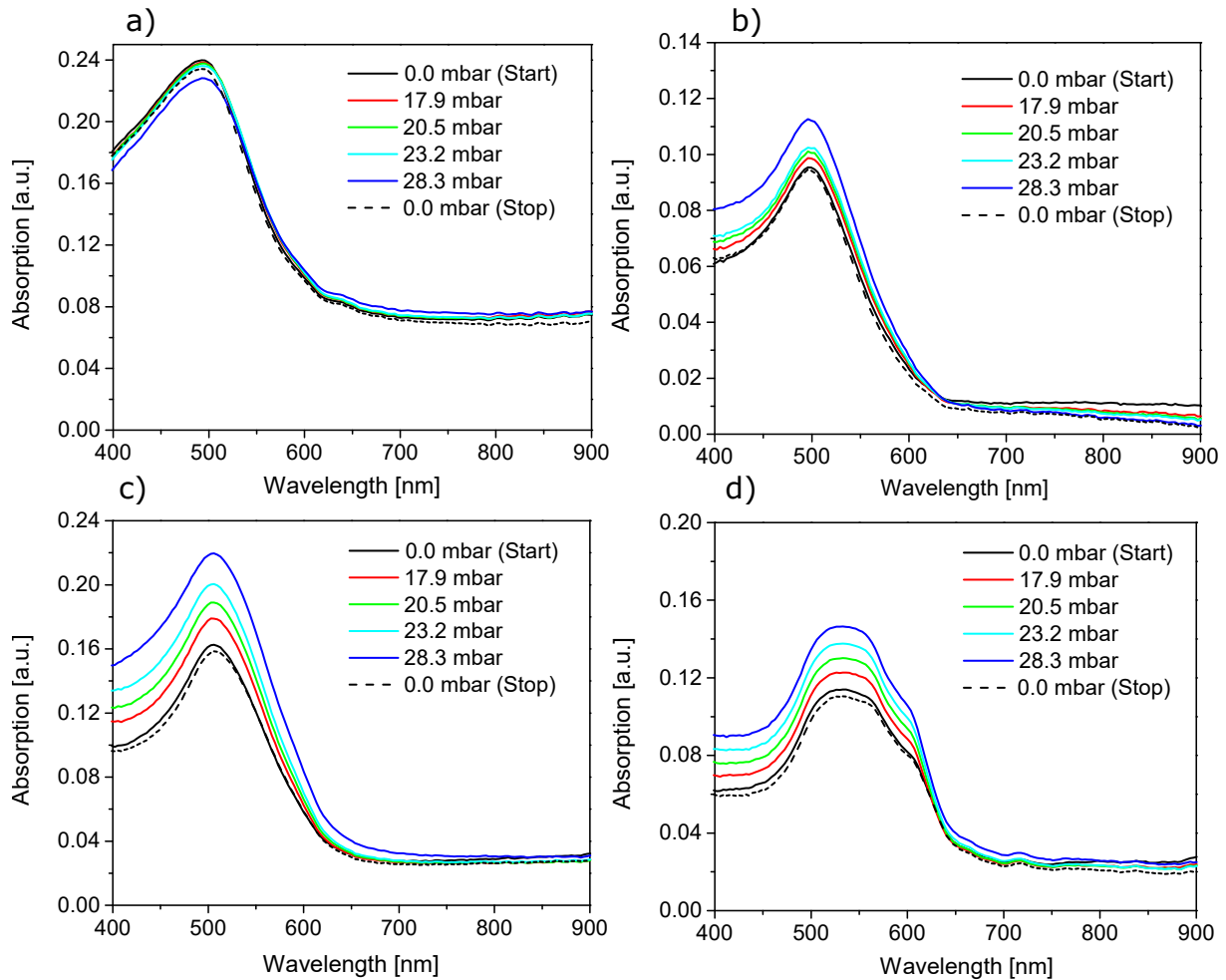


Figure 4.7: UV/Vis absorption spectra of PTS films on gold substrates during the water partial pressure ramp at 25°C. a) PTS-TBA spin coated from 5 mg/ml $\text{H}_2\text{O}/\text{THF}$, b) PTS-Na spin coated from 5 mg/ml $\text{H}_2\text{O}/\text{THF}$, c) PTS-TBA spin coated from 5 mg/ml H_2O and d) PTS-Na spin coated from 5 mg/ml H_2O .

The UV/Vis absorption spectrum of PTS-Na from H_2O shows the typical spectrum of an aggregated polythiophene backbone as previously observed. Both PTS films spin coated from $\text{H}_2\text{O}/\text{THF}$ and PTS-TBA from H_2O show the previously observed non-aggregated spectrum, in which the non-aggregated spectrum in case of PTS-TBA from H_2O might be due to a deterioration of the aggregated film structure (as shown in figure 4.3). For PTS-TBA from H_2O , PTS-Na from $\text{H}_2\text{O}/\text{THF}$ and PTS-Na from H_2O in figure 4.7 b), c) and d) a general trend in the $p\text{H}_2\text{O}$ ramp can be observed: starting with a low absorption intensity in the dry state at 0 mbar H_2O (black line), the absorption intensity increases with increasing $p\text{H}_2\text{O}$ and reaches its highest absorption intensity at 29 mbar H_2O (blue line). After switching back to 0 mbar H_2O (black dashed line), the absorption intensity decreases back to the previous absorption intensity at 0 mbar H_2O . Therefore it can be stated, that the effect leading to a higher absorption intensity at high $p\text{H}_2\text{O}$ is reversible. The UV/Vis absorption behavior of the PTS-TBA from $\text{H}_2\text{O}/\text{THF}$ film (figure 4.7 a))

shows only minor dependency of $p\text{H}_2\text{O}$, in which the reason for the different behavior is unknown.

In figure 4.8, the absorption intensity of the wavelength of maximum absorption from the respective UV/Vis spectra in figure 4.7 during the $p\text{H}_2\text{O}$ ramp is shown.

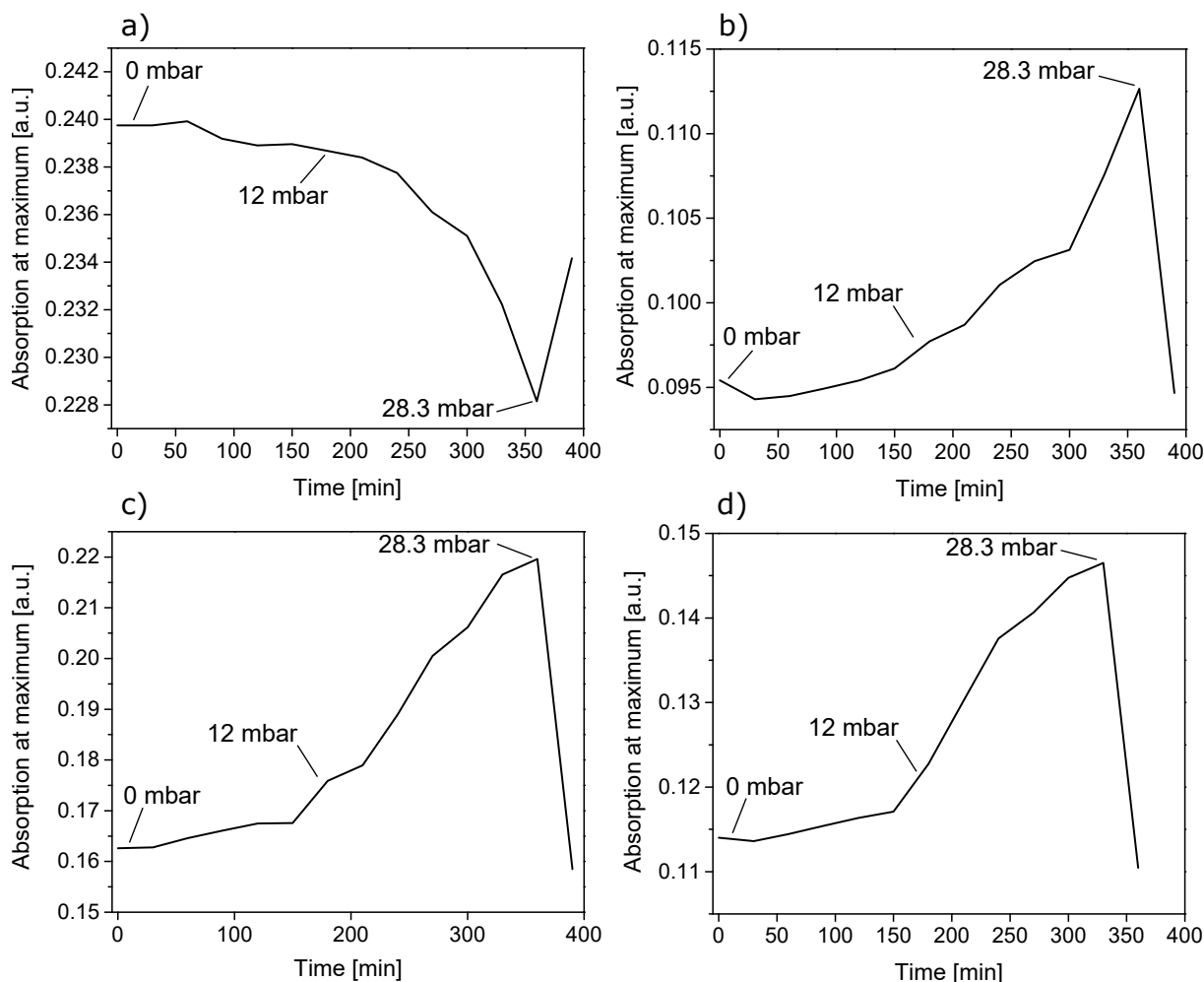


Figure 4.8: Absorption intensity at the wavelength of maximum absorption at 25°C , extracted from figure 4.7. a) PTS-TBA spin coated from 5 mg/ml $\text{H}_2\text{O}/\text{THF}$, b) PTS-Na spin coated from 5 mg/ml $\text{H}_2\text{O}/\text{THF}$, c) PTS-TBA spin coated from 5 mg/ml H_2O and d) PTS-Na spin coated from 5 mg/ml H_2O .

As previously mentioned, the absorption intensity of PTS-TBA from $\text{H}_2\text{O}/\text{THF}$ (figure 4.8 a)) shows no variation over time, this measurement is therefore not further discussed. A characteristic behavior can be identified in the absorption intensity trend of PTS-TBA from H_2O , PTS-Na from $\text{H}_2\text{O}/\text{THF}$ and PTS-Na from H_2O : whereas the absorption intensity increases only slightly in the approximately first 150 minutes of the $p\text{H}_2\text{O}$ ramp (at this time, 12 mbar H_2O is applied), the absorption intensity increases significantly stronger with every time step or $p\text{H}_2\text{O}$ step in the high $p\text{H}_2\text{O}$ range. This trend resembles therefore the water uptake trend of the PTS materials (section 4.2.2.2 and might

be explained with a change of the refractive index as observed in literature [4] (see also the discussion in 4.1.3). In literature, only few examples for relative humidity dependent UV/Vis absorption and reflection are known, mainly addressing relative humidity sensing [190, 191].

Stability tests of PTS films: Influence of humidity at temperature ramps

In addition to the in-situ UV/Vis absorption spectroscopy in reflection, the temperature ramp depicted in figure 4.4 was applied in UV/Vis measurements of PTS-TBA from H₂O and PTS-Na from H₂O at various $p\text{H}_2\text{O}$ (with the only difference that the temperature ramp here was started and stopped at 25°C instead of 20°C), in which the UV/Vis absorption spectra were measured in transmission on glass substrates. The UV/Vis absorption chamber with the PTS film was kept under the constant $p\text{H}_2\text{O}$ for several hours in prior to starting the temperature ramp. In order to prevent the vanishing of the aggregated PTS structure in case of PTS-TBA, it was taken care to conduct the temperature ramps directly after spin coating. In figure 4.9, the UV/Vis absorption spectra of PTS-TBA from H₂O at 0 and 29 mbar H₂O during the temperature ramp are shown.

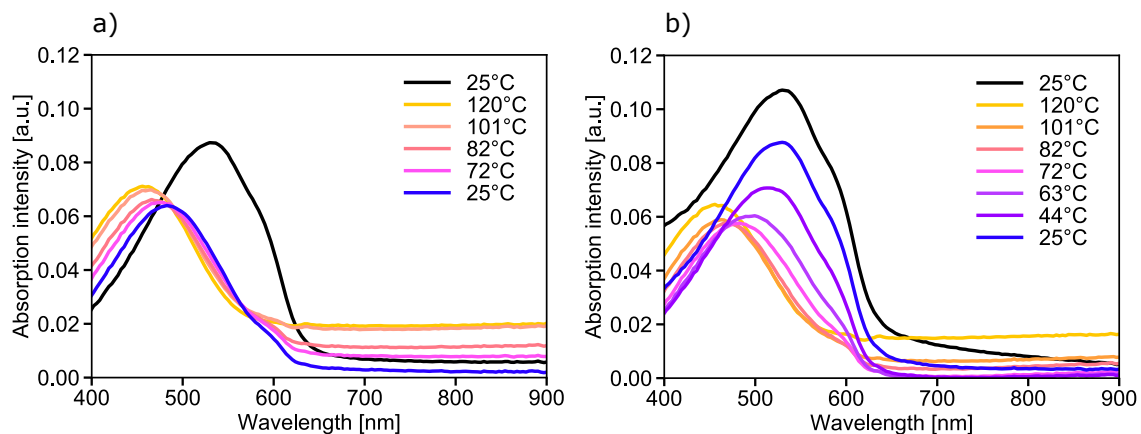


Figure 4.9: UV/Vis absorption spectra of PTS-TBA on glass substrates spin coated from 5 mg/ml H₂O at various temperatures during the temperature ramp depicted in figure 4.4 at a) 0 mbar H₂O and b) 29 mbar H₂O.

In the temperature ramp at 0 mbar H₂O in figure 4.9 a), changing the temperature from 25°C (black curve) to 120°C (yellow curve) leads to a decrease of the absorption intensity and a significant blue shift of the wavelength of maximum absorption. This corresponds to the same trends as observed upon heating in the UV/Vis absorption measurements in reflection on gold substrates as shown in section 4.1.1.1. Therefore it can be stated that even though two different substrate types were used (gold or glass), similar film structures were obtained.

In the UV/Vis absorption spectra at 29 mbar H_2O in figure 4.9 b), firstly it can be seen that the absorption intensity is in general higher than the absorption intensity at 0 mbar H_2O , which can be explained by the fact that the film was stored in an atmosphere of 29 mbar H_2O for several hours in prior to starting the temperature ramp, which leads to an increase of the absorption intensity as shown in figure 4.8. Interestingly, the UV/Vis absorption spectrum of PTS-TBA at 0 mbar and 29 mbar H_2O is similar at 120°C and even resembles with a slight red-shift and a decrease of the absorption intensity the same trend upon cooling down to 82°C . However, in case of the measurements at 29 mbar H_2O , after the similar trends upon cooling down to 82°C , the measurements at 0 and 29 mbar H_2O vary significantly: whereas the wavelength at 25°C in the measurements at 0 mbar H_2O remains significantly blue-shifted as at 120°C , in case of the measurements at 29 mbar H_2O the wavelength of the absorption maximum after switching back to 25°C corresponds to the wavelength of the absorption maximum prior to the temperature ramp and also the absorption intensity is almost fully recovered. This observation indicates that H_2O promotes aggregation only at temperatures when water uptake into the PTS-TBA films becomes significant. The in-situ measurements on glass substrates in transmission confirm the trends observed in the in-situ measurements in reflection on gold substrates in reflection: presence of atmospheric H_2O allows PTS-TBA to recover to its initial, aggregated structure. The results confirm therefore also the previously obtained observations that ambient relative humidity (approximately 30 % r.h.) promotes recovery of the UV/Vis absorption spectra of PTS-TBA whereas in dry N_2 the UV/Vis absorption spectrum is not recovered [160].

In figure 4.10, the UV/Vis absorption spectra of PTS-Na from H_2O at 0 and 29 mbar H_2O at various temperatures during the temperature ramp are shown.

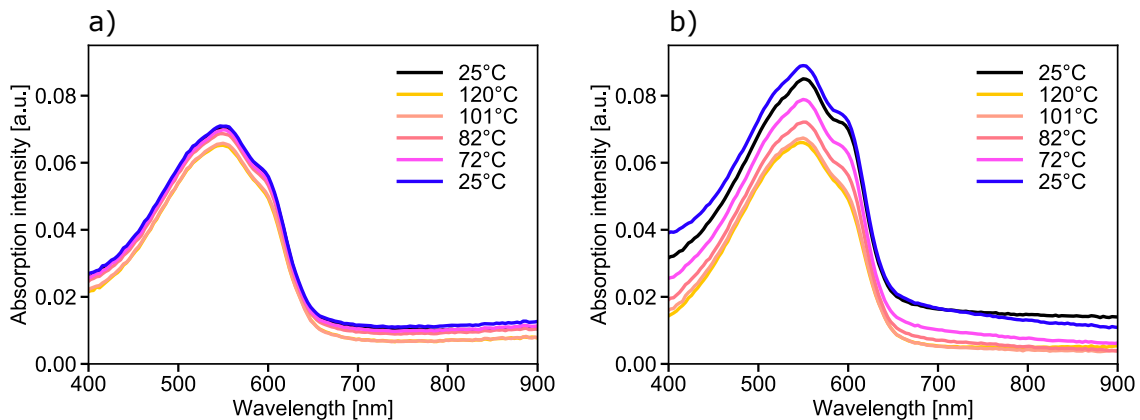


Figure 4.10: UV/Vis absorption spectra of PTS-Na on glass substrates spin coated from 5 mg/ml H_2O at various temperatures during the temperature ramp depicted in figure 4.4 at a) 0 mbar H_2O and b) 29 mbar H_2O .

The UV/Vis absorption spectra reveal at both $p\text{H}_2\text{O}$ the aggregated PTS structure, which

does for both pH_2O not vanish during the entire temperature ramp. This might be explained by the fact that in spite of an increased temperature, the small ion size of Na^+ or the stable aggregation of PTS-Na from H_2O does not lead to a vanishing of the aggregation. At 0 mbar H_2O (figure 4.10 a), the absorption intensity does not vary significantly during the temperature sweep, whereas at 29 mbar H_2O (figure 4.10 b), the absorption intensity varies significantly. This might be explained by the fact that at $25^\circ C$ the absorption intensity is high due to a high water content in the polymer film (see also the discussion in 4.1.3), therefore the absorption intensity decreases upon going to high temperatures due to the evaporation of water from the PTS-Na film.

4.1.1.2 Doped states

Chemical doping

In order to examine the variation of the UV/Vis absorption of PTS films upon doping, a PTS-Na film spin coated from H_2O/THF was chemically doped with a sequential doping procedure as described in 3.2.2. The UV/Vis absorption spectra of PTS-Na from fresh and aged H_2O/THF solution and from fresh solution and subsequent chemical doping with F_4TCNQ can be found in figure 4.11.

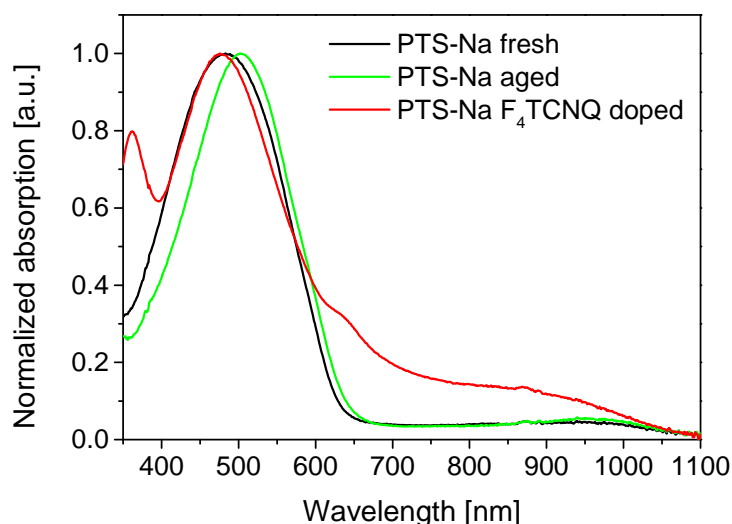


Figure 4.11: UV/Vis absorption spectra of PTS-Na on glass substrates spin coated from 5 mg/ml H_2O/THF film from freshly prepared solution (black curve), from an aged solution which was stored for two months after preparation (green curve) and from a fresh solution after chemically doping with 0.5 mg/ml F_4TCNQ/THF (red curve).

For all three films, the absorption band with an absorption maximum at around 500 nm which indicates the neutral polythiophene backbone. The film from the aged solution

(green curve) shows a slightly red-shifted absorption maximum. This might be explained by an enhanced aggregation of polythiophene backbones resulting from evaporation of THF even though the vial was properly sealed, which decreases the concentration of the polythiophene dissolving THF [160]. Occasionally, but in a very unreproducible manner, pristine PTS films showed without chemical doping an increased electronic conductivity, as shown for a PTS-Na film from aged solution (figure A.15). The slight absorption at 900 – 1000 nm in case of the PTS-Na film from fresh and from aged solution might give indication for a slight oxidation of the polythiophene backbone, which could result in increased electronic conductivities.

In the chemical doping procedure, after spin coating the PTS film on the respective substrate, the F₄TCNQ/THF solution was applied on the PTS film and after a waiting time of 5 seconds, the solution was spun off. In measurements of the UV/Vis absorption, of the water uptake in QCM measurements or electronic conductivity in AC impedance and DC measurements big variations for identically prepared films were observed. A reason for the large variations for identically prepared films might therefore be different spreading of the F₄TCNQ solution on the PTS films. The temperature when the F₄TCNQ solution is applied on the PTS film or in the spin coating step might also have an influence since the solvent THF is very volatile, an only slightly higher temperature might therefore result in a significantly higher evaporation of the solvent, which might result in different amount of dopant molecules on top of the PTS films. Upon sequential doping with F₄TCNQ (red curve), the additional absorption bands at 650 and 950 nm (and eventually an absorption shoulder at 570 nm) indicate radical cation/polaron states [45]. From literature it is known that F₄TCNQ shows absorption at 350 nm and F₄TCNQ radical anions show absorption at 760 and 870 nm, which superimpose the radical cation/polaron absorption of PTS [160].

Electrochemical doping

In order to compare the chemical doping with electrochemical doping and in order to identify the electronic species upon doping of PTS, spectroelectrochemistry studies of PTS-TBA from H₂O/THF on glass substrates were conducted. PTS-TBA from H₂O/THF was chosen as an exemplary PTS system since it also can be compared best to previous studies on PTS-TBA [160]. Due to the fact that the PTS materials are in their undoped state after spin coating, first the charge sweep (from negative to positive potentials) and then the discharge sweep (from positive potentials to negative potentials) of the cyclic voltammogram was conducted. In figure 4.12, three cycles of the cyclic voltammogram and the in-situ UV/Vis NIR absorption spectra of the first cycle are shown.

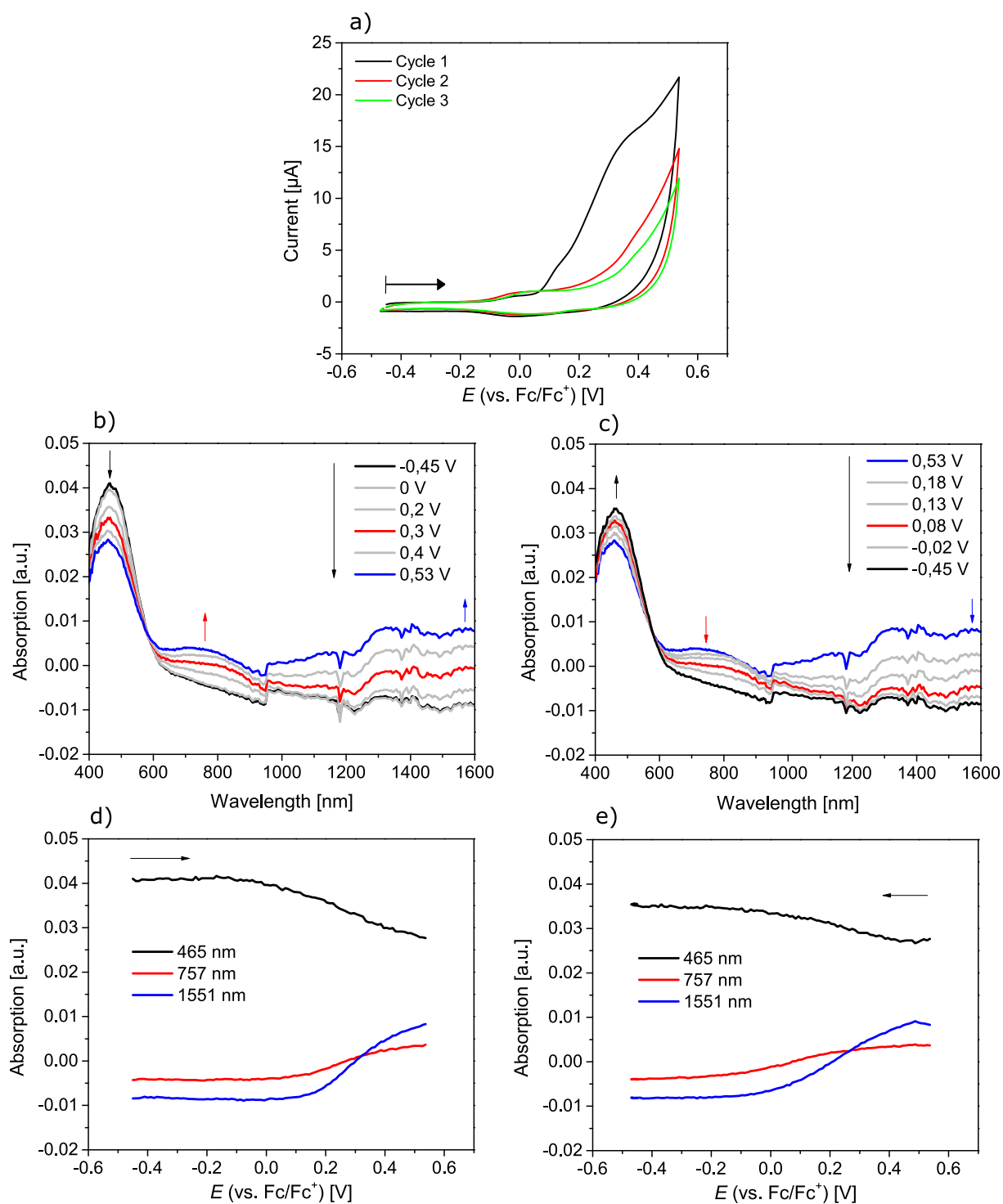


Figure 4.12: Spectroelectrochemistry studies of PTS-TBA from $\text{H}_2\text{O}/\text{THF}$ on ITO in 0.1 M $\text{NBu}_4\text{PF}_6/\text{MeCN}$ with a scan rate of 50 mV/s. a) cyclic voltammogram of the first three cycles, UV/Vis NIR absorption spectra recorded in the first cycle of the cyclic voltammogram during b) charge and c) discharge sweep and peak trend of selected wavelengths during charge d) and discharge sweep e).

In the cyclic voltammogram in figure 4.12 a) in the initial charge sweep in the first cycle (black curve), starting at low potentials the baseline current is detected. Upon reaching higher potentials, a broad oxidation wave with several overlaying redox processes can be observed. The broad oxidation wave corresponds to the oxidation of the polythiophene backbone of PTS and is typical for conducting polymers and has also been observed in the earlier studies of conjugated polyelectrolytes [46, 84]. In the backward sweep, only low reduction currents can be observed, which means that the conversion back to the neutral state does not or only partially occur, therefore it can be said that the cyclic voltammogram is chemically irreversible [177]. The irreversible redox reaction can be also observed on the decreasing currents from the first to the second and third cycle (red and green curve) of the cyclic voltammogram. A reason therefore might be overoxidation or dissolution from the electrode, the irreversibility of the conversion of PTS-TBA in cyclic voltammetry was observed before [192].

In figure 4.12 b) and c), the UV/Vis NIR spectra recorded during the charge and discharge sweep in the first cycle of the cyclic voltammogram are shown. Since the polythiophene backbone is identical to the polythiophene backbone of P3HT, the absorption band at ≈ 465 nm can be assigned to the neutral polythiophene backbone [98, 132, 193–196]. During the charge sweep (in case of initially neutral PTS from the neutral to the oxidized state, so from negative to positive potentials), the absorption intensity of the neutral band decreases slightly, whereas the absorption intensity ≈ 750 nm and ≈ 1500 nm of two absorption bands increases slightly. This mid- and low-energy absorption band can be assigned to oxidized states of the polythiophene backbone. Traditionally, the mid- and low-energy absorption band are assigned to polaron (radical cation) and bipolaron (dication) species, respectively [37]. Zozoulenko et al. showed that the traditional assignment of the mid-energy absorption band solely to the polaron band and the low-energy absorption band solely to the bipolaron band is presumably insufficient [197]. For the sake of simplicity the assignment to polaron and bipolaron band is however kept. In the discharge sweep, the absorption intensity of the neutral band increases and the absorption intensities of the charged states decrease, indicating a conversion from the oxidized, charged state back to the neutral state. Comparing the absorption intensity of the neutral band at the start of the cyclic voltammogram with the absorption intensity of the same at the end of the cyclic voltammogram, it can be seen that the absorption intensity is lower at the end of the cyclic voltammogram. This can be explained with an irreversible oxidation process, as can be seen in the cyclic voltammogram by the decrease of the currents from the first to the third cycle. In figure 4.12, the absorption intensity at 465, 757 and 1551 nm is shown, the plot is referred to as peak trend. The peak trends help to depict the trends discussed in the UV/Vis absorption spectra even more clearly: the absorption intensity of the neutral band decreased upon oxidizing, the absorption intensities of the charged

states increase. Since the absorption intensity of the neutral band is at all potentials higher than the absorption intensities of the charged states, it can be stated that only a partial conversion from the neutral to the oxidized states occurs.

The wavelengths of the UV/Vis absorption bands of the neutral and charged states of the chemically doped PTS-Na (figure 4.11) and electrochemically doped PTS-TBA (figure 4.12) are listed in table 4.2.

Table 4.2: Wavelengths of the UV/Vis absorption bands of chemically doped PTS-Na and electrochemically doped PTS-TBA.

	Neutral [nm]	Charged states [nm]
PTS-Na (chemical doping)	460	750, 1000
PTS-TBA (electrochemical doping)	500	650, 950

Considering the fact that two different PTS-solvent system combinations were examined and that different setup and device configurations were present in both the chemical and electrochemical doping of PTS, the UV/Vis absorption bands of the neutral and the oxidized states in PTS can be identified in both approaches.

4.1.2 PEDOT:PSS

As the second polymeric mixed conductor system in this thesis, PEDOT:PSS materials with two different PEDOT to PSS ratios were examined, the low PEDOT content batch PEDOT:PSS (1:6) and the high PEDOT content batch PEDOT:PSS (1:2.5) were investigated. At first, both PEDOT:PSS batches are examined by means of spectroelectrochemistry in order to identify the UV/Vis absorption properties at various oxidation states. Afterwards, in-situ conductance measurements are conducted in order to correlate the oxidation states of PEDOT:PSS to its conductivity properties. It is important to mention that in contrast to the PTS materials, the PEDOT:PSS materials are in the oxidized state after spin coating, therefore first the discharge sweep (from positive to negative potentials) and then the charge sweep (from negative to positive potentials) was conducted. All cyclic voltammetry and in-situ data are data from the second cycle of each measurement in order to eliminate possible memory effects [198].

4.1.2.1 Spectroelectrochemistry

In the following, spectroelectrochemistry measurements of both PEDOT:PSS batches on IDE substrates are shown. The cyclic voltammograms of both PEDOT:PSS (1:6) and PEDOT:PSS (1:2.5) in figure A.5 and A.6 exhibit an indistinct shape and are therefore not discussed any further.

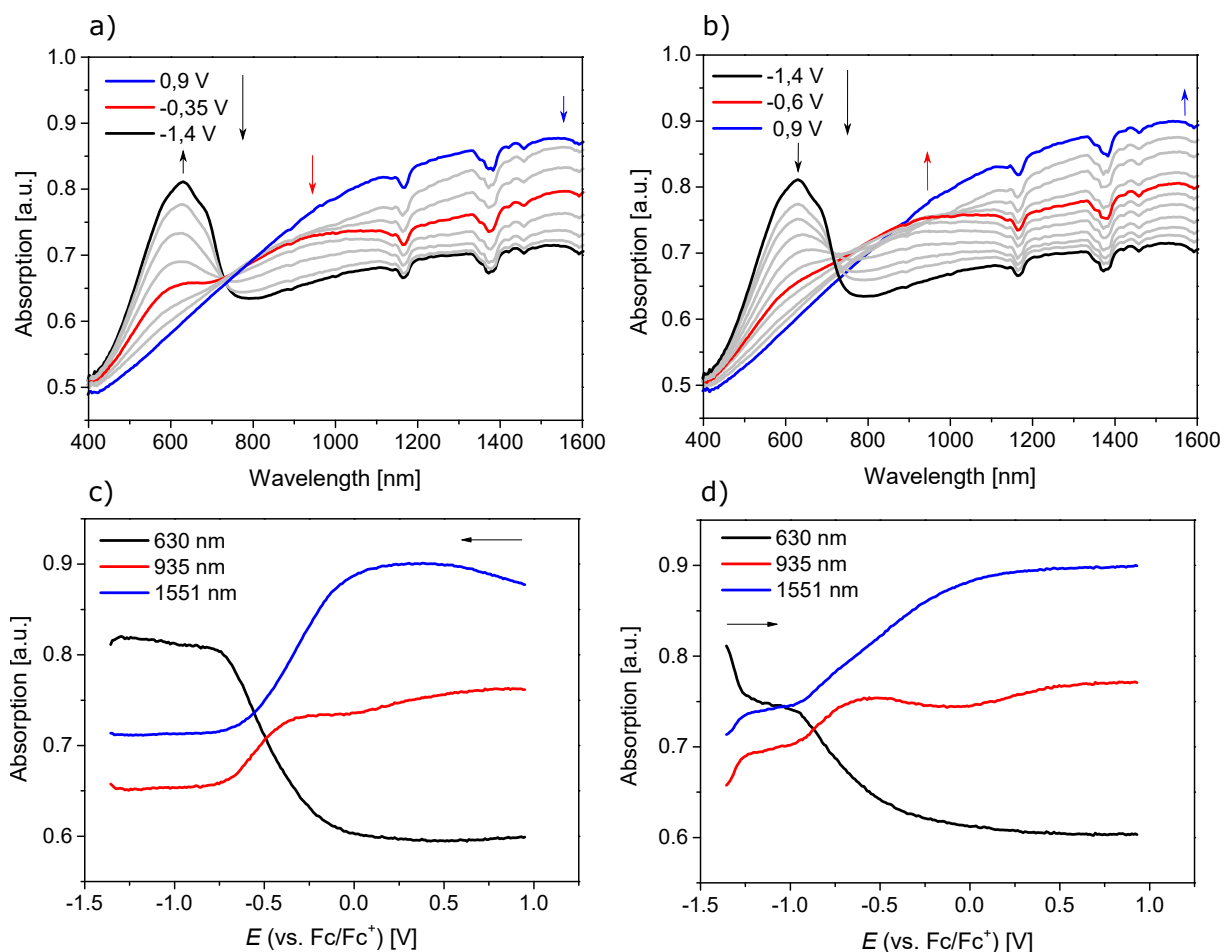


Figure 4.13: Spectroelectrochemistry measurements of PEDOT:PSS (1:2.5) on a 5 μm IDE in 0.1 M $\text{NBu}_4\text{PF}_6/\text{MeCN}$ with a scan rate of 10 mV/s. UV/Vis NIR absorption spectra recorded in the second cycle during a) discharge and during b) charge sweep and peak trends during c) discharge and d) during charge sweep.

In the UV/Vis NIR absorption spectra in figure 4.13 a), at the start of the discharge sweep (at +0.9 V, blue curve), a high absorption of the charged states (polaron and bipolaron) and no absorption of the neutral state can be observed. This is in strong contrast to PTS-TBA, where the absorption intensity of the neutral band is high at the start of the spectroelectrochemistry measurement. The here measured UV/Vis spectrum at the start of the cyclic voltammogram resembles the UV/Vis spectrum of pristine PEDOT:PSS films under ambient conditions as shown in figure 1.21. Upon decrease of the potential to -1.4 V, the absorption intensity of an absorption band at 630 nm increases whereas the absorption intensity of broad absorption bands at 950 and 1550 nm decreases. According to literature, the absorption band at 630 nm is assigned to neutral PEDOT and the broad absorption bands at 750 and 1550 nm to polaron and bipolaron states of PEDOT [98, 197]. In the case of PEDOT:PSS (1:2.5), at the end of the discharge sweep (-1.4 V) the absorption intensity of the neutral band exceeds the absorption intensities of the charged states, therefore it can be said that PEDOT:PSS (1:2.5) can be reduced from its oxidized

to the neutral state. Comparing the wavelength of the absorption maximum of the neutral band, it can be seen that PEDOT:PSS shows an absorption maximum at 630 nm and shoulders at higher and lower wavelengths and PTS-TBA shows an absorption maximum at 465 nm. The absorption maximum at significantly higher wavelengths in case of PEDOT:PSS can be explained by a significantly larger conjugation length in the PEDOT moieties than in the polythiophene moieties in PTS-TBA.

In the UV/Vis NIR absorption spectra recorded during the discharge sweep of PEDOT:PSS (1:2.5) in figure 4.13 a), a decrease of the polaronic and bipolaronic species and an increase of the neutral band can be observed. In the spectra during the charge sweep depicted in figure 4.13 b), the opposite evolution of the absorption intensities can be observed, indicating a good reversibility of the conversion from the charged to the neutral state and vice versa. In figure 4.13 c) and d), the peak trends of the neutral (black), polaron (red) and bipolaron (blue) in the discharge or charge sweep are depicted. During the discharge sweep, the absorption intensity at all three wavelengths remains constant up to ≈ 0 V, after which the absorption intensities of the polaron and bipolaron band decrease and the absorption intensity of the neutral band increases, indicating a conversion from the charged to the neutral state. After reaching -0.7 V, the absorption intensities of the three bands remain constant. Directly at the beginning of the charge sweep, the absorption intensity of the neutral band increases and the absorption intensity of the polaron and bipolaron band increase. After remaining roughly constant up to a potential of -0.95 V, the absorption intensities of the polaron and bipolaron band increase further and the absorption intensity of the neutral band decreases further. This step-wise evolution of the absorption intensities in the peak trends was also observed for a further PEDOT:PSS (1:2.5) film on a glass substrate in spectroelectrochemistry measurements as depicted in figure A.7. Since the step-wise conversion from the neutral to the charged state is typically not observed for conducting polymers, it could be explained by the presence of immobile PSS as counterion which stabilizes the oxidized states in PEDOT [97, 199, 200]. Since oxidized PEDOT is eventually stabilized very well by PSS, the conversion from the neutral to the oxidized state might occur immediately after starting the charge sweep, even though the applied potential is still very low. As in the discharge sweep, the polaron and bipolaron band behave slightly different: at -0.5 V the intensity of the polaron band remains roughly constant towards the end of the charge sweep, whereas the intensity of the bipolaron band further increases.

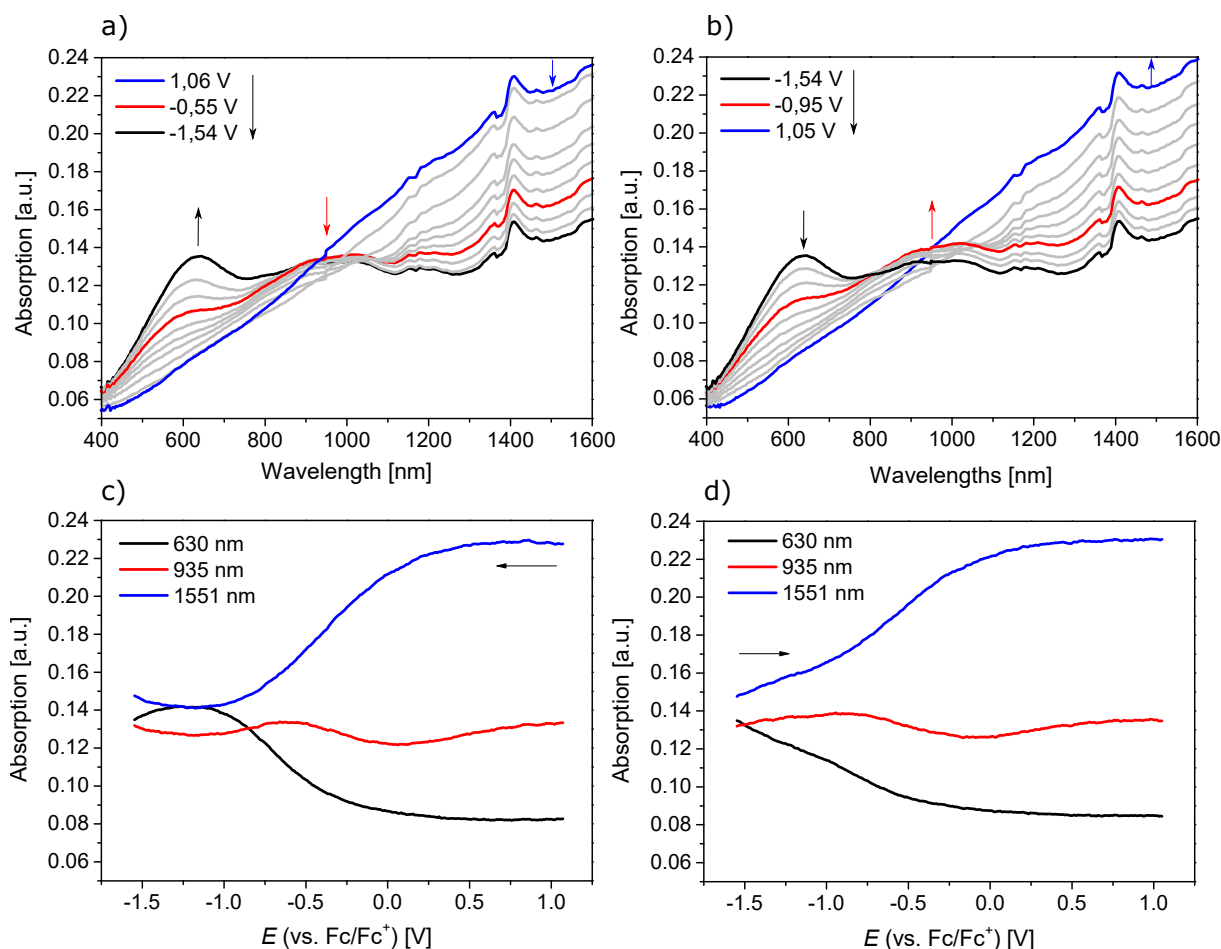


Figure 4.14: Spectroelectrochemistry measurements of PEDOT:PSS (1:6) on a 5 μm IDE in 0.1 M $\text{NBU}_4\text{PF}_6/\text{MeCN}$ with a scan rate of 10 mV/s. UV/Vis NIR absorption spectra recorded in the second cycle during a) discharge and during b) charge sweep and peak trends during c) discharge and d) during charge sweep.

The UV/Vis absorption spectrum in figure 4.14 a) resembles at the start of the cyclic voltammogram at +1.06 V (blue line) the typical spectrum of oxidized PEDOT:PSS. Upon decrease of the potential, the polaron and bipolaron bands at 935 nm and 1550 nm decrease in intensity and the neutral PEDOT band increases in intensity. Together with the fact that the intensity of the polaron band does not significantly change in intensity and the fact that the intensity of the bipolaron band exceeds the intensity of the neutral band at the negative turning potential, it can be assumed that even at a potential of -1.54 V a remarkable amount of PEDOT moieties is still in its oxidized state. The obtained differences between the PEDOT:PSS (1:2.5) and PEDOT:PSS (1:6) material can also be observed in spectroelectrochemistry measurements on ITO substrates as shown in A.7 and A.8, the trends can therefore be confirmed. Comparing the wavelengths of the absorption bands of PEDOT:PSS (1:6) and PEDOT:PSS (1:2.5), it can be said that the absorption bands are at very similar wavelengths, the electronic structure of the PEDOT moieties in both batches is therefore assumed to be similar. In the spectra recorded during

the charge sweep in figure 4.14 b), an intensity decrease of the neutral band and intensity increase of the bipolaron band can be observed, indicating reversibility of the PEDOT reduction.

4.1.2.2 In-Situ conductance

After examining absorption properties with UV/Vis absorption spectroscopy as function of the applied potential and therefore as function of charge state, in-situ conductance measurements were conducted in order to investigate the conductance properties as function of the applied potential. In figure 4.15, the cyclic voltammograms and in-situ conductance of PEDOT:PSS (1:6) and PEDOT:PSS (1:2.5) are shown.

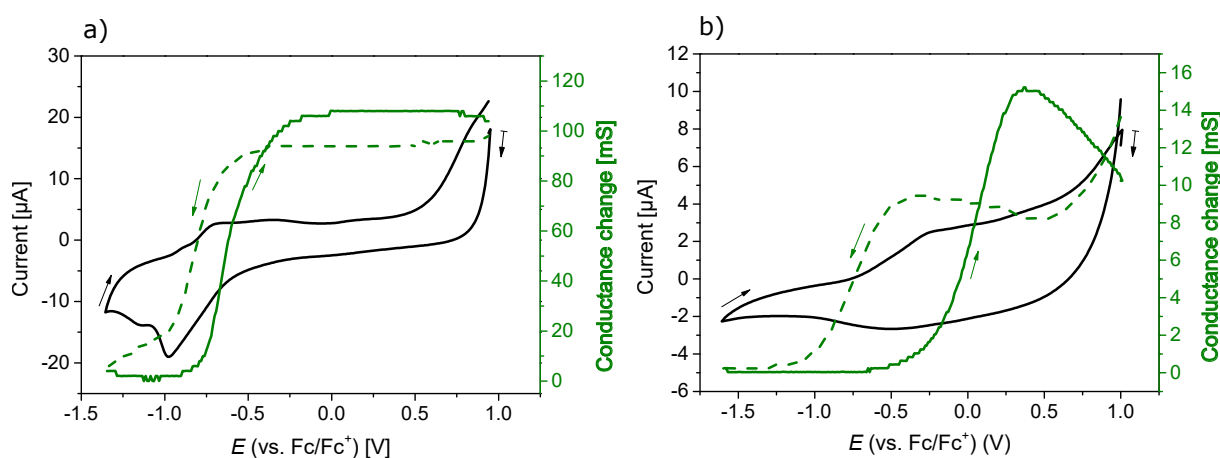


Figure 4.15: Cyclic voltammogram (black curve) and in-situ conductance (green curve) of a) PEDOT:PSS (1:6) and b) PEDOT:PSS (1:2.5) in 0.1 M $NBu_4PF_6/MeCN$ with a scan rate of 10 mV/s on 5 μ m IDEs.

In the cyclic voltammogram (black curve) in figure 4.15 a), in the discharge sweep (the first half wave of the cyclic voltammogram) and the subsequent charge sweep (second half of the cyclic voltammogram) multiple reduction or oxidation waves can be observed. As for PTS, the abundance of several redox waves is typical for conjugated polymers. In contrast to the cyclic voltammogram of PTS-TBA in figure 4.12, the presence of both oxidation and reduction waves indicates chemical reversibility of the electrochemical conversion. The in-situ conductance (green curve) shows a plateau of high in-situ conductance at potential values superior to -0.3 V in the charge sweep or -0.6 V in the discharge sweep. The plateau-like in-situ conductance profile is typical for conducting polymers [46, 166].

The cyclic voltammogram in figure 4.15 b) resembles the cyclic voltammogram of PEDOT:PSS (1:2.5): an indistinct shape with several overlapping oxidation and reduction waves can be observed. The in-situ conductance findings are however significantly different: in the discharge sweep (green dashed curve), the in-situ conductance reaches after a

slight initial decrease a local maximum at ≈ -0.4 V. Upon further decrease of the potential, the in-situ conductance decreases. In the charge sweep (green curve), the in-situ conductance starts to increase at a potential of -0.5 V. After reaching a maximum at $+0.4$ V, the in-situ conductance decreases again upon further potential increase. In contrast to the plateau-like in-situ conductance of PEDOT:PSS (1:2.5), PEDOT:PSS (1:6) shows therefore high in-situ conductance values only at distinct potentials.

4.1.3 Discussion and summary of absorption characteristics

Summarizing section 4.1, at first the influence of the counterion and the solvent system from which the respective PTS film was spin coated on the UV/Vis absorption was examined. The UV/Vis absorption was observed to be blue shifted for PTS-TBA independent from the solvent system, which indicates a lower conjugation length of the polythiophene backbone presumably due to increased disturbance of the polythiophene backbone by the bulky TBA⁺ cation. Therefore the properties of PTS depend in general on the type and size of the counterion as observed previously [1, 2, 90, 91, 95]. For both PTS-Na and PTS-TBA, using H₂O as solvent system instead of H₂O/THF resulted in red shifted UV/Vis absorption spectra of the spin coated films, which can be attributed to the presence of aggregated PTS in aqueous solution, which are maintained in the film. However for PTS-TBA spin coated from H₂O, the aggregation in film was observed to vanish over time, which as for the blueshift in case of all PTS-TBA films can be explained by the bulky TBA⁺ cation.

Additionally, the influence of temperature and relative humidity on the UV/Vis absorption was examined. For PTS-TBA, a blue shift at high temperatures was observed, which might be explained by an increased disturbance of the polythiophene aggregation due to the movement of the butyl moieties in the alkyl side chains of TBA⁺ at high temperatures. Presence of humid atmospheres was observed to lead to a recovery of the aggregation of PTS which can be observed at room temperatures after heating, whereas dry N₂ atmospheres prevented recovery of the aggregation. In case of PTS-Na, high temperatures were not observed to lead to changes in the shape of the UV/Vis absorption spectrum, which might be explained by a stable aggregation due to the small ion size of Na⁺. Variations of the relative humidity lead also only to a variation of the absorption intensity. The UV/Vis absorption at room temperature as function of water partial pressure was observed to increase slowly in the low water partial pressure range and increase steeply in the high water partial pressure range, therefore showing similar trends as the QCM water uptake as function of water partial pressure as shown in section 4.2.2. The amount of light absorbing particles is however constant and independent from the water uptake, therefore other reasons such as a variation of the refractive indices of the water rich and the PTS moieties and accordingly higher reflection or variation of the extinction coeffi-

cient as observed in literature could be assumed [4]. Both the counterion and the solvent system did not seem to influence the morphology as observed in the AFM images.

Regarding the in-situ conductance measurements of PEDOT:PSS, PEDOT:PSS (1:2.5) exhibits a plateau-like in-situ conductance whereas PEDOT:PSS (1:6) shows a more bell-shaped in-situ conductance profile. In literature, presence of the plateau-like in-situ conductance is typically observed for conjugated polymers and is traditionally explained with the presence of multiple, overlapping mixed redox states that are each passed upon charging of the polymer [46]. On the other hand, the bell-shaped in-situ conductance profile is known for mixed valence conductivity behavior, for example in case of polymers based on tetraphenylbenzidine units or terthiophene-functionalized dendrimers [201–203]. According to the theories in literature, PEDOT:PSS (1:2.5) would be assigned to a conducting polymer, whereas PEDOT:PSS (1:6) would correspond to a polymer possessing mixed valence conductivity. The difference between both materials is however only the PEDOT to PSS ratio, and the fact that the absorption maximum of the neutral band for both PEDOT:PSS materials is at around ≈ 630 nm presumably indicates that the electronic structure of the PEDOT moieties is in both materials similar. Therefore it is suggested that both PEDOT:PSS materials behave according to the mixed valence model, in which the higher amount of PEDOT in PEDOT:PSS (1:2.5) (29 wt% PEDOT in PEDOT:PSS (1:2.5) vs. 14 wt% PEDOT in PEDOT:PSS (1:6), see also the discussion in section 4.2.2.3) leads to a better connectivity between the PEDOT moieties, accordingly to more valence states which can be passed upon charging or discharging and therefore to a broader potential window where PEDOT:PSS (1:2.5) is in its highly conducting state. In the in-situ conductance trend of PEDOT:PSS (1:2.5) in figure 4.15 b), a small decrease of the in-situ conductance can be observed at very high potentials, which might indicate that the in-situ conductance behavior of PEDOT:PSS (1:2.5) is actually not plateau-like but rather bell-shaped as in PEDOT:PSS (1:6), in which the bell-profile is significantly widened. This observation supports the assumption that the underlying conductance mechanism is for both PEDOT:PSS materials the same. The decrease of the in-situ conductance at very high potentials was also observed in literature [204, 205].

The worse connectivity between the PEDOT moieties in case of PEDOT:PSS (1:6) compared to PEDOT:PSS (1:2.5) might be additionally concluded from four further experimental observations. Firstly it can be seen in the hysteresis of the forward and backward scan in the respective in-situ conductance trends: whereas the curves are separated by ≈ 0.2 V in case of PEDOT:PSS (1:2.5), the potentials of maximum conductance are separated by ≈ 0.7 V in case of PEDOT:PSS (1:6). Small hysteresis in in-situ conductance measurements indicate fast and reversible charge/discharge processes [182]. Also increasing the film thicknesses is observed to increase the hysteresis effects [206]. Secondly, the

higher tilt of the baseline in the cyclic voltammogram of PEDOT:PSS (1:6) might indicate a higher internal resistance than in PEDOT:PSS (1:2.5) [207]. Thirdly, also in the spectroelectrochemistry observations of PEDOT:PSS (1:6) and PEDOT:PSS (1:2.5) on IDEs indications for better connectivity between the PEDOT moieties in PEDOT:PSS (1:2.5) can be assumed: whereas a full conversion between the neutral and the charged states can be obtained in case of PEDOT:PSS (1:2.5), the conversion to the neutral state can be achieved only to a small extent in case of PEDOT:PSS (1:6) (the differences between the PEDOT:PSS batches can also be obtained on ITO substrates, therefore confirming the observations on IDEs). Therefore, in PEDOT:PSS (1:6), a significantly worse accessibility of charged states compared to PEDOT:PSS (1:2.5) can be assumed. It has to be noted however that the reliability of the measurements of PEDOT:PSS (1:6) might be reduced by significant dissolution of the polymer films during the spectroelectrochemistry measurements. Fourthly, the worse connectivity can also be seen by comparing the electronic conductivities of the high and low PEDOT content PEDOT:PSS materials (as observed in [103] and see section 4.3.5 of this thesis): the high PEDOT content PEDOT:PSS (1:2.2) batch shows electronic conductivities in the range of 1 S/cm (PEDOT:PSS (1:2.5) and PEDOT:PSS (1:2.2) are expected to have very comparable properties), the low PEDOT content PEDOT:PSS (1:6) shows electronic conductivities in the range of 10^{-5} – 10^{-4} S/cm.

As a summary of the characterization of PEDOT:PSS and PTS with spectroelectrochemistry and in-situ conductance measurements, different results were obtained for the PEDOT:PSS materials: PEDOT:PSS (1:2.5) showed a reversible conversion from the oxidized to the neutral state, whereas PEDOT:PSS (1:6) showed only slight, fairly irreversible conversion towards the oxidized state. For PEDOT:PSS (1:2.5) a large potential window where the polymer is in its highly conducting state was found (plateau-like in-situ conductance profile), whereas PEDOT:PSS (1:6) showed maximum in-situ conductance at one specific potential value (bell-shaped in-situ conductance profile). These results might indicate that high connectivity between the conjugated polymer moieties is necessary for a high amount of accessible redox states and high conductivity.

4.2 Water uptake studies in controlled atmospheric conditions

After studying the UV/Vis absorption properties of the PTS and PEDOT:PSS systems as function of the doping state in the previous chapter, the following chapter deals with the water uptake measurements (the water uptake is calculated as mass of water per mass polymer in wt% and amount of water molecules per repeating unit in λ , for details about the calculation method see section 3.3.4) at different water partial pressure and temperature conditions. Throughout this thesis, the terms water uptake and water content refer both to the water uptake per mass and in λ . If not otherwise mentioned in the following section and in the conductivity section 4.3, all PTS materials were spin coated from H₂O/THF. In section 4.2.1, the water uptake measurements of bulk materials determined with preliminary thermogravimetric analysis (TGA) studies are shown and in section 4.2.2 the water uptake measurements of thin films using quartz crystal microbalance (QCM) measurements are discussed. For both techniques, a discussion about the validity and applicability of the respective technique is included. In section 4.2.3, the results are discussed and summarized.

4.2.1 Preliminary Thermogravimetric Analysis

At first, the water uptakes determined with preliminary TGA studies are discussed. As mentioned in the experimental part in section 3.3.4, the water uptake was determined with the PTS material in bulk form, whereas the PEDOT:PSS materials are measured in the form of small film crumbs.

4.2.1.1 PTS materials

In figure 4.16, the calculated water uptake per mass (in wt%) and in λ of pristine PTS-TBA as function of $p\text{H}_2\text{O}$ at various temperatures and in figure 4.17, the water uptake per mass (in wt%) and in λ of pristine PTS-Na as function of $p\text{H}_2\text{O}$ at various temperatures is shown. The data for PTS-TBA are determined in an identical way as the data for PTS-Na in figure 4.17 and are taken from [160]. Due to the identical measurement procedure and in order to easily compare them to the respective water uptake data of PTS-Na, the water uptake data for PTS-TBA are shown here. As described in experimental section 3.3.4, the water uptake in wt% is defined as mass of taken up water per mass polymer and the water uptake in λ is defined as number of taken up water molecules per repeating unit or per PSS repeating group in case of PEDOT:PSS. As also mentioned, in order to be able to compare the water uptake values of the PTS materials determined with TGA with the respective values determined with QCM, the water uptake values of the PTS materials are extrapolated with the help of the hydration enthalpy constant K_{hy} based

on the measured water uptake at 16.7 mbar H_2O , assuming a linear increase of the water content with increasing $p\text{H}_2\text{O}$. This assumption was shown to be valid for data from literature for PTS-TBA and the cationic conjugated polyelectrolyte PTImBr [160], for the TGA measurements of PEDOT:PSS in section 4.2.1.2 and approximately also for the water uptake measurements with QCM (see section 4.2.2) up to water partial pressures of 20 mbar H_2O .

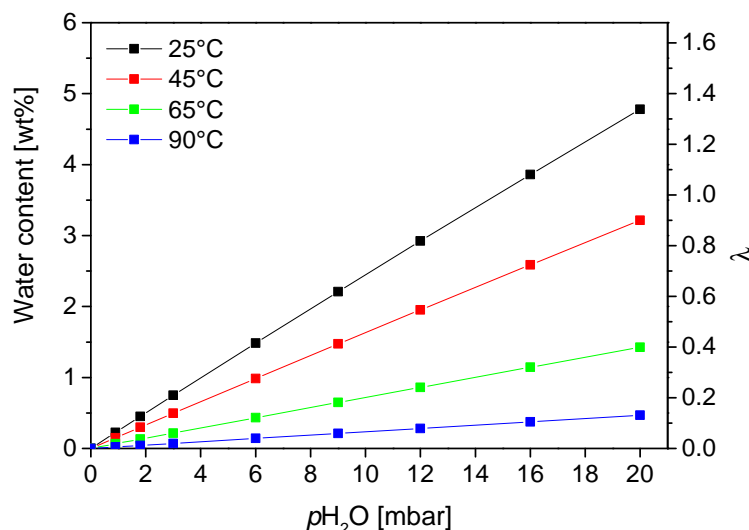


Figure 4.16: Extrapolated water uptake of PTS-TBA determined with TGA in wt% and λ at various temperatures as function of water partial pressure. Adapted with permission from [160], © 2019, Elsevier.

Regarding the water uptakes at a certain $p\text{H}_2\text{O}$ as function of temperature, it can be seen that the water uptake decreases with increasing temperature [160]. The temperature dependency can be explained with the fact that with increasing temperature at a constant $p\text{H}_2\text{O}$, the relative humidity of the atmosphere decreases. Therefore, more water evaporates from the polymer material. The maximum water uptake of PTS-TBA amounts to 4.8 wt% or $\lambda \approx 1.3$ at 25°C and 20 mbar H_2O . In figure 4.17, the water uptake of PTS-Na as function of $p\text{H}_2\text{O}$ at various temperatures is shown.

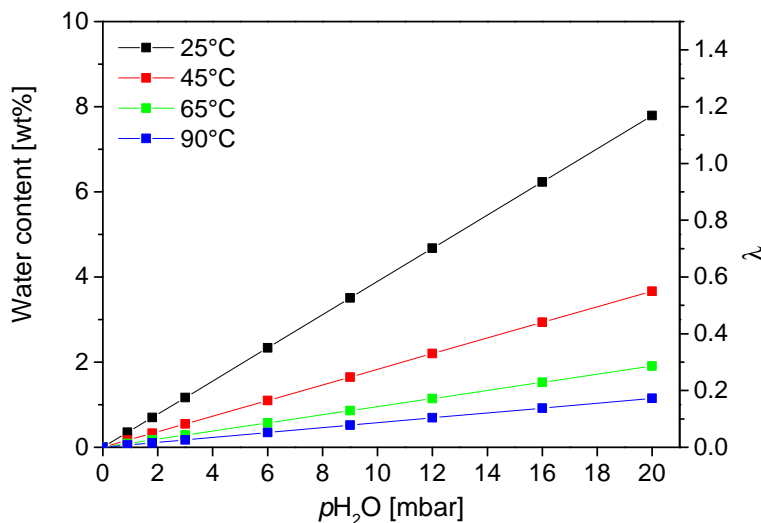


Figure 4.17: Extrapolated water uptake of PTS-Na determined with TGA in wt% and λ at various temperatures as function of water partial pressure.

The water uptake of PTS-Na shows the same dependency as PTS-TBA: with increasing temperature, the water uptake decreases. The values of the water uptake per mass (water content in wt%) are however different compared to PTS-TBA: at 25°C and 20 mbar H_2O , the water content amounts to 4.8 wt% in case of PTS-TBA, whereas at the same atmospheric conditions the water content of PTS-Na amounts to 7.8 wt% (even the actually measured water uptake values at 16.7 mbar H_2O show the same relative deviation between PTS-TBA and PTS-Na). This effect can be explained with the molecular weights of the components of PTS-TBA and PTS-Na: the repeating unit of PTS without cation has a molecular weight of 245.35 g/mol, TBA^+ has a molecular weight of 242.47 g/mol and Na^+ has a molecular weight of 22.99 g/mol. Therefore, processing of the same masses of polymer results in higher shares of polymer backbone and therefore also to higher shares of side chains or ionic groups in the bulk material in case of PTS-Na. Even though not the same mass of polymer is used in each TGA measurement, due to the calculation of the water uptake per mass or per repeating unit, the water uptake is "normalized" with respect to the polymer mass or polymer weight. For the same mass of material, the amount of ionic groups is around 80 % higher in PTS-Na. Regarding the different water uptakes per weight, it can be seen that PTS-Na takes up around 60 % more water than PTS-TBA. Therefore, the higher share of ionic groups might be the reason for the higher water uptake per weight in case of PTS-Na. Regarding the water uptake in λ , it can be seen that PTS-TBA at 25°C and 20 mbar H_2O takes up around 1.3 water molecules, whereas PTS-Na at the same conditions takes up around 1.2 water molecules. The small difference might be explained by measurement inaccuracies or to a partial shielding of ionic moieties in PTS-Na due to higher aggregation in PTS-Na. In general, the amount

of water molecules per repeating unit is similar for both PTS materials. As described in section 4.1.1.1, TBA⁺ corresponds to a soft cation whereas Na⁺ corresponds to a hard cation. However, since the different character of the cations does apparently not result in different water uptake per repeating unit, it can be assumed that mostly the ionic character of the SO₃⁻ group rather than the specific properties of the cation are relevant for the water uptake.

4.2.1.2 PEDOT:PSS materials

In the following, the water uptake values for PEDOT:PSS materials as measured with TGA are shown. The previously examined PEDOT:PSS (1:6) low PEDOT content batch is examined, as high PEDOT content PEDOT:PSS batch PEDOT:PSS (1:2.2) was examined. Since the PEDOT to PSS ratio is not significantly different in the PEDOT:PSS (1:2.5) and PEDOT:PSS (1:2.2) batch, both PEDOT:PSS batches are assumed to be very comparable. In figure 4.18, the water uptake of PEDOT:PSS as water content per weight at 25°C as function of $p\text{H}_2\text{O}$ is shown. Whereas the previously shown water uptake for PTS-TBA and PTS-Na was extrapolated from the water uptake at 16.7 mbar H₂O to other $p\text{H}_2\text{O}$, the water uptakes of the PEDOT:PSS materials were directly determined at various $p\text{H}_2\text{O}$ steps in a water partial pressure range up to 16.7 mbar H₂O.

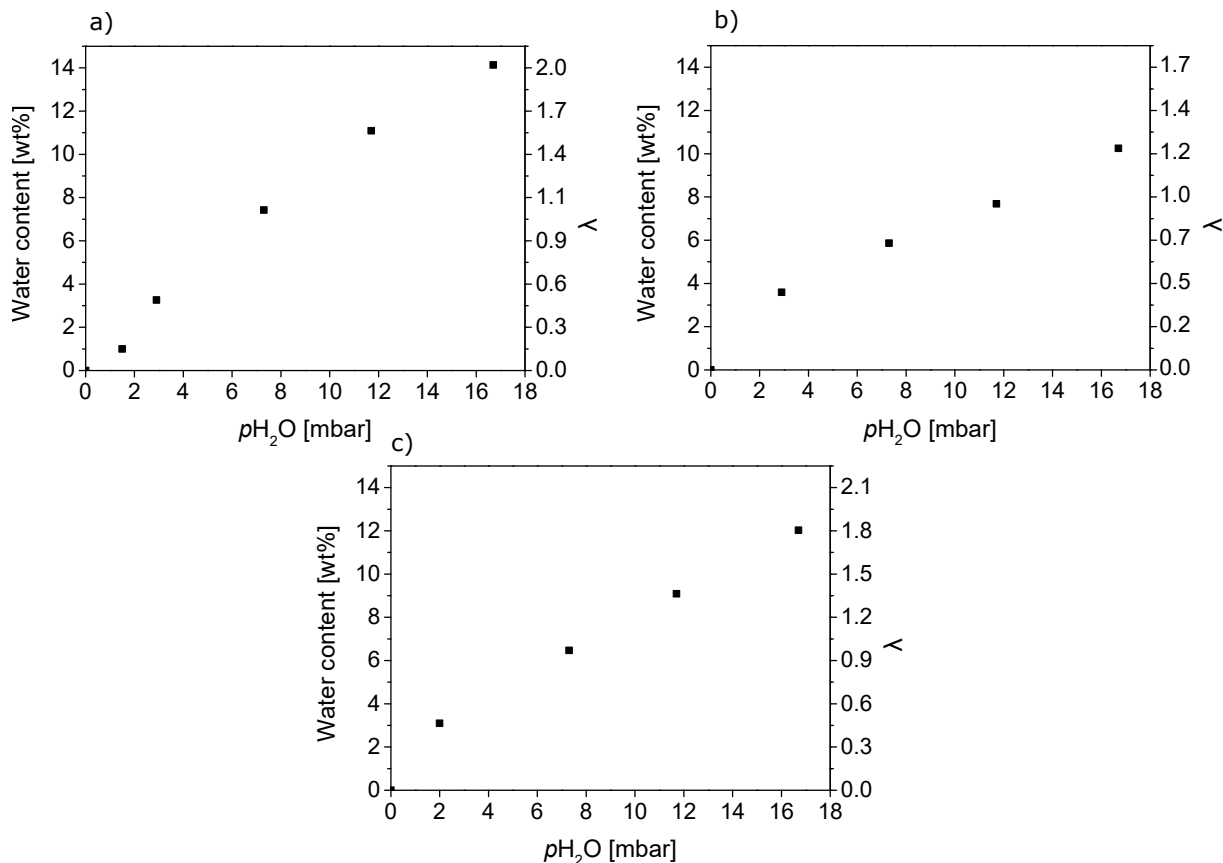


Figure 4.18: Water uptake of PEDOT:PSS materials determined with TGA at 25°C as function of water partial pressure. a) PEDOT:PSS (1:6), b) PEDOT:PSS-Na (1:6) and c) PEDOT:PSS (1:2.2).

The experimental trend of the water uptake of the PEDOT:PSS materials shows the trend expected also for the PTS materials: the water content per mass increases with increasing p_{H_2O} . In the water partial pressure from 2 – 3 to 16.7 mbar H_2O , it seems that the water content increases linearly with p_{H_2O} . In contrast to the moderate increase in the water partial pressure range between 2 – 3 and 16.7 mbar H_2O , the water content increases significantly upon switching from dry N_2 (0 mbar H_2O) to 2 – 3 mbar H_2O . The high increase at low p_{H_2O} might be explained by the fact that in addition to the water uptake into the bulk material, water is adsorbed at the surface of the bulk material. Going towards higher p_{H_2O} , the surface of the bulk material is already saturated, therefore the water content increases only moderately with p_{H_2O} since water is increasingly taken up in the bulk material.

Comparing the water uptakes of the different PEDOT:PSS materials, it can be seen that at 16.7 mbar H_2O , PEDOT:PSS (1:6) shows with 14 wt% the highest water content, PEDOT:PSS (1:2.2) shows with 12 wt% the second highest water uptake and PEDOT:PSS-Na (1:6) shows with 10 wt% the lowest water uptake. The highest water uptake for PEDOT:PSS (1:6) could be explained by the high weight content of PSS in the material

mixture PEDOT:PSS, as described in section 3.3.4. In case of PEDOT:PSS (1:2.2) the lower water uptake might be explained by the lower content of PSS, which leads to a total decrease of the hydrophilic moieties. The lowest water uptake of PEDOT:PSS-Na (1:6) might eventually be explained by the fact that the hydrophilicity of the $\text{SO}_3^- \text{-Na}^+$ ion pairs is lower than the hydrophilicity of the $\text{SO}_3^- \text{-H}^+$ ion pair. Worth noticing is that the cationic conjugated polyelectrolyte PTImBr shows similar water uptakes as PTS-TBA in spite of a similar ion concentration per volume as PTS-Na [160]. The reason therefore could be the lower hydrophilicity of the cationic imidazolium moiety compared to the sulfonate group.

In general, the water uptakes of the PEDOT:PSS materials at in wt% and λ are by around a factor of 2 higher than the water uptakes of the PTS materials. This finding is unexpected, since in both materials SO_3^- groups are present and as could be shown by comparing the λ values for PTS-Na and PTS-TBA, the water uptake is rather not dependent of the cation. It could be assumed that the difference between the TGA measurements of PTS and PEDOT:PSS might be explained by the fact that the PEDOT:PSS materials are present in form of small crumbs originating from polymer films with thicknesses of few micrometer, which are expected to have a very high surface area whereas on the other hand, the PTS materials are present in powder form with particle diameters of few millimeters. All water uptake measurements in this thesis were conducted in a way that at least one hour was set for equilibrating (so that the water uptake reaches its equilibrium state) after a new atmospheric condition was set. The lower water uptake for the PTS materials can therefore not be explained by the fact that the equilibration time was not sufficiently high enough and the absorbed water could not reach the inner parts of the PTS particles, but rather by the fact that due to the particle form of the PTS materials some hydrophilic moieties are isolated and can not take up water. In addition to that, a second factor are the temperature conditions of the TGA measurements. After conducting all measurements, it was found out that the temperature which was thought to be set at 25°C in all measurements amounted actually to roughly 28°C. Therefore, since the water uptake was observed to decrease with increasing temperature, the actual water uptake at 25°C is estimated to be higher.

Since all conductivity and UV/Vis absorption measurements were conducted with the polymer materials in film form, a QCM was established during the PhD thesis to determine the water uptake of the polymer materials in film form. The QCM results are discussed in the following section.

4.2.2 Quartz Crystal Microbalance

In sections 4.2.2.1, the general measurement procedure and the applicability and limits of the technique are discussed. After that, the results for the PTS and PEDOT:PSS materials are discussed in sections 4.2.2.2 and 4.2.2.3. A summary of the results, a comparison to the TGA results and the discussion in respect to the materials characterization of PTS and PEDOT:PSS is given in section 4.2.3. All QCM measurements were conducted if not otherwise mentioned at 25°C as function of $p\text{H}_2\text{O}$.

4.2.2.1 General discussions

General measurement procedure

In figure 4.19, the frequency and the calculated weight trend (for details about the calculation see section 3.3.5) of a polymer coated QCM crystal in a typical QCM measurement including the initialization step and the reversibility check, here in the case of a PEDOT:PSS (1:2.5) film, is shown.

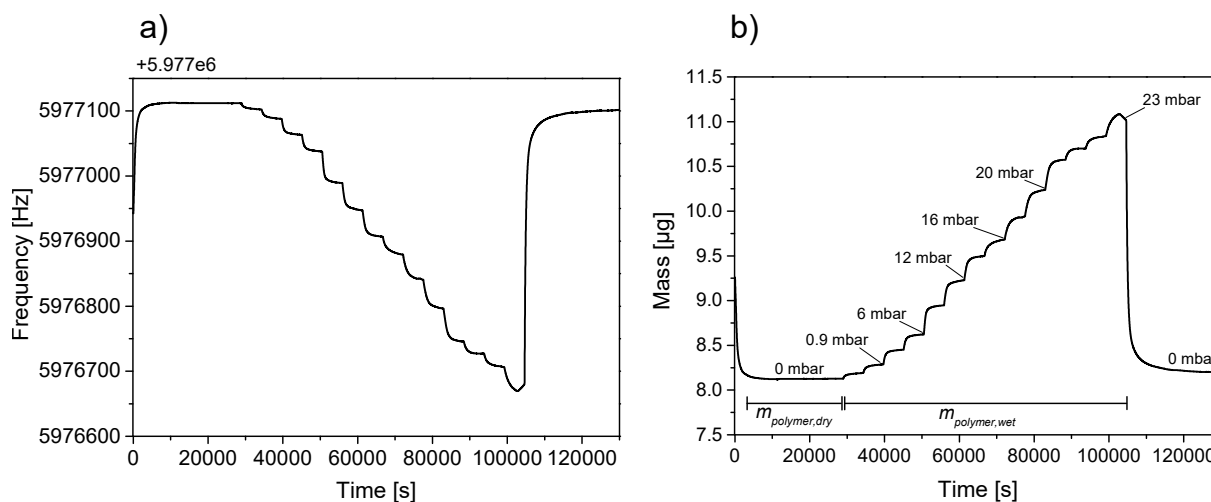


Figure 4.19: a) Frequency and b) weight trend during a typical QCM measurement.

As can be seen, increasing $p\text{H}_2\text{O}$ leads to a decrease of the frequency (4.19 a) and a concurrent increase of the crystal mass (4.19 b). The contrary trend can be explained with the fact that upon water uptake, the oscillation frequency decreases since the polymer film mass is increasing. At the start of the QCM measurement, the initial mass amounts to 9.25 μg . Before spin coating the polymer film onto the QCM crystal, the crystal is installed in the measurement cell and the resonance frequency of the empty crystal is measured and the depicted mass, which is an arbitrary number, is set to $m_0 = 0 \mu\text{g}$. The initial mass corresponds therefore to the mass of the polymer film (since the empty crystal was set to $m_0 = 0 \mu\text{g}$) with water still remaining in the polymer film after spin coating. During the initialization step of the QCM measurement, a dry N_2 stream is lead

through the measurement chamber and the chamber is heated up to 45°C for a short time. As consequence, all water remaining in the polymer film after spin coating is evaporated from the polymer film. The weight of the polymer film decreases therefore during the initialization and the polymer film weight in its dry state $m_{\text{polymer,dry}}$ is obtained, in the shown weight trend $m_{\text{polymer,dry}} = 8.2 \mu\text{g}$. After the initialization, the temperature of the measurement chamber is set to 25°C and the $p\text{H}_2\text{O}$ is step-wise increased, applying equilibration times of 90 minutes. As can be seen in the weight trend, the stepwise increase of $p\text{H}_2\text{O}$ leads to a stepwise increase of the QCM mass. Since the indicated mass corresponds to the polymer film with water taken up, the mass is referred to as $m_{\text{polymer,wet}}$. Due to the fact that after setting a new $p\text{H}_2\text{O}$, which results initially in a strong increase of $m_{\text{polymer,wet}}$, the value for $m_{\text{polymer,wet}}$ does not further change after longer waiting times, it can be said that an equilibration time of 90 minutes is sufficient. At 23 mbar H_2O , the QCM mass is decreasing after the initial increase, even though $p\text{H}_2\text{O}$ was kept constant. This effect is in the depicted mass trend only observed at this high $p\text{H}_2\text{O}$ and was also observed in further QCM measurements in this thesis at 23 mbar H_2O and higher $p\text{H}_2\text{O}$. For a discussion about the validity of the Sauerbrey equation at high $p\text{H}_2\text{O}$ see the discussion about the applicability and validity in section 4.2.2.1. After reaching the highest $p\text{H}_2\text{O}$ which is in the shown measurement 23 mbar H_2O , dry N_2 (0 mbar H_2O) is applied. Due to the fact that the QCM mass decreases back to the same value which was reached at 0 mbar H_2O at the initial drying step, it can be said that the water uptake is reversible. With the $m_{\text{polymer,wet}}$ values at each $p\text{H}_2\text{O}$ and with the help of equations 16 and 17 in the methods part 3.3.4, the water uptake in water content per mass polymer film (in wt%) and as number of water molecules per repeating unit (in λ) can be calculated. The water uptake results for the PTS and PEDOT:PSS materials can be found in sections 4.2.2.2 and 4.2.2.3. In the following section, the applicability and validity of the QCM technique is discussed.

Applicability and validity

As could be seen in the QCM mass trend of the water uptake measurement of PEDOT:PSS (1:2.2) (figure 4.19) at the $p\text{H}_2\text{O}$ step of 23 mbar H_2O before switching back to 0 mbar H_2O , a drop of $m_{\text{polymer,wet}}$ during the time of constant $p\text{H}_2\text{O}$ can be observed. This effect occurred only at high $p\text{H}_2\text{O}$ and was observed in several QCM measurements conducted in this thesis. The mass trend drop during the time of constant $p\text{H}_2\text{O}$ is likely to correspond to the fact that the validity of the Sauerbrey equation is not fulfilled anymore. Developed in 1959, in the first years the QCM technique was mainly used for precise determining of thicknesses of metal layers deposited on the QCM crystals [175]. The maximum thickness of a deposited aluminium layer up to which the Sauerbrey equation is still valid was determined to 300 kÅ and the maximum frequency change between the bare crystal and the metal covered crystal was determined to 15 %

[208, 209]. The film thicknesses of the studies in this thesis, as calculated from the weight of the polymer film $m_{\text{polymer,wet}}$ in the QCM measurements, are usually below 1 kÅ (except for the drop casted PEDOT:PSS films, see section 4.2.2.3) and the frequency change between the blank QCM crystal and the polymer film with high water uptake amounts at maximum to $0.05 \approx \%$, which would indicate that the validity of the Sauerbrey equation can presumably still be assumed, which was also assumed in other water uptake measurements of polymeric thin film materials with QCM [210]. However, the materials in this thesis are soft polymeric materials whereas the above mentioned limitations of QCM were examined in case of rigid and stiff metal coatings.

When a viscoelastic material is brought into oscillation, the oscillation is damped due a dissipation of energy. A measure of the dissipated energy is the dissipation factor D . QCM measurements can be conducted with an in-situ monitoring of this dissipation factor, the technique is therefore called QCM-D [211]. Typically, QCM-D is utilized in measuring the dissipation in solutions. The water uptake of polyelectrolyte films in liquid water was shown to exhibit significant dissipation, whereas only minor dissipation was observed in case of water uptake from humid atmosphere, therefore the validity of the Sauerbrey equation is not influenced [176]. Vogt et al. examined the dissipation of polyelectrolyte films with varying film thicknesses at different humidities [212]. They observed viscoelastic behavior for polyelectrolyte films with film thicknesses of more than 900 Å and water uptakes of more than 100 wt%. At these conditions, the Sauerbrey equation was found to be not valid anymore. As already mentioned, the film thicknesses for most of the polymer films in this thesis are below 1 kÅ and the maximum water uptakes on the other hand amounted to $\approx 90 \%$. Therefore, the validity of the Sauerbrey equation in the present study is assumed, even though deviations from the Sauerbrey equation at high water uptakes might still be existent, which could be seen by the previously described deviations at high $p\text{H}_2\text{O}$.

A further issue which was observed in the measurements was the change of the resonance frequency of a QCM crystal upon removing the crystal from the sensor and reinstalling the same crystal in the sensor again. This effect was also observed in literature before [176]. The frequency change upon inserting and reinserting of the crystal amounts to ≈ 10 ppm (parts per million, so $10^{-4}\%$). A possible explanation for this effect might be different orientations or rotational positions of the crystal in the sensor head. Since the frequency changes between the dry polymer film $m_{\text{polymer,dry}}$ and the wet polymer film $m_{\text{polymer,wet}}$ were typically between 150 and 300 ppm and the deviations between water uptake measurements of identically prepared films were observed to be significantly higher than 10 ppm, this inserting and reinserting error was not further elucidated. In the QCM experiments in this thesis it could also be observed that crystals, which theoretically should be manufactured equally, showed deviations of the resonance frequency

up to 1000 ppm. This underlines the necessity to determine the resonance frequency of each individual crystal.

A third consideration is the temperature in the measurement cell, at which the QCM measurements are conducted. As described in section 4.2.1, the TGA measurements were conducted at temperatures of up to 90°C. QCM crystals are piezoelectric quartz crystals, which are cut in the so-called AT-Cut from the seed crystal. In the AT-Cut, the crystal disk is cut out in an angle of 35°15' with respect to the optical z-axis from the seed crystal [174]. At this specific angle, the temperature coefficient of the resonance frequency shows an inflection point at 25°C, which means that QCM measurements can be conducted in the range of room temperatures at 25°C±15°C without relevant change of the resonance frequency. Outside this range, small temperature changes of only 1°C (which might occur due to fact that the oven utilized for controlling the temperature in the atmospheric conditions setup could only heat and not cool the measurement cell) could lead to changes of the resonance frequency which are higher than the frequency change due to water uptake. Due to this, QCM measurements were conducted at only 25°C and not conducted in a temperature range up to 90°C as for the TGA measurements. For PTS-Na, one QCM measurement was conducted at 25°C and one at 35°C (see figure 4.21). The observed slight frequency instability at 35°C can be explained by the temperature fluctuations resulting from the aforementioned shift of the resonance frequency.

Reliability and reproducibility test

Due to the fact that the QCM was newly set up in a laboratory as a method to determine the water uptake of polymer materials in thin films, several test measurements were conducted initially to confirm the reliability and reproducibility of the QCM technique and measurement procedure.

In order to test the functionality of the QCM sensor, a fresh QCM crystal was installed in the sensor and according to the *STM-2* manual, as a test it was breathed heavily onto the crystal [213]. The indicated mass increased, which is due to adsorbed water originating from the exhaled air. Since the increase was in the indicated range, the functionality of the sensor utilized for this thesis was confirmed.

In order to examine the water uptake behavior of a pure polyelectrolyte material, the water uptake of poly(sodium 4-styrenesulfonate) (PSS-Na) at 25°C as function of water partial pressure was measured (figure A.11). The water uptake trend is similar to the PTS and PEDOT:PSS materials in this thesis (which will be discussed in sections 4.2.2.2 and 4.2.2.3), therefore the polyelectrolyte behavior of both material classes can be confirmed. Comparing QCM measurements of PTS-TBA and PTS-Na, it could be observed

that PTS-Na shows significantly higher water uptakes per weight (water content in wt%), but comparable water uptakes per repeating unit (in λ). The same trend was observed in the TGA measurements, therefore the QCM measurements can be regarded as reliable. Several QCM measurements were repeated with new, identically prepared films in order to examine the reproducibility of the measurements. It could be observed that the general trends could be reproduced well (for example that the chemically doped PTS-Na films showed lower water uptakes than the pristine PTS-Na films (section 4.2.2.2), or the pristine film weights of films from PEDOT:PSS materials showed significant deviations depending on the utilized PEDOT:PSS dispersion (section 4.2.3)). The deviation between the measurements was determined to be as high as 20% at 29 mbar H_2O (see figure 4.24), in the water partial pressure range up to 20 mbar H_2O the deviation was typically below 5%. This might be explained by slight deviations in the temperature or water partial pressure in the measurement cell or different polymer film morphologies or film surfaces resulting from the general issues of irreproducibility in the spin coating procedure.

In the following, the water uptake results for the PTS and PEDOT:PSS materials in various $p\text{H}_2\text{O}$ ranges are given. For some measurements, the results were validated by conducting identical measurements and calculating the average water uptake values. For all QCM measurements in this thesis, the dry polymer film masses $m_{\text{polymer,dry}}$ was determined (in case several identical measurements were conducted the average $m_{\text{polymer,dry}}$ values are given). The values will be given and discussed in table 4.3 in the summary section 4.2.3.

4.2.2.2 PTS materials

As PTS materials, pristine PTS-Na and PTS-TBA films and chemically doped PTS-Na and PTS-TBA films were examined.

PTS-Na

In figure 4.20, the water uptake of PTS-Na at 25°C as function of $p\text{H}_2\text{O}$ can be seen. For determining the water uptake, measurements over 5 films were averaged. As for all QCM measurements shown in this thesis, the averaged values are given together with the standard deviation (indicated by error bars).

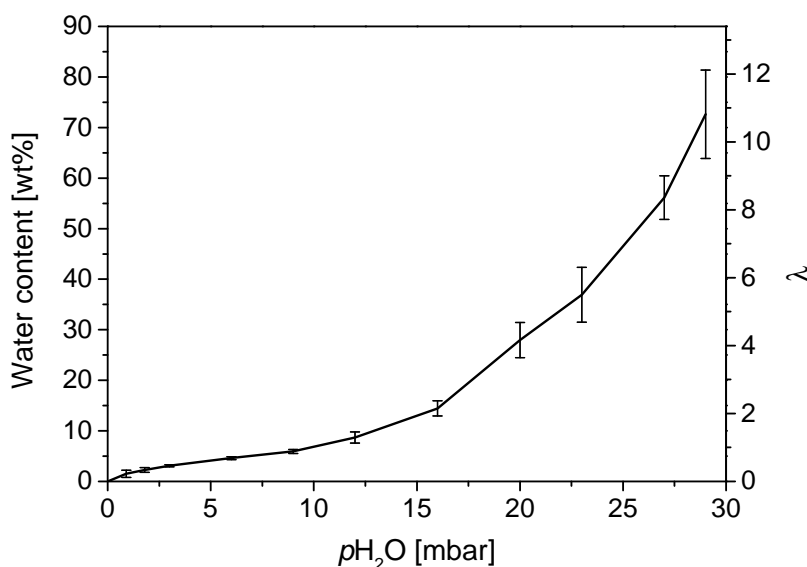


Figure 4.20: Water uptake of PTS-Na at 25°C as function of water partial pressure.

Regarding the trend of the water uptake as function of $p_{\text{H}_2\text{O}}$, it can be seen that after a step increase up to 1.8 mbar H_2O , the water uptake increases moderately with $p_{\text{H}_2\text{O}}$. The steep increase at very low H_2O was seen in the TGA measurements of PEDOT:PSS in section 4.2.1.2 and in further QCM measurements. Upon increase of $p_{\text{H}_2\text{O}}$ to higher values than 16 mbar H_2O , the slope of the water uptake increase is getting steeper. The trends in the water uptake of PTS-Na were also observed for PSS-Na as shown in figure A.11, which confirms the polyelectrolyte properties of PTS-Na. The trends of the water uptake for all PTS and PEDOT:PSS materials is discussed in section 4.2.3.

Comparing the water uptake at 20 mbar H_2O determined with QCM with the water uptakes determined with TGA (figure 4.17), it can be seen that the values determined with QCM (≈ 30 wt% or $\lambda \approx 4$) are around three to four times higher than the values determined with TGA (≈ 8 wt% or $\lambda \approx 1.2$). This significant difference can be explained with the fact that in case of the QCM measurements, the polymer material is characterized in form of thin films, whereas in the TGA measurements the polymer material is characterized in powder form. The thin films seem to be therefore much more accessible for water.

PTS-Na temperature test

In figure 4.21, the water uptake of a pristine PTS-Na film at 25°C and 35°C as function of water partial pressure is shown. The frequency trend of the measurement at 25°C and 35°C can be seen in figure A.12.

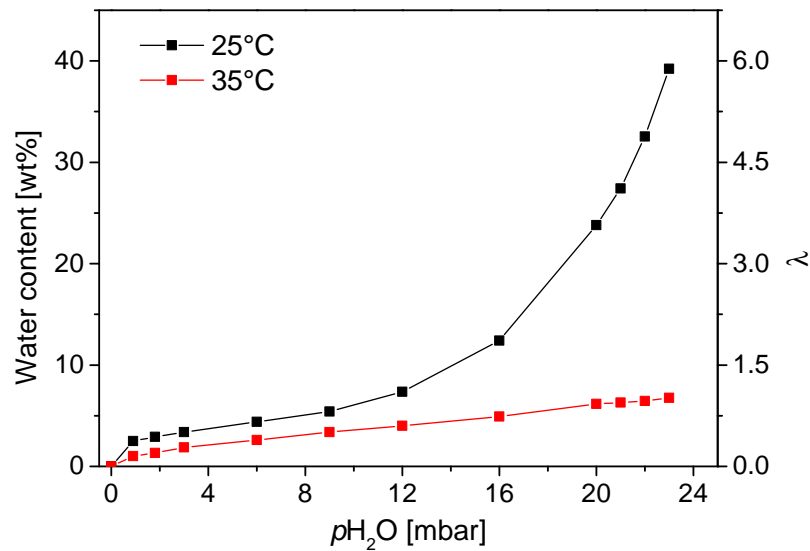


Figure 4.21: Water uptake of PTS-Na at 25°C (black symbols) and 35°C (red symbols).

According to the supplier specifications of the QCM crystals, QCM measurements can be conducted at $25 \pm 15^\circ\text{C}$, so measurements at temperatures 35°C of should be possible [213]. The larger the difference of the measurement temperature to 25°C is, the more noisy the resonance frequency signal of the QCM crystal is (see also the previous discussion about the QCM technique in section 4.2.2.1). As can be seen in the frequency trend in figure A.12, the frequency change at 35°C with $p_{\text{H}_2\text{O}}$ variation is smaller than the frequency changes at 25°C. Therefore, the error in extracting the frequency and therefore also the error in the value for $m_{\text{polymer,wet}}$ gets larger. Due to this, the water uptake values at 35°C might be partially incorrect. Regarding the trend of the water uptake at 25°C, it can be seen that the water uptake shows a strong increase at very low $p_{\text{H}_2\text{O}}$, a moderate increase at up to 12 mbar H_2O and a steeper increase towards the highest $p_{\text{H}_2\text{O}}$ and therefore the same trends as the averaged water uptakes of PTS-Na in figure 4.20. At 35°C (red symbols), the water uptake values decrease with ≈ 7 wt% at 23 mbar H_2O to less than a fifth compared to the water uptake of ≈ 40 wt% at 25°C and 23 mbar H_2O . The decrease of the water uptake with increasing temperature is therefore significantly higher than in the TGA measurements of PTS-Na (figure 4.17), where the water uptake at a temperature of 45°C was the half of the water uptake at 25°C. As discussed in section 4.2.1.2, due to the powder form of the PTS material placed in the TGA measurement chamber, hydrophilic moieties might not be accessible for water. When switching from 25°C to 35°C in case of the PTS-Na film in QCM measurements as shown in figure 4.21, the water uptake values might therefore decrease significantly.

PTS-TBA

In order to compare PTS-Na and PTS-TBA, the water uptake of a PTS-TBA film was determined with QCM in the water partial pressure range from 0 – 23 mbar H_2O . In figure 4.22, the water uptake of PTS-TBA at 25°C as function of $p\text{H}_2\text{O}$ is shown.

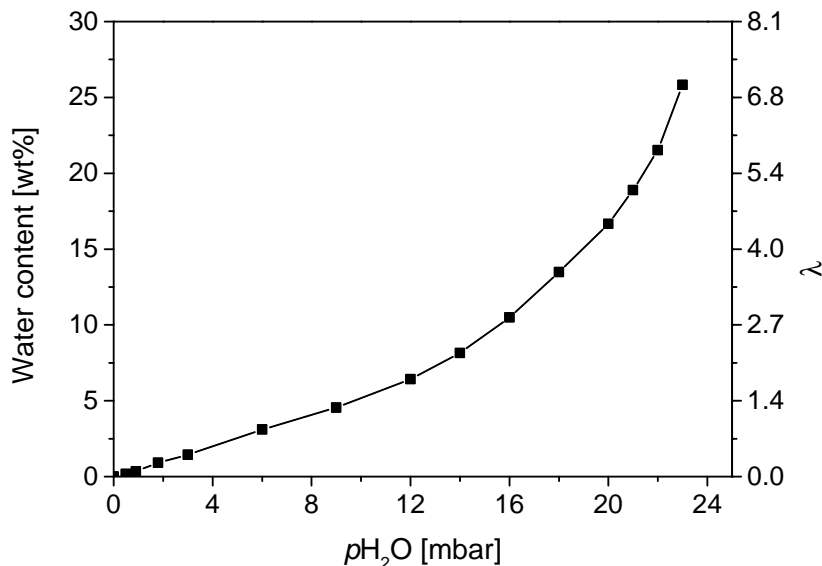


Figure 4.22: Water uptake of PTS-TBA at 25°C as function of water partial pressure.

Comparing the water uptake of PTS-TBA with the water uptake of PTS-Na (figure 4.20), it can be seen that PTS-TBA shows a water content of around 25% at 23 mbar H_2O , whereas PTS-Na shows a water content of ≈ 37 wt% at 23 mbar H_2O . The water uptake per repeating unit amounts to $\lambda \approx 7$ for PTS-TBA and $\lambda \approx 6$ for PTS-Na. Therefore, it can be said that very comparable trends could be obtained in the water uptake measurements of PTS-TBA and PTS-Na with QCM as for the water uptake measurements of PTS-TBA and PTS-Na with TGA: at 20 mbar H_2O the water uptake per mass (in wt%) is significantly higher for PTS-Na (≈ 8 wt% for PTS-Na and ≈ 5 wt% for PTS-TBA), the water uptake per repeating unit is however comparable ($\lambda \approx 1.2$ for PTS-Na and $\lambda \approx 1.4$ for PTS-TBA). Therefore, the same differences in the water uptake behavior between PTS-TBA and PTS-Na are obtained with both techniques, which again confirms the reliability of the QCM technique.

Chemically doped PTS

In addition to the pristine PTS-Na and PTS-TBA films, the water uptake of chemically doped PTS films is determined. Chemical doping is utilized in this thesis to increase the electronic conductivity of PTS films (see section 4.3.1). In figure 4.23, the water uptake of

chemically doped PTS-Na and chemically doped PTS-TBA at 25°C as function of $p_{\text{H}_2\text{O}}$ is shown. For both PTS materials, the water uptake was averaged by measuring the water uptake of two films.

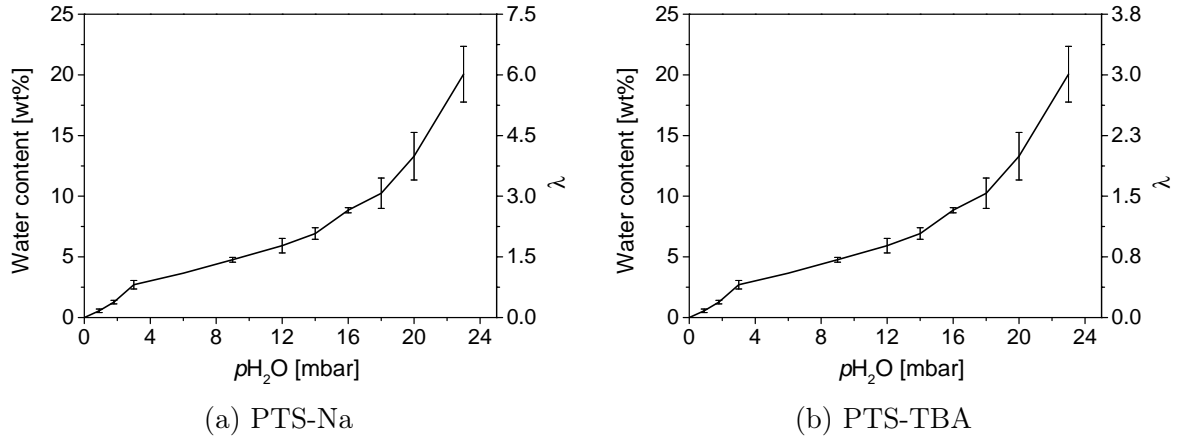


Figure 4.23: Water uptake of PTS after chemically doping with 0.5 mg/ml $\text{F}_4\text{TCNQ/THF}$ at 25°C as function of water partial pressure.

As can be seen from the standard deviation of the water uptake measurements of the chemically doped PTS films, the measurements were not very reproducible, as discussed for UV/Vis measurements of chemically doped PTS films in section 4.1.1.2) and as also observed for AC Impedance and DC measurements of chemically doped PTS films (see section 4.3.1). Due to the different content of polythiophene in PTS-Na and PTS-TBA as discussed in section 3.3.4, the degree up to which the PTS films are doped might vary in PTS-Na and PTS-TBA. This might also lead to different water uptakes of PTS-Na and PTS-TBA. In general, the water uptakes of the chemically doped PTS films show lower water uptakes than the pristine PTS films. This might be explained by the fact that hydrophilic moieties might be shielded due to the chemical doping. Eventually, F_4TCNQ molecules or F_4TCNQ^- radical anions are not only located in the polymer film, but also to a large extent on top of the polymer film. Therefore, the water uptake into hydrophilic moieties in the PTS film might be inhibited. Nevertheless, a time-delayed water uptake due to inhibition of the water uptake can be excluded, since for every $p_{\text{H}_2\text{O}}$ step a reaching of the plateau value of $m_{\text{polymer,wet}}$ was obtained.

4.2.2.3 PEDOT:PSS materials

In the following section, the water uptake of PEDOT:PSS materials determined with QCM are discussed. At first, the Na-exchanged PEDOT:PSS-Na (1:6) is examined in which, similar to PTS-Na, Na^+ counterions are predominantly present (see also 3.1.2). After that, the pristine PEDOT:PSS (1:6) and the high PEDOT content PEDOT:PSS (1:2.2), both mainly with H^+ counterions, are examined. The section is finalized with water uptake studies of drop casted PEDOT:PSS films.

PEDOT:PSS-Na (1:6)

In figure 4.24, the water uptake of PEDOT:PSS-Na (1:6) at 25°C as function of water partial pressure is shown. The water uptake of PEDOT:PSS-Na (1:6) was obtained by averaging over three films.

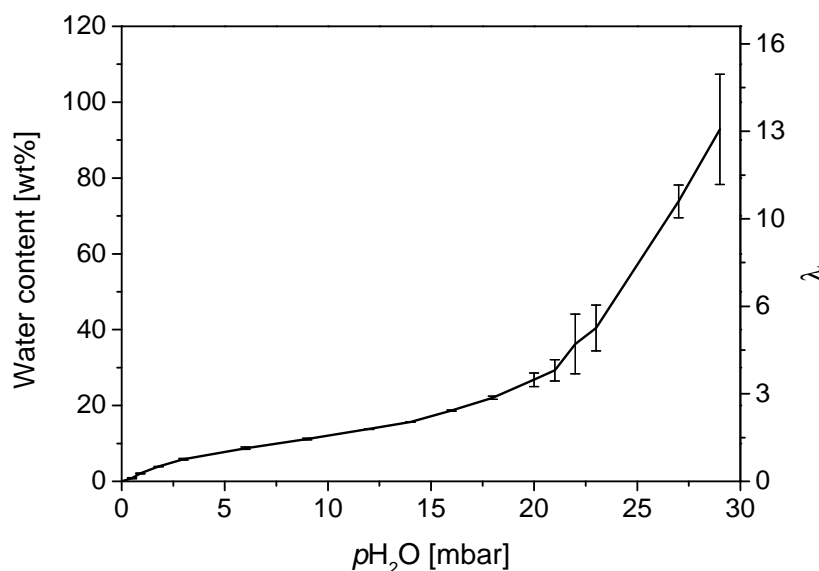


Figure 4.24: Water uptake of PEDOT:PSS-Na (1:6) at 25°C as function of water partial pressure.

The water uptake of PEDOT:PSS-Na (1:6) shows the same trends as the PTS materials and PSS-Na (figure A.11), therefore the polyelectrolyte properties of PEDOT:PSS can be confirmed. In comparison with the water uptake of PTS-Na, which was also determined by averaging over several measurements and which was also conducted up to 29 mbar H_2O , the trend of elevated increase of the water uptake at low $p_{\text{H}_2\text{O}}$, moderate increase at medium $p_{\text{H}_2\text{O}}$ and a steeper increase at high $p_{\text{H}_2\text{O}}$ can be identified even more clearly. The water uptake at 29 mbar H_2O is with ≈ 90 wt% or $\lambda \approx 13$ even higher than the value for PTS-Na at 29 mbar H_2O (≈ 70 wt% or $\lambda \approx 11$), even though the error at 29 mbar is quite high. The significant error at high $p_{\text{H}_2\text{O}}$ might be explained

by deviations of the Sauerbrey assumption at high $p_{\text{H}_2\text{O}}$ as discussed in section 4.2.2.1. At 20 mbar H_2O , the water uptake of PEDOT:PSS-Na (1:6) amounts to ≈ 25 wt% or $\lambda \approx 3.5$, whereas the water uptake of PTS-Na amounts to ≈ 30 wt% or $\lambda \approx 4$. At this medium $p_{\text{H}_2\text{O}}$, where no errors due to deviations from the validity of the Sauerbrey equation are expected, the similar water uptakes might be explained by the fact that for both materials Na^+ is present as counterion.

PEDOT:PSS (1:6)

In figure 4.25, the water content of PEDOT:PSS (1:6) at 25°C as function of water partial pressure can be seen. The water uptake of PEDOT:PSS (1:6) was obtained by averaging over two films.

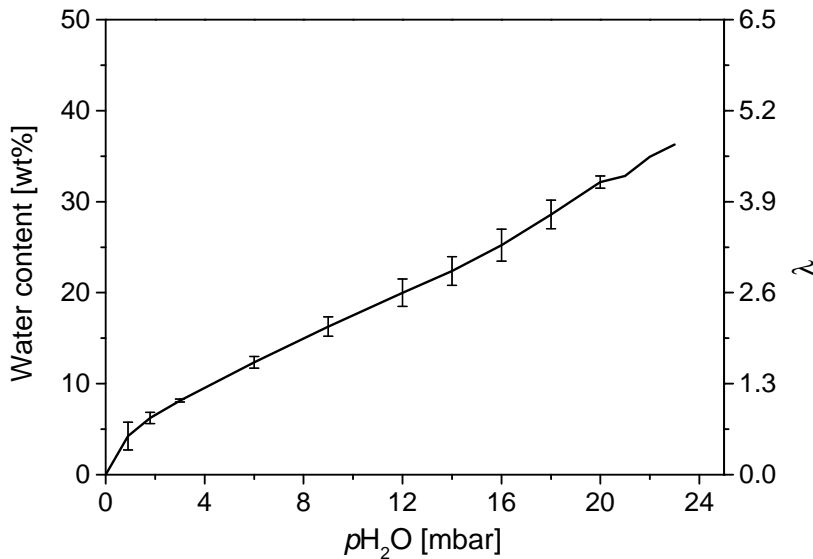


Figure 4.25: Water uptake of PEDOT:PSS (1:6) at 25°C as function of water partial pressure.

Regarding the trend of the water uptake as function of $p_{\text{H}_2\text{O}}$, the previously described steep increase at low $p_{\text{H}_2\text{O}}$ values can be recognized. The steeper increase of the water uptake, which could be observed in the previously shown water uptake trends and which was observed to start at $p_{\text{H}_2\text{O}}$ values of 16 or 20 mbar H_2O can not be recognized. If the water uptakes of PEDOT:PSS (1:6) would have been determined up to higher $p_{\text{H}_2\text{O}}$ than 23 mbar H_2O , a steeper increase of the water content might have been obtained eventually. Comparing the water uptakes of PEDOT:PSS (1:6) to the water uptakes of PEDOT:PSS-Na (1:6), it can be seen that the water contents are very comparable. At 20 mbar H_2O , PEDOT:PSS-Na (1:6) takes up ≈ 27 wt% H_2O and PEDOT:PSS (1:6) takes up ≈ 32 wt% H_2O . Also the λ values are with $\lambda \approx 4$ comparable. The reason for

the very similar water uptake values is that the same material is examined, the different counterion or the dilution of the PEDOT:PSS dispersion seems not to make a significant difference.

PEDOT:PSS (1:2.2)

In addition to the low PEDOT content PEDOT:PSS batches, the water uptake of high PEDOT content PEDOT:PSS materials were investigated as well. The here studied PEDOT:PSS (1:2.2) materials shows significantly higher electronic conductivities than the PEDOT:PSS (1:6) materials (see section 4.3.2). In figure 4.26, the water uptake of PEDOT:PSS (1:2.2) at 25°C as function of water partial pressure is shown. The water uptake of PEDOT:PSS-Na (1:2.2) was obtained by averaging over two films.

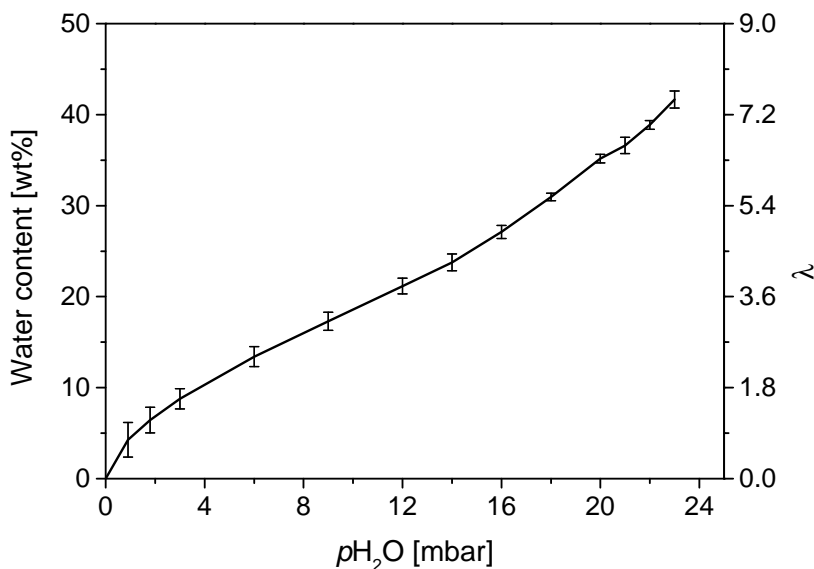


Figure 4.26: Water uptake of PEDOT:PSS (1:2.2) at 25°C as function of water partial pressure.

The water uptake of PEDOT:PSS (1:2.2) shows a similar water uptake trend as the previously discussed PEDOT:PSS batches. Regarding the water uptake values, PEDOT:PSS (1:2.2) shows at 23 mbar H_2O a water uptake per mass of ≈ 40 wt% and $\lambda \approx 7.5$ whereas both PEDOT:PSS (1:6) and PEDOT:PSS-Na (1:6) show at 23 mbar H_2O water uptakes of 35 – 40 wt% and $\lambda \approx 4 - 5$. Both the water uptake per mass and in λ is therefore slightly higher compared to the PEDOT:PSS-Na (1:6) and PEDOT:PSS (1:6) batches, which is rather unexpected due to the lower PEDOT content in PEDOT:PSS (1:2.2). As described in section 3.3.4, the PSS weight content which is expected to participate in water uptake amounts to 55 wt% in the PEDOT:PSS (1:2.2) batch, to 59 wt% in the other high PEDOT content batch PEDOT:PSS (1:2.5) (which was examined with

spectroelectrochemistry and in-situ conductance measurements in section 4.1.2.1) and to 80 – 81 wt% in the PEDOT:PSS (1:6) and PEDOT:PSS-Na (1:6) batches. Conversely, the PEDOT contents in the high PEDOT content batches PEDOT:PSS (1:2.2) and PEDOT:PSS (1:2.5) amount to 29 – 31 wt% and in the low PEDOT content batches PEDOT:PSS (1:6) and PEDOT:PSS-Na (1:6) to 13 – 14 wt%. The PSS content which is expected to participate in water uptake in the 1.2.2 batch is therefore lower than in the 1:6 batches, the content of hydrophilic moieties is accordingly also lower. Therefore also the water uptake of the PEDOT:PSS (1:2.2) batch should be lower. Considering a standard deviation between identically conducted QCM measurement of approximately 10 – 20% (for example at the values of the water uptake of PEDOT:PSS-Na (1:6) at 23 mbar H₂O in figure 4.24), this deviation is lower than the 40% lower PSS contents in the (1:2.2) batch compared to the (1:6) batches, therefore there might be other reasons than the standard deviation or error between identically conducted measurements for the higher water uptake of the PEDOT:PSS (1:2.2) batch. The morphology of the PEDOT:PSS (1:2.2) batch might also be different due to the higher PEDOT content, eventually larger PEDOT rich moieties might be present due to the higher PEDOT:PSS ratio. Additionally the synthesis procedure might influence the PEDOT:PSS dispersion and therefore also the morphology of the PEDOT:PSS films resulting from this dispersion. Furthermore the PDI or the molecular weight of PSS-H is also not known (typically in the range of $M_W \approx 75.000$ g/mol, [214]).

Drop casted PEDOT:PSS

In order to examine if the water uptake is mostly occurring on the surface or as expected in the volume of the polymeric material, two PEDOT:PSS films were prepared by drop casting 40 μ l PEDOT:PSS dispersion onto the quartz crystal, which was followed by drying at 75°C. The film weights of the drop casted films were approximately two orders of magnitude higher than the film weights of the spin coated films (see also section 4.2.3 for further discussion). In figure 4.27, the water uptake of a drop casted PEDOT:PSS (1:2.2) film and a drop casted PEDOT:PSS (1:6) film at 25°C as function of water partial pressure can be seen. Since significant deviations from the step-like decrease of the QCM frequency were obtained at $p_{H_2O} > 20$ mbar H₂O (as shown in figure 4.19), which might be explained by significant viscoelastic damping (as discussed in section 4.2.2.1), the measurements were only evaluated up to 20 mbar H₂O. Strong increase of the water uptake would have been obtained probably as observed in the previously shown QCM measurements that were measured up to 29 mbar H₂O.

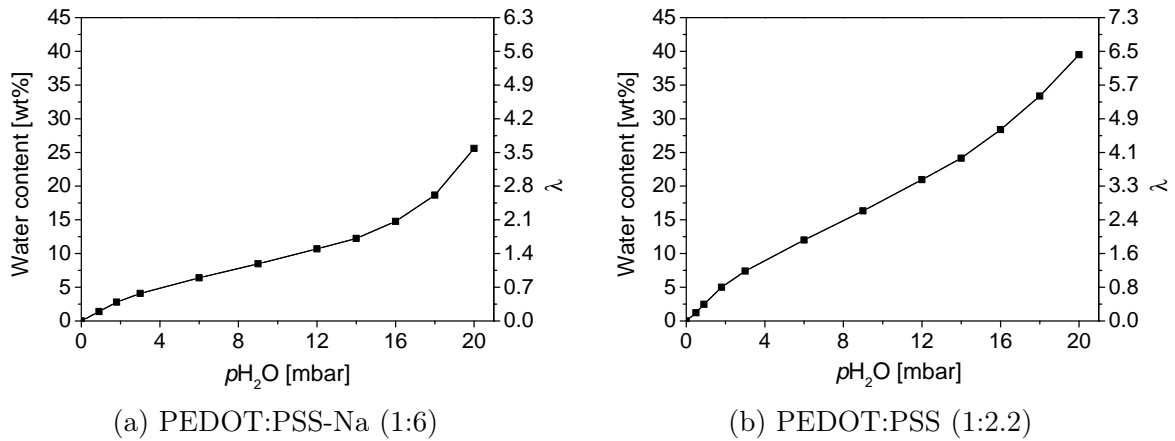


Figure 4.27: Water uptake of drop casted PEDOT:PSS at 25°C as function of water partial pressure.

Regarding the trend of the water uptake as function of $p_{\text{H}_2\text{O}}$, the previously described trend can be observed as well, so a steep increase at low $p_{\text{H}_2\text{O}}$, moderate increase at medium $p_{\text{H}_2\text{O}}$ and a steeper increase towards higher $p_{\text{H}_2\text{O}}$. In spite of the significantly higher polymer film mass and presumably also different morphology, which is due to the casting procedure, the PEDOT:PSS materials still show the typical polyelectrolyte behavior. Considering the level of the water uptake, the drop casted PEDOT:PSS-Na (1:6) films shows a water content of ≈ 25 wt% and $\lambda \approx 3.5$ at 20 mbar H_2O . The spin coated PEDOT:PSS-Na (1:6) films (as shown in figure 4.24) reveal with ≈ 27 wt% and $\lambda \approx 3.7$ almost identical water uptake values. For the drop casted PEDOT:PSS (1:2.2) film, a water content of 39 wt% and $\lambda \approx 6$ at 20 mbar H_2O is obtained. The values obtained for the spin coated PEDOT:PSS (1:2.2) films (as shown in figure 4.26) are with ≈ 35 wt% and $\lambda \approx 5$ slightly lower. In general, for the drop casted PEDOT:PSS films very comparable water uptake trends and values were obtained as for the spin coated PEDOT:PSS films, therefore it could be assumed that water uptake occurs also for the spin coated films mainly in the volume and not only on the surface of the polymer films.

4.2.3 Discussion and summary of water uptake studies

Summing up the previous section concerning the water uptake studies of PTS and PEDOT:PSS materials utilizing TGA or QCM, in case of the preliminary TGA measurements very low water uptake values for the PTS materials and higher values for PEDOT:PSS materials were obtained. The lower water uptake might be explained by the fact that the PTS materials are present in powder form which might limit the accessibility for water. Conversely, in the QCM measurements in general higher water uptakes than in the TGA measurements were obtained, which might be due to the fact that the polymer materials are measured as thin films, which seems to facilitate the water uptake. In both the TGA and the QCM measurements, PTS-Na shows significantly higher water uptake per mass than PTS-TBA due to the higher ion content, but comparable water uptake per repeating unit. This might be due to the fact that the water uptake is less governed by the ion character of the cation but rather by the hydrophilicity of the sulfonate group, which is the same in both PTS-TBA and PTS-Na. In the QCM measurements of PEDOT:PSS, the PEDOT:PSS (1:6) materials showed unexpectedly lower water uptake values compared to PEDOT:PSS (1:2.2), which might eventually be explained by a different synthesis procedure or by different film morphologies.

For measurements of PTS-Na and PEDOT:PSS-Na (1:6) that were conducted in a water partial pressure range from 0 to 29 mbar H_2O (which corresponds to a relative humidity range between 0 and 92 % r.h.) and that were averaged over several measurements, a typical water uptake trend could be identified: after a steep increase up to water contents of 5 – 10 wt% at ≈ 3 mbar H_2O , the water content increased moderately to water contents of 15 – 20 wt% at ≈ 16 mbar H_2O . Going to higher water partial pressures, the water uptake values increase significantly up to values of 70 – 90 wt% at 29 mbar H_2O . The same water uptake trend (determined in polymer film mass) as function of water partial pressure was also observed for PEDOT:PSS (1:2.5) films in QCM measurements [4] and for Nafion materials [3], the validity of the water uptake trends can therefore be confirmed. Interestingly, the water uptake trend resembles type II sorption isotherms, which implies that the water uptake occurs on internal interfaces, presumably the interfaces between hydrophilic moieties where the sulfonate groups are located and the more hydrophobic PEDOT moieties [215]. Water uptake as function of water partial pressure solely at the surface of the polymer film can be excluded due to the fact that the water uptake of drop casted polymer films (which are approximately two orders of magnitude thicker than the spin coated films, see table 4.3) is very similar to the water uptake of spin coated films and that the conductivity and UV/Vis absorption properties vary significantly as function of water partial pressure (which correspond to a variation of the properties of the bulk polymer films). For various polyelectrolyte materials, in a recent publication very comparable water uptakes as for the polyelectrolyte materials in this thesis were obtained, the

reliability of the QCM measurements can be therefore further confirmed [54].

The moderate increase of the water content at low and medium $p\text{H}_2\text{O}$ and the steeper increase at high $p\text{H}_2\text{O}$ was also observed for water uptake measurements of PEDOT:PSS using volumetric sorption measurements [5]. In the QCM measurements in this thesis at 27 mbar H_2O , PEDOT:PSS shows a water uptake of 87 wt%, which is very comparable to the values obtained for PEDOT:PSS-Na (1:6). As could be obtained in [5], the sorption enthalpy decreases from $Q_{ST} = 55$ kJ/mol at very low water contents to $Q_{ST} = 44$ kJ/mol at high water contents, which corresponds to an approaching of the sorption enthalpy of pure water. This observation can be explained with sorption into very hydrophilic, undissociated sulfonate-cation moieties at low water contents and sorption into practically pure water at high water contents. Therefore, the formation of water-rich moieties at high water contents can be proven.

In table 4.3, the dry polymer film masses of all QCM measurements are listed. For all measurements which were repeated identically, an averaged value including standard deviation is indicated.

Table 4.3: Dry polymer film masses.

Material	$m_{\text{polymer,dry}}$ [μg]
PTS-Na	2.6 ± 0.3
PTS-TBA	2.6
PTS-TBA, PTS-Na chemically doped	3 – 4
PEDOT:PSS (1:6)	3.7 ± 0.5
PEDOT:PSS-Na (1:6)	2.13 ± 0.01
PEDOT:PSS (1:2.5)	8.2
PEDOT:PSS (1:2.2)	15 ± 1
PEDOT:PSS-Na (1:6) drop casted	208.5
PEDOT:PSS (1:2.2) drop casted	228.0

Both the pristine PTS-TBA and PTS-Na films reveal dry polymer film masses of 2.6 μg . This might be explained by the same concentrations of both spin coating solutions, which presumably results in similar viscosities. Upon chemical doping, the values for $m_{\text{polymer,dry}}$ slightly increase, which is presumably due to the addition of F_4TCNQ molecules or F_4TCNQ^- radical anions into or on top of the PTS films. The average dry polymer film of the PEDOT:PSS (1:6) amounted to $m_{\text{polymer,dry}} = 3.7$ μg , whereas the average dry polymer film mass for the Na-exchanged PEDOT:PSS-Na (1:6) amounted to $m_{\text{polymer,dry}} = 2.1$ μg . This significant difference could be explained by the presumably higher viscosity of the pristine PEDOT:PSS (1:6) dispersion. The titration of the PEDOT:PSS (1:6) dispersion in order to replace the H^+ cations by Na^+ cations (see also section 3.1.2) corresponds

to a dilution of the dispersion, therefore the viscosity of the PEDOT:PSS (1:6) dispersion is expected to be higher than the viscosity of the PEDOT:PSS-Na (1:6) dispersion. For the PEDOT:PSS (1:2.5) and PEDOT:PSS (1:2.2) material, the dry film weights amount to $m_{\text{polymer,dry}} = 8.2 \mu\text{g}$ and $m_{\text{polymer,dry}} = 15 \mu\text{g}$ (averaged), respectively, which is 2 – 7 higher than the weights obtained for the PEDOT:PSS-Na (1:6) and PEDOT:PSS (1:6) materials, respectively. The viscosity of the PEDOT:PSS (1:2.2) dispersion is around 6 to 7 times higher than the viscosity of the PEDOT:PSS (1:6) dispersion [216, 217]. Therefore, the PEDOT:PSS (1:2.2) dispersion might not be spun off as quickly from the accelerating substrate in the spin coating procedure as the PEDOT:PSS (1:6) dispersion, which might result in higher amount of material remaining on the substrate after spin coating and therefore to higher dry film weights. The dry polymer film weight amounted to $m_{\text{polymer,dry}} = 208.5 \mu\text{g}$ for the PEDOT:PSS-Na (1:6) film and $m_{\text{polymer,dry}} = 228.0 \mu\text{g}$ for the PEDOT:PSS (1:2.2) film, respectively. The dry film weights of the drop casted films are therefore 1 – 2 magnitudes higher than the values for the spin coated films. This can be explained by the different film deposition procedure, since no polymeric material is spun off the crystal as in the spin coating procedure.

The water uptake values were calculated as water uptake per repeating unit in λ . As discussed in section 3.3.5, calculating λ requires several assumptions (see also section 3.3.4). For example in case of PEDOT:PSS the assumption that only one type of cation is present might be partially incorrect, which could lead to an error in λ . Furthermore, the precisely indicated weight ratio between PEDOT and PSS or the assumption that exactly one third of all EDOT repeating units are oxidized might could be wrong, therefore resulting in a further error of λ . The informative value of the water uptake might be questioned by a further issue: whereas the water uptake in wt% or λ is calculated for the entire mass or every repeating unit, respectively, this does not take into account that water is presumably taken up preferably in the hydrophilic, polyelectrolyte rich moieties. Zozoulenko et al. showed in a recent publication with molecular dynamic simulations on PEDOT:PSS materials that the water uptake occurs predominantly in hydrophilic, PSS-rich moieties [218]. Calculation of the distribution of water molecules into hydrophobic and hydrophilic moieties and the weight or volume fraction of the hydrophilic moieties in the bulk material, which might help to calculate more interpretable water uptake values, was not feasible.

In section 4.1.2.1, differences in the spectroelectrochemistry and in-situ conductance behavior in dependence of the PEDOT to PSS ratio were obtained. In the water uptake measurements, at 23 mbar H_2O a water uptake of $\approx 40 \text{ wt}\%$ for PEDOT:PSS (1:2.2) and a water uptake of $\approx 35 \text{ wt}\%$ for PEDOT:PSS (1:6) were obtained, which can be considered with respect to the measurement errors as very similar. The significant differences

obtained in the spectroelectrochemistry and in-situ conductance measurements (for these measurements, PEDOT:PSS (1:2.5) was used, which is expected to behave similar as PEDOT:PSS (1:2.2)) and similar results in the water uptake measurements might indicate that the water uptake is governed mainly by the content of the PSS groups which are expected to participate in water uptake, which is for both PEDOT:PSS materials roughly comparable (55 wt% and 80 wt% weight content of PSS which is expected to participate in water uptake in PEDOT:PSS (1:2.5) and PEDOT:PSS (1:6), respectively). The redox activity and in-situ conductance behavior on the other hand is presumably governed by the content of PEDOT moieties and the connectivity or the percolation between these PEDOT moieties (see also the discussion about percolation effects in 4.3.5), which is expected to be remarkably different between both PEDOT:PSS batches.

4.3 Conductivity studies as function of water uptake

After examining the water uptake behavior of the PTS and PEDOT:PSS mixed conductor systems as function of water partial pressure in the previous chapter, the conductivity properties as function of water content are studied in the following chapter. All conductivity studies were conducted with the polymer films on interdigitated electrodes (IDEs) using a combination of AC impedance and DC measurements, as described in the methods part section 3.3.3. All measurements were conducted in a variable $p\text{H}_2\text{O}$ range from 0–29 mbar H_2O and were, if not otherwise mentioned, conducted at 25°C. All water uptake or water content values are taken from the QCM measurements as described in section 4.2.

In section 4.3.1, the three different cases of conductivity properties and its corresponding AC impedance and DC measurement findings are shown for the example of PTS materials: in section 4.3.1.1 undoped (pristine) PTS-Na is shown which shows ionic conductivity behavior, in sections 4.3.1.2 and 4.3.1.3 chemically doped PTS is discussed which either shows mixed conductivity or electronic conductivity behavior. Furthermore, PTS-Na 93% is discussed which shows mixed conductivity at elevated temperatures.

It is important to mention that all polymeric mixed conductor materials examined in this thesis possess at the entire examined water content range, at all doping degree conditions or in case of the PEDOT:PSS materials for both examined PEDOT:PSS ratios both electronic and ionic conductivity properties (also see the discussions in 4.3.1.2 and 4.3.1.3). However, depending on the mentioned conditions, either one of both conductivity mechanism (electronic or ionic conductivity) or both conductivity mechanisms (mixed conductivity) are dominating the electrical properties of the polymeric mixed conductor material. The sections of the PTS materials are indicated according to the dominating conductivity mechanisms.

In the following chapter, the conductivity results of the PEDOT:PSS materials are given in section 4.3.2, in which the batches PEDOT:PSS (1:6), PEDOT:PSS-Na (1:6) and PEDOT:PSS (1:2.2) were compared. In a collaboration with the group of Professor Myung-Han Yoon at the Gwangju Institute of Technology (Republic of Korea), the conductivity properties of PEDOT:PSS-PVA composite materials are studied, which are shown in section 4.3.3 and the comparison of all different IDEs geometries can be found in section 4.3.4. All conductivity results are discussed and summarized in section 4.3.5.

4.3.1 PTS materials

4.3.1.1 Pristine PTS-Na: ionic conductivity behavior

AC Impedance spectroscopy

At first, a pristine PTS-Na film was examined with AC impedance spectroscopy in a water partial pressure range of 0.9 – 29 mbar H_2O . The measurements at 0.9 – 9 mbar H_2O were conducted using a 5 μm IDE, whereas the measurements at 12 – 29 mbar H_2O were conducted using a 20 μm IDE. For the conductivity studies conducted in this thesis, IDEs with different electrode geometries were used. In section 4.3.4, it is shown that the same conductivities can be obtained independent from the IDE type. The 5 μm IDE allows to measure high ionic resistances in the low $p\text{H}_2\text{O}$ range whereas the 20 μm IDE allows to measure low ionic resistances at high $p\text{H}_2\text{O}$. In figure 4.28, representative AC impedance spectra of pristine PTS-Na at 25°C and 16 and 23 mbar $p\text{H}_2\text{O}$ can be seen. Since the real-part resistances Z'' are relevant for the discussions in this thesis, all AC impedance spectra are shown in the Nyquist plot since they allow to easily display the relevant resistances.

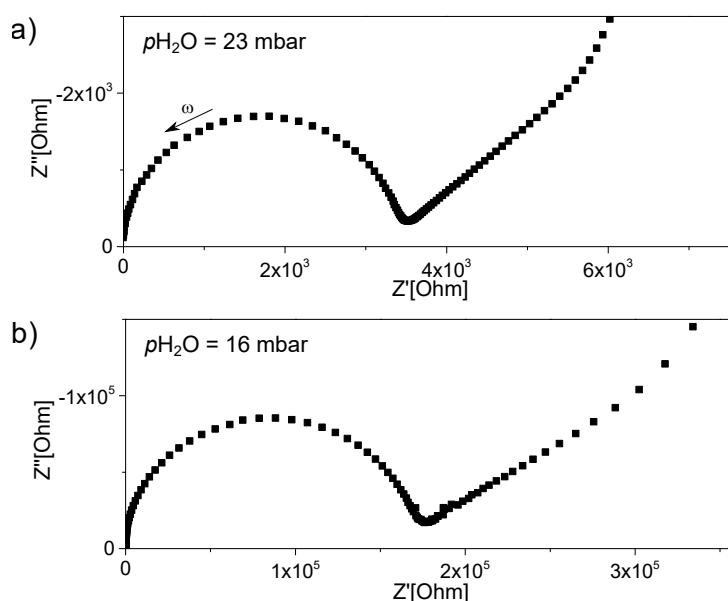


Figure 4.28: AC impedance spectra of undoped PTS-Na at 25°C on a 20 μm IDE at a) 23 mbar $p\text{H}_2\text{O}$ and b) 16 mbar $p\text{H}_2\text{O}$.

The spectra consist of a high-frequency semi-circle (the impedance at high frequencies ω is displayed at the origin of the Nyquist plot, the impedance at low frequencies is displayed at the right side of the Nyquist plot) and a sloping response at lower frequency. According to literature, the high frequency semi-circle can be assigned to the total resistance of the sample, which consists of contributions of both electronic and ionic resistances [219]. The low-frequency response (the part of the AC impedance spectra at frequencies lower than

the frequencies where the high-frequency semi-circle occurs) consists in the initial part of a straight line with a degree of $35 - 45^\circ$. Going to lower frequencies, the slope of the line increases.

Fitting of AC Impedance spectra

Since the sloping low-frequency response can be detected down to low frequencies, it can be assigned to the so called Warburg impedance [220, 221]. In general, the Warburg impedance can be observed for systems with electrodes that block either the ionic or electronic charge carriers [222]. The presence of the sloping low-frequency corresponds to the fact that in close proximity only ionic charge carriers contribute to the high-frequency semi-circle. In figure 4.29, the equivalent circuit for fitting ionically conducting materials is shown (the equivalent circuit is chosen according to literature [160]).

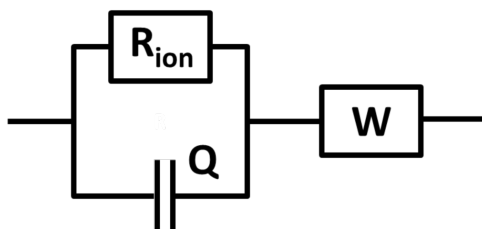


Figure 4.29: Equivalent circuit for fitting of AC impedance spectra of ionically conducting samples.

The equivalent circuit consists of a parallel RQ-element for the semi-circle at high frequencies. Since mainly ionic charge carriers contribute to the relaxation (response of the polymeric mixed conductor system to the application of current), the resistance of the RQ-element is assigned to an ionic resistance R_{ion} . A constant phase element Q instead of a capacitor element C was chosen to fit the high-frequency response, since constant phase elements allow to fit non-perfect capacitance behavior, whereas capacitor elements only allow to represent pure capacitive behavior [223]. For the low-frequency response, a Warburg element W is utilized. The fits of the AC impedance spectra are shown in figure 4.30 and the corresponding fit parameters are listed in table 4.3.

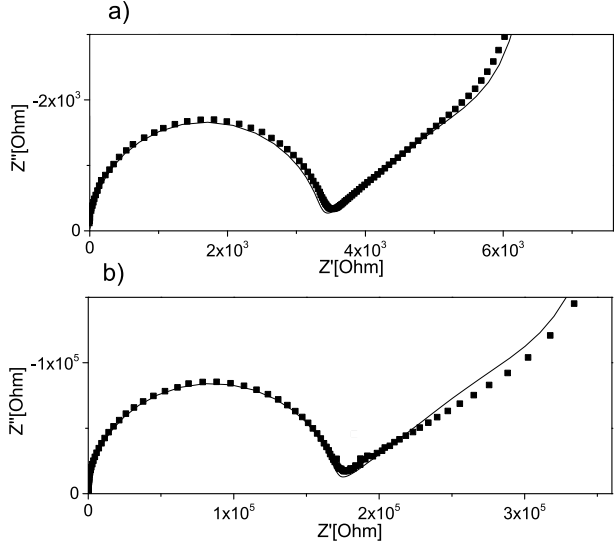


Figure 4.30: AC impedance spectra from figure 4.28 at a) 23 mbar H_2O and b) 16 mbar H_2O and corresponding fits.

	23 mbar H_2O	16 mbar H_2O
R_{ion} [Ω]	3249	165144
$Q - T$ [F]	$5.7 \cdot 10^{-11}$	$1.15 \cdot 10^{-10}$
$Q - P$	1	1
$W - R$ [Ω]	8508	550760
$W - T$ [s]	0.01	2.39
$W - P$	0.46	0.45

Table 4.4: Fitting parameters of fits from figure 4.30.

Since the resistances of the high-frequency semi-circles (the Z' value at the local minimum of Z'' , therefore referred to as high-frequency resistance R_{HF}) in figure 4.28 are assigned to approximately pure ionic resistance, the ionic resistances values correspond to the diameter of the semi-circles and can be therefore read out directly from the impedance spectra from the Z' value at the local minimum of the spectra. In the spectrum at 23 mbar H_2O in figure 4.30, the Z' value at the minimum of the spectrum between the high-frequency semi-circle and the sloping low-frequency signal amounts to 3.5 k Ω . Fitting the spectrum, a value of 3.2 k Ω was obtained for R_{ion} . For the spectrum at 16 mbar H_2O , a value of 178 k Ω could be read out whereas a value of 165 k Ω could be obtained from fitting the spectrum. The deviation between the value that can be read out and the value obtained after fitting is neglectable since the values for σ_{ion} of polyelectrolyte materials vary over several orders of magnitude as function of $p\text{H}_2\text{O}$ or water uptake. For ionically conducting samples the values for R_{ion} are read out directly from the impedance spectrum in all further measurements. For the parameter $Q - P$, values of 1.06 and 1.02 were obtained initially, but since values which exceed 1 are theoretically not possible, the values were set to $Q - P = 1$. If $Q - P$ equals 1, the corresponding relaxation process can be assigned to pure capacitive behavior. In case $Q - P$ equals 0, the process can be assigned to pure resistive behavior. The capacitance $Q - T$ of the high-frequency semi-circle is in the 10^{-10} F range, thus it can be assigned to the (parasitic) geometrical capacitance originating from the IDE substrate. The fact that $Q - T$ is at both $p\text{H}_2\text{O}$ roughly equal (the deviation between both fits might result from fitting errors) can be explained by the fact that the geometric capacitance is independent from $p\text{H}_2\text{O}$ or the water content of the polymer film.

For the parameter $W - T$ a decrease is obtained when decreasing $p\text{H}_2\text{O}$ from 23 mbar to 16 mbar H_2O . In the diffusion interpretation, $W - T = L^2/D$ (L corresponds to the thickness of the diffusion layer and D corresponds to the diffusion coefficient of the corresponding particle), therefore $W - T$ corresponds to a "diffusion time" of the ionic charge carriers [223]. Therefore, the increase of $W - T$ can be interpreted as an increase of the long-range diffusion time of the ionic charge carrier towards the ion-blocking electrode. For the parameter $W - P$, independent of $p\text{H}_2\text{O}$ a value of $W - P = 0.45$ was obtained, which is close to 0.5 in case of an ideal Warburg element.

Conductivities

With the ionic resistance R_{ion} values, the geometric parameters $l = 5 \mu\text{m}$ and $w = 191.70 \text{ cm}$ for the $5 \mu\text{m}$ IDE and $l = 20 \mu\text{m}$ and $w = 47.95 \text{ cm}$ for the $20 \mu\text{m}$ IDE, the film thickness $h = 56 \text{ nm}$ (for the PTS-Na film on the $5 \mu\text{m}$ IDE a thickness of 57 nm and for the PTS-Na film on the $20 \mu\text{m}$ IDE a thickness of 56 nm was determined) and using eq. 13, the ionic conductivities σ_{ion} are calculated. The ionic conductivity of undoped PTS-Na σ_{ion} as function of $p\text{H}_2\text{O}$ and as function of water content is shown in figure 4.31. Over the course of this chapter the conductivities (which are determined with the help of AC impedance and DC measurements) are plotted as function of the applied water partial pressure on the bottom x-axis and the water uptake (in case the water uptake was determined and reproducible and reliable values could be obtained) on the top x-axis.

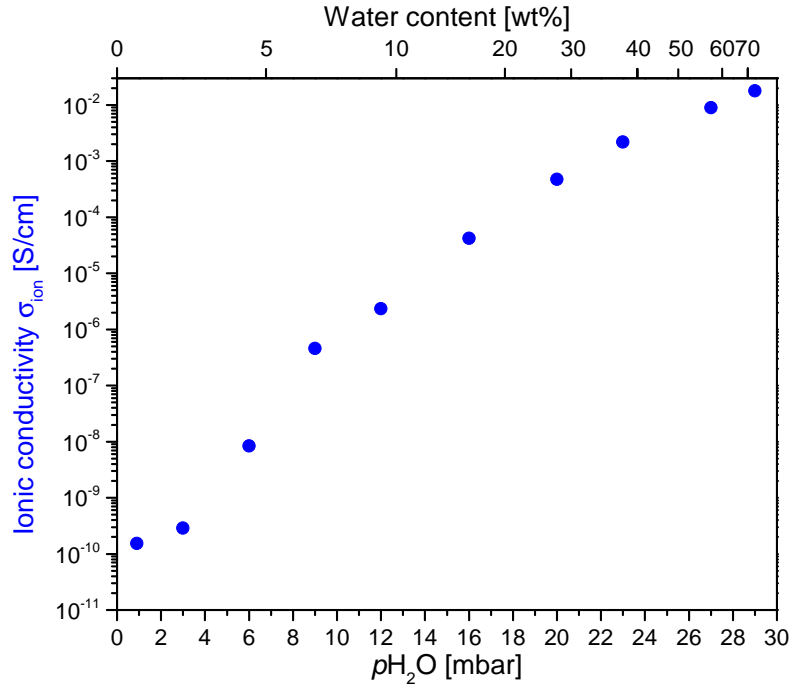


Figure 4.31: Ionic conductivity of undoped PTS-Na at 25°C as function of water partial pressure and as function of water content, the measurements at 0.9 – 9 mbar H₂O were conducted using a 5 μm IDE, the measurements at 12 – 29 mbar H₂O were conducted using a 20 μm IDE.

Starting from σ_{ion} in the range of 10^{-10} S/cm at 0.9 mbar H₂O (which corresponds to 3 % r.h.) or 1 wt% water content, values in the range of 10^{-2} S/cm are reached at 29 mbar H₂O (which corresponds to 92% r.h.) and 70 wt% water content. This means that σ_{ion} can be significantly increased over 8 orders of magnitude. In the low water content range, σ_{ion} increases significantly from 10^{-10} S/cm up to 10^{-6} S/cm upon increasing the water content to 10 wt%. At high water contents on the other hand, σ_{ion} increases from 10^{-3} S/cm up to 10^{-2} S/cm upon increasing the water content from 40 wt% to 70 wt%. The values for σ_{ion} increase therefore much more significantly at low water contents than at high water contents. The dependency of σ_{ion} from the water content was explained for Nafion with the presence of percolation paths [3]. In case of Nafion, at low water contents taking up of water molecules leads to an increase of the dissociation of protons from the SO₃⁻ groups. No ionic conductivity can be measured until a percolating network of water cluster forms. After the initial formation of the percolating network, further water uptake leads to an increase of the ionic conductivity. However, after a certain water uptake further water uptake does only slightly increase the ionic conductivity since the additional water uptake leads only to the formation of domains with water moieties. In case of PTS-Na in figure 4.31 and in case of PTS-TBA [160], σ_{ion} values could be determined even at the lowest water uptakes and no minimum water uptake was necessary, which might indicate that the formation of percolation paths is less relevant for σ_{ion} (percolation effects were

however assumed in the electronically conducting phases, see section 4.3.5). The plateau-like σ_{ion} values at high water contents could however also be observed for the PTS and PEDOT:PSS materials in this thesis, the presence of water moieties could therefore also be assumed.

4.3.1.2 Chemically doped PTS-Na: mixed conductivity behavior

AC Impedance spectroscopy

For PTS-Na films from aged solutions, so solutions that were left standing for several weeks after preparation, measurable electronic conductivities in the range of $\sigma_e \approx 10^{-6}$ S/cm were observed (A.13–A.15). This effect might be explained by a slight oxidation due to the so-called auto-doping effect, which is known for conducting polyelectrolytes [75]. For conducting polyelectrolytes with different counterions it could be shown that the auto-doping effects is more pronounced for smaller counterions [90]. In order to obtain increased electronic conductivities in a reliable way, a PTS-Na film was chemically doped via sequential doping with a 0.5 M solution of $F_4\text{TCNQ}$ in THF (see experimental part section 3.2.2). This was done by sequential doping with $F_4\text{TCNQ}$ as reported in literature [163, 164]. The AC impedance spectra of a chemically doped PTS-Na film as function of $p\text{H}_2\text{O}$ at 25°C can be seen in figure 4.32.

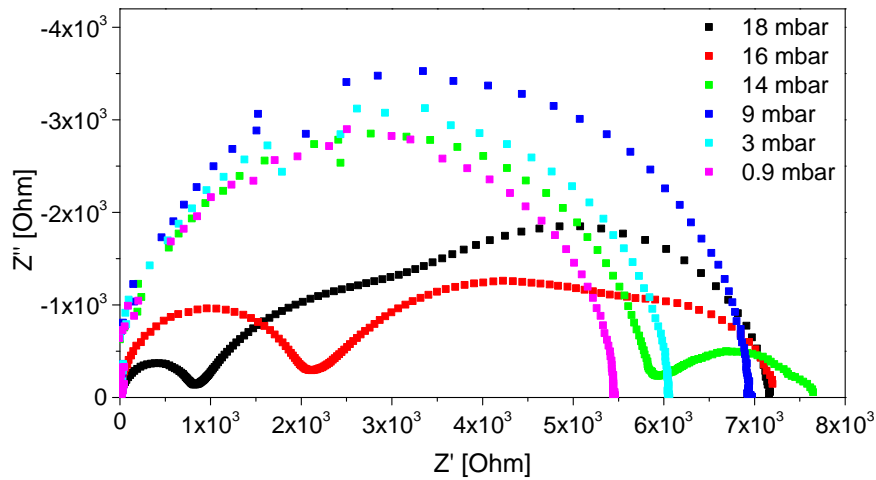


Figure 4.32: AC impedance spectra of PTS-Na doped with 0.5 M $F_4\text{TCNQ}/\text{THF}$ on a 5 μm IDE as function of water partial pressure at 25°C.

At 18 mbar H_2O (black symbols), the spectrum consists of a high-frequency semi-circle with high-frequency resistance of $R_{\text{HF}} = 8 \cdot 10^2 \Omega$. Instead of a sloping low-frequency response (as was observed for the low-frequency response in the AC impedance spectra of undoped PTS-Na in figure 4.28), the spectrum consists of two overlaying semi-circles with a low-frequency resistance of $R_{\text{LF}} = 7.2 \cdot 10^3 \Omega$ (intercept of the spectrum with the x-axis). Decreasing $p\text{H}_2\text{O}$ to 16 mbar H_2O (red symbols) and further down to

14 mbar H₂O (green symbols), the resistance of the high-frequency semi-circle increases to $R_{\text{HF}} = 6 \cdot 10^3 \Omega$. Simultaneously, the resistance of the low-frequency semi-circle slightly increases to $R_{\text{LF}} = 7.6 \cdot 10^3 \Omega$. Decreasing $p\text{H}_2\text{O}$ further down to 9 mbar H₂O (blue symbols), instead of two semi-circles, only one semi-circle with a low-frequency resistance of $R_{\text{LF}} = 6.9 \cdot 10^3 \Omega$ can be observed. Further decrease of $p\text{H}_2\text{O}$ to 3 mbar H₂O (turquoise symbols) and 0.9 mbar H₂O (pink symbols) leads to a decrease of the resistance of the low-frequency signals to $R_{\text{LF}} = 6.1 \cdot 10^3 \Omega$ and $R_{\text{LF}} = 5.5 \cdot 10^3 \Omega$.

DC measurements

In order to extract the R_e and R_{ion} values (which are required for calculating σ_e and σ_{ion}) from the R_{HF} and R_{LF} values obtained in the AC impedance measurements, at first supplementary DC measurements were conducted. A constant current of $I = 10 \mu\text{A}$ was applied so that the resulting potential did not exceed 100 mV (as described in section 3.3.3). The potential trends of the DC measurements can be seen in figure 4.33.

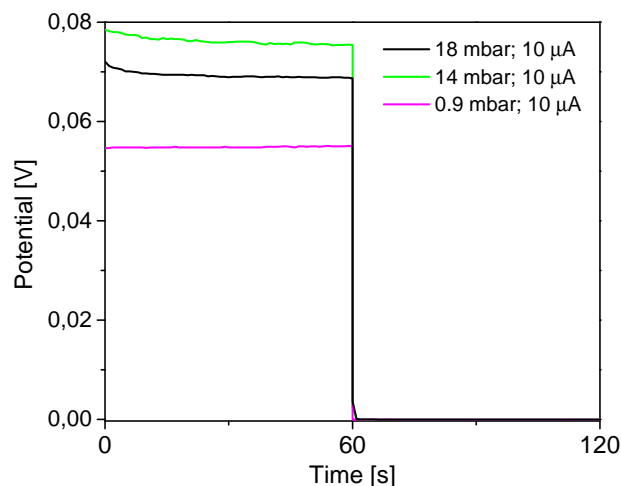


Figure 4.33: DC measurements of PTS-Na doped with 0.5 M F₄TCNQ/THF on a 5 μm IDE at 25°C as function of water partial pressure.

During the time when a constant current is applied between the electrodes, both electronic and ionic charge carriers move through the polymer film. Whereas the Pt electrode structure is permeable for electronic charge carriers, ionic charge carriers are blocked at the electrode. Since ionic charge carriers are the more blocked at the electrodes the longer a constant polarization is applied between the electrodes, the potential at the end of the time of the applied current (end of the polarization time) corresponds to the resistance when only electronic charge contributes to current conduction. Since the potential trend at the end of the polarization approaches constant values, it corresponds to a steady

state potential $U_{\text{steady state}}$. With the help of $U_{\text{steady state}}$, the applied current I and with the Ohmic Law as given in eq. 4, the electronic resistance R_e can be calculated. The electronic conductivities σ_e can be calculated from R_e and the geometric parameters. As can be seen in the potential trends, in the measurements at 18 and 14 mbar H_2O (black and green curve) the potential decreases slightly during the time of the applied current of $I = 10 \mu\text{A}$. The slight decrease of the potential was only observed for chemically doped PTS films and might therefore be related to unknown influences from the chemical doping procedure. After switching off the constant current, very low potentials around 0 mV can be measured, since no resistance towards current flow occurs any more. However, as can be seen at the potential trend at 60 seconds, the potential does not directly fall back to 0 mV, but only after 61 seconds a potential of 0 mV is reached. This relaxation effect can not be further elucidated in this measurement since a time resolution (time between the potential measurements) of 1 second was set, in the DC measurements of PEDOT:PSS in chapter 4.3.2 the relaxation is studied in further detail.

In order to examine the physical origin of the low-frequency resistance R_{LF} in the AC impedance spectra, σ_e was also calculated utilizing the R_{LF} . In figure 4.34, σ_e calculated either from R_{LF} in the AC impedance spectra or the electronic resistance R_e extracted from $U_{\text{steady state}}$ from the DC measurements is shown.

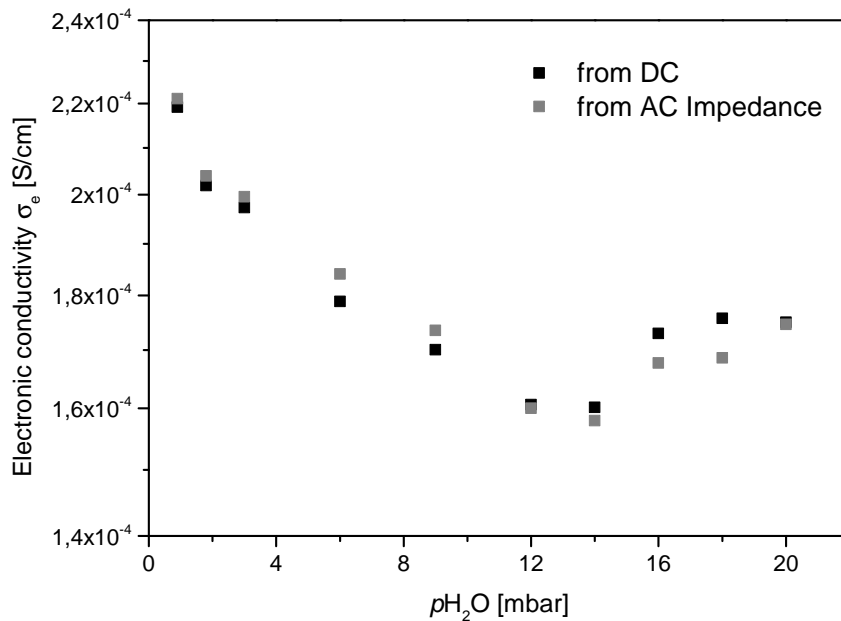


Figure 4.34: Electronic conductivities of PTS-Na doped with 0.5 M $\text{F}_4\text{TCNQ}/\text{THF}$ on a $5 \mu\text{m}$ IDE determined from AC impedance spectra and DC measurements.

Comparing the values for σ_e it can be seen that with both AC impedance as well as DC

measurements very comparable values can be obtained. The deviations between both measurements, which are below 5 %, could be explained with instrument specific inaccuracies. The fact that R_{LF} corresponds to the steady-state resistance (at the end of the polarization time) in the DC measurements can be explained with the fact that the sine-wave in a AC impedance measurement at a frequency of 15 mHz corresponds to a DC measurement with a polarization time of roughly 33 seconds since one sine-wave with a frequency of 15 mHz keeps the direction of its polarization for roughly 33 seconds. In the following, the low-frequency resistance in the AC impedance spectra at the intercept with the real-part axis is referred to as electronic resistance R_e . If not otherwise mentioned, all σ_e values are calculated with R_e from DC measurements.

Fitting of AC Impedance spectra

In addition to the extraction of the electronic resistances from DC measurements, the ionic resistances R_{ion} need to be extracted from the AC impedance spectra. In literature, mixed conductors are described with the Maxwell's model [8, 221, 224]. The equivalent circuit can be seen in figure 4.35.

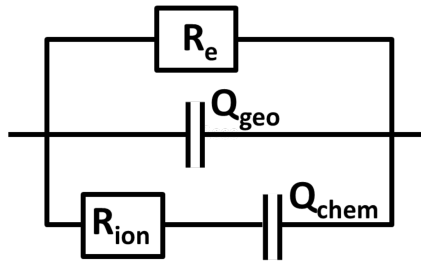


Figure 4.35: Equivalent circuit for fitting of AC impedance spectra of mixed conducting samples.

The equivalent circuit consists of two resistors, one for the electronic resistance R_e and one for the ionic resistance R_{ion} . Both resistors are toggled in parallel, since both resistances contribute in parallel to the total current conduction. One constant phase element Q_{geo} is in parallel to both resistors and accounts to the (parasitic) geometrical capacitance of the electrode. A second constant phase element Q_{chem} is in series with R_{ion} and is attributed to the chemical capacitance of the polymer film, originating from the mixed conducting properties and ion-blocking electrodes [219]. Maier et al. derived an equivalent circuit for a inorganic mixed conductor system sandwiched between two electrodes, in which the thickness of the mixed conductor is large compared to the Debye length [225]. They found that the chemical capacitance determines if the AC impedance spectrum shows Warburg impedance. Additionally the influence of the carrier concentration, the carrier mobility and the rate constants of both the electronic and ionic charge carriers on the impedance

spectrum were additionally examined by the authors. The simplified equivalent circuit in figure 4.35 can be deduced from the model of Maier et al. [225].

The Debye length is a measure for the distance by which two opposite charges are separated in liquid electrolytes [226]. Initial water uptake in the polyelectrolyte moieties of the mixed conductor systems in this thesis is assumed to lead to a dissociation of the mobile cations from the immobile sulfonate groups. The mean distance of the cations from the sulfonate groups presumably increases upon further water uptake until the Debye length is reached, which might roughly correspond to the Debye length in liquid electrolytes. Further increase of the mean distance of the opposite charges upon uptake of more water might be not favored thermodynamically, therefore the water is taken up in water rich moieties between the screened mobile cations. Eventually, the reaching of the Debye length might be observed in the dependency of the ionic conductivity σ_{ion} as function of water uptake (as in figure 4.31 or 4.61): starting at low water uptake, σ_{ion} might increase significantly as function of water uptake until the Debye length is approximately reached. After reaching the Debye length, further water uptake might only lead to minor increase of σ_{ion} since the water is predominantly taken up in water rich domains. The Debye length in the present polyelectrolyte systems can be estimated to be in the range of 1 nm [227].

In the shown AC impedance spectra of the mixed conductor (figure 4.36 at 18 mbar H₂O), both R_e and R_{ion} contribute to the high-frequency resistance R_{HF} according to eq. 23 (according to [8, 224, 225]):

$$R_{\text{HF}} = \frac{R_e \cdot R_{\text{ion}}}{R_e + R_{\text{ion}}} \quad (23)$$

In order to extract the values for R_{ion} from R_{HF} and R_e , the equation can be rearranged:

$$R_{\text{ion}} = \frac{R_e \cdot R_{\text{HF}}}{R_e - R_{\text{HF}}} \quad (24)$$

In case of $R_e \gg R_{\text{HF}}$, R_{ion} corresponds approximatively to R_{HF} :

$$R_{\text{ion}} \approx \frac{R_e \cdot R_{\text{HF}}}{R_e} \approx R_{\text{HF}} \quad (25)$$

If the impedance spectra of undoped PTS-Na in figure 4.28 would be measured down to very low frequencies in the mHz range, a second semi-circle with a very high resistance would be obtained due to the finite electronic resistance of the undoped PTS-Na. In this case, since a low-frequency resistance or an electronic resistance could be determined as well, the equivalent circuit for the mixed conductors could be applied as well and eq. 24 would simplify to eq. 25. The high-frequency resistance of the first semi-circle R_{HF} and the electronic resistance R_e can be obtained from the impedance spectrum at 18 mbar H₂O as indicated in figure 4.36:

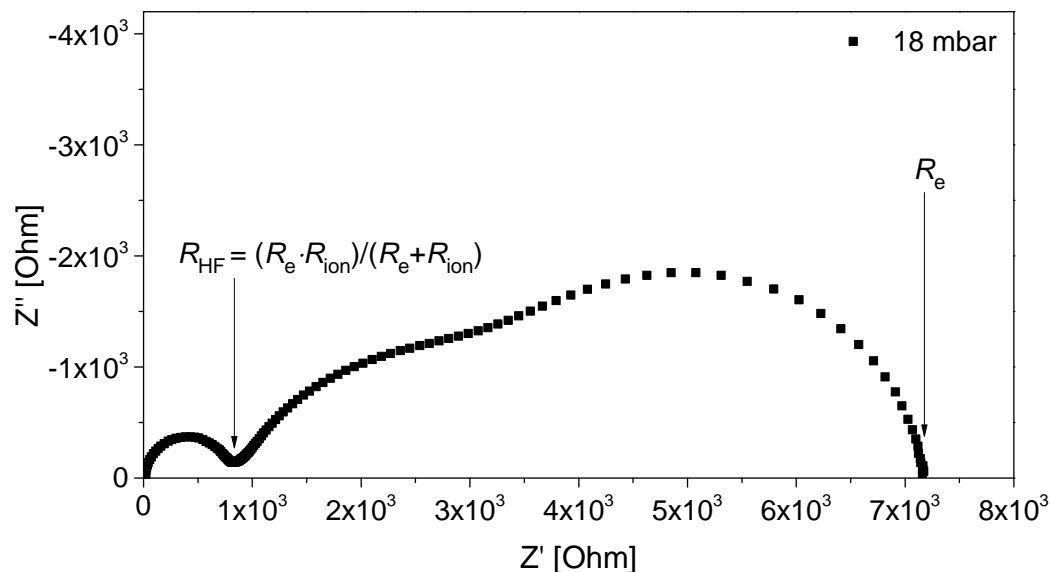


Figure 4.36: AC impedance spectra of PTS-Na doped with 0.5 M F_4TCNQ/THF on a $5 \mu m$ IDE at $25^\circ C$ and a water partial pressure of 18 mbar H_2O with indicated resistances.

Whereas the high-frequency response consists clearly visible of one semi-circle, the low-frequency response consists as already mentioned not from one, but from two overlaying semi-circles. This might occur due to the presence of grain boundaries between the electronically conducting PTS backbone moieties. By adding more circuit elements to the equivalent circuit in figure 4.35, the two overlaying semi-circles could be fitted properly, but since the reason or physical meaning of the overlaying semi-circles can not be further elucidated, no further circuit elements are added. An equivalent circuit which could be used to describe the mid-frequency features can be seen in figure A.16.

Whereas the AC impedance spectra at 14 mbar H_2O and higher pH_2O show a high-frequency semi-circle and a low-frequency response and are fitted with the equivalent circuit for mixed conductors (figure 4.35, the respective fits are shown in figure 4.46), the AC impedance spectrum at 9 mbar H_2O and lower pH_2O , the AC impedance spectra in figure 4.32 consist of one semi-circle. In general, an AC impedance spectrum that shows one semi-circle in the Nyquist plot, can be fitted with one parallel RQ-element. In figure 4.37, the equivalent circuit to fit the spectra with one semi-circle can be seen.

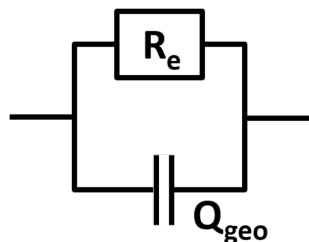


Figure 4.37: Equivalent circuit for fitting of AC impedance spectra of electronically conducting samples.

Since it could be already confirmed that the low-frequency resistance of the semi-circle can be assigned to R_e , the R -element of the equivalent circuit can be assigned to R_e . The Q -element in parallel to R_e is assigned as for the mixed conductor to the geometrical capacitance Q_{geo} .

After establishing equivalent circuits for the two different types of AC impedance spectra (either the mixed conducting behavior for the AC impedance spectra at 14 mbar H_2O and higher $p\text{H}_2\text{O}$ or the electronic conducting behavior at 9 mbar H_2O and lower $p\text{H}_2\text{O}$), the AC impedance spectra can be fitted. In figure 4.38, exemplary fits and in table 4.5 the obtained fit parameters are shown. It is important to mention that the $Q_{\text{chem}} - T$ values do not correspond to actual capacitance values. In order to obtain the actual capacitance values, the $Q_{\text{chem}} - P$ values have to be taken into consideration (for Q_{geo} the $Q_{\text{geo}} - T$ values are equal or very close to 1, therefore the $Q_{\text{chem}} - T$ values correspond to the actual capacitance values) [228]. The existing model in literature to recalculate the actual capacitance values is however only valid for one parallel R-CPE equivalent circuit (such as in figure 4.37), calculation of the capacitance values for the Q_{chem} element in the equivalent circuit for mixed conductors (figure 4.35) is not possible. Calculating the actual capacitance values with the parallel resistance R_e , values which are in between one order of magnitude with the $Q_{\text{chem}} - T$ values obtained from the fits are obtained. Therefore, small deviations of the Q_{chem} values between different samples or upon variation of $p\text{H}_2\text{O}$ can not be discussed. However, since the obtained values for $Q_{\text{geo}} - T$ and $Q_{\text{chem}} - T$ (as shown in table 4.5) are differentiating over several orders of magnitude, the magnitude of $Q_{\text{chem}} - T$ can be discussed.

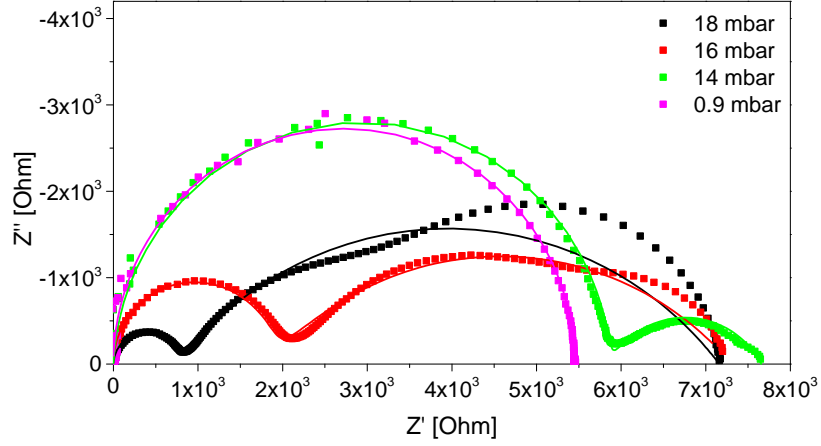


Figure 4.38: AC impedance spectra of PTS-Na doped with 0.5 M F_4TCNQ/THF from figure 4.32 with exemplary fits.

As can be seen by comparing the spectrum and the fit result in case of the spectra at 14 mbar, 16 mbar and 18 mbar H_2O , the high-frequency response is modeled with high accuracy. This could be explained by the fact that solely the geometrical capacitance can be assigned to this relaxation process. The low-frequency response, especially the measurements at 18 and 16 mbar H_2O , are on the other hand not well modeled in the AC impedance spectra. This might result from the fact that in the measurements at 18 and 16 mbar H_2O , the low-frequency response is composed of two-overlapping processes, in which the reason for the overlaying processes is as discussed not known. In table 4.5, the fit parameters are given.

Table 4.5: Fit parameters of fits in figure 4.38.

Circuit parameter	18 mbar H_2O	16 mbar H_2O	14 mbar H_2O	0.9 mbar H_2O
R_e [Ω]	7161	7307	7658	5450
$Q_{geo} - T$ [F]	$3.4 \cdot 10^{-10}$	$1.4 \cdot 10^{-10}$	$3.4 \cdot 10^{-10}$	$2.6 \cdot 10^{-10}$
$Q_{geo} - P$	0.98	1	0.97	1
R_{ion} [Ω]	850	2495	25069	
$Q_{chem} - T$ [F]	$4.6 \cdot 10^{-6}$	$3.5 \cdot 10^{-6}$	$1.2 \cdot 10^{-6}$	
$Q_{chem} - P$	0.58	0.55	0.68	

The obtained values for R_e decrease in the order 18 – 0.9 mbar H_2O , which corresponds to the R_{LF} values from the AC impedance spectra and which is consistent with the values obtained from the DC measurements. For $Q_{geo} - P$ values close to 1 were obtained as for the fits in table 4.5, which corresponds to a pure capacitive behavior. Values for $Q_{geo} - T$ in the range of $10^{-10} - 10^{-11}$ F were obtained, which is typical for geometric capacitances [8, 160]. On the other hand, $Q_{chem} - T$ in the range of 10^{-6} F were obtained, which is around four orders of magnitude higher than the capacitance values obtained for $Q_{geo} - T$ and which is typical for chemical capacitance values [160].

For the Q_{geo} -element in the equivalent circuit of the AC impedance spectrum with one semi-circle, the obtained $Q_{\text{geo}} - T$ and $Q_{\text{geo}} - P$ parameters are very similar as for the values of the Q_{geo} -element in the fits with the mixed conductor equivalent circuit in case of the AC impedance spectra with two semi-circles. This can be explained with the fact that the geometric stray capacitance is independent from the conductivity properties and independent from the water partial pressure or water uptake. All obtained AC impedance spectra in this thesis showing one semi-circle resulted in $Q - T$ in the range of 10^{-10} F and $Q - P$ values equal to or close to 1 and are therefore not discussed any further. In table 4.6, the values for R_{ion} of the AC impedance spectra at 18, 16 and 14 mbar H_2O either calculated via eq. 24 and with the help of R_{HF} (as obtained from AC impedance spectra) and R_e (which can be determined from the steady-state resistance in DC measurements or R_{LF} from AC impedance spectra) or obtained from the fits in table 4.5 are listed.

Table 4.6: Comparison of resistance values obtained either via calculation or fitting.

Spectrum	R_{ion} [Ω]-calculated	R_{ion} [Ω]-obtained from fit
18 mbar H_2O	938	850
16 mbar H_2O	2994	2495
14 mbar H_2O	26403	25069

Comparing the calculated and the fitted values, it can be seen that within a maximum error of 10%, the values match well. Therefore, for all following evaluations of AC impedance spectra of mixed conductors, R_{ion} was calculated with the read-out value R_{HF} and R_e from the DC measurements. Additionally further AC impedance spectra were fitted in order to validate the utilized approach.

Conductivities

The calculated electronic and ionic conductivities of the chemically doped PTS-Na film at 25°C as function of $p\text{H}_2\text{O}$ are shown in figure 4.39.

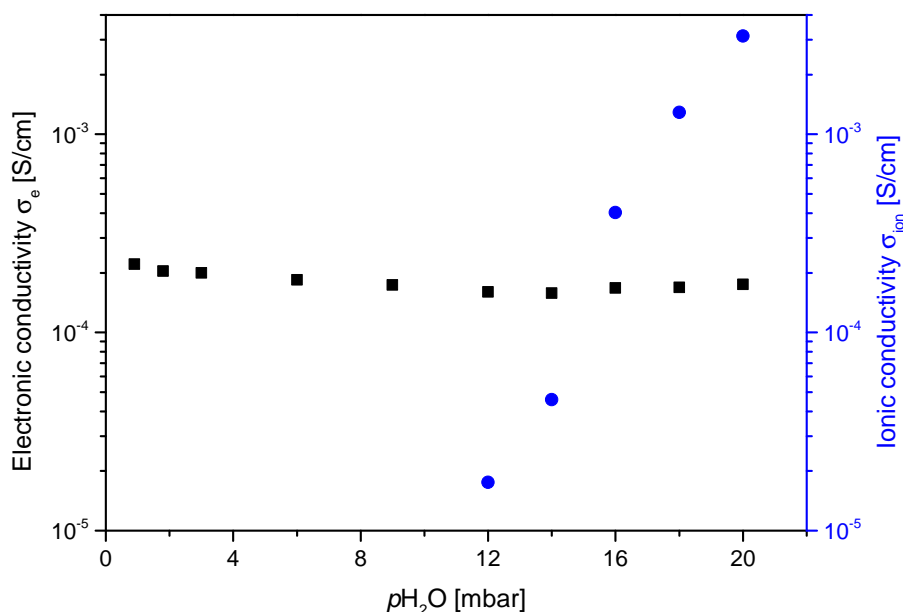


Figure 4.39: Electronic and ionic conductivity of PTS-Na on a 5 μm IDE doped with 0.5 M $\text{F}_4\text{TCNQ}/\text{THF}$ at 25°C as function of water partial pressure.

Whereas the electronic conductivity σ_e of the chemically doped PTS-Na film can be detected over the entire examined $p\text{H}_2\text{O}$ range, the ionic conductivity σ_{ion} can only be determined at $p\text{H}_2\text{O}$ of equal and higher than 12 mbar H_2O since only at these $p\text{H}_2\text{O}$ steps the high-frequency semi-circle in the AC impedance spectra can be utilized to determine σ_{ion} . Starting at $\sigma_e \approx 10^{-4}$ S/cm, σ_e decreases slightly upon increasing $p\text{H}_2\text{O}$ to 14 mbar H_2O and remains nearly constant until 20 mbar H_2O . The ionic conductivity on the other hand changes significantly as function of $p\text{H}_2\text{O}$: starting at $\sigma_{\text{ion}} \approx 10^{-5}$ S/cm at 12 mbar H_2O , σ_{ion} increases monotonically until a value of $\sigma_{\text{ion}} \approx 10^{-3}$ S/cm at 20 mbar H_2O is reached. The increase of σ_{ion} with increasing $p\text{H}_2\text{O}$ can be explained as for the undoped PTS-Na with an increase of the free Na^+ concentration caused by an increasing dissociation of the Na^+ cation from the immobile SO_3^- units. The observation that σ_e varies inconsistently (at low $p\text{H}_2\text{O}$ decrease with increasing $p\text{H}_2\text{O}$, at higher $p\text{H}_2\text{O}$ increase with increasing $p\text{H}_2\text{O}$) was not observed in the measurement of σ_e as function of $p\text{H}_2\text{O}$ for any other material in this thesis and might be explained by the unknown influence of F_4TCNQ molecules or F_4TCNQ^- anions in or on top of the polymer film.

4.3.1.3 Chemically doped PTS-TBA: electronic conductivity behavior

AC Impedance spectroscopy

For comparison, PTS-TBA was chemically doped by sequential doping with a 0.5 M solution of F_4TCNQ in THF. The obtained AC impedance spectra can be seen in figure 4.40.

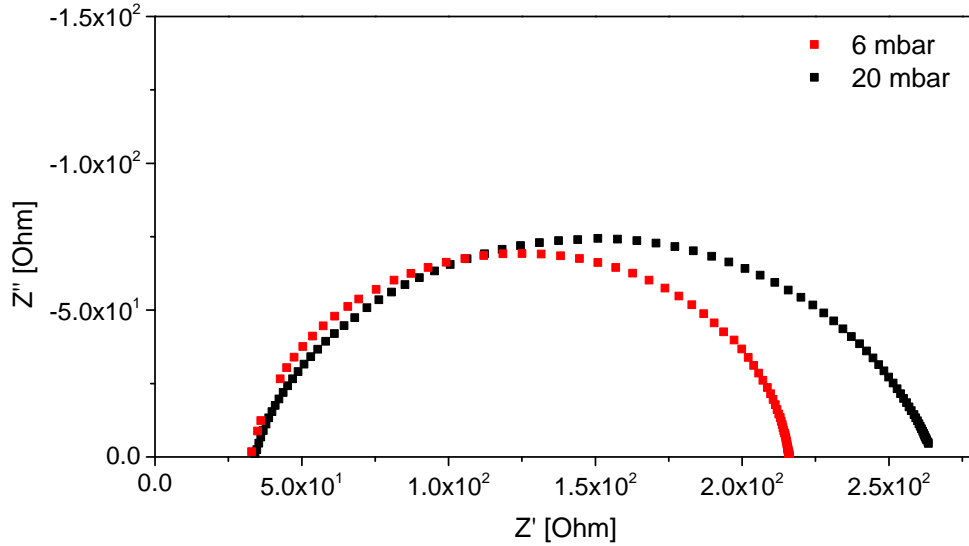


Figure 4.40: AC impedance spectra of PTS-TBA doped with 0.5 M F_4TCNQ/THF on a $5 \mu m$ IDE at $25^\circ C$ and various water partial pressures.

Interestingly, the AC impedance spectra of the chemically doped PTS-TBA show at all pH_2O one semi-circle. This is in contrast to the chemically doped PTS-Na, which showed at low pH_2O one semi-circle, but from medium pH_2O up to at high pH_2O a distinguishable high-frequency semi-circle and a low-frequency response. Since no high-frequency semi-circle is obtained, no R_{ion} can be determined for the chemically doped PTS-TBA film. The electronic resistance R_e of the semi-circle (which is also the low-frequency resistance) is in the range of 100Ω , whereas for the chemically doped PTS-Na, R_e is in the range of $10 k\Omega$. In figure 4.40, it can be seen that the AC impedance spectra do not start at the origin of the Nyquist plot, but at real-part impedances of $Z' = 30 \Omega$. This offset might be explained with wiring resistances (the sum of all resistances from the measurement device over the wires to the polymer film coated IDE) or contact resistances, which occur in the electrical circuit between the electrode walls and the polymer film. For calculating σ_e , the value of the offset was therefore subtracted from the R_e values. The wiring resistance of the electrical circuit of the measurement system was determined to 8Ω with the help of a short-circuited IDE. As can be seen in figure 4.40 at the start of the semi-circle from the resistance of $Z' = 30 \Omega$, it can be seen that not only the 8Ω wiring resistance contributes to the x-axis offset of the AC impedance spectra. The remaining $\approx 20 \Omega$ might result from contact resistances between the IDE and the PTS film. Since the contact resistance can

not be determined in the utilized two-point measurement, the IDE type for all measurements in this thesis were chosen in a way that the determined resistances are not in the Ω range but rather in the $k\Omega$ range (see section 4.3.4 for the discussion about the choice of the suitable IDE). This was done because the relative contribution of the wiring resistance or the contact resistance to the resistance values of the polymer film becomes smaller with increasing resistances of the polymer film, assuming that the wiring resistance and contact resistance are constant. This assumption can be seen when comparing the AC impedance spectra in figure 4.32 and 4.40: whereas no offset can be seen in figure 4.32 since the resistances are in the $k\Omega$ range, the offset can be observed in figure 4.40 since the resistance values are in the Ω range. For polymer films with resistance values below 50Ω , IDEs with a higher channel lengths were chosen, which results in higher resistances values and which leads to a decrease of the influence of the wiring resistance and contact resistance. In case of resistance values lower than 50Ω and already the highest channel length IDE ($100 \mu\text{m}$ IDE), the offset value was subtracted from the resistance values. In case of resistances in the $k\Omega$ or $M\Omega$ range were obtained, the offset value was not taken into consideration since the relative influence of the offset value is below the measurement uncertainty.

DC measurements

In figure 4.41, the DC measurements of the chemically doped PTS-TBA are shown.

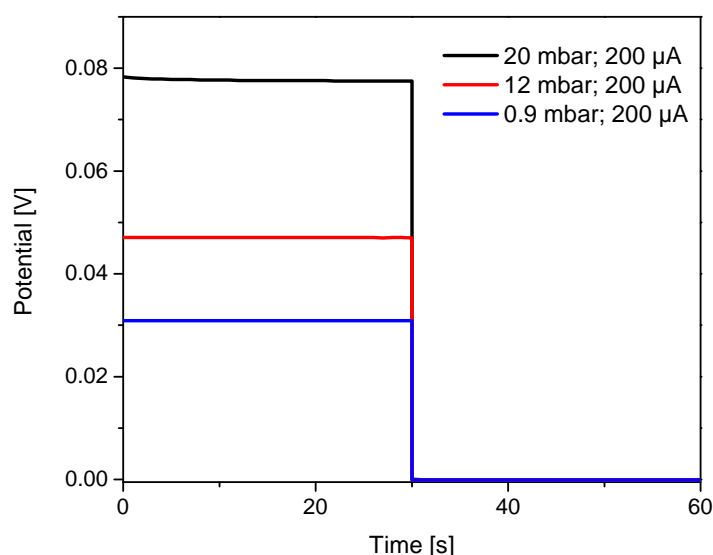


Figure 4.41: DC measurements of PTS-TBA doped with $0.5 \text{ M F}_4\text{TCNQ/THF}$ on a $5 \mu\text{m}$ IDE at 25°C and various water partial pressures.

Regarding the potential trends of the DC measurements, in the measurement at

20 mbar H_2O (black curve) the potential decreases slightly during the time of the applied current (polarisation time). At the measurements at 12 and 0.9 mbar H_2O (red and blue curve), no change of the potential during the time of the applied current can be observed. The slight decrease of the potential at high $p\text{H}_2\text{O}$ was also observed in the DC measurements of the chemically doped PTS-Na in figure 4.33 and might be therefore explained by the influence of F_4TCNQ molecules or F_4TCNQ^- anions in or on top of the PTS-TBA film.

Conductivities

In figure 4.42, the calculated σ_e of the chemically doped PTS-TBA film at 25°C as function of $p\text{H}_2\text{O}$ is plotted.

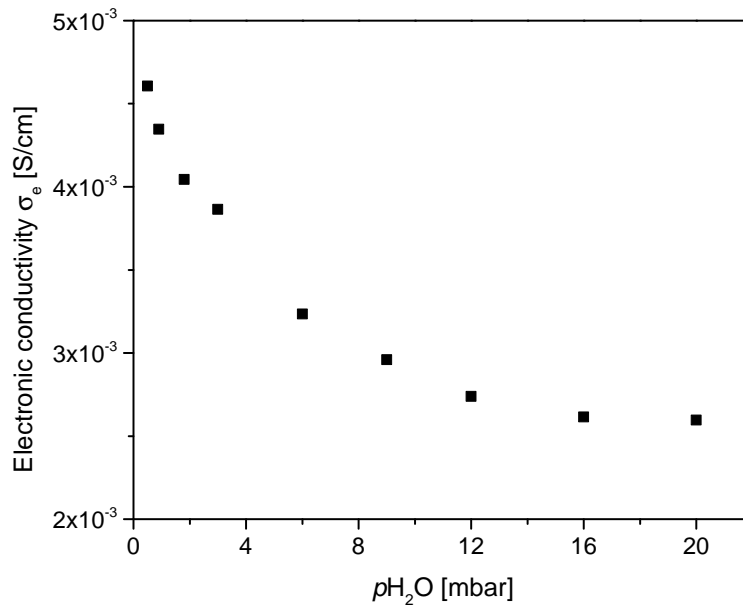


Figure 4.42: Electronic conductivity of PTS-TBA doped with 0.5 M $\text{F}_4\text{TCNQ}/\text{THF}$ on a $5 \mu\text{m}$ IDE at 25°C as function of water partial pressure.

As can be seen from the trend of σ_e , the values decrease first strongly at $p\text{H}_2\text{O} < 12$ mbar H_2O and are rather constant at $p\text{H}_2\text{O} \geq 12$ mbar H_2O . This trend is similar as for the chemically doped PTS-Na (figure 4.39) and might therefore be explained by the influence of the chemical doping procedure. Considering the level of σ_e , it can be understood why no high-frequency semi-circle or no σ_{ion} can be determined for this material: the maximum σ_{ion} of the undoped PTS-TBA at 20 mbar H_2O was determined to $8 \cdot 10^{-5} \text{ S/cm}$ (according to literature [160]), which is lower than the σ_e values in the range of $\approx 10^{-3} \text{ S/cm}$ for the chemically doped PTS-TBA. The chemical doping of PTS-Na on the other hand led to σ_e in the range of 10^{-4} S/cm , which is lower than the maximum σ_{ion} of the undoped

PTS-Na ($5 \cdot 10^{-4}$ S/cm at 20 mbar H_2O , figure 4.31), therefore σ_{ion} of the chemically doped PTS-Na can be determined at 20 mbar H_2O whereas no σ_{ion} can be determined for the chemically doped PTS-TBA. It is important to note that even though only electronic conductivity behavior can be found for chemically doped PTS-Na at low water partial pressures and for PTS-TBA in the entire applied water partial pressure range, both materials still possess ionic conductivity properties in the entire water partial pressure range. The electronic conductivity is however just short-circuiting the ionic conductivity when it is approximately at least one order of magnitude higher than the ionic conductivity. This can be explained according to the equivalent circuit of the mixed conductors in figure 4.35: When the ionic resistance R_{ion} is at least one order of magnitude higher than R_{e} , all current flows over the R_{e} branch, therefore leaving out the $R_{\text{ion}} - Q_{\text{chem}}$ branch entirely. Therefore the equivalent circuit would simplify to the equivalent circuit for electronic conductors in figure 4.37. Chemical doping of PTS films with identical procedures was observed to result in large variations of the resulting electronic conductivities (also see the discussion in section 4.1.1.2), the variations of σ_{e} between the chemically doped PTS-Na and PTS-TBA can therefore not be discussed.

4.3.1.4 Pristine PTS-Na at elevated temperatures: Mixed conductivity behavior

Since it is known that the electronic conductivity of insulators and semiconductors increases with increasing temperature [29], pristine PTS-Na 93% was examined at various temperatures. The water uptake of PTS-Na 93% as function of $p\text{H}_2\text{O}$ was not determined, but since only 7% TBA⁺ remain in PTS-Na 93%, similar water uptake values as for the quantitatively exchanged PTS-Na can be expected. At first, AC impedance spectroscopy is conducted to analyze the dependence of the ionic conductivity as function of water partial pressure. In figure 4.43, σ_{ion} of undoped PTS-Na 93% at various temperatures as function of $p\text{H}_2\text{O}$ is shown.

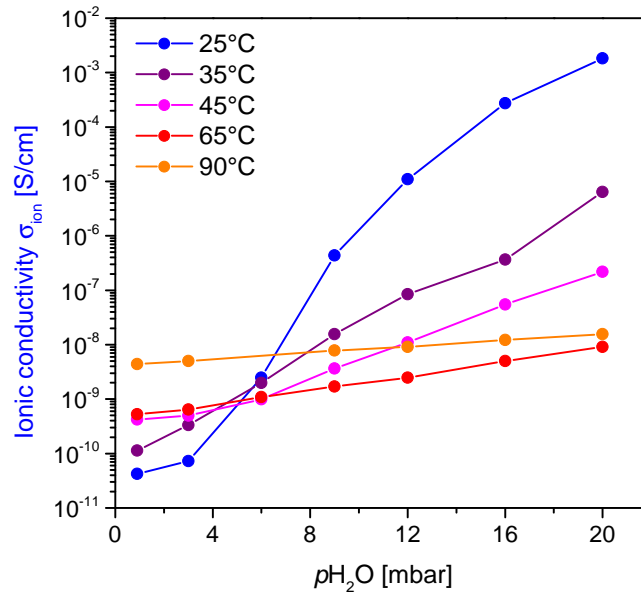


Figure 4.43: Ionic conductivity of undoped PTS-Na 93% on a 5 μm IDE at various temperatures as function of water partial pressure.

It can be seen that the trend of σ_{ion} at 25°C (blue symbols) follows the same trend as for the quantitatively exchanged PTS-Na in figure 4.31: starting from low σ_{ion} values in the range of $10^{-11} - 10^{-10}$ S/cm at 0.9 mbar H_2O , σ_{ion} increases up to around 10^{-3} S/cm at 20 mbar H_2O . Differences of the conductivities by a factor of 3 – 4, which are relatively small on a conductivity scale ranging over several orders of magnitude, are observed for all identically conducted measurements in this thesis and might be attributed to variations in the film morphology or small variations of $p_{\text{H}_2\text{O}}$ or the temperature. The variations in the film morphology might also result from the rather unreproducible spin coating procedure. The remaining amount of 7% TBA⁺ in PTS-Na 93 % is not expected to have a significant influence since the cation with the higher expected conductivity, so the Na⁺ cation, is the predominantly present species. Considering the conductivities of PTS-Na 93% in figure 4.43, σ_{ion} shows the strongest dependency of $p_{\text{H}_2\text{O}}$ at 25°C, since the water uptakes are in general highest at 25°C (the temperature dependency of the water uptakes is also discussed in detail in section 4.2.1). With increasing temperature, σ_{ion} at 20 mbar H_2O decreases since the water uptake decreases with increasing temperature. At low $p_{\text{H}_2\text{O}}$ values such as 9 or 12 mbar H_2O , the decrease of σ_{ion} with increasing temperature is smaller, since the water content is lower compared to 20 mbar H_2O , therefore also the dependency from the temperature is smaller. At $p_{\text{H}_2\text{O}} = 0.9$ mbar, σ_{ion} increases with increasing temperature presumably due to a thermally induced mobility of the mobile Na⁺ cations. The measurements at 65°C (red symbols) deviate from the trend due to unknown effects.

In figure 4.44, the calculated σ_{ion} of PTS-Na 93% at various water partial pressures as function of temperature is shown.

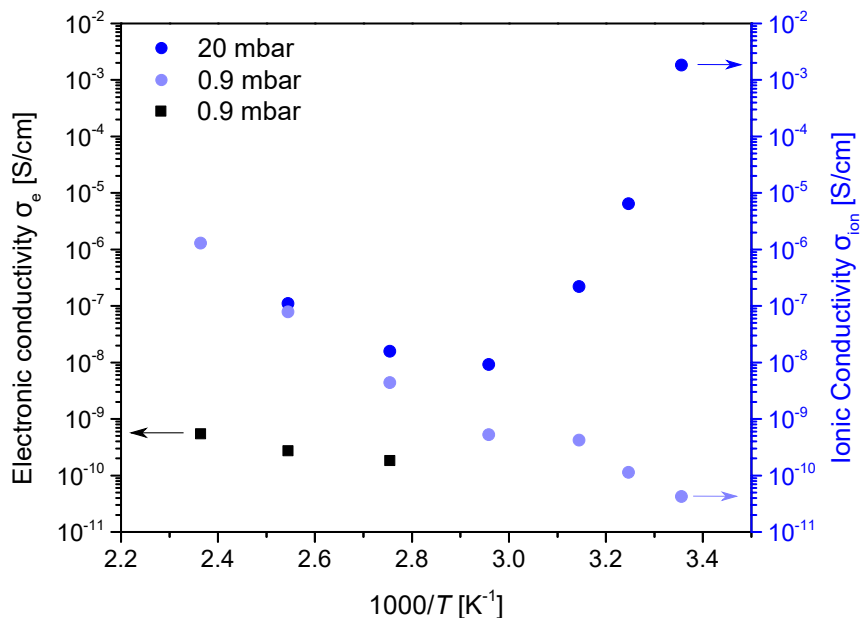


Figure 4.44: Electronic and ionic conductivity of undoped PTS-Na 93% on a 5 μm IDE at various water partial pressures as function of temperature.

Regarding σ_{ion} at 20 mbar (blue symbols), it can be seen that the values first decrease when going from a high temperature of 150°C to medium temperatures of 90°C (left to middle in figure 4.44), which can be explained by a decrease of the thermally induced dissociation between Na^+ cations and SO_3^- groups. Decreasing the temperature further (further right in figure 4.44), σ_{ion} increases due to an increasing water uptake. At 0.9 mbar H_2O , σ_{ion} continuously decreases due to the decrease of the thermally induced dissociation between Na^+ cations and SO_3^- groups [229].

At high temperatures, AC impedance spectroscopy measurements were measured down to very low frequencies of 1 mHz. Only at temperatures above 90°C (black symbols), bending of the low-frequency response was observed, indicating a second semi-circle which allowed to estimate the electronic resistance R_e from the diameter of the second semi-circle (see section 4.3.1.2). From these estimated R_e values the electronic conductivity σ_e could be calculated. For pristine PTS-Na 93%, it is therefore only at temperatures of 90°C and higher temperatures possible to determine the electronic conductivity. With values of σ_e in the range of $10^{-10} - 10^{-9}$ S/cm, the values are significantly lower than σ_{ion} and also several orders of magnitude lower than the electronic conductivity of the PTS-Na film doped with 0.5 M $\text{F}_4\text{TCNQ/THF}$.

4.3.2 PEDOT:PSS materials

As second polymeric mixed conductor system PEDOT:PSS was studied. In section 4.3.2.1 and 4.3.2.2 the results for the pristine PEDOT:PSS (1:6) and PEDOT:PSS-Na (1:6) are discussed and in section 4.3.2.3 the results for the high PEDOT content PEDOT:PSS (1:2.2) are shown.

4.3.2.1 PEDOT:PSS (1:6)

AC Impedance spectroscopy

As first PEDOT:PSS system, PEDOT:PSS (1:6) was examined with AC impedance/DC measurements at 25°C in a water partial pressure range from 0 – 20 mbar H₂O. In figure 4.45, the AC impedance spectra of PEDOT:PSS (1:6) are shown.

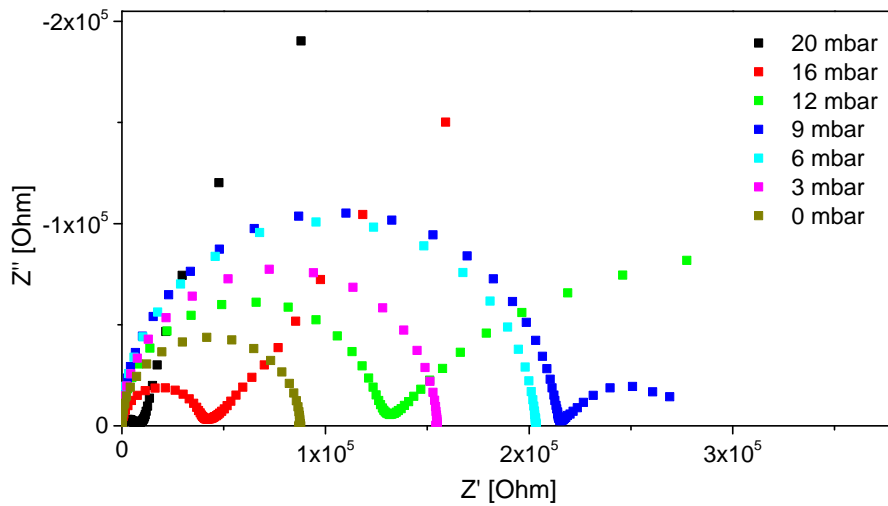


Figure 4.45: AC impedance spectra of PEDOT:PSS (1:6) on a 50 μm IDE at 25°C and various water partial pressures.

Regarding at first the high-frequency response, at 20 mbar H₂O (black symbols), the high-frequency response resembles a semi-circle with a resistance of $R_{\text{HF}} = 6.9 \text{ k}\Omega$. Decreasing $p\text{H}_2\text{O}$ to 16 mbar H₂O (red symbols), 12 mbar H₂O (green symbols) and 9 mbar H₂O (blue symbols), the high-frequency resistance increases continuously from 42 k Ω over 131 k Ω to 216 k Ω . Whereas at 20 mbar H₂O only a slight bending of the low-frequency response can be observed, the low-frequency response evolves to a second semi-circle upon decreasing $p\text{H}_2\text{O}$ down to 9 mbar H₂O. At 6 mbar H₂O (turquoise symbols), the spectrum consists of only one semi-circle with a resistance of $R_e = 203 \text{ k}\Omega$. Decreasing $p\text{H}_2\text{O}$ further down to 0 mbar H₂O, the resistance of the semi-circle decreases to $R_e = 87 \text{ k}\Omega$. Regarding the trends in the AC impedance spectra upon varying $p\text{H}_2\text{O}$, PEDOT:PSS (1:6) shows similar trends as chemically doped PTS-Na (figure 4.39). This can be explained with the fact that both materials are polymeric mixed conductors, in which the

increased values for σ_e in case of PTS-Na were only obtained after chemical doping whereas PEDOT:PSS (1:6) shows increased σ_e already in its pristine state. This is due to the chemical synthesis route of PEDOT:PSS, which yields PEDOT in its oxidized state after synthesis.

Fitting of AC Impedance spectra

Selected AC impedance spectra with corresponding fits (according to the equivalent circuit of mixed conductors in figure 4.35) of PEDOT:PSS (1:6) at selected $p\text{H}_2\text{O}$ are shown in figure 4.46.

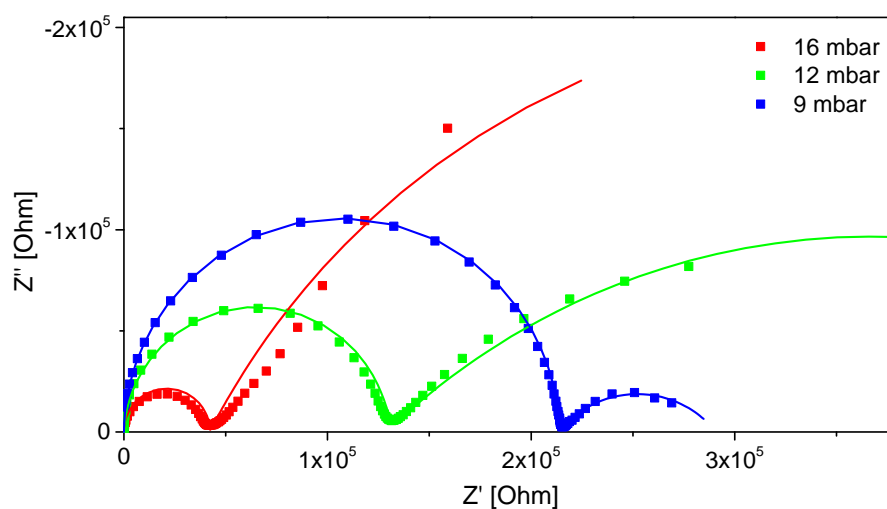


Figure 4.46: AC impedance spectra of PEDOT:PSS (1:6) on a 50 μm IDE at 25°C and various water partial pressures with fits.

As it could be observed for the fits of the chemically doped PTS-Na (figure 4.38), the high-frequency response (high-frequency semi-circle) can be described well with the utilized equivalent circuit. On the other hand, the low-frequency response is not modelled as properly, especially for the fit of the AC impedance spectra at 16 mbar H_2O (red line). The origin of the additional process, which appears to occur at the higher frequencies of the low-frequency response, can not be further elucidated. In table 4.7, the parameters of the fits in figure 4.46 are listed.

Table 4.7: Fit parameters of fits in figure 4.46.

Circuit parameter	16 mbar H ₂ O	12 mbar H ₂ O	9 mbar H ₂ O
R_e [Ω]	717990	606280	290880
$Q_{\text{geo}} - T$ [F]	$1.2 \cdot 10^{-10}$	$2.1 \cdot 10^{-10}$	$1.4 \cdot 10^{-10}$
$Q_{\text{geo}} - P$	1	0.97	0.99
R_{ion} [Ω]	44713	164030	802320
$Q_{\text{chem}} - T$ [F]	$5.3 \cdot 10^{-6}$	$5.2 \cdot 10^{-6}$	$2.1 \cdot 10^{-6}$
$Q_{\text{chem}} - P$	0.7	0.49	0.57

Whereas the obtained values for R_e decrease with $p\text{H}_2\text{O}$, the values for R_{ion} increase with increasing $p\text{H}_2\text{O}$. As for the fit parameters for the chemically doped PTS-Na, the high-frequency response can be modelled with a pure capacitive behavior with $Q_{\text{geo}} - P \leq 1$ and with capacitances in the range of 10^{-10} F. For the low-frequency response, non-ideal capacitive behavior with $Q_{\text{chem}} - P$ values in the range of 0.5 – 0.7 is obtained. Due to the fact that the fit parameters of the Q_{geo} and Q_{chem} elements for the chemically doped PTS-Na and PEDOT:PSS (1:6) are very similar, it can be stated that the electrode - polymeric mixed conductor system properties are comparable for both materials.

DC measurements

The DC measurements of PEDOT:PSS (1:6) are shown in figure 4.47. As described in section 3.3.3, the currents I in the DC measurements were set in a way that the resulting potentials did not exceed 100 mV in order to avoid decomposition of the PEDOT:PSS films. At low potentials currents of $I = 500$ nA could be applied, whereas at higher $p\text{H}_2\text{O}$ lower currents of $I = 200$ nA and $I = 100$ nA had to be applied to keep the resulting potential under 100 mV, the significant increase of R_e with increasing $p\text{H}_2\text{O}$ could therefore already be seen during the measurements.

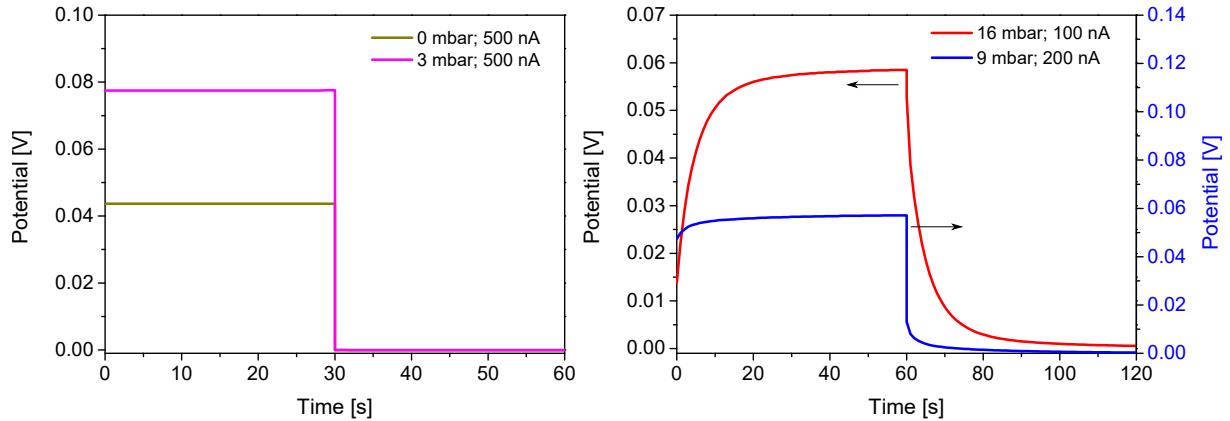


Figure 4.47: DC measurements of PEDOT:PSS (1:6) on a 50 μm IDE at 25°C and low (left) and medium to high water partial pressures (right).

The effect that R_e increases with increasing $p\text{H}_2\text{O}$ as observed in DC measurements is therefore consistent with the trend that can be observed in the AC impedance spectra regarding the low-frequency resistance. Comparing the measurements at 3 and 0 mbar H_2O (left graph in figure 4.47) and at 16 and 9 mbar H_2O (right graph in figure 4.47), it can be seen that the DC measurements at low $p\text{H}_2\text{O}$ show no change of the potential during the polarization, whereas the measurements at high $p\text{H}_2\text{O}$ show a change of the potential during the time of the applied current. The presence and the absence of the potential changes in the DC measurements coincide therefore with the presence of the high-frequency semi-circle in the AC Impedance spectra: at low $p\text{H}_2\text{O}$ no high-frequency semi-circle can be distinguished from the low-frequency response, whereas at high $p\text{H}_2\text{O}$ the high-frequency semi-circle can be observed. As a result, it can be concluded that as soon as σ_{ion} can be determined from the high-frequency semi-circle in the AC impedance spectra, the potential increase during the polarization in the DC measurements can be observed. The presence of the potential changes in the DC measurements at high $p\text{H}_2\text{O}$ can be explained as follows: upon switching on the constant current, both electronic and ionic charge carriers contribute to current conduction. During the time when the current is switched on, the ionic charge carriers become increasingly blocked at the ion-blocking electrode, in this case the combs/walls of the IDE. After the ions are blocked at the electrode, only the electronic charge carriers can contribute to current conduction and the potential reaches the steady-state potential $U_{\text{steady state}}$. After the constant current is switched off (relaxation), differences in the DC measurements can be seen as well: whereas the potential in the DC measurements at low $p\text{H}_2\text{O}$ immediately reaches 0 mV, the potential slowly decreases in case of the DC measurements at high $p\text{H}_2\text{O}$. This effect can as well be explained by the movement of the mobile ions: after switching off the current, the ions distribute over the whole volume of the polymer film back to the state before the polarization. The increasing potential during the time when the current is switched on is referred to as polarization effect in the following and the slow decrease of the potential after the current is switched off is referred to as relaxation effect in the following. The DC measurements of the chemically doped PTS in figure 4.33 and 4.41 showed a decrease of the potential at high water partial pressures, which contradicts the here given explanation and might be explained by further influences of the chemical doping of the films. Comparing the DC measurements at 16 mbar H_2O (red curve) and at 9 mbar H_2O (blue curve), it can be seen that the polarization/relaxation effects are pronounced differently. At 9 mbar H_2O , the steady state is approximately reached after 10 seconds whereas in the measurement at 16 mbar H_2O the steady state is approximately reached only after 40 seconds. Also the relaxation in the DC measurement at 16 mbar H_2O is slower compared to the measurement at 9 mbar H_2O . As a consequence, it can be concluded that the polarization/relaxation effects increase with increasing $p\text{H}_2\text{O}$ (hence also the water content). This might be explained with the higher degree of dissociation at high water

contents, which leads to an increase of the free ion concentration and so to an increase of the amount of ions which contribute to current conduction.

Conductivities

In figure 4.48, the calculated σ_e and σ_{ion} of PEDOT:PSS (1:6) at 25°C as function of p_{H_2O} and water content determined with QCM are plotted.

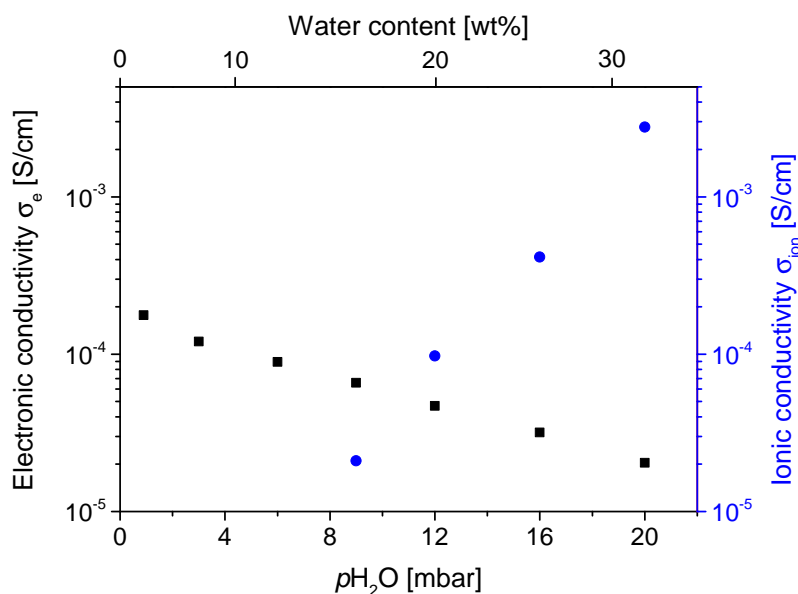


Figure 4.48: Electronic and ionic conductivity of PEDOT:PSS (1:6) on a 50 μm IDE at 25°C as function of water partial pressure and water content.

While σ_e can be detected over the entire p_{H_2O} and water content range, σ_{ion} can be determined only at p_{H_2O} equal or higher than 9 mbar H_2O or 17 wt% water content. Consequently, it can be concluded that PEDOT:PSS (1:6) shows similar behavior as chemically doped PTS-Na (figure 4.39), in which for chemically doped PTS-Na σ_{ion} could be determined only at p_{H_2O} equal or higher than 12 mbar H_2O . Starting at values in the range of 10^{-4} S/cm, σ_e decreases to around 10^{-5} S/cm upon going to 20 mbar H_2O . On the other hand, σ_{ion} increases more significantly from 10^{-5} to 10^{-4} S/cm upon increasing p_{H_2O} from 9 to 20 mbar H_2O . The similarity of the conductivity trends between chemically doped PTS-Na and PEDOT:PSS (1:6) can be explained by the similarity between both materials, which both contain ion-conducting polyelectrolyte moieties and electron-conducting polythiophene moieties.

4.3.2.2 PEDOT:PSS-Na (1:6)

AC Impedance spectroscopy

As second PEDOT:PSS material, the Na^+ exchanged PEDOT:PSS-Na (1:6) was examined. AC impedance and DC measurements were conducted at 25°C in a $p\text{H}_2\text{O}$ range from 0 – 29 mbar H_2O (note that PEDOT:PSS (1:6) was only examined in a $p\text{H}_2\text{O}$ range from 0 – 20 mbar H_2O). All conductivities in the $p\text{H}_2\text{O}$ range from 0 – 23 mbar H_2O and the electronic conductivities at 27 and 29 mbar H_2O were determined utilizing a $20\ \mu\text{m}$ IDE, the ionic conductivities at 27 and 29 mbar H_2O were determined on a $50\ \mu\text{m}$ IDE (see also the discussion about different IDEs in section 4.3.4). Exemplary AC impedance spectra in the $p\text{H}_2\text{O}$ range between 0.9 and 16 mbar H_2O are shown in figure 4.49.

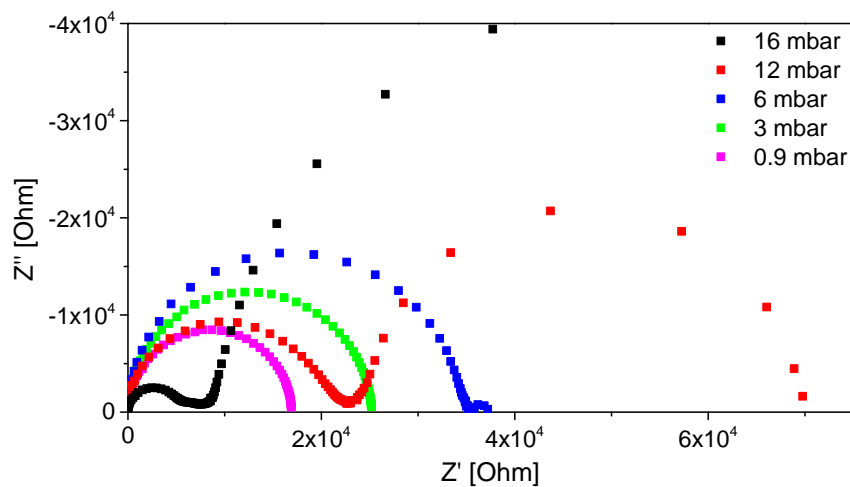


Figure 4.49: Exemplary AC impedance spectra of PEDOT:PSS-Na (1:6) on a $20\ \mu\text{m}$ IDE at 25°C and various water partial pressures.

The AC impedance spectra of the Na-exchanged PEDOT:PSS-Na (1:6) show very similar trends as the pristine PEDOT:PSS (1:6): at low $p\text{H}_2\text{O}$ only one semi-circle can be observed whereas at medium and high $p\text{H}_2\text{O}$ two semi-circles can be observed. For the pristine PEDOT:PSS (1:6) the high-frequency and low-frequency signal could be distinguished at $p\text{H}_2\text{O}$ equal or higher than 9 mbar H_2O , for PEDOT:PSS-Na (1:6) after the high-frequency semi-circle a slight low-frequency response can be recognized already at 6 mbar H_2O (blue symbols). The general trends are however the same: the high-frequency resistance R_{HF} increases when going from 16 to 6 mbar H_2O and the low-frequency R_{LF} decreases when decreasing $p\text{H}_2\text{O}$ from 12 to 0.9 mbar H_2O . Also the DC measurements in figure 4.50 show the same trends as the DC measurements of the pristine PEDOT:PSS (1:6).

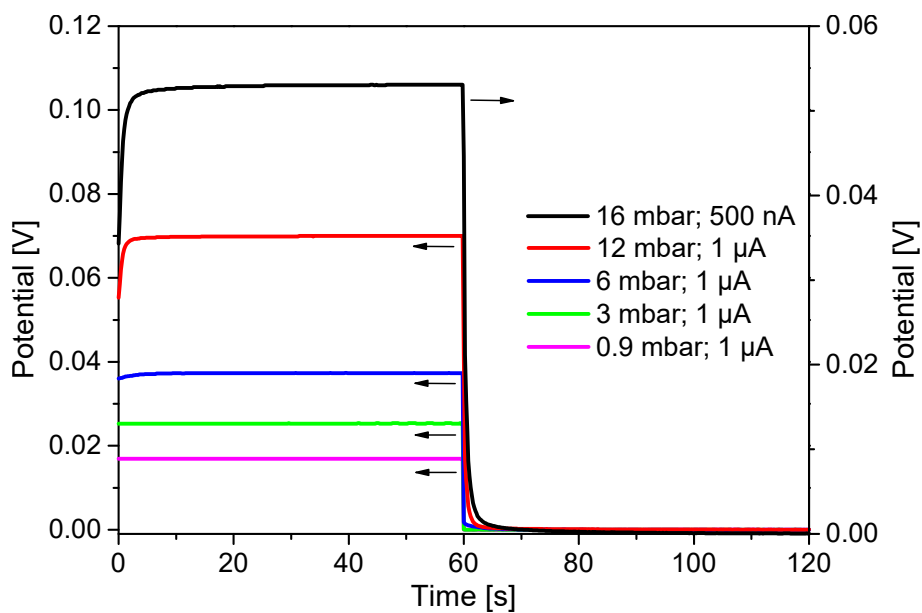


Figure 4.50: Exemplary DC measurements of PEDOT:PSS-Na (1:6) on a 20 μm IDE at 25°C and various water partial pressures.

The DC measurements resemble the same trend as the DC measurements of the pristine PEDOT:PSS (1:6): the steady state potential increases with increasing $p\text{H}_2\text{O}$. Also the potential trends show the same behavior: at low $p\text{H}_2\text{O}$ no polarization/relaxation effects can be observed and starting at 6 mbar H_2O (blue line), polarization/relaxation effects can be recognized which intensify with increasing $p\text{H}_2\text{O}$.

In figure 4.51, the calculated σ_e and σ_{ion} as function of pH_2O and water content are shown.

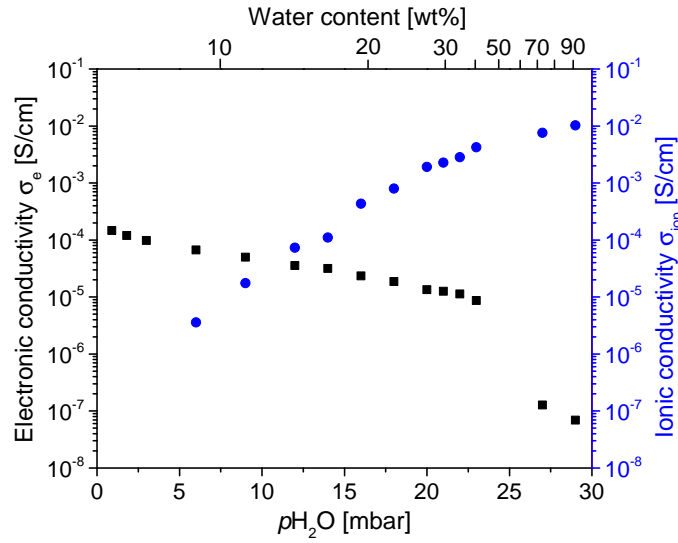


Figure 4.51: Electronic and ionic conductivity of PEDOT:PSS-Na (1:6) at 25°C as function of water partial pressure and water content. All conductivities in the water partial pressure range from 0 – 23 mbar H_2O and the electronic conductivities at 27 and 29 mbar H_2O were determined using a 20 μm IDE, the ionic conductivities at the water partial pressures of 27 and 29 mbar H_2O were determined using a 50 μm IDE.

The values for σ_{ion} at 27 and 29 mbar H_2O were determined with a PEDOT:PSS-Na film on a 50 μm IDE since only the measurements on the 50 μm IDE resulted in a high-frequency semi-circle because the measurements on the 20 μm IDE would lead to a resistance of the high-frequency semi-circle which is too low to be determined (see also the discussion in section 4.3.4). The DC measurements for the determination of σ_e at very high pH_2O had to be repeated twice with new films on 20 μm IDEs since in the first two attempts no steady state was reached which could have allowed the determination of a value for R_e . Only for the third film, a steady state in the DC measurements could be obtained.

Whereas the conductivities for the pristine PEDOT:PSS (1:6) were conducted in a pH_2O range from 0–20 mbar H_2O , the conductivities for PEDOT:PSS-Na (1:6) were determined in a range from 0–29 mbar H_2O . In the pH_2O range from 0–20 mbar H_2O , PEDOT:PSS-Na (1:6) shows very similar behavior as PEDOT:PSS (1:6): σ_e decreases from $\approx 10^{-4}$ to 10^{-5} S/cm and starting at 6 mbar H_2O , σ_{ion} increases from $\approx 10^{-6}$ S/cm to low values in the range of 10^{-3} S/cm at 20 mbar H_2O . Upon going to the highest pH_2O range up to 29 mbar H_2O , σ_{ion} increases only slightly up to 10^{-2} S/cm, therefore resulting in a plateau value of σ_{ion} . In contrast to that, σ_e decreases significantly down to 10^{-7} S/cm. The strong decrease of σ_e might be explained with the strong increase of the water con-

tent from ≈ 40 wt% at 23 mbar H_2O to ≈ 90 wt% at 29 mbar H_2O , which might result in a significant increase of the distance between electronically conducting PE-DOT moieties. The electronic conductivity σ_e shows therefore a very similar dependency from $p\text{H}_2\text{O}$ as the water uptakes (as can be seen in figure 4.24): whereas σ_e decreases only slightly and the water uptake increases only slightly in the $p\text{H}_2\text{O}$ range up to 23 mbar H_2O , σ_e decreases substantially and the water uptake increases considerably upon going to 29 mbar H_2O . This strong correlation between σ_e and the water uptake could be explained with the fact that σ_e depends on the distance between the electronically conducting moieties and this distance increases most significantly at high $p\text{H}_2\text{O}$ or water uptakes [4, 8]. On the other hand, the minor increase of σ_{ion} upon switching from 23 mbar H_2O to 29 mbar H_2O could be explained with the fact that at 23 mbar H_2O , the dissociation of the Na^+ cation from the SO_3^- group is already high and further water uptake does not lead to significantly more dissociation. All conductivity values as function of water content are depicted in section 4.3.5.

Analysis of transient behavior

As can be seen in the DC measurements shown in figure 4.50, the polarization/relaxation effects are more significant when the system transforms from a predominantly electronic conductor towards a predominant ionic conductor, which means that the factor $\sigma_{\text{ion}}/\sigma_e$ becomes larger [219]. Regarding the conductivity values in figure 4.51, this is the case when $p\text{H}_2\text{O}$ becomes larger.

The transient behavior was evaluated for the DC measurement at each water partial pressure. From the steady state potential $U_{\text{steady state}}$ at the end of the polarization time, the potential at each time $U(t)$ and the start potential $U_{t=0}$ from the potential trend in the DC measurements, the normalized voltage can be calculated according to $U_{\text{norm}} = \ln((U_{\text{steady state}} - U(t))/(U_{\text{steady state}} - U_{t=0}))$ [230, 231]. From the plot of U_{norm} versus t , the long time limit of the slope of the regression line can be obtained. The slope of the regression line corresponds to the characteristic time $\tau = L^2/(\pi^2 D^\delta)$, from which together with L as the electrode distance, the chemical diffusion coefficient D^δ of the blocked carrier (here the ions that are blocked at the electrode walls) in combination with its compensating carrier (electrons) can be calculated [160, 219]. In figure 4.52, the diffusion coefficient D^δ as function of $p\text{H}_2\text{O}$ is shown.

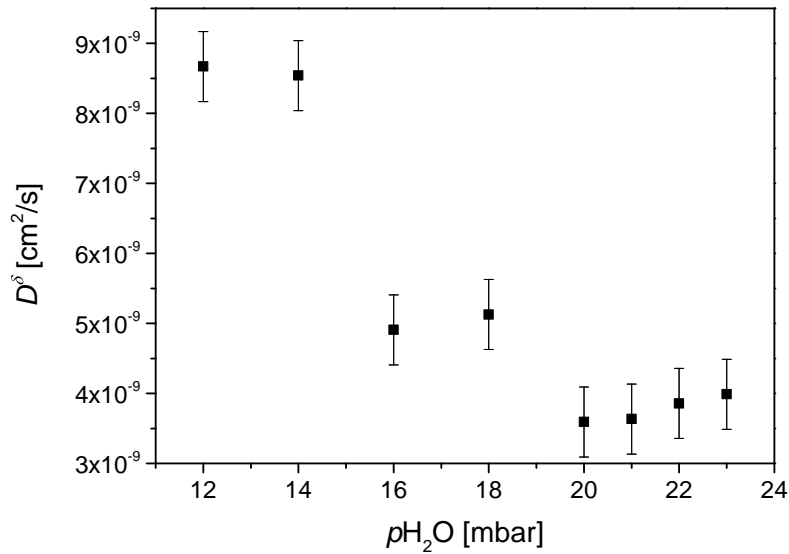


Figure 4.52: Analysis of the transient behavior of the DC measurements of PEDOT:PSS-Na (1:6) in figure 4.50: diffusion coefficient D^δ as function of water partial pressure.

Initially one would assume that D^δ increases with $p_{\text{H}_2\text{O}}$ since σ_{ion} increases with $p_{\text{H}_2\text{O}}$ or R_{ion} decreases with $p_{\text{H}_2\text{O}}$. Regarding the dependency of the chemical diffusion coefficient D^δ from $p_{\text{H}_2\text{O}}$, it can however be seen that D^δ decreases with increasing $p_{\text{H}_2\text{O}}$. The chemical diffusion coefficient is limited by the charge carrier with the lowest transference number. At high $p_{\text{H}_2\text{O}}$, the electronic carrier has the lowest transference number. Therefore, the general tendency is that D^δ decreases with increasing $p_{\text{H}_2\text{O}}$.

4.3.2.3 PEDOT:PSS (1:2.2)

DC measurements

In addition to low-PEDOT content PEDOT:PSS batches with a PEDOT to PSS weight ratio of 1 to 6, a high PEDOT content PEDOT:PSS batch with a PEDOT to PSS ratio of 1 to 2.2 was examined. Since AC impedance measurements showed inductive signals at very low resistance values, which presumably result from contributions from the cable system, no AC impedance spectra were recorded. The DC measurements of PEDOT:PSS (1:2.2) at 25°C at various $p\text{H}_2\text{O}$ are shown in figure 4.53.

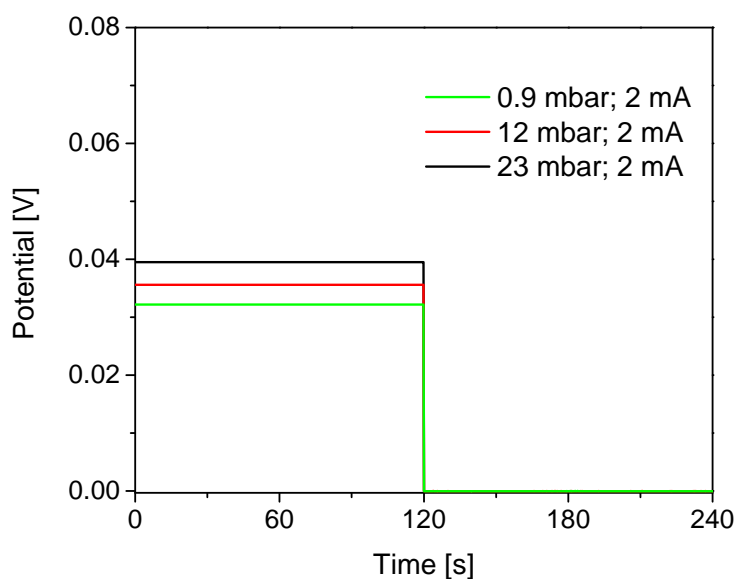


Figure 4.53: DC measurements of PEDOT:PSS (1:2.2) on a 50 μm IDE at 25°C as function of water partial pressure.

In the potential trends of all depicted DC measurements, no polarization/relaxation effects can be seen. All previously shown DC measurements had to be conducted with constant currents in the nA to μA range in order to prevent the resulting potential from exceeding over 100 mV. The DC measurements of PEDOT:PSS (1:2.2) however could be conducted with constant currents of $I = 2 \text{ mA}$, which results in low R_e values. In spite of the large $p\text{H}_2\text{O}$ range up to 23 mbar H_2O , the resulting potential does increase only very slightly when going from 0.9 mbar H_2O (green line) to 23 mbar H_2O (black line).

Conductivities

The electronic conductivity σ_e as function of $p\text{H}_2\text{O}$ and water content is shown in figure 4.54.

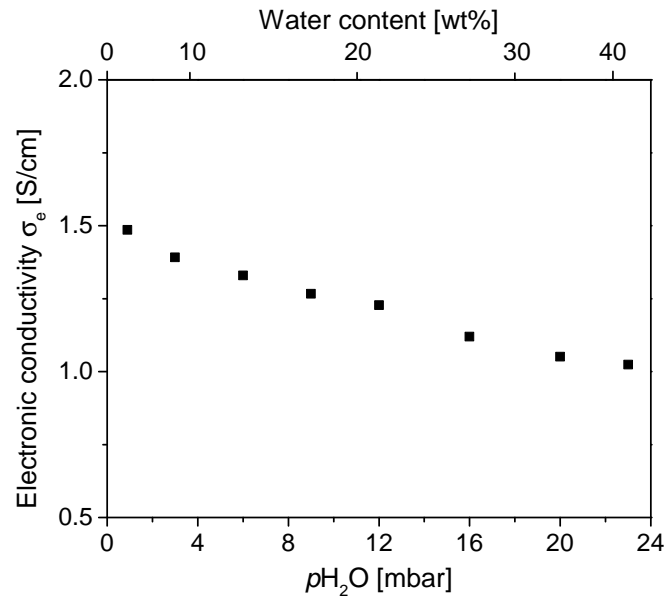


Figure 4.54: Electronic conductivity of PEDOT:PSS (1:2.2) on a 50 μm IDE at 25°C as function of water partial pressure and water content.

The values of σ_e for PEDOT:PSS (1:2.2) are in the range of 1 S/cm, which is consistent with the literature data for high PEDOT content PEDOT:PSS batches like PEDOT:PSS (1:2.5) without further treatment [134]. PEDOT:PSS (1:2.2) shows therefore values for σ_e which are four to five orders of magnitude higher than the values of σ_e for PEDOT:PSS (1:6) and PEDOT:PSS-Na (1:6). This significant difference can be explained with the higher content of PEDOT in the PEDOT:PSS (1:2.2) material as described in section 4.2.2.3. One possible consequence of this might be that the connection between the electronically conducting PEDOT moieties in the PEDOT:PSS (1:6) materials (the different morphology models about the phase separation of PEDOT and PSS moieties are summarized in [106]) is significantly worse than in the PEDOT:PSS (1:2.2) materials. The dependency of σ_e as function of $p\text{H}_2\text{O}$ or water content is also different between the 1:6 and the 1:2.2 PEDOT:PSS batches: for the PEDOT:PSS (1:6) materials σ_e changes by around one order of magnitude upon increasing $p\text{H}_2\text{O}$ from 0.9 to 23 mbar H_2O . On the other hand, σ_e of PEDOT:PSS (1:2.2) changes by only around 50% in the $p\text{H}_2\text{O}$ range from 0.9 to 23 mbar H_2O . This effect could be explained with the PEDOT to PSS ratio as well: the uptake of water leads to a decrease of the already weak connection between the PEDOT moieties in the PEDOT:PSS (1:6) materials even more, whereas on the other hand the good connectivity between the PEDOT moieties in the PEDOT:PSS (1:2.2) material is not significantly disturbed by additional water. The low decrease of σ_e for high PEDOT content PEDOT:PSS with increasing water uptake was

also observed previously in literature [4, 161]. As discussed for chemically doped PTS-TBA in section 4.3.1.3, it is important to note that PEDOT:PSS (1:2.2) still possesses ionic conductivity behavior, the ionic conductivity behavior is however observable due to the high electronic conductivity of PEDOT:PSS (1:2.2).

4.3.3 PEDOT:PSS-PVA composite materials

In a collaboration with the Bio-Electronics Laboratory of Professor Myung-Han Yoon at the Gwangju Institute of Technology (Republic of Korea) the conductivity behavior of films consisting of composite materials from PEDOT:PSS and poly(vinyl alcohol) (PVA) were examined as function of the composition and water partial pressures. The structure of PVA is shown in figure 4.55.

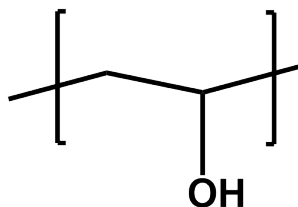


Figure 4.55: Chemical structure of poly(vinyl alcohol).

For PEDOT:PSS, the pristine dispersion of either PEDOT:PSS (1:2.5) or PEDOT:PSS (1:6) was used and for PVA, a 1 vol% solution of PVA ($\overline{M}_W = 146000 - 186000$ kg/mol, purchased from *Sigma Aldrich*) in water was utilized in order to prepare the composite materials. All films from PEDOT:PSS-PVA mixtures are prepared according to literature [137]. At first, a fixed volume of either PEDOT:PSS or PVA dispersion is mixed with a small volume of PVA or PEDOT:PSS. The resulting composite materials are referred to as according to the contents of the spin coating solution. For example, in order to prepare "PEDOT:PSS/PVA 10%" or "PVA/PEDOT:PSS 2%", a fixed volume of PEDOT:PSS is mixed with 10% PVA solution of this volume or a fixed volume of PVA solution is mixed with 2% of this volume of a PEDOT:PSS dispersion, respectively. After vigorous stirring of the solution, films are spin coated onto the IDE substrates at 1500 rotations per minute. Chemical crosslinking between PEDOT:PSS and PVA is provided by heating the films at 120°C for four hours.

Two different composition types were analyzed: firstly either PEDOT:PSS - PVA composite materials with high PEDOT:PSS contents and low PVA contents (therefore referred to as PEDOT:PSS/PVA in the following) and secondly composite materials with high PVA and low PEDOT:PSS contents (therefore referred to as PVA/PEDOT:PSS in the following). For the high PEDOT:PSS content composite materials PEDOT:PSS

(1:6) was used, for the high PVA content composite materials PEDOT:PSS (1:2.5) was used. Both compositions were examined in order to determine the minimum required PEDOT:PSS content which is required to maintain the conductivity properties of pure PEDOT:PSS since PVA corresponds to an electronically and ionically insulating material. The low PEDOT:PSS content composite materials were analyzed since it is known that tissues made from PVA materials (due to their water uptake properties referred to as hydrogels) have potential for biomedical applications and show high transparency, in which PEDOT:PSS was added in the present study to add also conducting properties to the hydrogels [232, 233]. For the high PEDOT:PSS content PEDOT:PSS/PVA composite materials, four different PEDOT:PSS - PVA mixture ratios with PVA contents of 0%, 10%, 30% and 50% were utilized. The resulting composite materials are referred to as PEDOT:PSS (1:6)/PVA 0%, PEDOT:PSS (1:6)/PVA 10%, PEDOT:PSS (1:6)/PVA 30% and PEDOT:PSS (1:6)/PVA 50% in the following. For the high PVA content PVA/PEDOT:PSS, PEDOT:PSS (1:2.5) contents between 2 and 6% in PVA were utilized, the resulting composite materials are referred to as PVA/PEDOT:PSS (1:2.5) 3%, PVA/PEDOT:PSS (1:2.5) 5% and PVA/PEDOT:PSS (1:2.5) 7%.

4.3.3.1 PEDOT:PSS/PVA

With the help of AC impedance and DC measurements, the conductivities of the aforementioned PEDOT:PSS/PVA materials (PEDOT:PSS (1:6) was utilized) with different PVA contents were determined, in which the measurements were conducted at 27°C. The AC impedance and DC measurements resemble the same features as the previously shown measurements for PEDOT:PSS (1:6) and PEDOT:PSS-Na (1:6), the AC impedance and DC measurements are therefore not shown. The obtained film thicknesses decrease from 40 ± 1 nm obtained for PEDOT:PSS (1:6)/PVA 0% over 25 ± 7 nm for PEDOT:PSS (1:6)/PVA 10% and 25 ± 3 nm for PEDOT:PSS (1:6)/PVA 30% to 24 ± 0 nm for PEDOT:PSS (1:6)/PVA 50%. This might eventually be explained by a decreasing viscosity of the PEDOT:PSS/PVA mixture with increasing PVA content or a variation of the hydrophilicity of the mixture. In figure 4.56 and 4.57, σ_e and σ_{ion} of PEDOT:PSS (1:6)/PVA as function of pH_2O is shown.

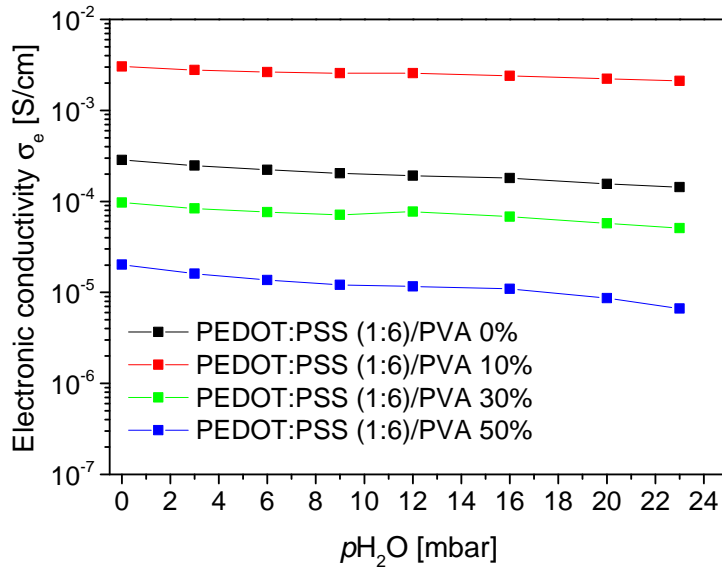


Figure 4.56: Electronic conductivity of PEDOT:PSS (1:6)/PVA composite materials with various PVA contents on 10 μm IDEs at 27°C as function of water partial pressure.

Comparing σ_e for the different PEDOT:PSS/PVA materials in figure 4.56, it can be seen that σ_e strongly depends on the PVA content. At 0% PVA content (black symbols), the PEDOT:PSS film shows σ_e in the range of 10^{-4} S/cm, which is very comparable to the values obtained for the previously shown PEDOT:PSS (1:6) and PEDOT:PSS-Na (1:6) in figures 4.48 and 4.51. Increasing the PVA content to 10% (red symbols), σ_e increases for around one order of magnitude up to 10^{-3} S/cm. This could be explained by the fact that PVA increases the phase separation between PEDOT and PSS rich moieties. Increasing the PVA content further up to 30% and 50% (green and blue symbols), σ_e decreases for two orders of magnitude down to values of 10^{-5} S/cm. This decrease might be explained with the increasing amount of electronically insulating PVA, which leads to a decrease of σ_e of the composite material as was observed in literature [149, 154, 234]. It has to be noted however that in literature only PEDOT:PSS/PVA composite materials with the PEDOT:PSS (1:2.5) batches were examined.

Comparing the dependency of σ_e from $p\text{H}_2\text{O}$, it can be seen that σ_e of PEDOT:PSS (1:6)/PVA 10% decreases only for around 50% when switching from the lowest to the highest $p\text{H}_2\text{O}$ in the examined $p\text{H}_2\text{O}$ range. In contrast to that, σ_e of PEDOT:PSS/PVA (50%) changes by a factor of 3 in the examined $p\text{H}_2\text{O}$ range. The different dependency of σ_e from $p\text{H}_2\text{O}$ was observed for the PEDOT:PSS (1:6) and PEDOT:PSS (1:2.2) batches as well, therefore the same explanation can be used here as well: the higher σ_e already is, the lower the dependency from $p\text{H}_2\text{O}$ seems to be. This can be explained with the fact that if the connectivity between the electronically conducting

PEDOT moieties is good, water uptake does disturb the connectivity only slightly. On the other hand, if the connectivity is already not sufficient in case of low σ_e values, water uptake disturbs the connectivity significantly.

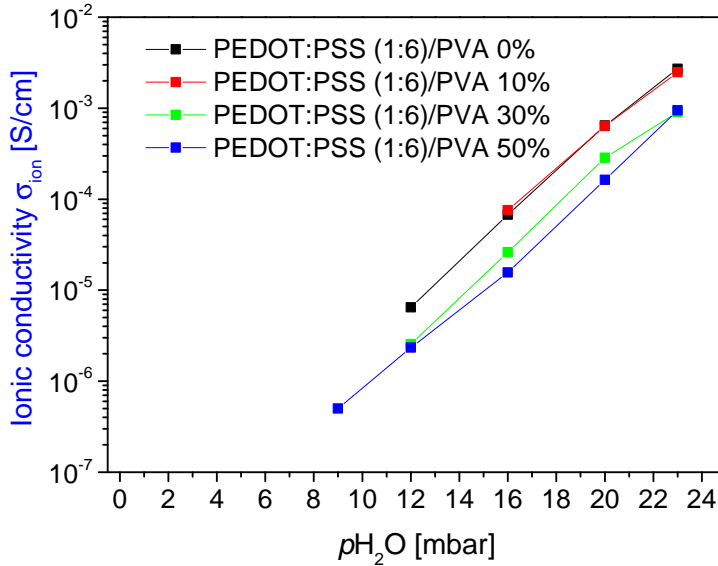


Figure 4.57: Ionic conductivity of PEDOT:PSS (1:6)/PVA composite materials with various PVA contents on 10 μ m IDEs at 27°C as function of water partial pressure.

Comparing the values for σ_{ion} for the different PEDOT:PSS (1:6)/PVA compositions, it can be seen that the values are only slightly dependent from the PVA content. This is in significant contrast to the strong dependency of σ_e from the PVA content as shown in figure 4.56. The obtained σ_{ion} values are for all compositions very comparable. The observation that σ_{ion} shows only a very small dependency from the composition might be explained by the fact that the PEDOT:PSS content and therefore also the cation content is except from a decrease by 50%, which is in the range of the measurement error of the conductivities, constant.

Considering the fact that on the one hand σ_e shows a strong dependency from the PVA content, whereas on the other hand σ_{ion} shows only a minor dependency from the PVA content, it could be assumed that different effects influence the two conduction mechanisms. For the electronic conductivity, the percolation between the electronically conducting PEDOT moieties might be significantly disturbed by the presence of PVA in the composite material (at PVA contents of 30% and 50%), the electronic conductivity is therefore assumed to be dependent on macroscopic percolation of the PEDOT moieties in the PEDOT:PSS/PVA material. For the ionic conductivity on the other hand, the decrease of the ion concentration in the composite material due to a decrease of the con-

centration of the ion containing PEDOT:PSS (assuming constant film thicknesses) leads to a decrease of the ionic conductivity by roughly the same factor. Therefore, it can be assumed that the ionic conductivity results from microscopic properties of the material since it originates from the concentration of ions in the PEDOT:PSS/PVA composite material. The water uptake was neither determined for PEDOT:PSS (1:6)/PVA nor for pure PVA which might have allowed to examine the variations of σ_{ion} and σ_e further.

4.3.3.2 PVA/PEDOT:PSS

For the films from PVA/PEDOT:PSS mixtures (for these composite materials high volumes of PVA solution were mixed with low volumes of PEDOT:PSS (1:2.5) dispersion), significantly different film thickness values than for the low PVA content PEDOT:PSS/PVA composite materials were obtained. Whereas for the PEDOT:PSS/PVA films thicknesses in the range between 25 – 40 nm were obtained, film thicknesses ranging from 4 – 7 μm were obtained for the PVA/PEDOT:PSS (1:2.5) films. A film thickness of 220 nm was assumed for calculation of the conductivities, since it was assumed that only the polymer material in between the combs (the interdigitated Pt structure has a thickness of 220 nm) contributes to the current conduction. The contribution of the part of the polymer material which is above the Pt structures remains unknown, therefore the conductivities might be error containing. A second issue in determining the conductivities was that the obtained resistance values amounted to 30 Ω and lower. The contributions of the wiring and contact resistances are therefore unknown, which makes the calculation of the conductivities even more difficult. In figure 4.58, the electronic and ionic conductivity of PVA/PEDOT:PSS (1:2.5) composite materials at 25°C as function of water partial pressure is shown.

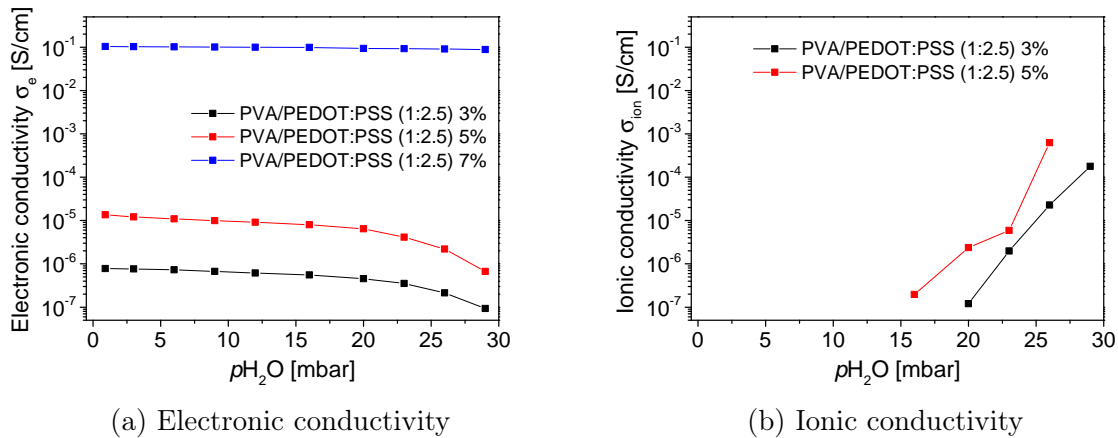


Figure 4.58: Conductivities of PVA/PEDOT:PSS (1:2.5) composite materials with various PEDOT:PSS contents on 20 μm IDEs at 25°C as function of water partial pressure.

Regarding σ_e as shown in figure 4.58a, a clear increase of σ_e with increasing PEDOT:PSS content can be observed. Whereas the PVA/PEDOT:PSS (1:2.5) materials with PEDOT:PSS contents of 3% (black symbols) and 5% (red symbols) show electronic conductivities in the range of $\sigma_e \approx 10^{-6} - 10^{-5}$ S/cm, the PVA/PEDOT:PSS (1:2.5) composite material with a PEDOT:PSS content of 7% (blue symbols) shows significantly higher values in to the range of $\approx 10^{-1}$ S/cm. In case of the 7% PEDOT:PSS sample, the PEDOT:PSS content might be sufficiently high enough to provide good connectivity between the electronically conducting PEDOT moieties, whereas in the 3% and 5% PEDOT:PSS content samples no connectivity seems to be possible. For P3HT-polyethylene copolymers with various P3HT contents a similar effect could be observed: whereas for the entire P3HT content range of 10% or higher the field effect mobility μ_{ef} is roughly constant, for P3HT contents below 10% μ_{ef} decreases significantly [235]. A similar explanation might also be taken for the dependency of σ_e from pH_2O : whereas the 3% and 5% PEDOT:PSS content samples expose already a weak connectivity which is further weakened by water taken up (note the strong decrease of σ_e at pH_2O above 20 mbar H_2O), the good connectivity in the 7% PVA/PEDOT:PSS (1:2.5) material is not significantly disturbed by absorbed water. Even though σ_e of PEDOT:PSS (1:2.2) (as shown in section 4.3.2.3) was not analysed at pH_2O values higher than 23 mbar H_2O , it might accordingly not be expected that σ_e decreases significantly at 26 or 29 mbar H_2O , a more pronounced decrease compared to the slight decrease at low pH_2O might eventually still be observable. As for the PEDOT:PSS (1:6)/PVA materials, also for the PVA/PEDOT:PSS (1:2.5) materials no water uptake was determined, which might have allowed to discuss the variations of σ_e upon variation of pH_2O further.

Considering σ_{ion} as depicted in figure 4.58b, it can be seen that no values could be determined for the 7% PVA/PEDOT:PSS (1:2.5) material. This can be explained by the fact that σ_e is at all pH_2O higher than σ_{ion} . Starting at 16 mbar H_2O in case of the 5% PEDOT:PSS containing composite material and at 20 mbar H_2O for the 3% PEDOT:PSS containing composite material, values for σ_{ion} can be determined. As typical polyelectrolyte behavior, σ_{ion} increases with pH_2O . Comparing the values for σ_{ion} at a given pH_2O , the 5% PEDOT:PSS containing composite material shows higher values than the 3% PEDOT:PSS composite material, which can be explained by the higher ion content.

4.3.4 Comparison of different interdigitated electrode geometries

During the course of the present study, IDEs with different geometrical parameters were used as substrates for the polymeric mixed conductor systems to determine their conductivity properties (as listed in table 3.1). Theoretically, the calculated electronic and ionic conductivities (according to equations 13 and 14) are independent of the geometrical factor g ($g = l/(w \cdot h)$, here h corresponds to the film thickness, l to the channel length

and w to the channel width) of the IDE, since the analyzed material with its conductivity properties is the same in each case. According to the equations, this would mean that an increase of g by a certain factor would result in an increase of R_{ion} or R_e by the same factor, so that the calculated conductivity is the same in each case. For example, the 5 μm IDE has a channel length of $l = 5 \mu\text{m}$ and a channel width of $w = 191.70 \text{ cm}$, on the other hand the 10 μm IDE has a channel length of $l = 10 \mu\text{m}$ and a channel width of $w = 95.85 \text{ cm}$. Switching from the 5 μm to the 10 μm IDE results thus in an increase of g by a factor of 4 since the channel length in the nominator of g doubles and the channel length in the denominator of g is halved. In order to prove the assumption that the determined conductivities are independent of the utilized IDE geometry, PEDOT:PSS (1:6) was spin coated on IDEs with each of the 5 different geometries (as listed in table 3.1). AC impedance and DC measurements in ambient conditions, so without applying certain temperature or water partial pressure conditions. The AC impedance spectra resemble the high- and low-frequency semi-circle typical for mixed conducting samples as for the chemically doped PTS-Na or the PEDOT:PSS (1:6) materials and are therefore not shown. In table 4.8, the values determined for R_{ion} and R_e for each IDE type are listed. Additionally, the factors by which R_{ion} and R_e increase with respect to the resistance values obtained for the 5 μm IDE are listed in brackets after the corresponding resistance values. Furthermore, the increase of the geometry factor g in relation to the 5 μm IDE are listed.

Table 4.8: Obtained resistances for comparison measurements on the different IDE types.

IDE type	R_{ion} [Ω] (incr. factor)	R_e [$\text{k}\Omega$] (incr. factor)	incr. factor of g
5 μm	206 -	5 -	-
10 μm	699 (3.4)	21 (4.1)	4
20 μm	2662 (12.9)	71 (13.9)	16
50 μm	22813 (110.7)	465 (91.4)	100
100 μm	106906 (518.9)	1825 (358.5)	400

Comparing the increase factors of the resistances in table 4.8 (in brackets in columns 2 and 3) to the increase factors of g (column 4), it can be seen that the values fit with a deviation of up to 30 %. The deviation might result for example from the deviations due to the spin coating procedure, due to variation of the film thickness h or from varying coverages of the IDEs and can thus be estimated to be present for all films in the present study. Since the increase factors of the resistances equal the increase factors of g , it can be stated that the same conductivities can be calculated on all different IDE types. Due to technical limitations of the utilized spectrometer device (here the *IM6* device from *Zahner*), the resistance values that can be measured have a lower and upper detection limit. The lower detection limit at low resistance values, roughly 300 Ω for AC impedance measurements and 20 Ω for DC measurements, results from the presence of inductive effects in case of

AC measurements and contact resistances (resistance from the electrical contact at the interface between the Pt combs of the IDE and the polymer film) and wiring resistances (resistance of summed up electrical contacts in the electrical circuit from measurement device till polymer film) for both AC impedance and DC measurements. The influence of both, the inductive effects and the contact and wiring resistances, is difficult to be eliminated, thus proper choice of the IDE type is important. For example, if the high electronic conductivity of a polymer film results in R_e values of $10\ \Omega$ on a $5\ \mu\text{m}$ IDE which is in the range of the contact and wiring resistances and can therefore not be evaluated, R_e values of $1000\ \Omega$ would be obtained using a $50\ \mu\text{m}$ IDE which is much larger than the contact and wiring resistances. The relative contribution of the inductive effects and the wiring resistance to the measured resistance value becomes therefore smaller. The upper limit on the other hand, which is in the low $\text{G}\Omega$ range, is due to technical device limitations. Lower resistance values can be obtained by choosing IDE types with a lower channel length instead of higher channel lengths. Resistances in AC impedance and DC measurements can be determined best if the resistance values are in the $\text{k}\Omega$ and the low to mid $\text{M}\Omega$ range.

As it was already mentioned, for all 5 pristine films, both AC impedance as well as DC measurements were conducted. The DC measurement were conducted with a polarization time and a relaxation time of each 30 seconds. The normalized potential trends can be found in figure 4.59.

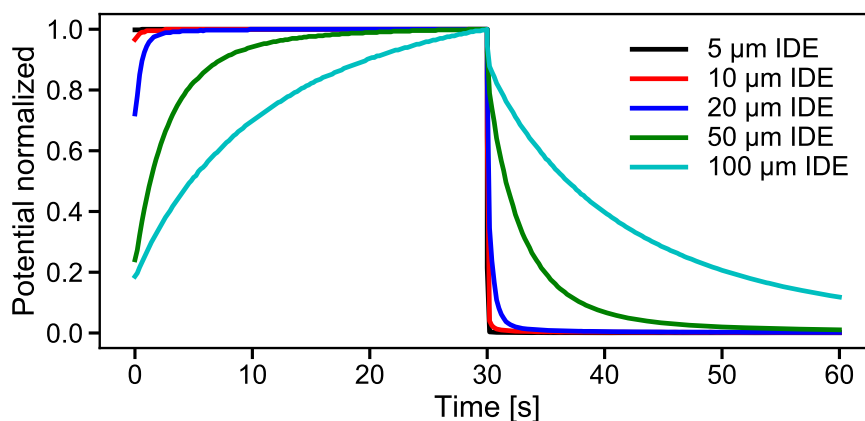


Figure 4.59: DC measurements of pristine PEDOT:PSS (1:6) films at 25°C on different IDE types.

Comparing the potential trends on the different IDE types, it can be seen that in case of the $5\ \mu\text{m}$ IDE the time until the steady state is reached is after around 1 second. At higher channel lengths, the time until the steady state is reached increases, e.g. for the $20\ \mu\text{m}$ IDE the steady state is reached after around 10 seconds. For the $100\ \mu\text{m}$ IDE, the steady state is not even reached after 30 seconds. This can be explained with the fact that the time until the ions reach the ion-blocking electrode walls increases with the distance

that the ions need to cover, so the time until the steady state is reached increases with increasing channel length. Therefore, with the dependency of the steady state time from the channel length the ion movement through films of the polymeric mixed conductor PEDOT:PSS can presumably be detected.

4.3.5 Discussion and summary of conductivity studies

The conductivity chapter is discussed and summarized with various data of σ_{ion} and σ_e for the different studied materials as function of water content. In figures 4.60 and 4.61, σ_e and σ_{ion} of pristine PTS-Na, chemically doped PTS-Na, pristine PTS-TBA (the data are taken from [160]), chemically doped PTS-TBA, PEDOT:PSS (1:6), PEDOT:PSS-Na (1:6) and PEDOT:PSS (1:2.2) are shown as function of water content. Additionally, σ_{ion} as function of λ is displayed in figure 4.62. It is important to mention that firstly the water partial pressure ranges at which the water contents and conductivities were determined varied and secondly that the water uptake differed significantly between the various materials, the respective conductivities cover therefore significantly different ranges of the displayed water content ranges. Subsequently, the percolation theory is discussed in order to relate various in-situ conductance and conductivity observations in this thesis to percolation effects.

Electronic conductivity as function of water uptake in wt%

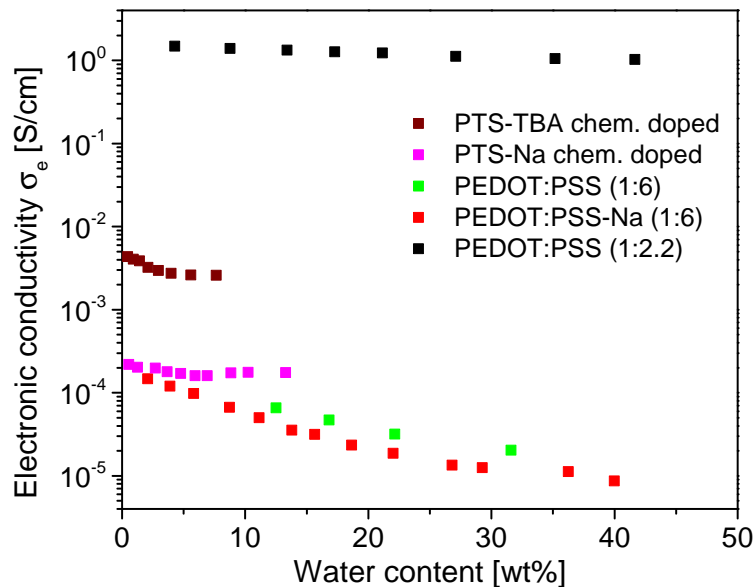


Figure 4.60: Electronic conductivity of various polymer materials at 25°C as function of water content.

As previously described, PEDOT:PSS (1:2.2) (black symbols) shows σ_e in the range of 1 S/cm and no significant decrease upon increase of the water content. On the other hand, both the pristine and the Na-exchanged PEDOT:PSS-Na (1:6) materials (red and green symbols) show σ_e values in the range of 10^{-4} S/cm in the dry state and a decrease to 10^{-5} S/cm upon increase of the water content. The four order of magnitude smaller values of σ_e can be explained with the lower PEDOT content in the PEDOT:PSS (1:6) materials. The PEDOT content dependent electronic conductivity was also observed in a series of PEDOT:PSS materials with varying PEDOT to PSS ratios from 1:1 to 1:30 in literature [103]. For a variety of PEDOT materials, Wang et al. found for materials with high PEDOT content (like PEDOT doped with tosylate) AC impedance spectra which consisted of one semi-circle with low resistances [8]. For pristine PEDOT:PSS with a PEDOT to PSS weight ratio of 1:4 two semi-circles and for PEDOT:PSS mixed with poly(sodium 4-styrenesulfonate) (PSS-Na, pure PSS-Na was not examined in this thesis however) one semi-circle with high resistance values (a slopping response was presumably not obtained since the AC impedance spectra were recorded only down to 5 Hz) was obtained. These results are therefore in accordance with the results in this thesis. Rolland et al. studied PEDOT materials with computational models and revealed that the crystallization of the PEDOT units is independent from the water content, whereas the connectivity between different crystallites strongly decreases with the water content [236]. This could mean that the different electronic conductivity behavior of the high and low PEDOT content PEDOT:PSS materials in this thesis could be explained by varying interactions between the PEDOT moieties rather than different properties of the PEDOT moieties itself.

The spectroelectrochemistry and in-situ conductance studies of PEDOT:PSS batches in section 4.1.2.1 and 4.1.2.2 with two different PEDOT to PSS ratios support this assumption: the wavelength of maximum absorption of the neutral PEDOT band is for both PEDOT:PSS batches at ≈ 630 nm, which indicates that the electronic structure of the PEDOT moieties or PEDOT crystallites is in both batches comparable. The in-situ conductance observations also support this assumption: due to a high connectivity in the PEDOT moieties in PEDOT:PSS (1:2.5) the amount of accessible redox states is high, which leads to a broad potential window where PEDOT:PSS (1:2.5) is in its highly conducting state. On the other hand, the limited interactions in PEDOT:PSS (1:6) lead to a very small potential window where PEDOT:PSS is in its highly conducting state. It was also found that PEDOT:PSS (1:6) (PEDOT:PSS is in its oxidized, conducting state after spin coating) could not be reduced to its neutral, non-conducting state, so conversion between the redox states appears to be inhibited. On the other hand, PEDOT:PSS (1:2.5) could be reduced to its neutral state. Also this observation might be related to the worse connectivity of the PEDOT moieties in PEDOT:PSS (1:6) compared to PEDOT:PSS (1:2.5).

In literature, for PEDOT:PSS batches which were chemically synthesized at different pH conditions of the reaction mixture, $\approx 50\%$ higher conductivities were obtained for the batch which was synthesized at a $\text{pH} \approx 3$ compared to the batch synthesized at $\text{pH} \approx 11$ [237]. This is explained by the presence of hydroxyl ions OH^- which disturb the interactions between PEDOT and PSS. Increase of pH from 1.7 to 13 was even observed to cause a decrease of the electronic conductivity by six orders of magnitude and increase of the pH value of the spin coating dispersion was observed to cause an effect similar to dedoping of PEDOT:PSS as detected by optoelectronic properties [238, 239]. The slightly lower electronic conductivity of PEDOT:PSS-Na (1:6) could therefore also be explained by an increase of the pH of the dispersion from which the film is spin coated, even though the difference between the PEDOT:PSS (1:6) and PEDOT:PSS-Na (1:6) is in within the error of the measurements. For the PEDOT:PSS-Na (1:6) dispersion a pH of 7.4 was obtained after titration (as described in 3.1.2, for the pristine PEDOT:PSS (1:6) dispersion a pH of 1 – 2 is indicated [217]).

As can be seen in figure 4.60, the chemically doped PTS-TBA (brown symbols) shows σ_e values in the range of 10^{-3} S/cm, whereas the chemically doped PTS-Na shows one order of magnitude lower values of σ_e . Several identical sequential doping procedures for chemical doping of PTS films resulted in σ_e values which deviated for one to two orders of magnitude, therefore the level of σ_e of the shown PTS-Na and PTS-TBA can not be further discussed. However, the level of σ_e allows to predict if the ionic conductivity σ_{ion} can be determined (σ_{ion} as function of water content in [wt%] and λ is shown in figures 4.61 and 4.62): since the maximum values for σ_{ion} for pristine PTS-TBA are in the range of 10^{-4} S/cm which is lower than σ_e for the chemically doped PTS-TBA no σ_{ion} can be determined. On the other hand, pristine PTS-Na shows maximum σ_{ion} values in the range of 10^{-3} S/cm which is higher than σ_e for the chemically doped PTS-Na, therefore σ_{ion} of the chemically doped PTS-Na can be determined. If the AC Impedance/DC measurements of the chemically doped PTS-TBA would have been conducted at higher water contents than 9 wt% (or $p\text{H}_2\text{O}$ higher than 20 mbar H_2O), a high-frequency semi-circle might have been observed. The values for σ_e of both chemically doped PTS materials decrease only slightly in the examined water content range. The σ_{ion} values of the chemically doped PTS-Na show the same values as the pristine PTS-Na (see pink symbols in figure 4.62), but the values are reached at significantly lower water contents. Together with the fact that the chemically doped PTS materials show significantly lower water uptakes than the pristine PTS materials (as shown in section 4.2.2), it could be assumed that the sequential doping results in a considerable change of the film morphology, which was not further elucidated in this thesis. Few F_4TCNQ dopant molecules could also be attached on the film surface and might inhibit further water uptake. Since values for σ_{ion} in the range of 10^{-3} S/cm

were obtained for both the pristine and the chemically doped PTS-Na at 20 mbar H₂O (as shown in figure 4.61), comparable water uptakes were expected. However as can be seen in figure 4.23a, the water contents at 20 mbar H₂O are around 30 wt% for pristine PTS-Na but only around 10 wt% for the chemically doped PTS-Na. A possible explanation therefore might be that structural changes occur due to the chemical doping, which facilitate ion conduction so that comparable σ_{ion} can be observed at lower water uptakes.

Ionic conductivity as function of water content in wt%

In figure 4.61, σ_{ion} as function of water content is shown for the pristine PTS-Na and PTS-TBA (the values for σ_{ion} are taken from [160]), the chemically doped PTS-Na and both PEDOT:PSS (1:6) and PEDOT:PSS-Na (1:6).

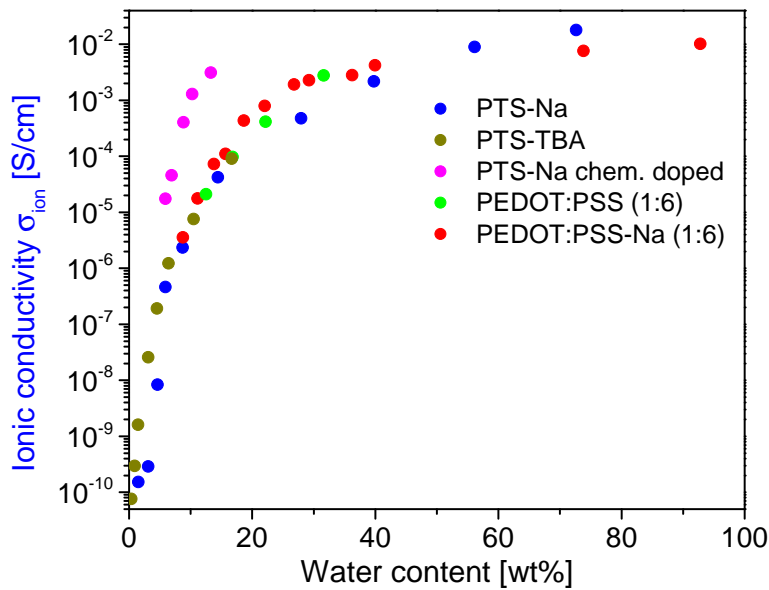


Figure 4.61: Ionic conductivity of various polymer materials at 25°C as function of water content, the ionic conductivity values of PTS-TBA were taken from [160]. Adapted with permission from [160], © 2019, Elsevier.

Regarding the trend of σ_{ion} as function of water content for the pristine PTS and the PEDOT:PSS (1:6) materials, it can be seen that upon increasing the water content up to 10 wt%, σ_{ion} increases significantly from 10⁻¹⁰ to 10⁻⁶ S/cm. Increasing the water content further up to 30 wt%, the values for σ_{ion} increase moderately up to 10⁻³ S/cm. For all materials, reaching of the plateau of σ_{ion} above water contents of 30 wt% is therefore clearly recognizable. Upon further increase to very high water contents of 70-90 wt%, σ_{ion} increases only slightly up to 10⁻² S/cm. The obtained dependency of σ_{ion} from the water

content is typical for polyelectrolyte materials [3, 6, 7]. Pristine PTS-Na (blue symbols) and PTS-TBA (dark yellow symbols) appear to show very comparable σ_{ion} values as function of water content. However, it should be taken into consideration that both materials show different water uptake per mass (in wt%) as function of $p\text{H}_2\text{O}$, but very similar values for the water uptake per repeating unit (in λ , see section 4.2.3). Therefore, σ_{ion} as function of λ for both pristine PTS-Na and PTS-TBA and PEDOT:PSS (1:6) and PEDOT:PSS-Na (1:6) is shown in figure 4.62. For the pristine PTS materials and the PEDOT:PSS materials it is assumed that the water uptake occurs mainly in the hydrophilic moieties, therefore the amount of water molecules per repeating unit can be calculated. For the chemically doped PTS materials, this assumption can not be made since the morphology of the chemically doped PTS films was not further elucidated, therefore the water uptake in λ is not determined for the chemically doped PTS materials. Also the fact that chemically doped PTS-Na shows at the same water contents more than one order of magnitude higher σ_{ion} values compared to the pristine PTS films can not further be elucidated due to the unknown morphology of the chemically doped PTS films.

Ionic conductivity as function of water uptake in λ

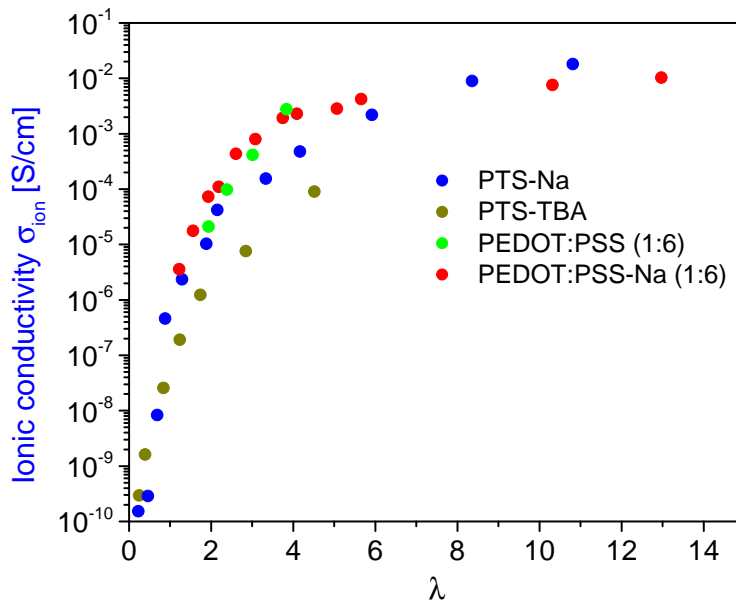


Figure 4.62: Ionic conductivity of various polymer materials at 25°C as function of λ , the ionic conductivity values of PTS-TBA were taken from [160]. Adapted with permission from [160], © 2019, Elsevier.

The trend of σ_{ion} as function of λ shows a similar trend as σ_{ion} as function of wt%: whereas the water uptake in a very dry state leads to a significant increase of the dissociation from

the immobile SO_3^- groups, further water uptake at high water contents leads only to a slight increase of σ_{ion} . This could be explained with the fact that at high water contents, Na^+ cations are already complexated in solvation shell with 5-6 or more H_2O molecules ($\lambda \approx 5 - 6$), further water uptake would not increase the amount of water molecules in the solvation shell of the cations but add more water molecules only in water rich moieties of the ion channels [3]. For Nafion membranes, it is also known that upon increasing the water content in the ion channels above $\lambda \approx 10$, the ion concentration in the center of the ion channel starts to be lower than in the proximity of the channel walls [7]. This could be explained with the fact that at high water contents further water molecules are incorporated in the center of the ion channels and do not affect the solvated cations. It has to be mentioned however, that the given references and the majority of studies on Nafion examine H^+ as mobile cation. For H^+ an exceptional conducting mechanism in aqueous media and in case of Nafion membranes more than one order of magnitude higher ionic conductivities compared to other cations (TBA⁺ was not examine) at equal λ values could be obtained [67, 240]. Therefore, the general trends and mechanisms might be therefore only partially valid for the Na^+ , H^+ and TBA⁺ containing polyelectrolyte materials in this thesis.

Discussion of water uptakes in λ

When comparing the dependency of σ_{ion} as function of λ , it has to be stated however that the ion concentrations in the different polymeric mixed conductor systems are however not the same as can be seen in table 4.9.

Table 4.9: Calculated ion concentrations of polymer materials utilized in this thesis.

Material	c [mol/cm ³]
PTS-TBA	0.00205
PTS-Na	0.00373
PEDOT:PSS (1:2.2)	0.00301
PEDOT:PSS (1:6)	0.00396
PEDOT:PSS-Na (1:6)	0.00432

For calculating the ion concentration no water uptake was assumed, a density of the polymer film of 1 g/cm³ and taking the positive charges of EDOT into account which partially counterbalance the negative charges instead of cations in case of PEDOT:PSS materials. The ionic conductivity σ_{ion} is related to the ion concentration c as follows [171]:

$$\sigma_{\text{ion}} = \mu_{\text{ion}} \cdot c \cdot z \cdot F \quad (26)$$

here μ_{ion} corresponds to the ion mobility, z to the ionic charge, F to the Faradaic constant. While assuming the ion mobility to be constant (effective ion mobilities in the range of

$10^{-8} - 10^{-7} \text{ cm}^2\text{V}^{-1}\text{s}^{-1}$ at 25°C and varying water content were obtained for PTS-TBA and PTImBr [160]), variation of the ion concentrations in the different polymeric mixed conductor materials as listed in table 4.9 leads therefore to a variation of σ_{ion} of approximately a factor of 2. However, the conductivity measurements contain an error of a factor of $\approx 2 - 3$, the different ion concentrations might therefore lead to only a minor error.

Comparing σ_{ion} of the pristine PTS materials as function of λ , it can be seen that PTS-TBA shows even higher values than PTS-Na at low λ values. This might be explained by the stronger association between cation and SO_3^- group in case of Na^+ , which might be due to the smaller and "harder" ion character of the Na^+ cation. At $\lambda > 1$ however, σ_{ion} is higher for PTS-Na than for PTS-TBA and at $\lambda \approx 5$, σ_{ion} of PTS-Na is around one order of magnitude higher than the σ_{ion} for PTS-TBA. Due to the smaller and less bulky ion size of Na^+ , sufficient water uptake in case of PTS-Na might lead to higher σ_{ion} values than for PTS-TBA. The same trend was observed for Nafion membranes with different cations [67], conducting polyelectrolytes bearing either TBA^+ or Br^- ions [160] and PSS with either H^+ or Na^+ counterions [61, 63]. At medium λ values of ≈ 5 , the PEDOT:PSS (1:6) materials show higher σ_{ion} than PTS-Na. This might eventually be explained by an increased phase separation into PEDOT rich and PSS rich (polyelectrolyte rich) phases in case of PEDOT:PSS, whereas the PTS materials might not show significant phase separation due to the fact that these materials were spin coated from $\text{H}_2\text{O}/\text{THF}$ mixtures.

As it was mentioned in the section 4.2.3, the values for λ might be misleading since they only quantify the mean amount of water molecules per repeating unit. Formation of water-rich hydrophilic moieties and water-poor hydrophobic moieties is not taken account in the λ values. Also the ion concentrations could be error-containing: especially at low water contents, it might not be taken for granted that the entirety of the cation-sulfonate pairs are in their dissociated form, which would lead to a lower effective ion concentration. Furthermore it might be also unclear if during the process of water uptake, the polymeric material is equally swelling.

According to Maier et al., transition from an impedance spectrum with predominant ionic conductivity to an impedance spectrum with predominant (but not only) electronic conductivity (as can be seen for example in figure 4.45 when decreasing $p\text{H}_2\text{O}$ from 16 mbar H_2O to 9 mbar H_2O) results from both a decrease of the ionic charge carrier mobility compared to the electronic charge carrier mobility as well a decrease of the ionic charge carrier concentration compared to the electronic charge carrier concentration [219]. Therefore, it is difficult to quantify only one of both effects, so on the one hand the change of the carrier mobility or on the other hand the change of the carrier concentration.

Further discussions

Since the IDEs with the highest channel length of 100 μm still does not allow to measure polymer materials with electronic conductivities with approximately more than 10 S/cm (see also the discussions in 4.3.4), new electrode with channel lengths of far more than 100 μm and channel widths of less than 12 μm might be examined. The usability of the potential new electrode can be recognized from resistance values, which strongly changes with water partial pressure. A strongly varying resistance means that this resistance is mainly determined by the water content, so a resistance originating from the intrinsic properties of the polymer material. On the other hand, only slightly varying resistance values especially in the resistance value range below 100 Ω would hint to significant contribution of contact and/or wiring resistances. If the geometry of the potentially new electrodes could not be changed further (for example due to the confined space in the measurement cell), changing from the utilized two point measurements to four point measurements might help to measure conductivities of more than 10 S/cm since contact resistances can be eliminated in four point measurements.

The stray capacitance originating from the substrate and the chemical capacitance originating from the mixed conducting properties of the polymer material were typically in the range of 10^{-10} F and 10^{-6} F, respectively. In case of AC impedance spectra which showed mixed conductivity behavior (high- and low-frequency semi-circles), the chemical capacitance originating from the mixed conducting properties and ion-blocking electrodes could be determined. Increase of the water partial pressure or water uptake was observed to result in only minor increase of the chemical capacitance, which could be explained by a stronger contribution of ionic charge carriers at high water contents. For future investigations the chemical capacitance could be investigated in more detail, for example the dependency of the chemical capacitance from the water content or the ion content.

Relation of in-situ conductance and conductivity observations to percolation effects

With the help of the percolation theory, critical phenomena in various fields such as bottlenecks in traffic systems or population density thresholds for spreading of plagues can be described [241–244]. Usually percolation theory is explained by using the model of a square network grid consisting of vertex points (black points in figure 4.63 a) of a random subgraph in a indefinitely large grid. With a certain probability p , the edges between each vertex point are open ($p = 1$, a connection between vertex points exists) or closed ($p = 0$, no connection exists). The so-called percolation function Θ , which is defined as the probability that infinitely many vertex points can be reached over open bonds between the vertex points from one fixed starting vertex point is a function of p .

The dependency of Θ from p is displayed in figure 4.63 b).

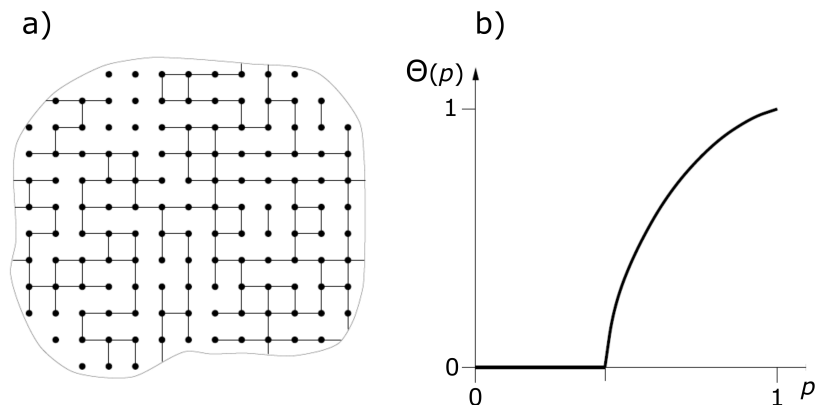


Figure 4.63: a) Two-dimensional percolation network of vertex points in a square grid and b) percolation function Θ as function of p . Adapted with permission from [241].

From the dependency of Θ as function of p it can be seen that a critical value of p has to be reached in order to provide a non-zero probability that all vertex points in the sub-graph can be reached. The conductivity behavior of a system which consists of randomly distributed metallic and dielectric phases has been modeled successfully with the help of the percolation theory [245]. It could be shown that the system shows a transition to a metallic-like conductivity behavior after reaching a threshold volume fraction of the metallic phases. After exceeding the volume content of carbon nanotubes over a critical volume content threshold, the electrical conductivity of polymer/carbon nano tube composites was observed to increase over several orders of magnitude [246].

Several observational findings in this thesis might eventually be explained by the presence of percolation effects in the studied polymeric mixed conductor systems. The higher content of PEDOT in the high PEDOT:PSS batches eventually leads to a high amount of interactions between the PEDOT moieties in the PEDOT:PSS material, which might correspond to the case when many connections between the PEDOT moieties exist (vertex points) in the matrix of electronically insulating PSS (area between the vertex points) exist as visualized in figure 4.63 a), whereas in the low PEDOT content PEDOT:PSS batches only few connections might exist. Firstly, this might lead to a high amount of redox states which can be surpassed during electrochemical cycling and therefore to a broad electrochemical window of high in-situ conductance (as shown in figure 4.15). Secondly also the significantly higher electronic conductivity (≈ 1 S/cm) in the dry state of the high PEDOT content PEDOT:PSS (1:2.2) batch compared to the lower electronic conductivity of PEDOT:PSS (1:6) (10^{-4} S/cm) might be explained by better percolation

between conducting PEDOT moieties (figure 4.60). Thirdly, also the significantly different dependency of the electronic conductivity from the water content for the high and low PEDOT content PEDOT:PSS batches (almost no decrease of σ_e for PEDOT:PSS (1:2.2), but decrease of more than one order of magnitude for PEDOT:PSS (1:6) when increasing the water content up to ≈ 40 wt%, as shown in figure 4.60) might give indication for the presence of percolation effects: the low decrease of σ_e might correspond to a small decrease of the probability p values (starting from high p values) in figure 4.63 b), whereas the stronger decrease of the electronic conductivity in case of PEDOT:PSS (1:6) might correspond to a significant decrease of p (starting at already lower p values) towards p values close to the threshold value of p . Finally, also the significant decrease of the electronic conductivity with increasing PVA content (as shown in figure 4.56) might correspond to a significant decrease of the percolation between electronically conducting PEDOT moieties. Percolation effects in PEDOT:PSS composite materials were proposed due to the dependency of the conductivity as function of insulating filler content, as observed for composite materials consisting of PEDOT:PSS and polystyrene nanospheres or PEDOT:PSS and PVA [154, 247]. Molecular dynamic simulations on PEDOT:PSS materials showed that in spite of the phase separation into PEDOT and PSS rich moieties, PEDOT connections exist between PEDOT-rich moieties, therefore forming percolating networks [218]. Percolating networks of conductive phases as requirement for macroscopic conductivity were also proposed in case of electropolymerized PEDOT [205].

5 Conclusion and outlook

In the present thesis the polymeric mixed conductor systems PTS and PEDOT:PSS were examined according to their UV/Vis absorption properties in the neutral and doped state, water uptake at variable atmospheric conditions and conductivity properties as function of water uptake. Several variations of mixed conductor systems were examined, in case of PTS two different counterions, namely TBA⁺ and Na⁺ were studied. Additionally, PTS was spin coated from two different solvent systems, either from pure H₂O or from a 1:1 H₂O/THF mixture. Two different types of the mixed conductor system PEDOT:PSS were examined, namely the high PEDOT content PEDOT:PSS (1:2.2) or PEDOT:PSS (1:2.5) batches and the low PEDOT content PEDOT:PSS (1:6) batch. An important difference between the PTS and PEDOT:PSS materials is that PTS is in its neutral (undoped), non-conducting state upon deposition whereas PEDOT:PSS is in its oxidized (doped), electronically conducting state due to the chemical synthesis route. All examinations (except from the thermogravimetric measurements) in this thesis are conducted with thin films of the polymeric mixed conductor materials.

Absorption characteristics in neutral and doped state

In order to examine the influences of the counterion of PTS and the solvent system from which PTS is spin coated on the UV/Vis absorption properties, both PTS-TBA and PTS-Na were spin coated from either H₂O or H₂O/THF and the UV/Vis absorption was recorded under ambient conditions, as shown in figure 5.1.

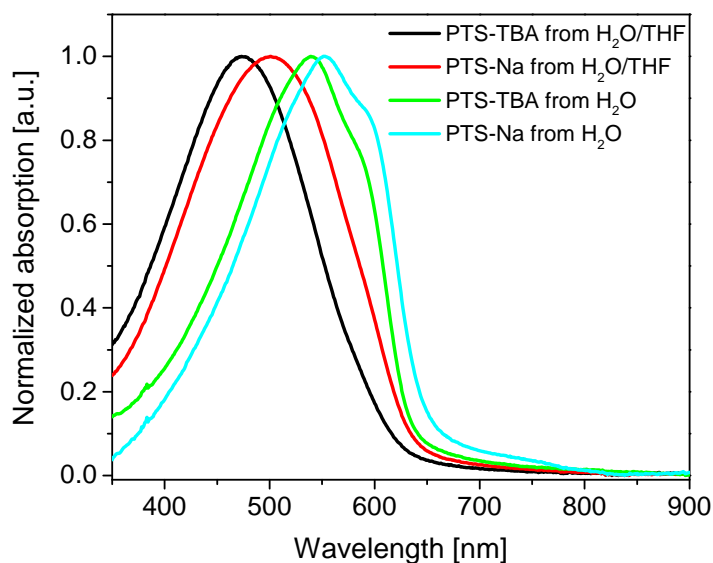


Figure 5.1: UV/Vis absorption spectra of PTS-TBA and PTS-Na spin coated from 5 mg/ml H₂O or H₂O/THF on glass substrates.

It could be shown that using pure H₂O as solvent system leads to an UV/Vis absorption spectrum with an absorption maximum at lower wavelengths structure and an aggregation shoulder compared to the featureless absorption spectra of PTS films spin coated from the solvent mixture H₂O/THF. This means that higher conjugation and aggregation of the polythiophene backbone are present in the PTS spin coated from H₂O, from which can be concluded that more interchain and intrachain interactions are present. Also the counterion had influence on the UV/Vis absorption spectrum: for both solvent systems. For PTS-Na the absorption maximum was at lower wavelengths, which might indicate that Na⁺ facilitates backbone aggregation. The absorption intensity increase in water partial pressure ramps showed with a moderate increase at low water partial pressures and a steep increase at high water partial pressures similar trends as the water uptake trends measured with QCM, which might be explained with variations of the refractive index or the extinction coefficient of the PTS films. During temperature ramps at various water partial pressures, the increased disturbance of the PTS structure by the TBA⁺ cation was observed by a significant blue shift of the absorption maximum upon heating the PTS films, which was not observed in case of the PTS-Na films. Conducting temperature ramps in either dry or at very high water partial pressure conditions, it could be seen that a dry N₂ atmosphere results in a rather amorphous structure at the end of the temperature ramp (back at room temperature) whereas at high water partial pressure recovering of the aggregated PTS structure after cooling down can be observed. This can be explained with the fact that presence of water in the PTS materials might lead to increased flexibility of the polymer chain segments.

In order to examine the UV/Vis absorption characteristics of the polymeric mixed conductor systems as function of doping state, spectroelectrochemistry measurements of one high PEDOT content PEDOT:PSS batch (PEDOT:PSS (1:2.5)) and of one low PEDOT content PEDOT:PSS batch (PEDOT:PSS (1:6)) were conducted. The UV/Vis absorption spectra recorded during the discharge sweep (from oxidized to neutral state) in spectroelectrochemistry measurements are shown in figure 5.2.

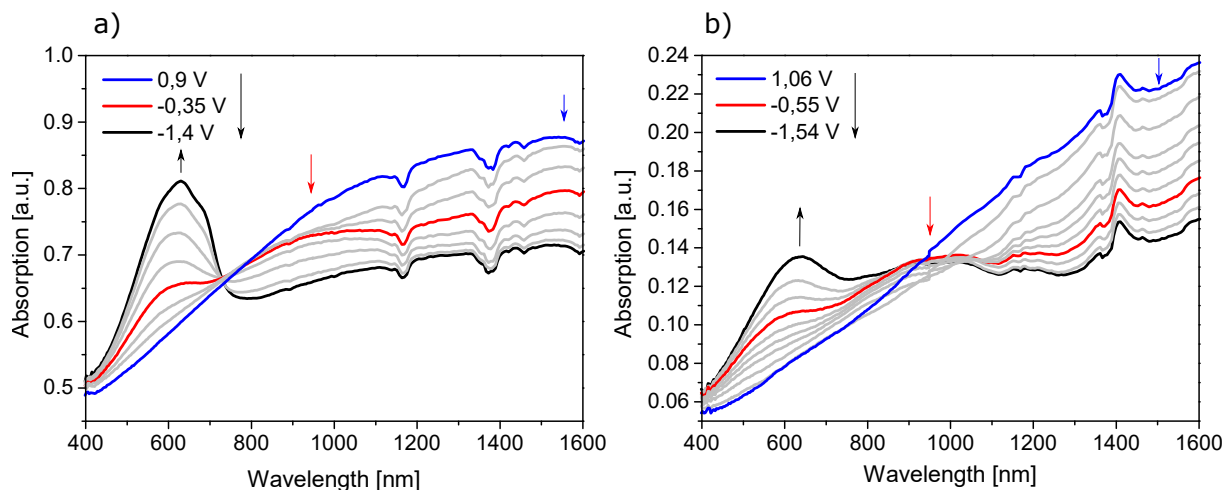


Figure 5.2: UV/Vis absorption spectra during the discharge sweep in spectroelectrochemistry measurements on 5 μm IDEs in 0.1 M NBu_4PF_6 of a) PEDOT:PSS (1:2.5) (second cycle, scan rate of 10 mV/s) and b) PEDOT:PSS (1:6) (second cycle, scan rate 10 mV/s).

Upon decrease of the potential, the absorption intensity of the neutral bands increases and the absorption intensities at wavelengths of the polaron and bipolaron bands decreases, which can be explained by a conversion from the neutral towards an oxidized state. The UV/Vis absorption bands at ≈ 650 nm for both PEDOT:PSS films indicate the absorption band of the neutral PEDOT moieties. However, differences between the materials can be observed: the absorption intensity of the neutral band of PEDOT:PSS (1:6) is low compared to the absorption intensity of the charged states. On the other hand, in PEDOT:PSS (1:2.5) the absorption intensity of the neutral state is significantly higher compared to the absorption intensities of the charged states. This can be explained with the fact that PEDOT:PSS (1:2.5) was reduced to a higher extent to its neutral state whereas PEDOT:PSS (1:6) is even at a more negative potential of -1.54 V partially in its oxidized state.

In addition to the UV/Vis absorption characteristics upon electrochemical doping, in-situ conductance measurements (in-situ measurement of the conductance during electrochemical cycling of the polymer film) were conducted in order to examine the conductivity behavior as function of doping state. Hereby significantly different behavior of

the PEDOT:PSS materials depending on the PEDOT to PSS ratio was found: whereas PEDOT:PSS (1:2.5) showed a broad potential window of high in-situ conductance, PEDOT:PSS (1:6) showed a bell-shaped in-situ conductance profile, as shown in figure 5.3.

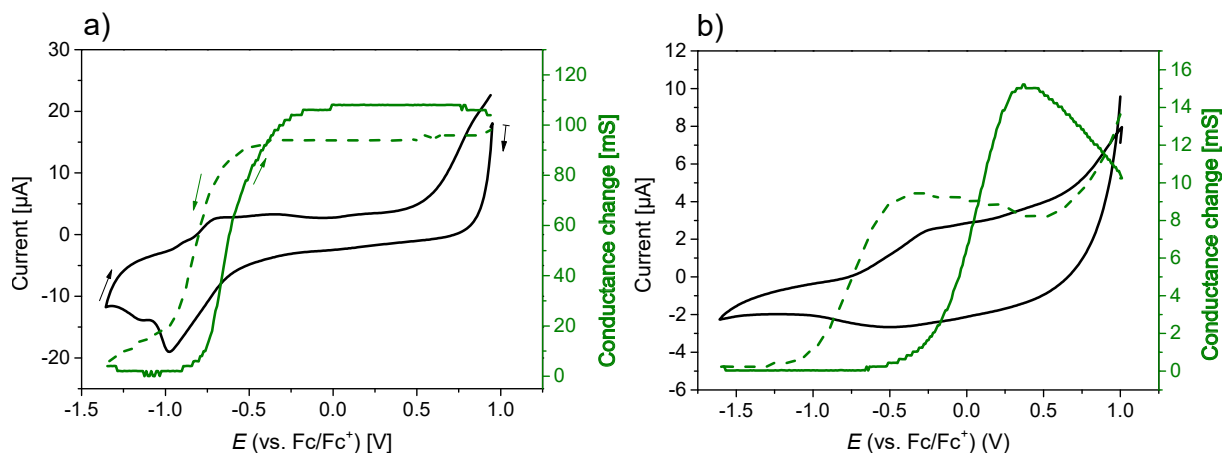


Figure 5.3: Cyclic voltammogram (black curve) and in-situ conductance (green curve) of a) PEDOT:PSS (1:6) und b) PEDOT:PSS (1:2.5) in 0.1 M $NBu_4PF_6/MeCN$ with a scan rate of 10 mV/s on 5 μ m IDEs.

The differences could be explained by higher amount of interactions in the high PEDOT content PEDOT:PSS material, leading to more accessible redox states and therefore to a broader potential window over which PEDOT:PSS (1:2.5) is in its highly conducting state. Since the electronic structure of the PEDOT moieties is presumably similar due to comparable UV/Vis absorption features of the neutral PEDOT moieties (as shown in figure 5.2, it could be assumed that in-situ conductance is a macroscopic material property, which relies on sufficient interactions between the electronically conducting PEDOT moieties.

Concluding, it can be stated that for PEDOT:PSS (1:2.5) full conversion between the redox states as observed in spectroelectrochemistry measurements and an in-situ conductance plateau over a broad potential window can be observed, on the other hand PEDOT:PSS (1:6) can be converted only partially to the neutral state and shows high conductance only at a very narrow potential window (bell-shaped in-situ conductance profile). Interestingly, the electronic conductivity as measured with DC measurements on IDEs appears to correlate with this trend: whereas high σ_e in the range of 1 S/cm were found for PEDOT:PSS (1:2.5), significantly lower σ_e in the range of $10^{-5} - 10^{-4}$ S/cm were found for PEDOT:PSS (1:6). It might be therefore assumed, that a high content of electronically conducting moieties as in PEDOT:PSS (1:2.5) leads to both high values for σ_e and good accessibility of the redox states, whereas lower PEDOT contents or eventually worse connectivity between the electronically conducting moieties lead to lower values for σ_e and lower accessibility of the redox states.

Water uptake studies in controlled atmospheric conditions

Since the PTS and PEDOT:PSS materials examined in this thesis contain hydrophilic polyelectrolyte moieties, the water uptake of thin films of both materials at various atmospheric conditions was investigated. The water uptake per mass in [wt%] and per repeating unit in λ was determined for the PTS and PEDOT:PSS materials as function of water partial pressure and temperature with preliminary TGA studies and QCM measurements. Using TGA to determine the water uptakes, extrapolated values of 8 and 5 wt% for PTS-Na and PTS-TBA and 10 – 15 wt% for the PEDOT:PSS materials at 20 mbar H_2O are obtained. The higher water uptake of the PEDOT:PSS materials might be explained by the fact that PEDOT:PSS was present in form of thin film crumbs, whereas the PTS materials were present in bulk powder form.

In order to determine the water uptake of the polymeric mixed conductors in the form of thin films as examined in the AC impedance and DC measurements, a QCM setup was newly established. The general measurement procedure was listed in detail, the applicability and the validity were examined and the reliability and reproducibility were studied. For PTS and PEDOT:PSS materials, a typical trend could be identified: after a step increase of the water uptake at low water partial pressures, the water uptake increases moderately at medium water partial pressures. Upon switching to higher water partial pressures, the water uptake increased more significantly. The obtained trends are very comparable to polyelectrolyte materials such as PSS or Nafion and with maximum water uptake values of $\lambda \approx 10 - 15$, the values are very similar to Nafion. A typical water uptake trend as function of water partial pressure, here the water uptake of PEDOT:PSS-Na (1:6), can be seen in figure 5.4.

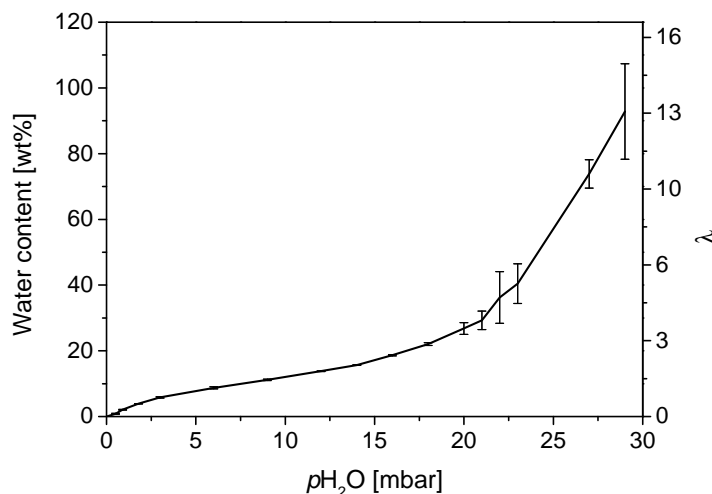


Figure 5.4: Exemplary water uptake of a polymeric mixed conductor thin film material at 25°C, here PEDOT:PSS-Na (1:6).

The water uptake trend can be explained as follows: at low water contents the counterions dissociate from the immobile SO_3^- group and solvated cations are present. In the medium water partial pressure range, multiple solvation shells form around the cation and in the high water partial pressure range, bulk-like water moieties are formed. In case of the PTS materials, higher water uptakes per mass were obtained for PTS-TBA than for PTS-Na, which can presumably be explained by the higher ion content in PTS-Na. However, similar water uptakes per repeating unit were obtained, which might be explained by a similar hydrophilicity of the cation-sulfonate group for both PTS materials. The water uptake of PTS films which were chemically doped with the strong electron acceptor F_4TCNQ after spin coating were observed to be lower than for the pristine PTS films, which might be due to the shielding of hydrophilic moieties in the polymer films. The water uptake of PEDOT:PSS materials was not observed to show a dependency from the PEDOT to PSS ratio, which might be due to different morphologies in the high and low PEDOT content PEDOT:PSS materials. Drop casted PEDOT:PSS films showed similar water uptake values as the spin coated films, from which might be deduced that the water uptake occurs mainly in the volume of the polymer film rather than just on the surface.

Conductivity studies in controlled atmospheric conditions

The conductivity behavior of the polymeric mixed conductors systems was studied with a combination of AC impedance and DC measurements. In AC impedance spectroscopy measurements of pristine PTS-Na a high-frequency (high ω values, left side of the impedance spectrum) semi-circle and a slopping low-frequency response was obtained. The high-frequency resistance (diameter of the high-frequency semi-circle) was observed to increase with decreasing water partial pressure. The conductivities at each water partial pressure could be coupled to water uptake (water content) values at the same water partial pressure since both the conductivity as well as the QCM measurements to determine the water uptake were conducted in the same water partial pressure and temperature conditions. In case of pristine PTS-Na, it can be therefore said that the high-frequency resistance increases with decreasing water uptake. Since the high-frequency semi-circle can be assigned predominantly to the ionic resistance, an increase of the high-frequency resistance corresponds to a decrease of the ionic conductivity. In figure 5.5, the AC impedance spectra at two water partial pressures and the ionic conductivity as function of water partial pressure and water content is shown.

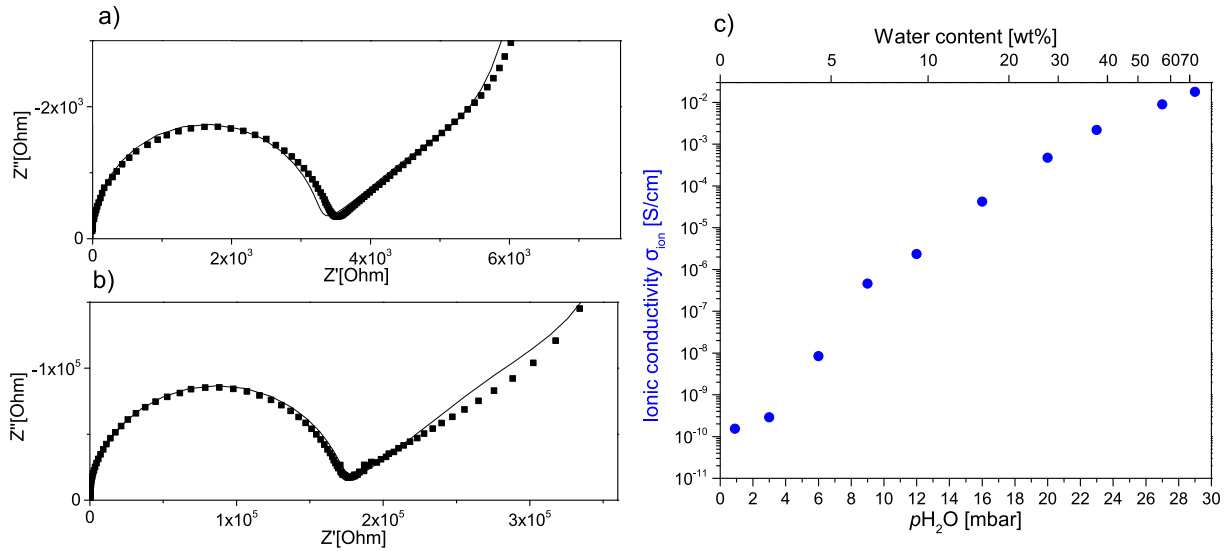


Figure 5.5: AC impedance spectra and corresponding fits of pristine PTS-Na at a) 23 mbar H₂O and b) 16 mbar H₂O and c) ionic conductivity as function of water partial pressure and as function of water uptake as determined with QCM measurements at 25°C.

The ionic conductivity was observed to increase from 10⁻¹⁰ S/cm up to 10⁻² S/cm upon increasing the water partial pressure from 0.9 to 29 mbar H₂O. Coupling the conductivity measurements with QCM measurements to determine the water uptake, a very strong increase of the ionic conductivity up to 10⁻³ S/cm upon an increase of the water content up to 30 wt% can be observed. The strong increase of the ionic conductivity can be explained with an increase of the dissociation between the mobile Na⁺ cation and immobile SO₃⁻ groups, which leads to an increase of the mobility of the Na⁺ cation. However, the ionic conductivity increases only further up to 10⁻² S/cm when the water content increases significantly up to 70 %. This plateau value of the ionic conductivity can presumably be explained by the fact that water is taken up only in bulk-like water moieties, which does increase the cation mobility only marginally.

An increased electronic conductivity was obtained for chemically doped PTS films. Similar trends as for the chemically doped PTS were obtained for the PEDOT:PSS (1:6) materials. The AC impedance spectra of PEDOT:PSS-Na (1:6) at various partial pressures are shown in figure 5.6.

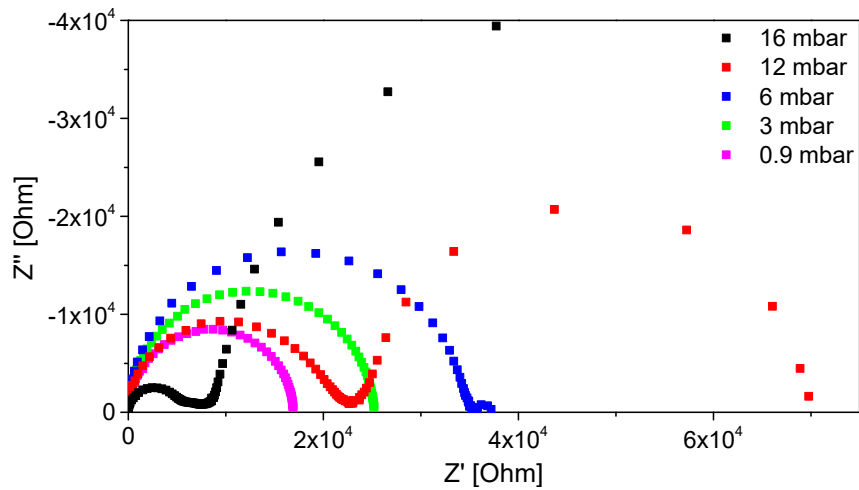


Figure 5.6: AC impedance of PEDOT:PSS-Na (1:6) on a 20 μm IDE at 25°C as function of water partial pressure.

Whereas the AC impedance spectra of the undoped PTS-Na consisted of a high-frequency semi-circle and a sloping low-frequency response, in the AC impedance spectra of PEDOT:PSS-Na (1:6) in addition to the high-frequency semi-circle an additional semi-circle at low frequencies could be obtained for the spectra equal or higher than 6 mbar H_2O . As for undoped PTS-Na, the resistance of the high-frequency semi-circle increased with decreasing water partial pressure. In contrast to the high-frequency semi-circle, the resistance of the low-frequency semi-circle decreased upon decreasing the water partial pressure. Below 6 mbar H_2O , only the low-frequency semi-circle can be detected. In addition to the AC impedance measurements, DC measurements were conducted which are shown in figure 5.7.

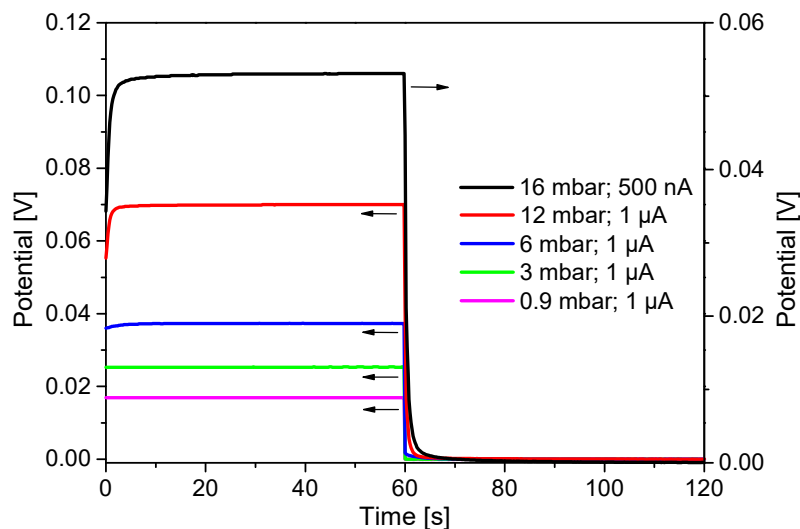


Figure 5.7: DC measurements of PEDOT:PSS-Na (1:6) on a 20 μm IDE at 25°C as function of water partial pressure.

At low water partial pressures, the potential remains constant over the time of the ap-

plied current. In the DC measurements at 6 mbar H_2O and higher water partial pressures, a more and more pronounced potential increase during the time of the applied current can be observed. This polarization effect can be explained with the contribution of both electronic and ionic charge carriers at the start of the DC measurement, which leads to a low resistance and therefore to a low potential. Whereas the ionic charge carriers are increasingly blocked at the electrode and can not contribute to current conduction any more, the electronic charge carriers contribute to current conduction over the entire time. Accordingly, from the steady state potential at the end of the time of constant current the electronic resistance can be calculated. The strong contribution of ionic charge carriers to current conduction at high water partial pressures can therefore be concluded from DC measurements.

From the observations that the presence of polarization effects in the DC measurements can be observed when the low-frequency semi-circles can be seen in the AC impedance spectra it can be concluded that PEDOT:PSS-Na (1:6) shows mixed conductivity at water partial pressures equal or higher than 6 mbar H_2O . At lower $p\text{H}_2\text{O}$, the presence of one semi-circle in AC impedance spectra and the absence of polarization effects in the DC measurements can be explained by the fact that only electronic conductivity can be detected. The electronic resistance as calculated from the steady state potential in the DC measurements corresponds to the resistance of the low-frequency semi-circle in the AC impedance spectra, therefore it can be shown that the resistance of the low-frequency semi-circle corresponds to the electronic resistance. Whereas the high-frequency resistance in the AC impedance spectra of the undoped PTS-Na could be approximately assigned to ionic resistance, the high-frequency resistance of the mixed conducting PEDOT:PSS-Na (1:6) corresponds to the total (ionic + electronic) resistance, from which the ionic resistance can be extracted by taking the electronic resistance into account. In figure 5.8, the electronic and ionic conductivity as function of water partial pressure and by coupling with QCM measurements also as function of water content are shown.

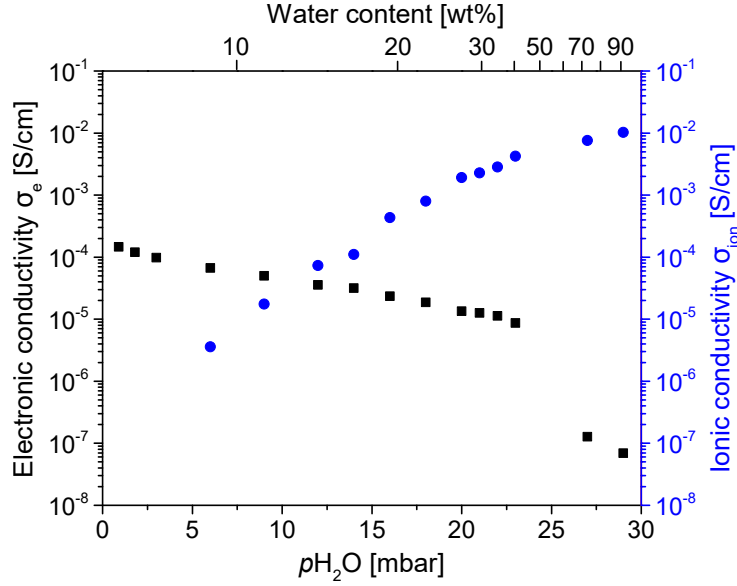


Figure 5.8: Electronic and ionic conductivity of PEDOT:PSS-Na (1:6) on a 20 μm IDE at 25°C as function of water partial pressure.

The electronic conductivity decreased moderately for around one order of magnitude upon increasing the water partial pressure up to water contents of ≈ 40 wt%, which can be explained by an increase of the distance between the electronically conducting PEDOT moieties. Increasing the water partial pressure further up to ≈ 90 wt%, the electronic conductivity decreases significantly for more than two orders of magnitude. This can be explained by the fact that the percolation between the PEDOT moieties gets significantly weakened. The ionic conductivity can be determined only for water partial pressures equal or higher than 6 mbar H_2O since the electronic conductivity up to these water partial pressures is more than one order of magnitude higher than the ionic conductivity. Similar to pristine PTS-Na, after a strong increase of the ionic conductivity at water contents up to ≈ 40 wt%, the ionic conductivity increases slightly further at water contents up to ≈ 90 wt% which might be explained by the fact that further water uptake increases the dissociation of the mobile cations only slightly or that additional water is taken up in pure water moieties.

For PEDOT:PSS (1:2.2) with higher PEDOT contents, a several orders of magnitude higher electronic conductivity was obtained, which can be explained with the higher amount of electronically conducting PEDOT, which presumably leads to better percolation between PEDOT moieties. The electronic conductivity was observed to show low dependency from the water uptake, which might be explained by the fact that the good percolation in case of the high PEDOT content PEDOT:PSS is not significantly disturbed by water uptake. Since the electronic conductivity exceeds in the entire applied water partial pressure or water content range typical values for the ionic conductivity of the ionic conductors or the mixed conductors, no ionic conductivity could be determined.

Outlook

Whereas PTS films spin coated from pure H₂O were already examined with UV/Vis absorption spectroscopy, the spectroelectrochemistry and in-situ conductance behaviour, the water uptake and conductivity properties of PTS films spin coated from H₂O could also be examined. The increased aggregation in the PTS materials spin coated from H₂O might result in different observations in the spectroelectrochemistry and in-situ conductance measurements. It might be also interesting to investigate the water uptake properties since the presence of aggregated polythiophene moieties in PTS films spin coated from H₂O might change the amount of accessible ionic groups and might therefore change the water uptake properties. It might also be worth investigating the conductivity properties of PTS materials further since presence of aggregated polythiophenes shows higher wavelengths of the absorption maximum and therefore higher conjugation lengths. Eventually, the different aggregation of the polythiophene backbones could also result in different structures of the the hydrophilic moieties, therefore also the ionic conductivity might be also different as for the PTS films spin coated from H₂O/THF. However, the structure change caused by switching from the solvent mixture H₂O/THF to pure H₂O would need to be large enough that it causes differences in the conductivity behavior which is larger than the error of the conductivity measurements, so larger than a factor 2 – 3. The conductivity properties of PTS materials spin coated from H₂O were already investigated, but no remarkable differences to PTS materials spin coated from H₂O/THF were obtained. Eventually, the aggregation of the PTS backbones would have to be increased in order to obtain measurable differences, for example by conducting temperatures ramps (as shown in 4.4) at high water partial pressure conditions. Use of the solvent mixture H₂O/THF for PTS materials resulted in dissolution of both the hydrophilic pendant side groups as well as dissolution of the polythiophene backbone moieties, whereas use of only H₂O resulted in the dissolution of the hydrophilic side groups and formation of polythiophene aggregates. Despite trying out various solvents, no organic solvent was found which showed dissolution of only the PTS backbone due to formation of "inverse" micelle-like aggregates. If such organic solvent could be found, different conductivity behavior would be expected since the ionic groups would be shielded.

Investigation of PTS with further counterions with different ionic radii than TBA⁺ or Na⁺ counterions might be interesting. This could lead to different aggregation tendencies which might be observed with UV/Vis absorption spectroscopy and which might eventually result in different water uptake properties (even though it was found that the water uptake in λ showed no dependency of the counterion) or conductivity properties. A further cation exchange of PTS has not been conducted yet since the available amount of PTS material was too low, therefore at first new PTS would have to be synthesized.

The assumption of insufficient connectivity between the PEDOT moieties in PEDOT:PSS (1:6) might be further elucidated by conducting spectroelectrochemistry and in-situ conductance measurements with several further PEDOT:PSS batches with different PEDOT to PSS ratios (which would have to be synthesized), for example PEDOT:PSS (1:4) or PEDOT:PSS (1:10). Determination of the water content in dependence of the PEDOT to PSS ratio might also help to elucidate the influence of the PSS content on the water content. The connectivity of the PEDOT moieties in the PEDOT:PSS batches with other PEDOT to PSS ratios might be also further investigated according to the level of the electronic conductivity and the dependency of the electronic conductivity from the water content.

In order to measure not only the water uptake as function of water partial pressure with quartz crystal microbalance measurements, mechanical properties like the viscoelasticity of the polymeric mixed conductor films could be examined with quartz crystal microbalance measurements with dissipation monitoring (QCM-D). This would for example allow to determine the water uptake at which the films start to become viscoelastic or would eventually allow to identify different water swelling behaviors of the PTS and PEDOT:PSS materials.

Whereas with the QCM measurements water uptake of the polymer mixed conductor materials from humid atmospheres could be proven, no information could be obtained about the moieties into which water is taken up or the dimensions of these moieties. The presence of water-rich hydrophilic moieties could only be strongly assumed due to similarities of the water uptake trends as function of humidity and the trends of the ionic conductivity as function of water uptake to trends in literature. Therefore, one possibility to further elucidate the water uptake of the polymer mixed conductor films might be to freeze the films in states of high water uptakes and examine the films with cryogenic transmission electron microscopy [248].

The studies in the present thesis might help to improve the utilization of polyelectrolyte materials in various applications. In general, variation of the conductivity properties as function of solvent content might also be helpful to improve energy storage systems such as batteries where both electronic and ionic conduction is necessary. Furthermore, in materials which require electronic conductivity and which consist of electronically conducting and electronically insulating moieties, the results of this thesis might help to find the minimum required amount of electronically conducting moieties in order to provide macroscopic electronic conductivity. Balancing of the ionic conductivity properties as function of water content is also crucial in Nafion membranes in polymer electrolyte membrane fuel cells. The variation of the mixed conductivity properties as function of

water content might help to improve the performance of polymeric mixed conductors in organic electrochemical transistors, since an optimal water content might be found (if the water content can be set) at which ions can diffuse fast from the electrolyte into the polymer film but electrons can still be removed efficiently from the polythiophene backbones in order to result in a variation of the current flowing through the polymeric mixed conductor material.

6 Bibliography

- [1] M. M. Schmidt, M. ElMahmoudy, G. G. Malliaras, S. Inal, M. Thelakkat, *Macrom. Chem. and Phys.* **2018**, *219*, 1700374.
- [2] R. D. McCullough, P. C. Ewbank, R. S. Loewe, *J. Am. Chem. Soc.* **1997**.
- [3] A. Kusoglu, A. Z. Weber, *Chem. Rev.* **2017**, *117*, 987–1104.
- [4] E. S. Muckley, C. B. Jacobs, K. Vidal, J. P. Mahalik, R. Kumar, B. G. Sumpter, I. N. Ivanov, *ACS Appl. Mater. Interfaces* **2017**, *9*, 15880–15886.
- [5] H. Okuzaki, K. Hosaka, H. Suzuki, T. Ito, *Sensors and Actuators A: Physical* **2010**, *157*, 96–99.
- [6] S. De, A. Ostendorf, M. Schönhoff, C. Cramer, *Polymers* **2017**, *9*, 550.
- [7] K.-D. Kreuer, S. J. Paddison, E. Spohr, M. Schuster, *Chem. Rev.* **2004**, *104*, 4637–4678.
- [8] H. Wang, U. Ail, R. Gabrielsson, M. Berggren, X. Crispin, *Adv. Energy Mater.* **2015**, *5*, 1500044.
- [9] <https://www.ipcc.ch/sr15/download>, accessed 20.03.2020.
- [10] <https://www.iapp.de/organische-elektronik.de/en/?Home>, accessed 25.03.2020.
- [11] <https://computerhistory.org/blog/13-sextillion-counting-the-long-winding-road-to-the-most-frequently-manufactured-human-artifact-in-history/?key=13-sextillion-counting-the-long-winding-road-to-the-most-frequently-manufactured-human-artifact-in-history>, accessed 05.06.2020.
- [12] H. Klauk, *Chem. Soc. Rev.* **2010**, *39*, 2643–2666.
- [13] L. Kergoat, B. Piro, M. Berggren, G. Horowitz, M.-C. Pham, *Anal. Bioanal. Chem.* **2012**, *402*, 1813–1826.
- [14] H. S. White, G. P. Kittlesen, M. S. Wrighton, *J. Am. Chem. Soc.* **1984**, *106*, 5375–5377.
- [15] G. P. Kittlesen, H. S. White, M. S. Wrighton, *J. Am. Chem. Soc.* **1984**, *106*, 7389–7396.

- [16] T. M. Swager, *Macromolecules* **2017**, *50*, 4867–4886.
- [17] S. Inal, G. G. Malliaras, J. Rivnay, *Nat. Comm.* **2017**, *8*, 1767.
- [18] E. Zeglio, O. Inganäs, *Adv. Mater.* **2018**, *30*, 1800941.
- [19] P. Romele, M. Ghittorelli, Z. M. Kovács-Vajna, F. Torricelli, **2019**, *10*, 3044.
- [20] H. Toss, C. Suspène, B. Piro, A. Yassar, X. Crispin, L. Kergoat, P. Minh-Chau, M. Berggren, *Organic Electronics* **2014**, *15*, 2420–2427.
- [21] A. Giovannitti, D.-T. Sbircea, S. Inal, C. B. Nielsen, E. Bandiello, D. A. Hanifi, M. Sessolo, G. G. Malliaras, I. McCulloch, J. Rivnay, *PNAS* **2016**, *113*, 12017–12022.
- [22] J. C. Brendel, M. M. Schmidt, G. Hagen, R. Moos, M. Thelakkat, *Chem. Mater.* **2014**, *26*, 1992–1998.
- [23] P. Schmode, D. Ohayon, P. M. Reichstein, A. Savva, S. Inal, M. Thelakkat, *Chem. Mater.* **2019**, *31*, 5286–5295.
- [24] S. Inal, J. Rivnay, P. Leleux, M. Ferro, M. Ramuz, J. C. Brendel, M. M. Schmidt, M. Thelakkat, G. G. Malliaras, *Adv. Mater.* **2014**, *26*, 7450–7455.
- [25] A. Savva, R. Hallani, C. Cendra, J. Surgailis, T. C. Hidalgo, S. Wustoni, R. Sheelamanthula, X. Chen, M. Kirkus, A. Giovannitti, A. Salleo, I. McCulloch, S. Inal, *Adv. Funct. Mater.* **2020**, *30*, 1907657.
- [26] J. Rivnay, S. Inal, A. Salleo, O. M. Róisín, M. Berggren, G. Malliaras, *Nat. Rev. Mater.* **2018**, *3*, 17086.
- [27] P. Lin, F. Yan, J. Yu, H. L. W. Chan, M. Yang, *Adv. Mater.* **2010**, *22*, 3655–3660.
- [28] D. Nilsson, N. Robinson, M. Berggren, R. Forchheimer, *Adv. Mater.* **2005**, *17*, 353–358.
- [29] <https://www.nobelprize.org/uploads/2018/06/advanced-chemistryprize2000.pdf>, accessed 28.07.2020.
- [30] H. Shirakawa, E. J. Louis, A. G. MacDiarmid, C. K. Chiang, A. J. Heeger, *J. Chem. Soc. Chem. Comm.* **1977**, 578–580.
- [31] C. Chiang, C. Fincher, Y. Park, A. Heeger, *Phys. Rev. Lett.* **1977**, *39*, 1098–1101.
- [32] Y. Liang, Z. Chen, Y. Jing, Y. Rong, A. Facchetti, Y. Yao, *J. Am. Chem. Soc.* **2015**, *137*, 4956–4959.
- [33] K. Bruchlos, PhD Thesis, University of Stuttgart, **2019**.

-
- [34] *Encyclopedia of Polymeric Nanomaterials*, (Eds.: S. Eds: Kobayashi, Müllen), Springer, Berlin, Heidelberg, **2015**.
- [35] A. Heeger, *Chem. Soc. Rev.* **2010**, *39*, 2354—2371.
- [36] H. Yan, Z. Chen, C. Newman, J. R. Quinn, F. Dötz, M. Kastler, A. Facchetti, *Nature* **2009**, *457*, 679–686.
- [37] J. L. Bredas, G. B. Street, *Acc. Chem. Res.* **1985**, *18*, 309–315.
- [38] *Conjugated Polymers*, 1st ed., (Eds.: J. Brédas, R. Silbey), Springer Netherlands, Dordrecht, Netherlands, **1991**.
- [39] Y. Yao, H. Dong, F. Liu, T. P. Russell, W. Hu, *Adv. Mater.* **2017**, *29*, 1701251.
- [40] R. Hoffmann, C. Janiak, C. Kollmar, *Macromolecules* **1991**, *24*, 3725—3746.
- [41] C. Winder, N. S. Sariciftci, **2004**, *14*, 1077–1086.
- [42] W. T. Neo, Q. Ye, S.-J. Chua, J. Xu, *J. Mater. Chem. C.* **2016**, *4*, 7364–7376.
- [43] A. G. MacDiarmid, R. J. Mammone, R. B. Kaner, S. J. Porter, *Phil. Trans. R. Soc. Lond.* **1985**, *314*, 3–15.
- [44] K. Tremel, S. Ludwigs, *Morphology of P3HT in Thin Films in Relation to Optical and Electrical Properties*. In: *P3HT Revisited – From Molecular Scale to Solar Cell Devices. Advances in Polymer Science*, (Ed.: S. Ludwigs), Springer, Berlin, Heidelberg, Germany, **2014**.
- [45] K. Bruchlos, D. Trefz, A. Hamidi-Sakr, M. Brinkmann, J. Heinze, A. Ruff, S. Ludwigs, *Electrochim. Acta* **2018**, *269*, 299–311.
- [46] J. Heinze, B. A. Frontana-Uribe, S. Ludwigs, *Chem. Rev.* **2010**, *110*, 4724–4771.
- [47] E. J. W. Crossland, K. Rahimi, G. Reiter, U. Steiner, S. Ludwigs, *Adv. Funct. Mater.* **2011**, *21*, 518–524.
- [48] F. C. Spano, C. Silva, *Ann. Rev. Phys. Chem.* **2014**, *65*, 477–500.
- [49] M. Hess, R. G. Jones, J. Kahovec, T. Kitayama, P. Kratochvil, P. Kubisa, W. Mormann, R. F. T. Stepto, D. Tabak, J. Vohlidal, E. S. Wilks, *Pure Appl. Chem.* **2006**, *78*, 2067–2074.
- [50] <https://roempp.thieme.de/lexicon/RD-16-03194>, accessed 21.08.2020.
- [51] J. Koetz, S. Kosmella, *Polyelectrolytes*. In: *Polyelectrolytes and Nanoparticles*, Springer, Berlin, Heidelberg, Germany, **2007**.
- [52] H. M. L. Thijs, C. R. Becer, C. Guerrero-Sanchez, D. Fournier, R. Hoogenboom, U. S. Schubert, *J. Mater. Chem.* **2007**, *17*, 4864—4871.

- [53] S. Christau, S. Thurandt, Z. Yenice, R. von Klitzing, *polymers* **2014**, *6*, 1877–1896.
- [54] P. Hummel, A. M. Lechner, K. Herrmann, P. Biehl, C. Rössel, L. Wiedenhöft, F. H. Schacher, M. Retsch, *Macromolecules* **2020**, *53*, 5528–5537.
- [55] C. Heitner-Wirguin, **1996**, *120*, 1–33.
- [56] K. Schmidt-Rohr, C. Qiang, *Nature Materials* **2008**, *7*, 75–83.
- [57] A. Eisenberg, J.-S. Kim, *Introduction to Ionomers*, John Wiley and Sons, New York, US, **1998**.
- [58] K. A. Mauritz, R. B. Moore, *Chem. Rev.* **2004**, *104*, 4535–4586.
- [59] T. Gierke, G. Munn, F. Wilson, *J. Polym. Sci.: Polym. Phys. Edition* **1981**, *19*, 1687–1704.
- [60] K.-D. Kreuer, *Solide State Ionics* **2013**, *252*, 93–101.
- [61] G. Wee, O. Larsson, M. Srinivasan, M. Berggren, X. Crispin, S. Mhaisalkar, *Adv. Funct. Mater.* **2010**, *20*, 4344–4350.
- [62] S. De, C. Cramer, M. Schönhoff, *Macromolecules* **2011**, *44*, 8936–8943.
- [63] H. Wang, D. Zhao, Z. U. Khan, S. Puzinas, M. P. Jonsson, M. Berggren, X. Crispin, *Adv. Electr. Mater.* **2017**, *3*, 1700013.
- [64] A. E. Aliev, I. N. Kholmanov, P. K. Khabibullaev, *Solid State Ionics* **1999**, *118*, 111–116.
- [65] J. R. Varcoe, *Phys. Chem. Chem. Phys.* **2007**, *9*, 1479–1486.
- [66] O. Larsson, E. Said, M. Berggren, X. Crispin, *Adv. Funct. Mater.* **2009**, *19*, 3334.
- [67] S. Shi, A. Z. Weber, A. Kusoglu, *Electrochim. Acta* **2016**, *220*, 517–528.
- [68] Y. Sakai, Y. Sadaoka, M. Matsuguchi, *Sensors and Actuators B: Chemical* **1996**, *35*, 85–90.
- [69] K.-D. Kreuer, *Chem. Mater.* **2014**, *26*, 361–380.
- [70] J. Peng, K. Lou, G. Goenaga, T. Zawodzinski, *ACS Appl. Mater. Interfaces* **2018**, *10*, 38418–38430.
- [71] H. L. Yeager, A. Steck, *J. Electrochem. Soc.* **1981**, *128*, 1880–1884.
- [72] N. P. Blake, G. Mills, H. Metiu, *The Journal of phys. chem. B* **2007**, *111*, 2490–2494.
- [73] *Conjugated Polyelectrolytes: Fundamentals and Applications*, 1. Aufl., (Eds.: B. Liu, G. C. Bazan), Wiley-VCH, Weinheim, DE, **2013**.

-
- [74] H. Jiang, P. Taranekar, J. R. Reynolds, K. S. Schanze, *Angew. Chem. Int. Ed.* **2009**, *48*, 4300–4316.
- [75] M. S. Freund, B. Deore, *Self-Doped Conducting Polymers*, Wiley, Chichester, England and Hoboken, NJ, **2007**.
- [76] M. Sato, S. Tanaka, K. Kaeriyama, **1986**, 873–874.
- [77] J. E. Frommer, *Acc. Chem. Res.* **1986**, *19*, 2.
- [78] A. O. Patil, Ikenoue Y., Wudl F., Heeger A. J., *J. Am. Chem. Soc.* **1987**, *109*, 1858–1859.
- [79] Y. Ikenoue, Y. Saida, M.-a. Kira, H. Tomozawa, H. Yashima, M. Kobayashi, *J. Chem. Soc. Chem. Comm.* **1990**, 1694–1695.
- [80] M. I. Arroyo-Villan, G. A. Diaz-Quijada, M. S. A. Abdou, S. Holdcroft, *Macromolecules* **1995**, *28*, 975–984.
- [81] L. Ying, F. Huang, G. C. Bazan, *Nat. Comm.*, *8*, 14047.
- [82] Y. Kim, S. Cook, S. M. Tuladhar, S. A. Choulis, J. Nelson, J. R. Durrant, D. D. C. Bradley, M. Giles, I. McCulloch, C.-S. Ha, M. Ree, *Nat. Mater.* **2006**, *5*, 197–203.
- [83] H. Sirringhaus, P. J. Brown, R. H. Friend, M. M. Nielsen, K. Bechgaard, B. M. W. Langeveld-Voss, A. J. H. Spiering, R. A. J. Janssen, E. W. Meijer, P. Herwig, D. M. de Leeuw, *Nature* **1999**, *401*, 685–688.
- [84] Y. Ikenoue, N. Outani, A. O. Patil, F. Wudl, A. J. Heeger, *Synth. Metals* **1989**, *30*, 305–319.
- [85] S. A. Chen, M. Y. Hua, *Macromolecules* **1993**, *26*, 7108–7110.
- [86] J. W. Jo, J. W. Jung, S. Bae, M. J. Ko, H. Kim, W. H. Jo, A. K.-Y. Jen, H. J. Son, *Adv. Mater. Interf.* **2016**, *3*, 1500703.
- [87] T. C. Doan, R. Ramaneti, J. Baggerman, H. D. Tong, A. T. Marcelis, C. J. van Rijn, *Electrochim. Acta* **2014**, *127*, 106–114.
- [88] G. Hostnik, M. Boncina, C. Dolce, G. Meriguet, A.-L. Rollet, J. Cerar, *Phys. Chem. Chem. Phys.* **2016**, *18*, 25036.
- [89] A. F. Thünemann, D. Ruppelt, *Langmuir* **2001**, *17*, 5098–5102.
- [90] C.-K. Mai, H. Zhou, Y. Zhang, Z. B. Henson, T.-Q. Nguyen, A. J. Heeger, G. C. Bazan, *Angew. Chem. Int. Ed.* **2013**, *52*, 12874–12878.
- [91] C.-K. Mai, R. A. Schlitz, G. M. Su, D. Spitzer, X. Wang, S. L. Fronk, D. G. Cahill, M. L. Chabynyc, G. C. Bazan, *J. Am. Chem. Soc.* **2014**, *136*, 13478–13481.

- [92] D. Bondarev, J. Zednik, I. Sloufova, A. Sharf, M. Prochazka, J. Pfeleger, J. Vohlidal, *J. Polym. Sci.: Part A: Polym. Chem.* **2010**, *48*, 3073–3081.
- [93] J. Kesters, S. Govaerts, G. Pirotte, J. Drijkoningen, M. Chevrier, N. Van den Brande, X. Liu, M. Fahlman, B. Van Mele, L. Lutsen, D. Vanderzande, J. Manca, S. Clement, E. Von Hauff, W. Maes, *ACS Appl. Mater. Interfaces* **2016**, *8*, 6309–6314.
- [94] R. Yang, H. Wu, Y. Cao, G. C. Bazan, *J. Am. Chem. Soc.* **2006**, *128*, 14422–14423.
- [95] D. Tordera, M. Kuik, Z. D. Rengert, E. Bandiello, H. J. Bolink, G. C. Bazan, T.-Q. Nguyen, *J. Am. Chem. Soc.* **2014**, *136*, 8500–8503.
- [96] A. Gutacker, C.-Y. Lin, L. Ying, T.-Q. Nguyen, U. Scherf, G. C. Bazan, *Macromolecules* **2012**, *45*, 4441–4446.
- [97] J. Rivnay, S. Inal, B. A. Collins, M. Sessolo, E. Stavrinidou, X. Strakosas, C. Tassone, D. M. DeLongchamp, G. G. Malliaras, *Nat. Comm.* **2016**, *7*, 11287.
- [98] A. Elschner, *PEDOT: Principles and Applications of an Intrinsically Conductive Polymer*, CRC Press, Boca Raton, Fla., **2011**.
- [99] F. Dallacker, V. Mues, *Chem. Ber.* **1975**, *108*, 569–575.
- [100] M. Dietrich, J. Heinze, G. Heywang, F. Jonas, *J. Electroanal. Chem.* **1994**, *369*, 87–92.
- [101] F. Jonas, W. Krafft, (Bayer AG) European Patent EP 440 957, March 10, **1991**.
- [102] F. Louwet, L. Groenendaal, J. Dhaen, J. Manca, J. Van Luppen, E. Verdonck, L. Leenders, *Synth. Met.* **2003**, *135–136*, 115–117.
- [103] T. Stöcker, A. Köhler, R. Moos, *J. Polym. Sci. Part B: Polym. Phys.* **2012**, *50*, 976–983.
- [104] V. Gogte, L. Shah, B. Tilak, K. Gadekar, M. Sahasrabudhe, *Tetrahedron* **1967**, *23*, 2437–2441.
- [105] X. Crispin, F. L. E. Jakobsson, A. Crispin, P. C. M. Grim, P. Andersson, A. Volodin, C. van Haesendonck, M. Van der Auweraer, W. R. Salaneck, M. Berggren, *Chem. Mater.* **2006**, *18*, 4354–4360.
- [106] M. Modarresi, J. F. Franco-Gonzalez, I. Zozoulenko, *Phys. Chem. Chem. Phys.* **2019**, *21*, 6699–6711.
- [107] A. Ugur, F. Katmis, M. Li, L. Wu, Y. Zhu, K. K. Varanasi, K. K. Gleason, *Adv. Mater.* **2015**, *27*, 4604–4610.

-
- [108] O. Bubnova, Z. U. Khan, H. Wang, S. Braun, D. R. Evans, M. Fabretto, P. Hojati-Talemi, D. Dagnelund, J.-B. Arlin, Y. H. Geerts, S. Desbief, D. W. Breiby, J. W. Andreasen, R. Lazzaroni, W. M. Chen, I. Zozoulenko, M. Fahlman, P. J. Murphy, M. Berggren, X. Crispin, *Nat. Mater.* **2014**, *13*, 190–194.
- [109] K. Aasmundtveit, E. Samuelsen, L. Pettersson, O. Inganas, T. Johansson, R. Feidenhans, *Synth. Met.* **1999**, *101*, 561–564.
- [110] T. Takano, H. Masunaga, A. Fujiwara, H. Okuzaki, T. Sasaki, *Macromolecules* **2012**, *45*, 3859–3865.
- [111] C. M. Palumbiny, F. Liu, T. P. Russell, A. Hexemer, C. Wang, P. Müller-Buschbaum, *Adv. Mater.* **2015**, *27*, 3391–3397.
- [112] M. N. Gueye, A. Carella, N. Massonnet, E. Yvenou, S. Brenet, J. Faure-Vincent, S. Pouget, F. Rieutord, H. Okuno, A. Benayad, R. Demadrille, J.-P. Simonato, *Chem. Mater.* **2016**, *28*, 3462–3468.
- [113] A. V. Volkov, K. Wijeratne, E. Mittraka, U. Ail, D. Zhao, K. Tybrandt, J. W. Andreasen, M. Berggren, X. Crispin, I. V. Zozoulenko, *Adv. Funct. Mater.* **2017**, *27*, 1700329.
- [114] U. Lang, E. Müller, N. Naujoks, J. Dual, *Adv. Funct. Mater.* **2009**, *19*, 1215–1220.
- [115] T. Horii, H. Hikawa, Y. Mochizuki, H. Okuzaki, *Trans. Mat. Res. Soc. Japan* **2012**, *4*, 515–518.
- [116] J.-S. Yeo, J.-M. Yun, D.-Y. Kim, S. Park, S.-S. Kim, M.-H. Yoon, T.-W. Kim, S.-I. Na, *ACS Appl. Mater. Interfaces* **2012**, *4*, 2551–2560.
- [117] A. M. Nardes, M. Kemerink, R. A. Janssen, J. A. Bastiaansen, N. M. Kiggen, B. M. Langeveld, A. J. Van Breemen, M. M. De Kok, *Adv. Mater.* **2007**, *19*, 1196–1200.
- [118] K.-C. Chang, M.-S. Jeng, C.-C. Yang, Y.-W. Chou, S.-K. Wu, M. A. Thomas, Y.-C. Peng, *J. Electr. Mater.* **2009**, *38*, 1182–1188.
- [119] H. Bednarski, B. Hajduk, J. Jurusik, B. Jarzabek, M. Domański, K. Łaba, A. Wanic, M. Łapkowski, *Acta Phys. Pol. A* **2016**, *130*, 1242–1244.
- [120] P. Vaccaa, M. Petrosinob, R. Misciosciaa, G. Nennaa, C. Minarinia, D. D. Salaa, A. Rubino, *Thin Solid Films* **2008**, *516*, 4232–4237.
- [121] P. Sakunpongpitiporn, K. Phasuksom, N. Paradee, A. Siriva, *RSC Adv.* **2019**, *9*, 6363–6378.

- [122] G. Zotti, S. Zecchin, G. Schiavon, F. Louwet, L. Groenendaal, X. Crispin, W. Osikowicz, W. Salaneck, M. Fahlman, *Macromolecules* **2003**, *36*, 3337–3344.
- [123] K. Reuter, A. Karbach, H. Ritter, N. Wrubbel, (Bayer AG) European Patent EP 1 440 974 A2, January 21, **2003**.
- [124] <https://www.gamry.com/application-notes/EIS/basics-of-electrochemical-impedance-spectroscopy/> accessed 22.07.2020.
- [125] D. Kim, I. Zozoulenko, *J. Phys. Chem. B* **2019**, *123*, 5160–5167.
- [126] S.-H. Jeong, S. Ahn, T.-W. Lee, *Macromol. Res.* **2019**, *27*, 2–9.
- [127] I. Lee, G. W. Kim, M. Yang, T.-S. Kim, *ACS Appl. Mater. Interf.* **2016**, *8*, 302–310.
- [128] H. Yamaguchi, K. Aizawa, Y. Chonan, T. Komiyama, T. Aoyama, E. Sakai, J. Qiu, N. Sato, *J. Electr. Mater.* **2018**, *47*, 3370–3375.
- [129] A. M. Nardes, M. Kemerink, M. M. de Kok, E. Vinken, K. Maturova, R. Janssen, *Org. Electr.* **2008**, *9*, 727–734.
- [130] H. Yan, T. Jo, H. Okuzaki, *Polym. J.* **2009**, *41*, 1028–1029.
- [131] N. Massonnet, A. Carella, J. Olivier, P. Rannou, G. Laval, C. Cellea, J.-P. Simonato, **2014**, *2*, 1278–1283.
- [132] Q. Wei, M. Mukaida, Y. Naitoh, T. Ishida, *Adv. Mater.* **2013**, *25*, 2831–2836.
- [133] Y. H. Kim, C. Sachse, M. L. Machala, C. May, L. Müller-Meskamp, K. Leo, *Adv. Funct. Mater* **2011**, *21*, 1076–1081.
- [134] Y. Xia, K. Sun, J. Ouyang, *Adv. Mater.* **2012**, *24*, 2436–2440.
- [135] N. Kim, B. H. Lee, D. Choi, G. Kim, H. Kim, J. Kim, J. Lee, Y. H. Kahn, K. Lee, *Phys. Rev. Lett.* **2012**, *109*, 106405.
- [136] N. Kim, H. Kang, J.-H. Lee, S. Kee, S. H. Lee, K. Lee, *Adv. Mater.* **2015**, *27*, 2317–2323.
- [137] N. Kim, S. Kee, S. H. Lee, B. H. Lee, Y. H. Kahng, Y.-R. Jo, B.-J. Kim, K. Lee, *Adv. Mater.* **2014**, *26*, 2268–2272.
- [138] S.-M. Kim, C.-H. Kim, Y. Kim, N. Kim, W.-J. Lee, E.-H. Lee, D. Kim, S. Park, K. Lee, J. Rivnay, M.-H. Yoon, *Nat. Comm.* **2018**, *9*, 3858.
- [139] J. Zhang, S. Seyedin, S. Qin, P. A. Lynch, Z. Wang, W. Yang, X. Wang, J. M. Razal, *J. Mater. Chem. A* **2019**, *7*, 6401–6410.

-
- [140] B. J. Worfolk, S. C. Andrews, S. Park, J. Reinspach, M. F. Liu, Nan Toney, S. C. B. Mannsfeld, Z. Bao, *PNAS* **2015**, *112*, 14138–14143.
- [141] K. Yasumoro, Y. Fujita, H. Arimatsu, T. Fujima, *Polymers* **2020**, *12*, 1–7.
- [142] A. Malti, J. Edberg, H. Granberg, Z. U. Khan, J. W. Andreasen, X. Liu, D. Zhao, H. Zhang, Y. Yao, J. W. Brill, I. Engquist, M. Fahlman, L. Wågberg, X. Crispin, M. Berggren, *Adv. Sci.* **2016**, *3*, 1500305.
- [143] S. D. Collins, O. V. Mikhnenko, T. L. Nguyen, Z. D. Rengert, G. C. Bazan, H. Y. Woo, T.-Q. Nguyen, *Adv. El. Mater.* **2017**, *3*, 1700005.
- [144] T. Johansson, N.-K. Persson, O. Ingan"as, *J. Electrochem. Soc.* **2004**, *151*, 119–124.
- [145] E. Stavrinidou, P. Leleux, H. Rajaona, D. Khodagholy, J. Rivnay, M. Lindau, S. Sanaur, G. G. Malliaras, *Adv. Mater.* **2013**, *25*, 4488–4493.
- [146] R. H. Friend, *Synthetic Metals* **1992**, *51*, 357–371.
- [147] P. Atkins, J. de Paula, *Physical Chemistry*, 10th ed., Oxford University Press, Oxford, UK, **2014**.
- [148] S. Inal, G. Malliaras, J. Rivnay, *J. Mater. Chem. C* **2016**, *4*, 3942–3947.
- [149] D. Li, B. Fu, Y. Wang, G. Lu, Y. Berezin, H. E. Stanley, S. Havlin, *PNAS* **2015**, *112*, 669–672.
- [150] K. Sun, S. Zhang, P. Li, Y. Xia, X. Zhang, D. Du, F. H. Isikgor, J. Ouyang, *J. Mater. Sci.: Mater. Electron.*, *26*, 4438–4462.
- [151] X. Fan, W. Nie, H. Tsai, N. Wang, H. Huang, Y. Cheng, R. Wen, L. Ma, F. Yan, Y. Xia, *Adv. Sci.* **2019**, *6*, 1900813.
- [152] Y.-T. Tseng, Y.-C. Lin, C.-C. Shih, H.-C. Hsieh, W.-Y. Lee, Y.-C. Chiu, W.-C. Chen, *J. Mater. Chem.* **2020**, *8*, 6013–6024.
- [153] C.-h. Chen, J. C. LaRue, R. D. Nelson, L. Kulinsky, M. J. Madou, *J. Appl. Polym. Sci.* **2012**, *125*, 3134–3141.
- [154] X.-Y. Wang, G.-Y. Feng, M.-J. Li, M.-Q. Ge, *Polymer Bulletin* **2019**, *76*, 2097–2111.
- [155] E. M. Ahmed, *J. Adv. Res.* **2015**, *6*, 105–121.
- [156] B. Lu, H. Yuk, S. Lin, N. Jian, K. Qu, J. Xu, X. Zhao, *Nat. Comm.* **2019**, *10*, 1043.

- [157] Y.-S. Hsiao, W.-T. Whang, C.-P. Chen, Y.-C. Chen, *J. Mater. Chem.* **2008**, *18*, 5948–5955.
- [158] X.-Y. Li, L.-P. Zhang, F. Tang, Z.-M. Bao, J. Lin, Y.-Q. Li, L. Chen, C.-Q. Ma, *RSC Advances* **2016**, *6*, 24501–24507.
- [159] P. A. Levermore, R. Jin, X. Wang, L. Chen, D. D. C. Bradley, J. C. de Mello, *J. Mater. Chem.* **2008**, *18*, 4414.
- [160] R. Merkle, P. Gutbrod, P. Reinold, M. Katzmaier, R. Tkachov, J. Maier, S. Ludwigs, *Polymer* **2017**, *132*, 216–226.
- [161] B. Sarkar, M. Jaiswal, D. K. Satapathy, *J. Phys.: Cond. Matter* **2018**, *30*, 225101.
- [162] P. Reinold, PhD Thesis, University of Stuttgart, **2018**.
- [163] D. T. Scholes, S. A. Hawks, P. Y. Yee, H. Wu, J. R. Lindemuth, S. H. Tolbert, B. J. Schwartz, *J. Phys. Chem. Lett.* **2015**, *6*, 4786–4793.
- [164] I. E. Jacobs, E. W. Aasen, J. L. Oliveira, T. N. Fonseca, J. D. Roehling, J. Li, G. Zhang, M. P. Augustine, M. Mascal, A. J. Moulé, *J. Mater. Chem. C* **2016**, *4*, 3454–3466.
- [165] *CRC Handbook of Chemistry and Physics*, 99th ed., (Ed.: J. R. Rumble), CRC, Boca Raton, Florida, US, **2018**.
- [166] *Encyclopedia of Electrochemistry*, 8th ed., (Eds.: A. Bard, M. Stratmann), Wiley-VCH, Weinheim, Germany, **2004**.
- [167] T. Osaka, D. Mukoyama, H. Nara, *J. Electrochem. Soc.* **2015**, *162*, A2529–A2537.
- [168] X.-Z. Yuan, C. Song, H. Wang, J. Zhang, *Electrochemical Impedance Spectroscopy in PEM Fuel Cells*, 1st ed., Springer Publishing, London, United Kingdom, **2010**.
- [169] <https://www.gamry.com/application-notes/EIS/eis-potentiostatic-galvanostatic-mode/>, accessed 10.01.2020.
- [170] V. F. Lvovich, *Impedance Spectroscopy*, John Wiley & Sons, Inc, Hoboken, NJ, USA, **2012**.
- [171] *Springer Handbook of Electronic and Photonic Materials*, 2nd ed., (Eds.: S. Kasap, P. Capper), Springer International Publishing AG, Basel, Switzerland, **2017**.
- [172] <http://www.abc.chemistry.bsu.by/vi/analyser/parameters.html>, accessed 24.02.2020.
- [173] A. Lasia, *Electrochemical Impedance Spectroscopy and its Applications*, Springer Science & Business Media, New York, US, **2014**.

-
- [174] F. R. Lack, G. W. Willard, I. E. Fair, *Bell System Technical Journal* **1934**, *13*, 453–463.
- [175] G. Sauerbrey, *Z. f. Phys.* **1959**, *155*, 206–222.
- [176] P. A. Tamirisa, D. W. Hess, *Macromolecules* **2006**, *39*, 7092–7097.
- [177] J. Heinze, *Angew. Chem.* **1984**, *96*, 823–916.
- [178] N. Elgrishi, K. J. Rountree, B. D. McCarthy, E. S. Rountree, T. T. Eisenhart, J. L. Dempsey, *J. Chem. Educ.* **2018**, *95*, 197–206.
- [179] G. Gritzner, J. Kuta, *Pure & Appl. Chem.* **1984**, *56*, 461–466.
- [180] W. Kaim, J. Fiedler, *Chem. Soc. Rev.* **2009**, *38*, 3373–3382.
- [181] G. Zotti, G. Schiavon, *Synth. Met.* **1989**, *30*, 151–158.
- [182] G. Salinas, B. A. Frontana-Uribe, *ChemElectroChem* **2019**, *6*, 4105–4117.
- [183] F. Panzer, H. Bässler, R. Lohwasser, R. Thelakkat, A. Köhler, *J. Phys. Chem. Lett.* **2014**, *5*, 2742–2747.
- [184] G. Schulz, S. Ludwigs, *Adv. Funct. Mater.* **2017**, *27*, 1603083.
- [185] Y. Marcus, *J. Chem. Soc. Faraday Transactions* **1993**, *89*, 713–718.
- [186] R. P. Pearson, *J. Am. Chem. Soc.* **1963**, *85*, 3533–3539.
- [187] G. N. Lewis, *Chemical Catalog Company* **1923**, 142.
- [188] Bruker, AFM enhancing traditional Electron Microscopy Applications, **2012**.
- [189] P. Boufflet, S. Wood, J. Wade, Z. Fei, J.-S. Kim, M. Heeney, *Beilstein Journal of Organic Chemistry* **2016**, *12*, 2150–2163.
- [190] B. Gu, C. Y. Aung, P. H. J. Chong, Y. L. Guan, K.-T. Yong, *IEEE Sensors Journal* **2018**, *18*, 1081–1086.
- [191] Z. Wang, M. Xue, H. Zhang, M. Zihui, J. K. Shea, L. Qiu, T. Ji, T. Xie, *RSC Adv.* **2018**, *8*, 9963–9969.
- [192] M. Katzmaier, Bachelor Thesis, University of Stuttgart, **2017**.
- [193] D. G. Harman, R. Gorkin, L. Stevens, B. Thompson, K. Wagner, B. Weng, J. H. Y. Chung, M. in Het Panhuis, G. G. Wallace, *Acta Biomater.* **2015**, *14*, 33–42.
- [194] J. Ouyang, Q. Xu, C.-W. Chu, Y. Yang, G. Li, J. Shinar, *Polymer* **2004**, *45*, 8443–8450.
- [195] W. Shi, Q. Yao, S. Qu, H. Chen, T. Zhang, L. Chen, *NPG Asia Mater.* **2017**, *9*, e405–e405.

- [196] J. C. Gustafsson, B. Liedberg, O. Inganäs, *Solid State Ionics* **1994**, *69*, 145–152.
- [197] I. Zozoulenko, A. Singh, S. K. Singh, V. Gueskine, X. Crispin, M. Berggren, *ACS Appl. Polym. Mater.* **2019**, *1*, 83–94.
- [198] B. Villeret, M. Nechtschein, *Phys. Rev. Lett.* **1989**, *63*, 1285–1287.
- [199] D. Ju, D. Kim, H. Yook, J. W. Han, K. Cho, *Adv. Funct. Mater.* **2019**, *5*, 1905590.
- [200] B. Fan, X. Mei, J. Ouyang, *Macromolecules* **2008**, *41*, 5971–5973.
- [201] O. Yurchenko, J. Heinze, S. Ludwigs, *ChemPhysChem* **2010**, *11*, 1637–1640.
- [202] H. John, R. Bauer, P. Espindola, P. Sonar, J. Heinze, K. Müllen, *Angew. Chem.* **2005**, *117*, 2501–2505.
- [203] P. Blanchard, C. Malacrida, C. Cabanetos, J. Roncali, S. Ludwigs, *Polym. Int.* **2018**, *68*, 589–606.
- [204] C. Song, T. M. Swager, *Macromolecules* **2005**, *38*, 4569–4576.
- [205] M. Lapkowski, A. Pron, *Synth. Met.* **2000**, *110*, 79–83.
- [206] M. Erginer, E. Sezer, B. Ustamehmetoğlu, J. Heinze, *Electrochim. Acta* **2012**, *67*, 181–186.
- [207] M. Marzocchi, I. Gualandi, M. Calienni, I. Zironi, E. Scavetta, G. Castellani, B. Fraboni, *ACS Appl. Mater. Interfaces* **2015**, *7*, 17993–18003.
- [208] D. R. Denison, *J. Vacuum Sci. Techn.* **1973**, *10*, 126–129.
- [209] C.-S. Lu, O. Lewis, *J. Appl. Phys.* **1972**, *43*, 4385–4390.
- [210] J. M. Torres, N. Bakken, J. Li, B. D. Vogt, *J. Phys. Chem. B* **2015**, *119*, 11928–11934.
- [211] K. Sittel, P. E. Rouse Jr., E. D. Bailey, *J. Appl. Phys.* **1954**, *25*, 1312.
- [212] B. D. Vogt, E. K. Lin, W.-l. Wu, C. C. White, *J. Phys. Chem. B* **2004**, *108*, 12685–12690.
- [213] STM-2 Rate and Thickness Monitor Operation Manual, Inficon, **2016**.
- [214] Product specification Poly(4-styrenesulfonic acid) solution, Sigma Aldrich, **2020**.
- [215] S. Brunauer, P. H. Emmett, E. Teller, *J. Am. Chem. Soc.* **1938**, *60*, 309–319.
- [216] Product specification PEDOT:PSS 1.1% in water, surfactant-free, high-conductivity grade, Sigma Aldrich, **2020**.
- [217] Product specification Clevios PVP AI 4083, Hereaus, **2019**.

-
- [218] M. Modarresi, A. Mehandzhiyski, M. Fahlman, K. Tybrandt, I. Zozoulenko, *Macromolecules* **2020**, *53*, 6267–6278.
- [219] J. Jamnik, J. Maier, *J. Electrochem. Soc.* **1999**, *146*, 4183–4188.
- [220] E. Warburg, *Annalen der Physik* **1899**, *3*, 494–499.
- [221] *Impedance Spectroscopy: Theory, Experiment, and Applications*, 2nd ed., (Eds.: E. Barsoukov, J. R. MacDonald), Wiley-VCH, Weinheim, Germany, **2005**.
- [222] M. Marzantowicz, J. Dygas, F. Krok, **2008**, *53*, 7417–7425.
- [223] ZView Operating Manual Version 3.5, Scribner Associates Inc., (accessible via ZView software), **2016**.
- [224] R. A. Huggins, *Ionics* **2002**, *8*, 300–313.
- [225] J. Maier, *Z. f. Phys. Chem.* **1984**, *140*, 191–215.
- [226] P. Debye, E. Hückel, *Physikalische Zeitschrift* **1923**, *24*, 305.
- [227] J. Israelachvili, *Intermolecular and Surface Forces*, Academic Press, Waltham, Massachusetts, US, **2011**.
- [228] J. Fleig, *Solid State Ionics* **2002**, *150*, 181–193.
- [229] A. Imre, M. Schönhoff, C. Cramer, *J. Chem. Phys.* **2008**, *128*, 134905.
- [230] *Physical Chemistry of Ionic Materials: Ions and Electrons in Solids*, Wiley & Sons, Ltd, Chichester, UK, **2004**.
- [231] I. Yokota, *J. Phys. Soc. Jpn.* **1961**, *16*, 2213–2223.
- [232] S. Jiang, S. Liu, W. Feng, *J. Mech. Beh. Biomed. Mater.* **2011**, *4*, 1228–1233.
- [233] Y. Hou, C. Chen, K. Liu, Y. Tu, L. Zhang, Y. Li, *RSC Adv.* **2015**, *5*, 24023–24030.
- [234] O. Carr, G. Gozzi, L. F. Santos, R. M. Faria, D. L. Chiniglia, *Transl. Mater. Res.* **2015**, *2*, 015002.
- [235] C. Müller, S. Goffri, D. W. Breiby, J. W. Andreasen, H. D. Chanzy, R. A. Janssen, M. M. Nielsen, C. P. Radano, H. Sirringhaus, P. Smith, N. Stingelin-Stutzmann, *Adv. Funct. Mater.* **2007**, *17*, 2674–2679.
- [236] N. Rolland, J. F. Franco-Gonzalez, R. Volpi, M. Linares, I. V. Zozoulenko, *Phys. Rev. Mater.* **2018**, *2*, 045605.
- [237] F.-F. Pang, S. Li, W.-Q. Sun, G.-Z. Han, *Mater. Chem. and Phys.* **2017**, *186*, 246–250.

- [238] Y. Mochizuki, T. Horii, H. Okuzaki, *Transactions Mater. Res. Soc. Japan* **2012**, *37*, 307–310.
- [239] M. M. de Kok, M. Buechel, S. I. E. Vulto, P. van de Weijer, E. A. Meulenlamp, S. H. P. M. de Winter, A. J. G. Mank, H. J. M. Vorstenbosch, C. H. L. Weijtens, V. van Elsbergen, *phys. stat. sol. (a)* **2004**, *201*, 1342–1359.
- [240] N. Agmon, *Chemical Physics Letters* **1995**, *244*, 456–462.
- [241] G. P. Grimett, *Percolation*, Springer, Berlin, Heidelberg, Germany, **1999**.
- [242] J. E. Steif, A mini course on percolation theory, Mathematical Sciences, Chalmers University of Technology, **2009**.
- [243] P. Li, K. Sun, J. Ouyang, *ACS Appl. Mater. Interfaces* **2015**, *7*, 18415–18423.
- [244] S. Davis, P. Trapman, H. Leirs, M. Begon, J. A. P. Heesterbeek, *Nature* **2008**, *454*, 634–637.
- [245] A. L. Efros, B. I. Shklovskii, *phys. stat. sol. (b)* **1976**, *76*, 475–485.
- [246] M. Loos, *Chapter 5 - Fundamentals of Polymer Matrix Composites Containing CNTs*. In: *Carbon Nanotube Reinforced Composites*, Elsevier, Amsterdam, Netherlands, **2014**, pp. 125–170.
- [247] D. J. Kang, H. Kang, K.-H. Kim, B. J. Kim, *ACS Nano* **2012**, *6*, 7902–7909.
- [248] A. Wittemann, M. Drechsler, Y. Talmon, M. Ballauff, *J. Am. Chem. Soc.* **2005**, *127*, 9688–9689.

7 Appendix

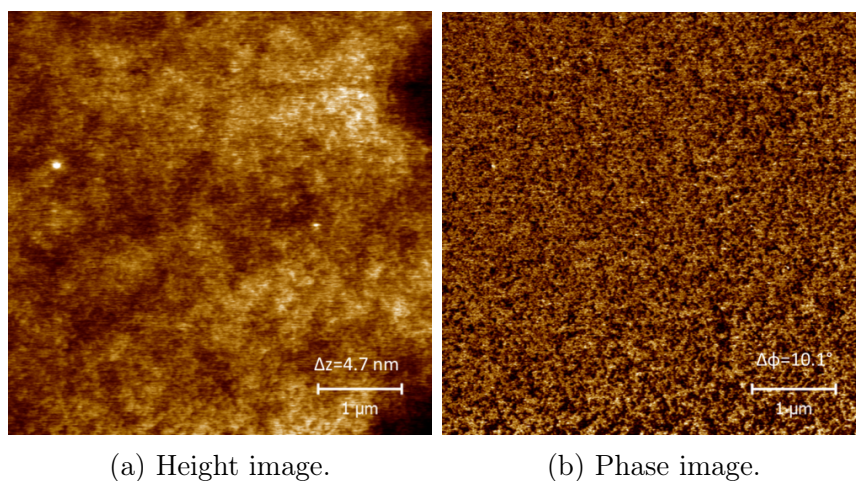


Figure A.1: AFM images of PTS-TBA on glass substrate spin coated from 5 mg/ml $\text{H}_2\text{O}/\text{THF}$.

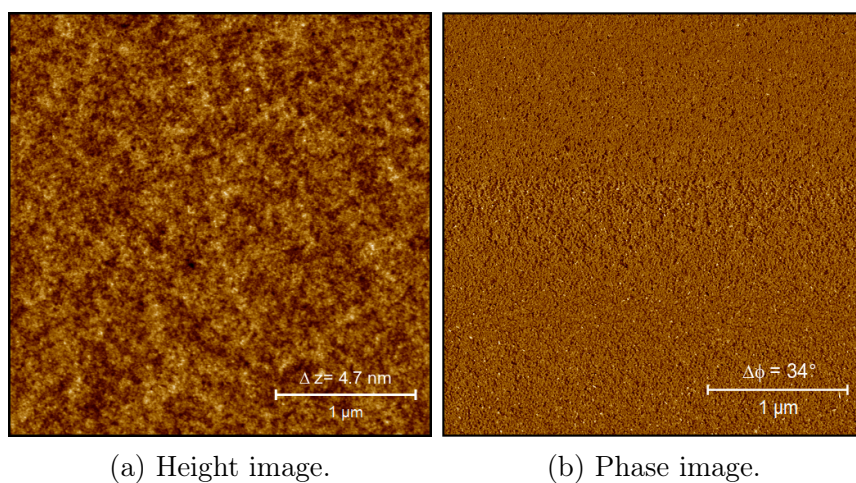


Figure A.2: AFM images of PTS-Na on glass substrate spin coated from 5 mg/ml $\text{H}_2\text{O}/\text{THF}$.

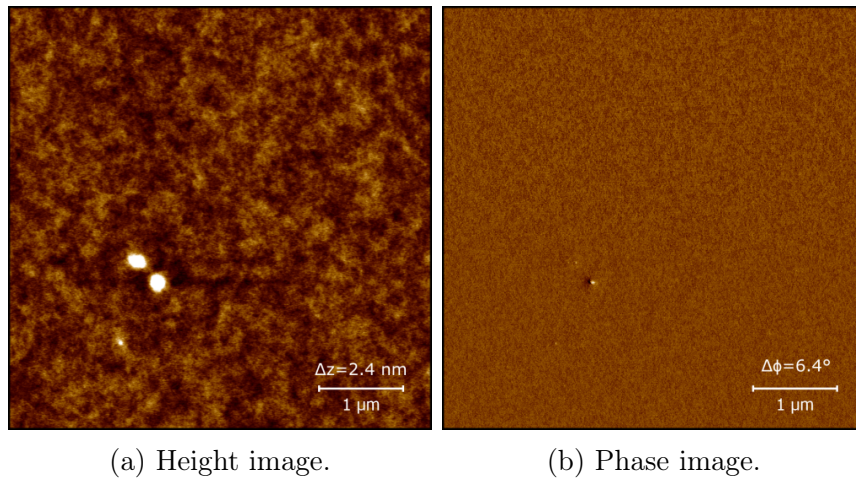


Figure A.3: AFM images of PTS-TBA on glass substrate spin coated from 5 mg/ml H₂O.

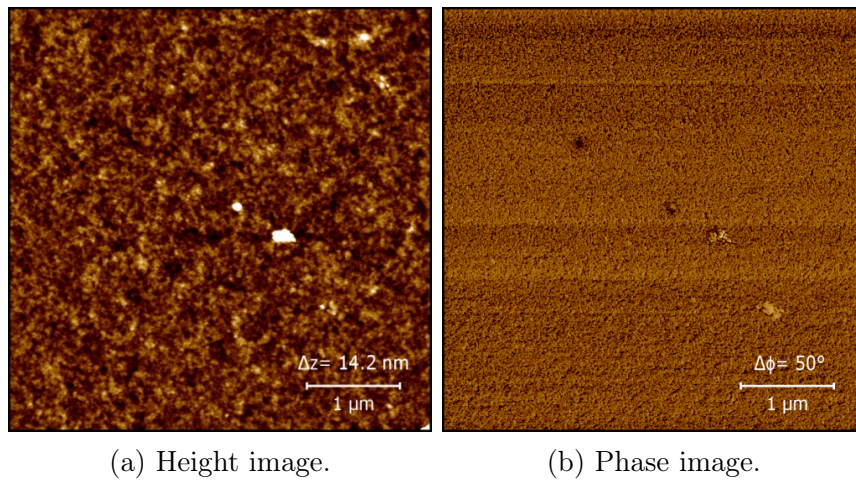


Figure A.4: AFM images of PTS-Na on glass substrate spin coated from 5 mg/ml H₂O.

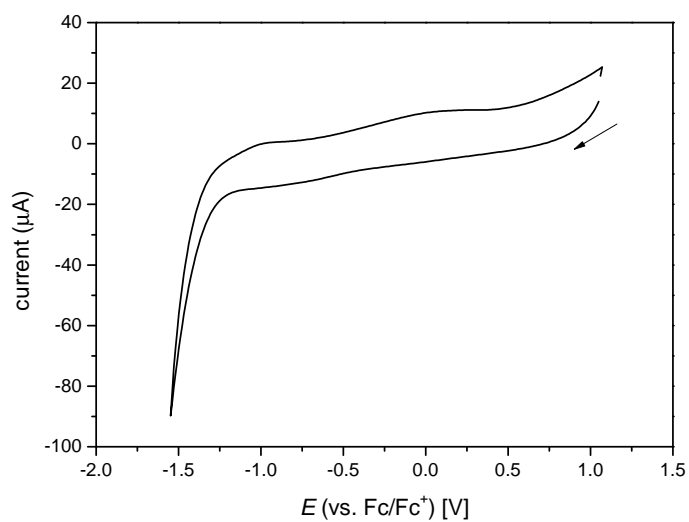


Figure A.5: Cyclic voltammogram of PEDOT:PSS (1:6) on a 5 μm IDE in 0.1 M $\text{NBu}_4\text{PF}_6/\text{MeCN}$ with a scan rate of 10 mV/s.

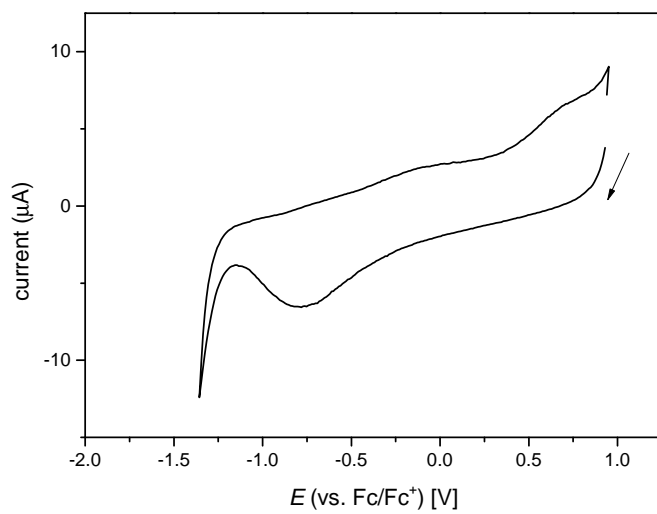


Figure A.6: Cyclic voltammogram of PEDOT:PSS (1:2.5) on a 5 μm IDE in 0.1 M $\text{NBu}_4\text{PF}_6/\text{MeCN}$ with a scan rate of 10 mV/s.

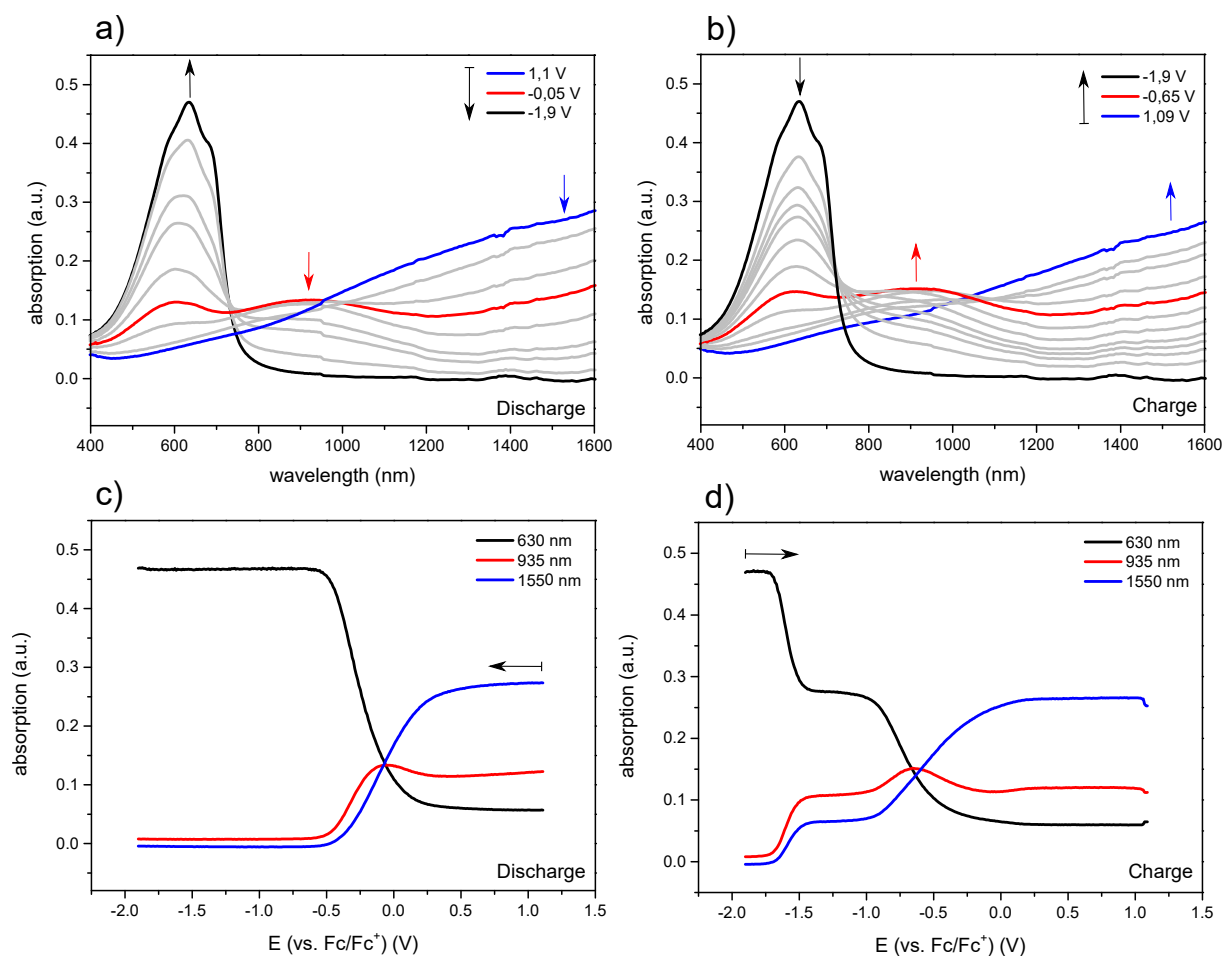


Figure A.7: Spectroelectrochemistry studies of PEDOT:PSS (1:2.5) on a glass substrate in 0.1 M $\text{NBU}_4\text{PF}_6/\text{MeCN}$ with a scan rate of 50 mV/s. a) and b) in-situ UV/Vis NIR spectra recorded during charge and discharge sweep, c) and d) peak trend of selected wavelengths during charge and discharge sweep.

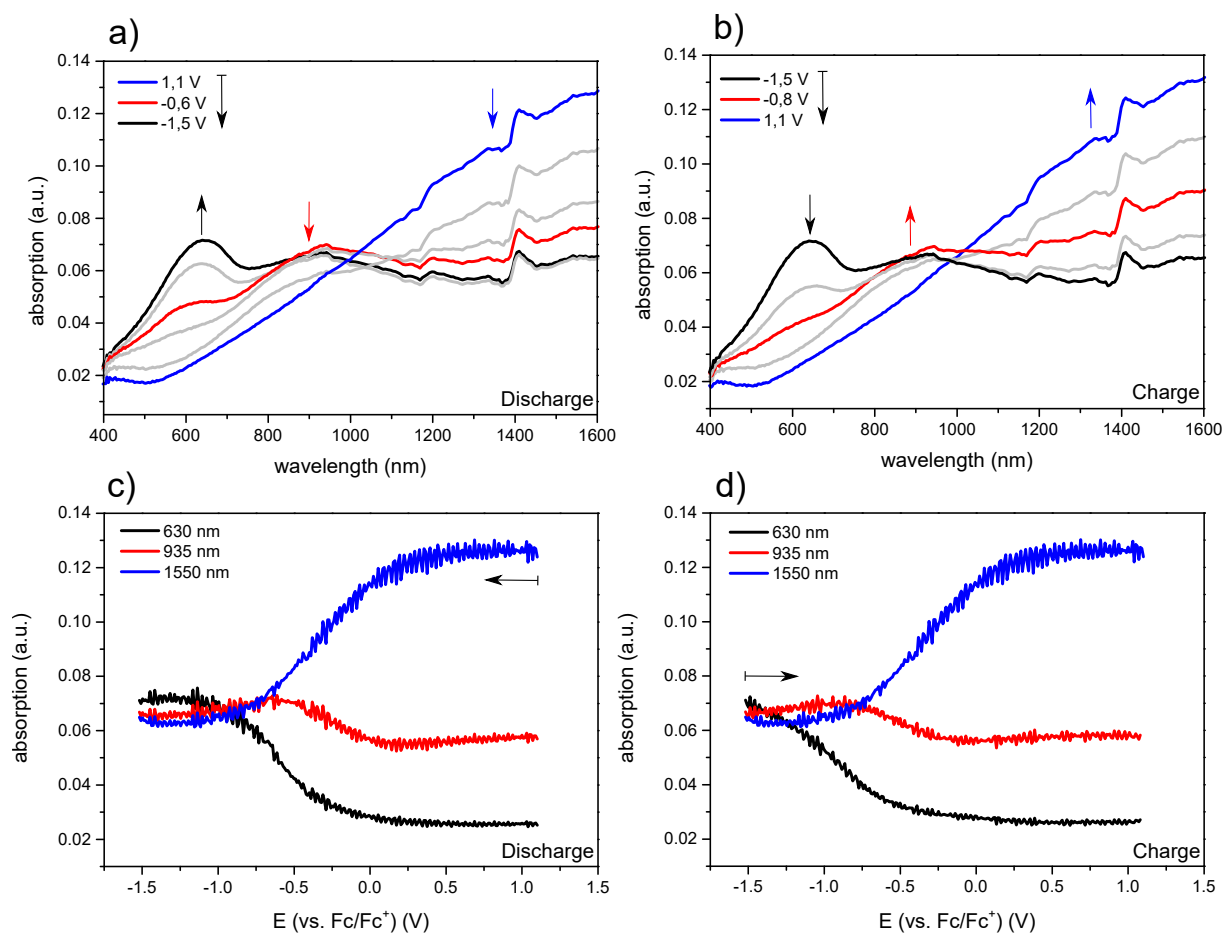


Figure A.8: Spectroelectrochemistry studies of PEDOT:PSS (1:6) on a glass substrate in 0.1 M $\text{NBu}_4\text{PF}_6/\text{MeCN}$ with a scan rate of 50 mV/s. a) and b) in-situ UV/Vis NIR spectra recorded during charge and discharge sweep, c) and d) peak trend of selected wavelengths during charge and discharge sweep.

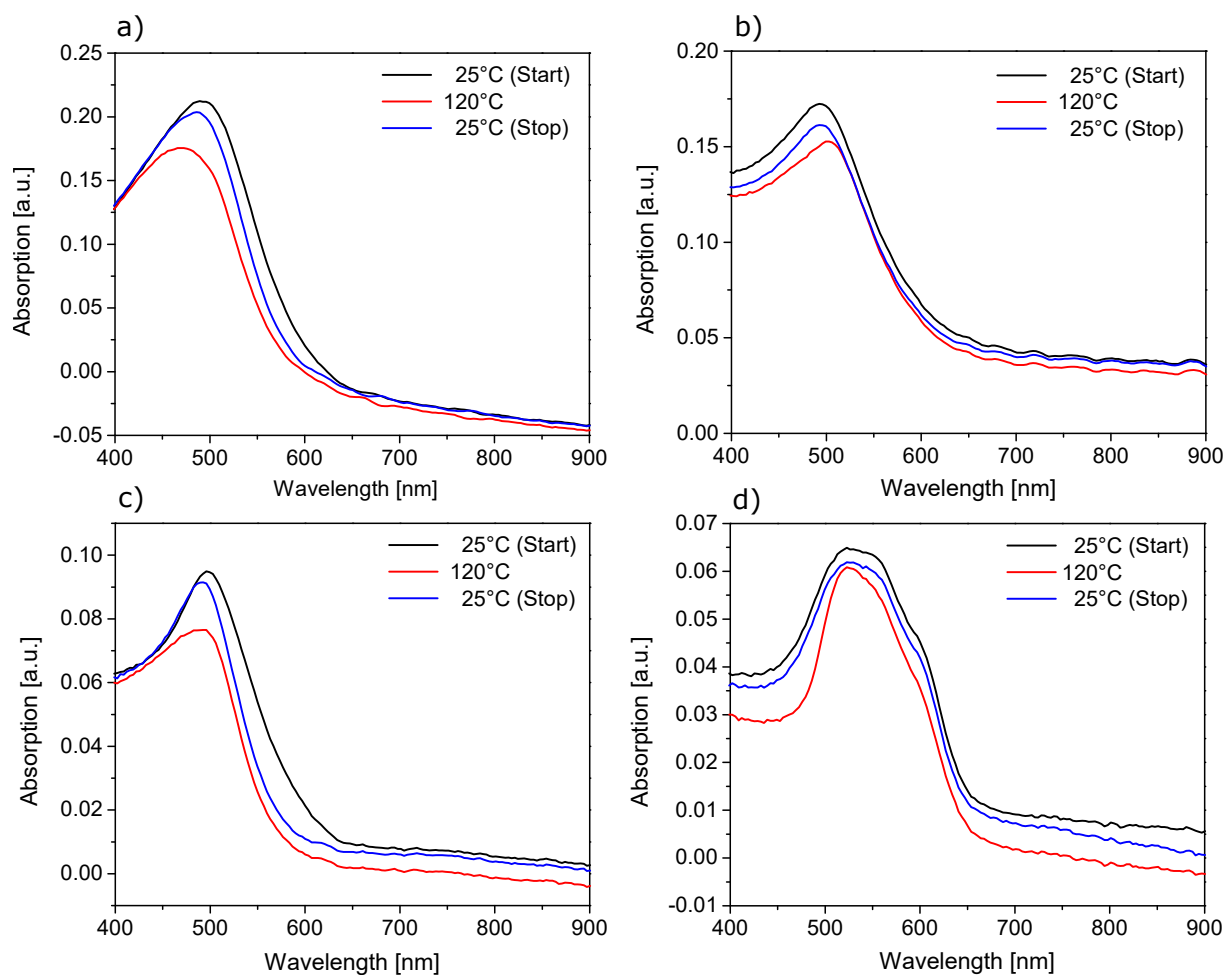


Figure A.9: In-situ UV/Vis absorption spectra on gold substrates during the temperature ramp at 0 mbar H₂O of a) PTS-TBA from H₂O/THF, b) PTS-Na from H₂O/THF, c) PTS-TBA from H₂O and d) PTS-Na from H₂O.

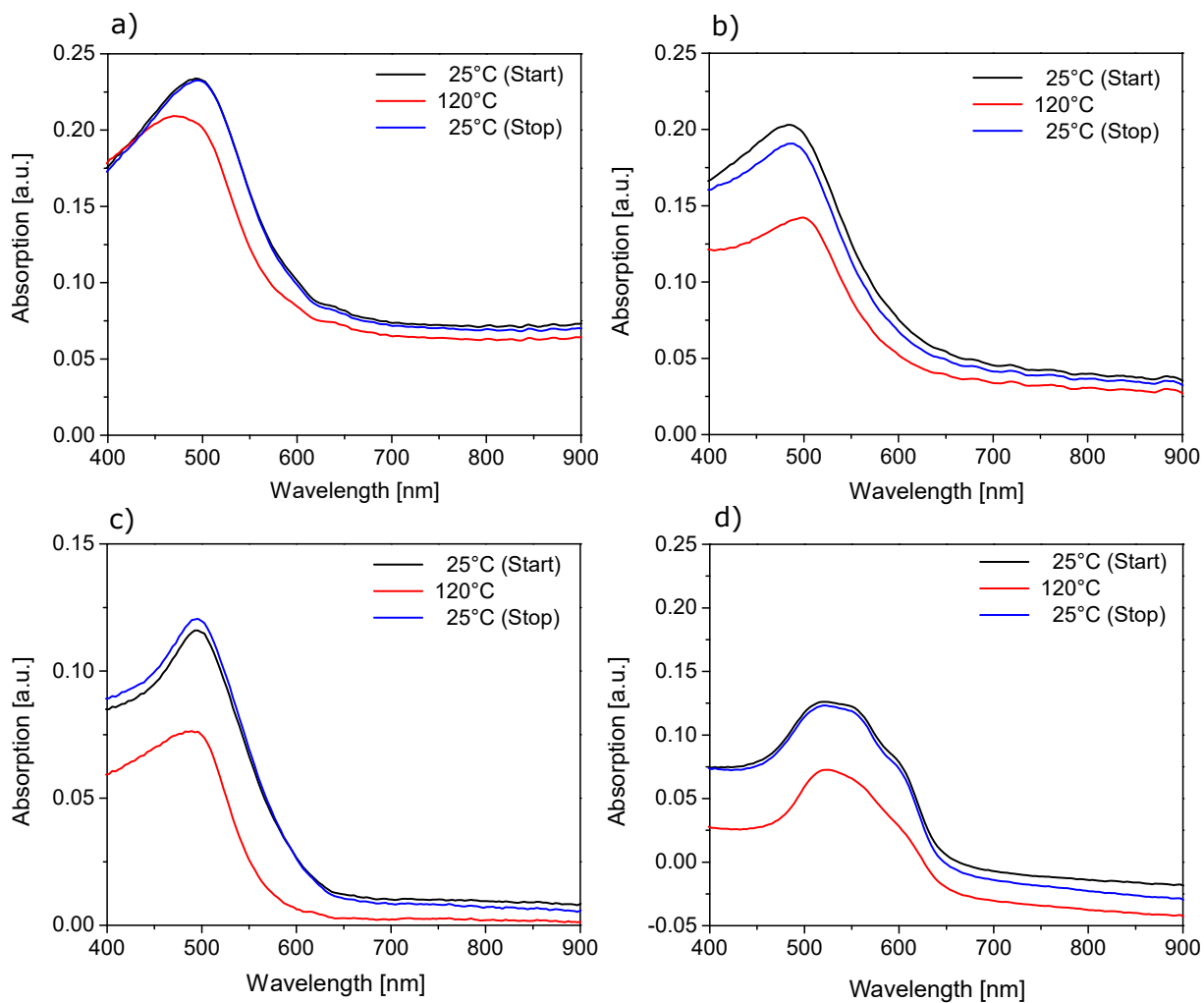


Figure A.10: In-situ UV/Vis absorption spectra on gold substrates during the temperature ramp at 29.8 mbar H₂O a) PTS-TBA from H₂O/THF, b) PTS-Na from H₂O/THF, c) PTS-TBA from H₂O and d) PTS-Na from H₂O.

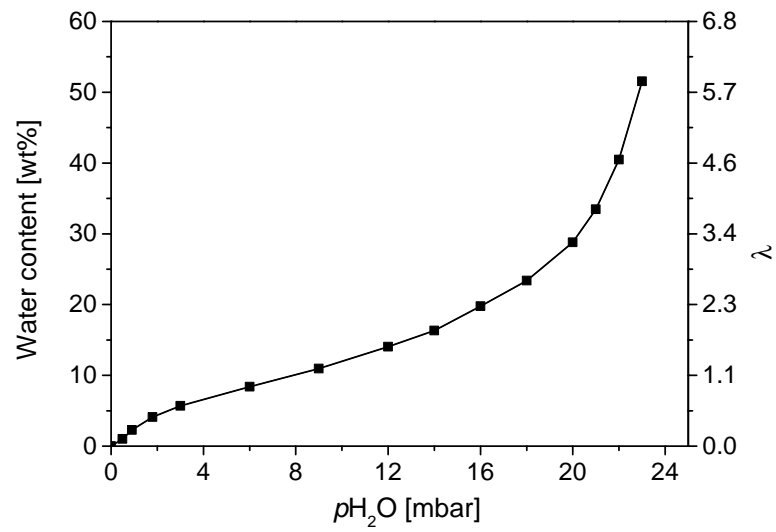


Figure A.11: Water uptake of PSS-Na at 25°C as function of water partial pressure.

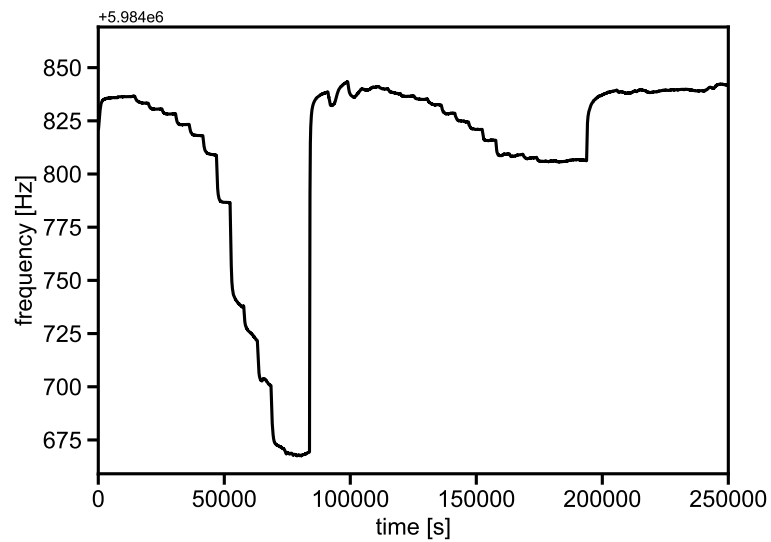


Figure A.12: Frequency trend of the water uptake measurement of PTS-Na at 25°C and 35°C.

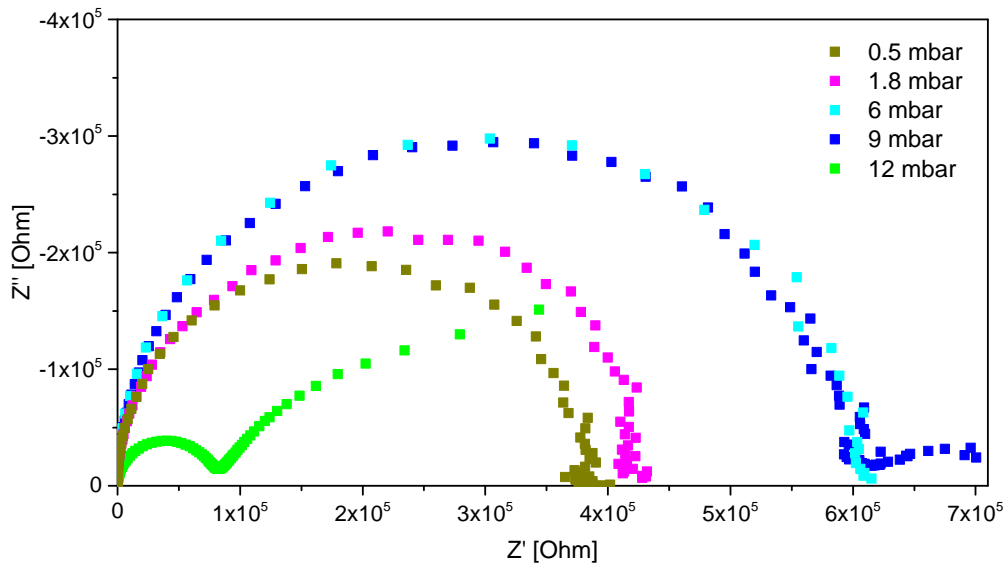


Figure A.13: AC impedance spectra of PTS-Na on a 5 μm IDE spin coated from aged solution at 25°C and various water partial pressures.

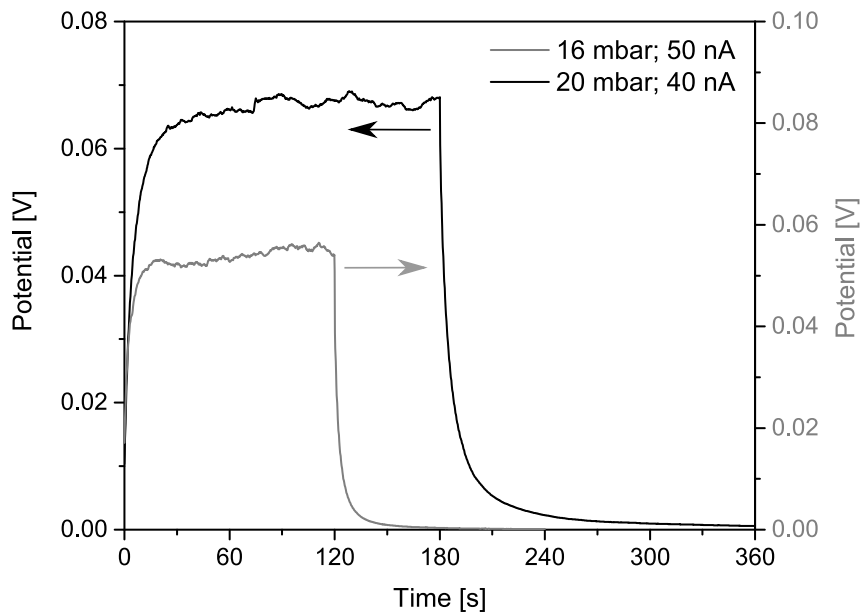


Figure A.14: DC measurements of PTS-Na on a 5 μm IDE spin coated from aged solution at 25°C and various water partial pressures.

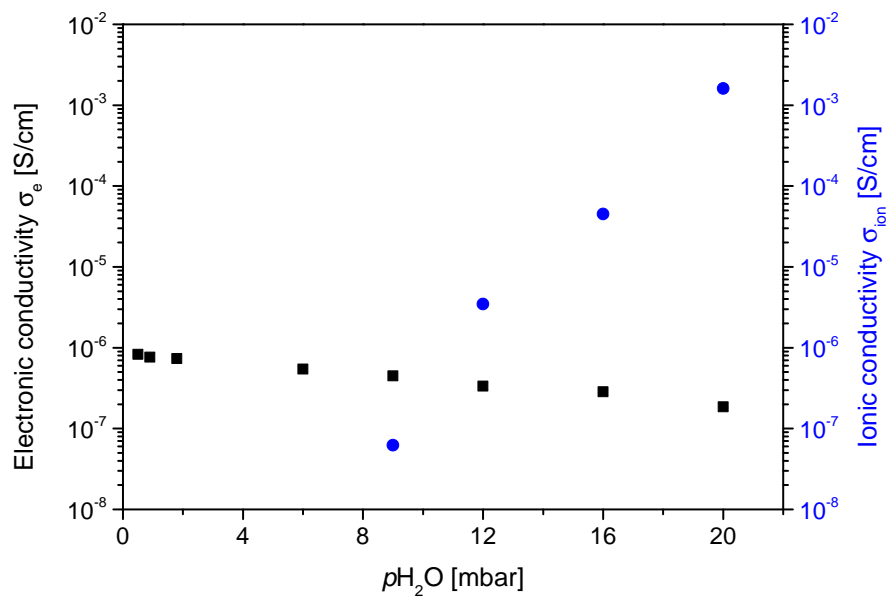


Figure A.15: Electronic and ionic conductivities of PTS-Na on a 5 μm IDE spin coated from aged solution at 25°C as function of water partial pressure.

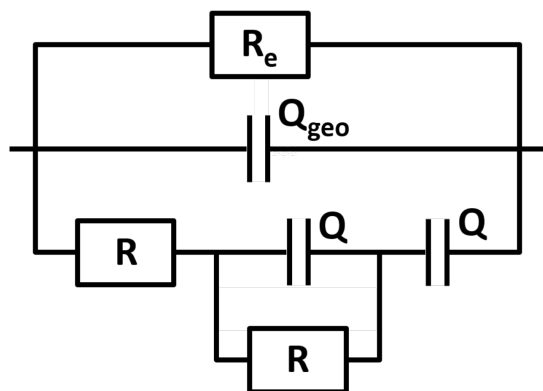


Figure A.16: Equivalent circuit for fitting AC impedance spectra with mid-frequency feature.